Department of Chemistry

Synthesis and Molecular Level Characterisation of Amorphous Microporous Networks

Thesis submitted in accordance with the requirements of the University of Liverpool for the degree of Doctor of Philosophy

By

Andrea Laybourn

September 2012

Dedication

This thesis is dedicated to my mum, dad and John.

No matter what life has dealt us, we have gotten through it together.

Acknowledgements

During the time it has taken to complete my PhD. many people have provided support, guidance and encouragement. Those who know me well would agree that I could write a whole thesis in acknowledgement of these people, however, the brightest stars are as follows:

I am very grateful to Andy Cooper for giving me the opportunity to undertake this research. Thank you for your enthusiasm, suggestions and towards the latter stages of this work, compassion.

I am truly indebted and thankful to Dave Adams for providing me with constant support in my project, future career and personal life. Thank you for the many hours spent reading versions of my thesis and discussing ideas and results. I couldn't have accomplished this work without you.

My sincere gratitude goes to Yaroslav **Z.** Khimyak without whom completion of this project would have been extremely difficult indeed. Although his supervision techniques have sometimes seemed harsh, I know he has always strived to get the best out of me. He has looked after every member of the ssNMR group during each of our individual PhD. journeys, adopting additional roles such as diplomat, confidante, counsellor and protector.

Thank you to members of the teaching staff, most notably Andrew Fogg and Darren Bradshaw, who have provided both academic support and interesting conversations about life during demonstrating sessions.

My utmost appreciation goes to Rob Clowes and Sean Higgins for help with processing data and technical assistance with the TGA, DSC, NMR, IR and gas sorption equipment. Also thank you to Tony Ellis for feeding our NMR magnet and working around my weekend work schedule.

Thank you to all of the secretarial and support staff, in particular Debbie Hitchell and Ann Coyne, for looking after me throughout my many years in the Chemistry Department.

I would also like to express my gratitude to my fellow Cooper Troopers, past and present. Thank you for interesting group talks, meetings and memorable BBQs. Special mentions go to Jia-Xing Jiang and Shijie Ren for providing me with interesting

materials to analyse, Tom Hasell for collecting EDX and SEM data, James Jones for sharing his invaluable ssNMR expertise, and Ev Stockel for all of her help in the lab. I am sincerely thankful to Rob Dawson for collecting tons of gas sorption data and SEM images, for his help in analysing gas selectivities and for sharing my enthusiasm for CMP materials. I would also like to thank Abbie Trewin for computer simulations and very helpful discussions.

Thank you to my undergraduate students, Josh and Georgie, for conducting additional experiments in the lab.

A big thank you goes to my friends in and around the department, Alex, Carly, Gemma and Fiona, for their support, understanding, and for keeping me smiling with welcome distractions of wine evenings, summer balls, games nights, Ann-themed parties, picnics, tea, Superlambanana hunting, running, shopping and the notorious Grad-school week. I hope we continue to share many more weird and wonderful adventures together.

My NMR family, Paul, Laura, Cate and Lucy have been there for me throughout. They have picked me up in the darkest of times, shared my elation when things worked, offered many hugs, advice, refuge and danced it all out with me on the nights out in town. I cannot think of another group of people with whom I would rather have shared this process with, you are my very best friends.

A special thanks goes to my mum, dad and John. Even though we each have had to deal with challenging and difficult times over the past few years, your encouragement, support and love has been endless. With our strength, endurance and humour, I truly believe that we can overcome the many obstacles that life throws in our path.

Last but certainly not least, a massive thank you to Craig who has saved me from multiple technology crises during the write-up stages, tolerated my extremely obnoxious moods when venting my frustration, patiently endured many, many long hours alone while I worked on my thesis, and moved his life to accommodate my career ambitions.

Abstract

Conjugated microporous polymers (CMPs) are a class of materials that have advantageous properties, such as extended π-conjugation, tuneable micropore size and surface area, and the ability to swell. Owing to the limited solubility and the amorphous nature of CMPs, little information is known about their structure and characterisation is dominated by solid-state NMR spectroscopy. NMR is a technique which is sensitive to both molecular level structure and dynamics. An increase in understanding of these networks is required to give an overall picture of their physical properties and origins of flexibility, ultimately leading to the design of such materials for specific applications.

In addition to the challenges with characterisation, a considerable disadvantage of CMPs is the cost of their synthesis. Many of the current routes to CMPs involve the use of heavy metal catalysts. Development of methodologies that use cheap monomers and do not require metal catalysts would increase the viability of CMPs for use in industrial applications.

In this work advanced structural elucidation and investigations of network flexibility and porosity were achieved using two approaches. The first involves identification of a reaction mechanism for the formation of CMP-1 by examination of the products of reaction after incremental time periods. The second involves employing advanced solid-state NMR techniques, specifically deuterium NMR, to probe the molecular motions of deuterated versions of CMP-1 and CMP-2. Swelling experiments of CMP-1 and CMP-2 with benzene-d_6 were also used to investigate changes in porosity for swollen and non-swollen networks.

A new synthetic route to CMPs was also developed by exploiting the reaction between aldehydes and amines. In particular the formation of aminal linkages shall be explored, as this would allow preparation of branched networks from bi-functional monomers. Newly synthesised materials are to be fully characterised and their gas sorption properties will be analysed.

Publications and Presentations Arising from this Thesis

"Microporous copolymers for increased gas selectivity" R. Dawson, T. Ratvijitvech, M. Corker, **A. Laybourn**, Y. Z. Khimyak, A. I. Cooper and D. J. Adams, *Polym. Chem.*, **2012**, *3*, 2034-2038.

"Porous, fluorescent, covalent triazine-based frameworks *via* room-temperature and microwave-assisted synthesis" S. Ren, M. J. Bojdys, R. Dawson, **A. Laybourn**, Y. Z. Khimyak, D. J. Adams, and A. I. Cooper, *Advanced Materials*, **2012**, *24*, 2357-2361.

"Functional Conjugated Microporous Polymers: From Benzene to 1,3,5-triazine" S. Ren, R. Dawson, **A. Laybourn**, J-X. Jiang, Y. Z. Khimyak, D. J. Adams, and A. I. Cooper, *Polym. Chem.*, **2012**, *3*, 928-934.

"Branching out with aminals: Microporous organic polymers from di-functional monomers" **A. Laybourn**, R. Dawson, R. Clowes, J. A. Iggo, A. I. Cooper, Y. Z. Khimyak, D. J. Adams, *Polym. Chem.*, **2012**, *3*, 533-537.

"Metal-organic Conjugated Microporous Polymers" J-X. Jiang, C. Wang, **A. Laybourn**, T. Hasell, R. Clowes, Y. Z. Khimyak, J. Xiao, S. J. Higgins D. J. Adams and A. I. Cooper, *Angew. Chem., Int. Ed.*, **2011**, *50*, 1072-1075.

"High surface area conjugated microporous polymers: The importance of reaction solvent choice" R. Dawson, **A. Laybourn**, Y. Z. Khimyak, D. J. Adams and A. I. Cooper, *Macromolecules*, **2010**, *43*, 8524-8530.

"A metal-organic framework with a covalently prefabricated porous organic linker" S. I. Swamy, J. Bacsa, J. T. A. Jones, K. C. Stylianou, A. Steiner, L. K. Ritchie, T. Hasell, J. A. Gould, **A. Laybourn**, Y. Z. Khimyak, D. J. Adams, M. J. Rosseinsky and A. I. Cooper, *J. Am. Chem. Soc.,* **2010**, *132*, 12773-12775.

"High surface area contorted conjugated microporous polymers based on spiro-biproplenedioxythiothiophene" J-X. Jiang, **A. Laybourn**, R. Clowes, Y. Z. Khimyak, J. Bacsa, S.J. Higgins, D.J. Adams and A.I. Cooper, *Macromolecules*, **2010**, *43*, 7577-7582.

"Functionalized conjugated microporous polymers" R. Dawson, **A. Laybourn**, R. Clowes, Y. Z. Khimyak, D. J. Adams and A. I. Cooper, *Macromolecules*, **2009**, *42*, 8809-8816.

Oral Presentations

"Conjugated Microporous Polymers: A Solid State NMR Study," July 2011, MACRO Young Researchers Meeting, University of Liverpool, UK. (Third Prize of £250 awarded).

Poster Presentations

"Solid-State NMR Studies of Deuterated CMPs," EUROMAR, August 2011, Frankfurt, Germany. (Student stipendium of 500 euros awarded).

"Molecular Level Characterisation of Functionalised Conjugated Porous Polymers by Solid-State NMR," Catalysis Summer School, July 2009, University of Liverpool, UK.

List of Abbreviations

ANW	Poly(azomethine) networks
BCMA	9,10'-bis(chloromethyl) anthracene
BCMBP	4,4'-bis(chloromethyl)-1,1'-biphenyl
BET	Brauner Emmet Teller
BILP	Benz-imidazole linked polymer
CME	Chloromethyl ether
CMP	Conjugated microporous polymer
COF	Covalent organic framework
CP	Cross-polarization
CSA	Chemical shift anisotropy
CTF	Covalent triazine frameworks
(*p*-DCX)	*para*-dichloroxylene
DMF	*N,N*-dimethylformamide
DMSO	Dimethylsulphoxide
DSC	Differential scanning calorimetry
EDX	Energy dispersive X-ray analysis
EOF	Element organic framework
FTIR	Fourier transform infra-red
GPC	Gel permeation chromatography
h	hours
HCP	Hyper-crosslinked polymers
HMB	Hexamethylbenzene
HPLC	High performance liquid chromatography
Im	Imidazolate
IUPAC	International Union of Pure and Applied Chemistry
IR	Infra-red
K	Kelvin
M	Metal

MAS	Magic angle spinning
min	minutes
MOF	Metal organic framework
MOP	Microporous organic polymer
NLDFT	Non-local density functional theory
NMP	*N*-Methyl-2-pyrrolidone
NMR	Nuclear magnetic resonance
PAE	Poly(aryleneethynylene)
PAF	Poly-aromatic framework
PECONF	Porous electron-rich covalent organonitridic frameworks
PIM	Polymers of intrinsic microporosity
POF	Porous organic framework
PPN	Porous polymer networks
ppm	parts per million (chemical shift)
PXRD	Powder X-ray diffraction
Q_{cc}	Quadrupolar coupling constant
SA_{Lang}	Langmuir surface area
SA_{BET}	BET surface area
SEM	Scanning electron microscopy
SNW	Schiff-base networks
T_{dec}	Temperature of onset of thermal decomposition
TFMS	Trifluoromethanesulfonic acid
T_g	Glass transition temperature
TGA	Thermogravimetric analysis
THF	Tetrahydrofuran
TMS	Tetramethylsilane
TPPM	Two phase pulse modulation
T_1	Spin-lattice/longitudinal relaxation
ZIF	Zeolitic imidazolate frameworks

Contents

List of Figures

List of Tables

Chapter 1:

Introduction

To put the research detailed in this thesis into context, the literature covered in this chapter encompasses many topics under the main theme of microporous materials. The first section discusses the different classes of porous solids and provides some examples of the microporous materials that are most relevant to this work. The second section describes the differences between crystalline and amorphous microporous materials. Since the main focus of this research is characterisation of amorphous networks, an overview of the methods used to characterise these materials is provided. However, more detailed technical descriptions of the characterisation techniques are given in **Chapter 2**.

1.1 Microporous materials

Porous solids are classified by the International Union of Pure and Applied Chemistry (IUPAC) according to their pore sizes.[1] Macroporous materials contain pores with widths greater than 50 nm. Mesoporous materials possess pore widths in the range of 2 to 50 nm. Finally, microporous materials have pore widths less than 2 nm. Although microporous materials are the main focus of the work in this thesis, some of the materials investigated also consist of meso- and macropores.

Much of the initial interest over microporous materials came from their potential application in areas such as gas storage,[2-5] separations[6] and heterogeneous catalysis.[7-9] However, owing to the increasing structural diversity of these materials, it has now become possible to exploit them in a wider variety of applications, examples of which are discussed below.

1.1.1 Types of microporous materials

1.1.1.1 Metal organic frameworks

Since the discovery of a permanently porous metal organic framework (MOF) by Yaghi and co-workers,[10] the area of MOF research has grown significantly.[11]

MOFs are a class of crystalline microporous materials synthesised by combination of a metal ion or cluster and an organic linker. Porosity is achieved by incorporation of an organic linker with more than one bonding site, thus leading to three-dimensional frameworks. For example, one of the most widely studied frameworks[12], MOF-5, is constructed from $Zn_4(O)O_{12}C_6$ clusters with a bi-dentate 1,4-benzenedicarboxylic acid linker.[10] The structure of MOF-5 is given in **Figure 1-1**.

This text box is where the unabridged thesis included the following third party copyrighted material:

"Design and synthesis of an exceptionally stable and highly porous metal-organic framework"
Li, H., Eddaoudi, M., O'Keeffe, M., Yaghi, O.M.,
Nature 1999, *402*, 276-279.

Figure 1-1: Structure of MOF-5. ZnO_4 tetrahedra (blue). Carbon atoms (grey). Oxygen atoms (green). Each unit cell contains eight clusters (seven visible) with a pore volume represented by a yellow sphere. Figure adapted from reference [10].

An advantage of their crystalline structure is that MOFs have well-defined pore sizes. Indeed, the ability to systematically vary the pore size of MOFs by increasing the size of the organic linker was demonstrated in 2002.[13]

Much of the initial interest over MOFs came from their high surface areas, enabling them to be exploited as gas storage materials in energy-related technologies.[14] The record for highest reported SA_{BET} (Brauner Emmet Teller surface area) for a metal-containing porous material is currently held by MOF-210 (6240 m^2g^{-1}).[15] However, other properties of MOFs, for example luminescence,[16] selective sorption[17], exposed metal sites and synthetically modified organic linkers,[14] have allowed the frameworks to be useful in further applications. Such applications include sensors,[16] gas separations,[17] biotechnology[18] and catalysis.[19, 20]

1.1.1.2 **Zeolitic imidazolate frameworks**

Zeolitic imidazolate frameworks (ZIFs) are a sub-class of MOFs. They are synthesised by reaction between a tetrahedral metal ion and an imidazolate linker, see **Scheme 1-1**.[21] Such materials possess crystalline structures analogous to zeolites.[22]

Many ZIFs have high chemical and thermal stability (up to 500 °C)[23] compared with other MOFs. For example, ZIF-8 can withstand several treatment conditions such as boiling in water or alkaline solutions and refluxing in organic solvents, without degradation of crystallinity or porosity.[23]

ZIFs exhibit SA_{BET} of around 1700 m^2g^{-1} and are able to selectively adsorb CO_2 from industrial gas mixtures.[21]

Scheme 1-1: Structural unit found in ZIFs. The unit comprises of tetrahedral metal ions (e.g. Zn, Co, Fe) bridged by an imidazolate.[21] The M-Im-M bond is analogous to the Si-O-Si bond found in zeolites.[24]

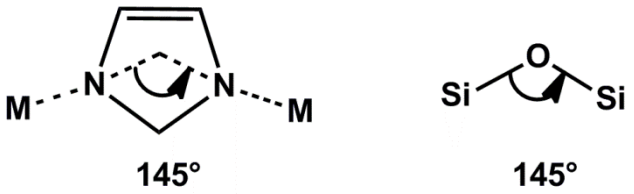

1.1.1.3 Covalent organic frameworks

Covalent organic frameworks (COFs) were first reported in 2005 by Yaghi and co-workers.[25] COFs are synthesised by self-condensation of boronic acids, for example benzene-1,4-diboronic acid (COF-1, **Scheme 1-2**).[25, 26] Another route to COFs involves reaction between boronic acids and alcohols, for example COF-5 (**Scheme 1-2**).[25, 26] Both methods lead to the formation of strong boron-oxygen covalent bonds.[27]

As COFs are porous, they have been established as materials for gas storage, particularly hydrogen, methane and carbon dioxide.[26]

A notable advancement in the area of COF research was the development of three-dimensional COFs, synthesised from reactions of tetrahedral monomers (**Scheme 1-2**).[28] The SA_{BET} of these materials were increased from *ca.* 1590 m^2g^{-1} for 2-D COFs, [25] to *ca.* 4210 m^2g^{-1} for 3-D COF-103.[26, 28] Such an increase in surface area resulted in the ability of COFs to adsorb greater quantities of gas. [26, 28]

Scheme 1-2: Examples of the condensation reactions used to synthesise COFs. Figure adapted from reference [26].

COFs have also been synthesised as photoconductive materials. For example, a luminescent, semi-conducting COF synthesised by self-condensation of pyrene di-boronic acid was reported by Wan *et al.*[29]

Another route to 3-D COFs was also demonstrated by reaction between tetra-(4-anilyl)methane and terephthaldehyde. The resulting framework (entitled COF-300) was found to consist of imine-linkages with an apparent SA_{BET} of 1360 m^2g^{-1}.[30]

1.1.1.4 Covalent Triazine frameworks

Covalent triazine frameworks (CTFs) are synthesised *via* trimerization of aromatic nitriles at temperatures in the range 400-700 °C (**Scheme 1-3**). The

reaction involves use of molten zinc chloride as both a solvent and catalyst. In some cases, SA_{BET} of *ca.* 3000 m^2g^{-1} have been reported for these materials.[31, 32] CTFs have high thermal stability and **CTF-1**[33]and **CTF-2**[34] also showed a limited degree of crystalline order.

Scheme 1-3: Reaction scheme to show the trimerisation of terephthalonitrile which leads to the formation of a 2-D CTF (idealised structure). Scheme adapted from references [31] and [33].

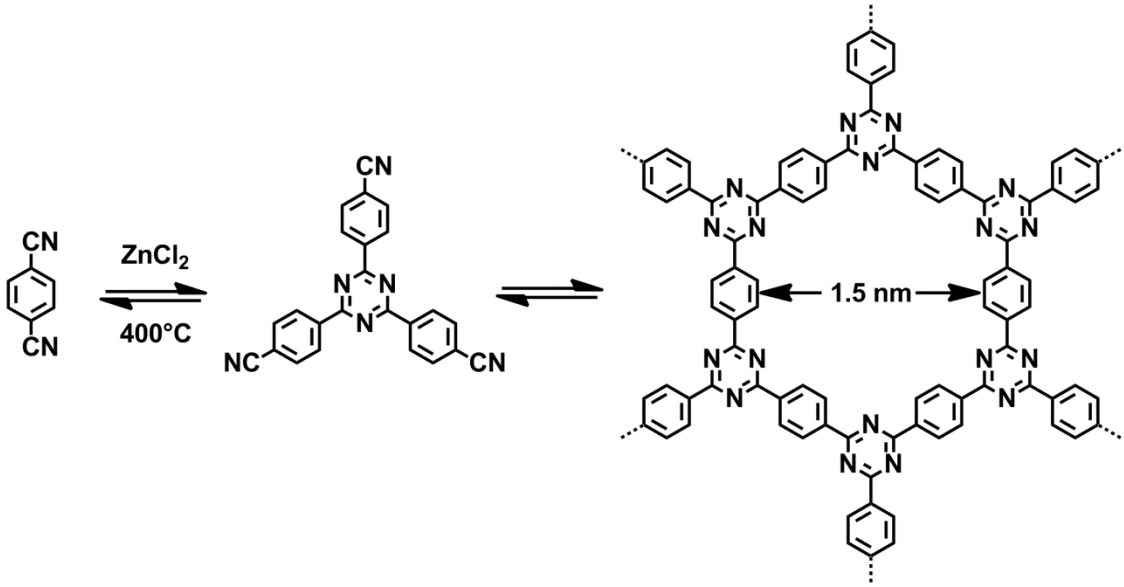

A significant disadvantage of these materials is their ionothermal synthesis conditions. Not all monomers are able to withstand such harsh reaction conditions (*i.e.* heating above 500 °C in molten zinc chloride) and the materials also suffer from a degree of carbonization.[33] Recently, Ren *et al.* reported the synthesis of CTFs *via* microwave and room temperature methods using a trifluoromethanesulfonic acid (TFMS) catalyst.[35] The resultant materials did not suffer from carbonization and as a result of the milder reaction conditions; polymerisation using less stable monomers was achieved.

1.1.1.5 **Polymers of intrinsic microporosity**

Polymers of intrinsic microporosity (PIMs) were first reported in 2002 by McKeown *et al.*[36, 37] They are synthesised by dioxane-forming reactions between *ortho*-dihalides (specifically fluoro- and chloro-aromatic monomers) and aromatic *ortho*- or *meta*-diols. PIMs exhibit SA_{BET} of *ca.* 400 – 1200 m^2g^{-1}. Microporosity in PIMs arises from poor packing in the solid state due to a contorted centre incorporated into the polymer backbone.[38] Dependent upon the monomer precursors, the resulting materials form either networks[39] or linear polymers,[40] **Scheme 1-4**.[39]

A unique advantageous property of linear PIMs is their solubility. Solution-processing enables these materials to be cast into porous films,[41] which may allow them to be exploited as gas separation membranes.[42] Solubility is also an advantage from a characterisation point-of-view, *i.e.* the molecular weights of linear PIMs can be experimentally derived.[40]

Scheme 1-4: Examples of the monomer combinations used to synthesise network and linear PIMs. 'RS' denotes the number of reactive sites that will dictate the dimension of the resultant networks. Scheme adapted from reference [39].

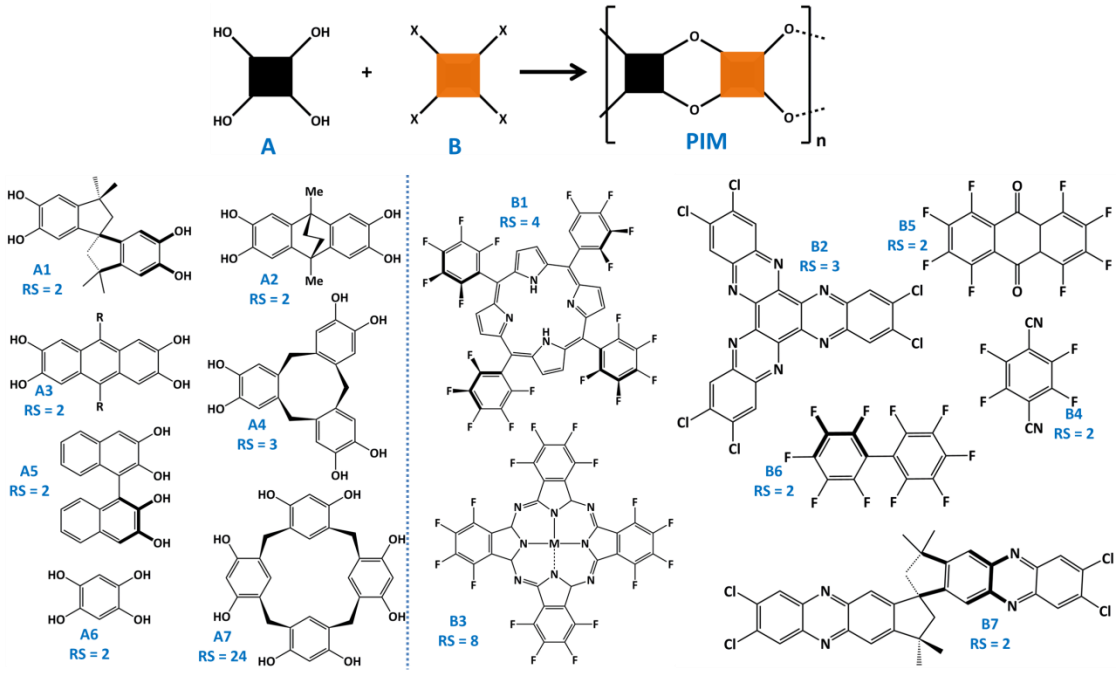

1.1.1.6 **Hyper-crosslinked polymers**

Hyper-crosslinked polymers (HCPs) were introduced by Davankov and co-workers in the 1970s.[43] Traditionally, HCPs are prepared *via* Friedel-Crafts reactions between highly swollen, lightly cross-linked, polystyrene and suitable bi-functional alkylating agents in the presence of a Lewis acid catalyst, such as iron(III) chloride,[44-48] Alkylating agents can either be present in the styrene network (*e.g.* as chloromethyl pendant groups,[49] **Scheme 1-5 (A)**) or they can be introduced externally, for example chloromethyl ether (CME)[50] and 1,4-dichloromethane (**Scheme 1-5 (B)**),[51] to name but a few. The structures given in **Scheme 1-5**[52] are a simplified representation of HCP networks, in reality the

position of crosslinks, amount of end groups and even macrocycles may exist within these materials.[53]

Scheme 1-5: Routes to Davankov-HCPs by formation of a methylene crosslink between two poly(4-vinylbenzyl chloride) networks (**A**) or polystyrene (**B**). Scheme adapted from reference [52].

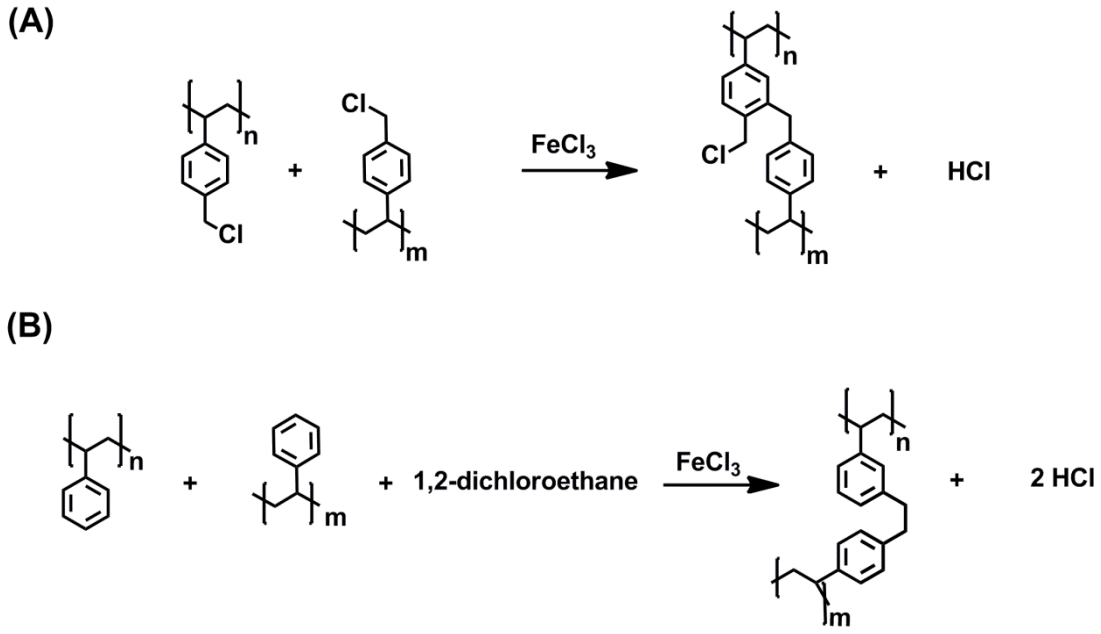

The Davankov approach involves exploitation of the enhanced distance between polymer chains in solvent-swollen polystyrene. Microporosity is achieved by rigidifying the swollen polymer with cross-links, thus preventing the collapse of the porous framework after the removal of solvent.[52] Surface areas of up to 2000 m^2g^{-1} have been reported.[49]

HCPs find application in areas such as stationary phases in high performance liquid chromatography (HPLC),[54, 55] separations of organic vapours[56] and liquids,[57] and ion-exchange resins.[58]

Recently, a direct method of preparing HCPs was reported by Wood *et al.*[4] This route negated the use of swollen cross-linked precursors. Microporous networks were constructed *via* Friedel-Crafts cross-linking between the following

bis(chloromethyl) monomers, *para*-dichloroxylene (*p*-DCX), 4,4'-bis(chloromethyl)-1,1'-biphenyl (BCMBP) and 9,10'-bis(chloromethyl) anthracene (BCMA), **Scheme 1-6**.[4]

Scheme 1-6: Monomers used to prepare HCPs by direct polymerisation.[4]

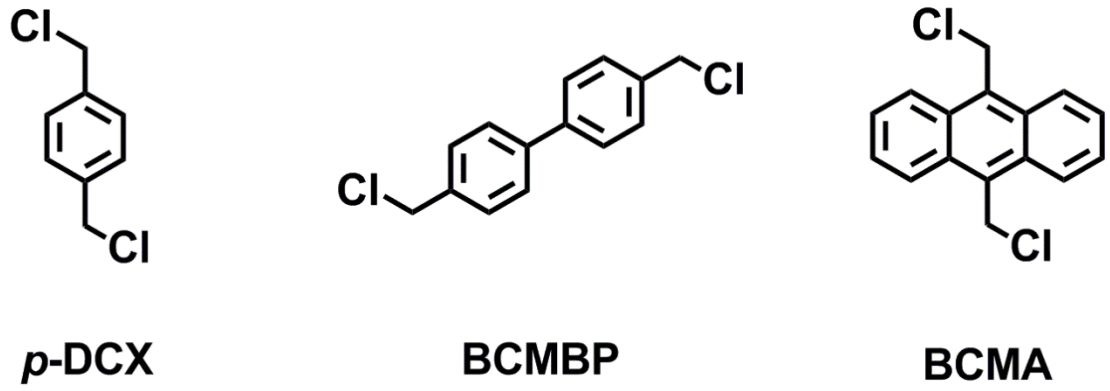

HCPs prepared *via* the direct polymerisation method exhibit SA_{BET} of up to 1900 m^2g^{-1} and have been investigated for the storage of hydrogen,[4] methane[59] and carbon dioxide.[60]

More recently, other routes for preparing HCPs have been reported. Some examples include, organo-lithiation reactions, which are used to prepare element organic frameworks (EOFs),[60] and CH_2 cross-linked linear polyaniline and polypyrroles.[61]

1.1.1.7 **Conjugated microporous polymers and analogues**

Conjugated microporous polymers (CMPs) are a class of materials predominantly synthesised *via* metal-catalysed reactions. Much of the research interest over CMPs arises from their unique extended π-conjugation, giving rise to potential applications in areas such as organic electronics and optoelectronics.[62-64]

CMPs, specifically poly(aryleneethynylene)s (PAEs), were first reported in 2007 by Jiang *et al.*[65] and are the focus of the work described in this thesis. PAEs are synthesised by Sonogashira-Hagihara palladium-catalysed cross-coupling reactions between aromatic halides and ethynylbenzene.[65, 66] A series of five PAE/CMPs were prepared with SA_{BET} of up to 1000 m^2g^{-1}, **Scheme 1-7**.[66]

Scheme 1-7: Simplistic structural representations of a series of PAE networks. The benzene 'nodes' are shown in red. Scheme adapted from reference [66].

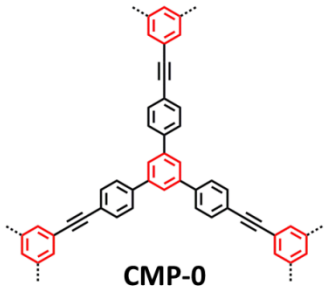

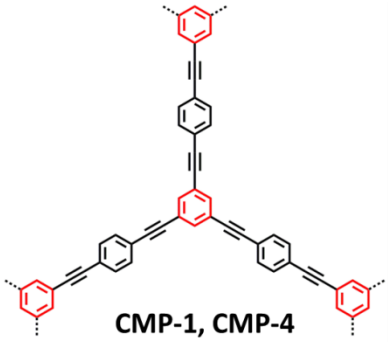

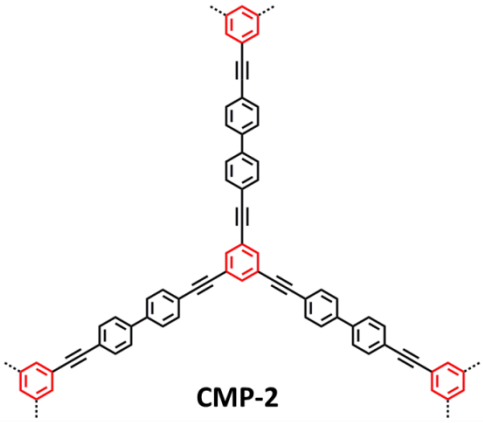

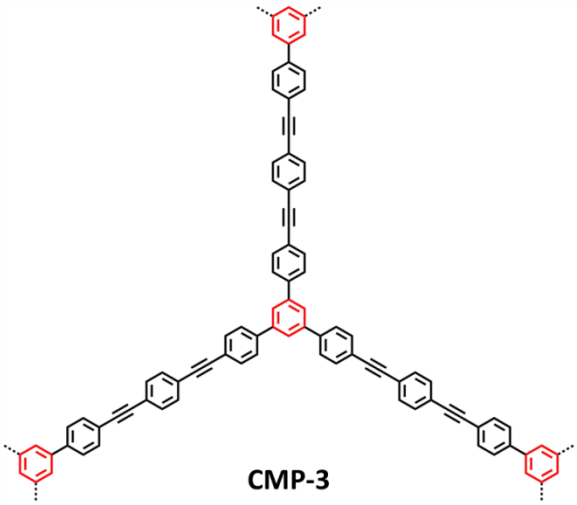

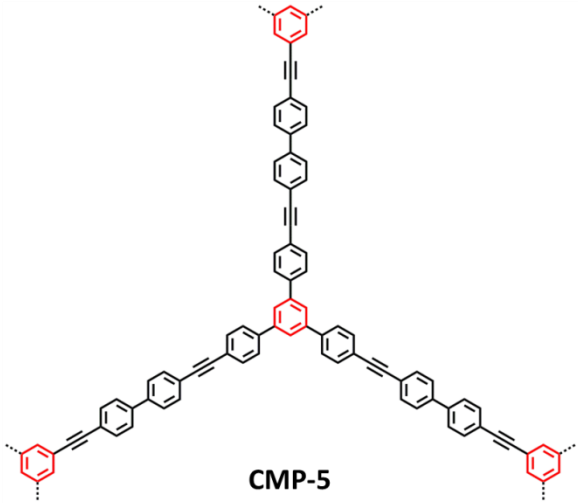

Interestingly, even though these materials lack long-range order, control over gas sorption properties, such as pore size, micropore volume and SA_{BET} was demonstrated by systematic variation of the strut length.[65, 66] For this series of CMP networks, the total number of benzene links per strut increases incrementally by one from two benzenes (CMP-0) to six benzenes (CMP-5). CMPs with longer struts were found to have the largest pore sizes. However, a decrease in both pore volume and SA_{BET} were observed with increasing strut length (**Figure 1-2**).[66] Such behaviour was ascribed to an increase in flexibility of the polymer struts with strut length, thus leading to a greater degree of interpenetration.[66] Indeed, these hypotheses were supported by atomistic simulations (**Figure 1-2**).[66] Disordered interpenetrated networks were calculated as the most energetically favourable structures and an increase in framework flexibility of the models were found with increasing strut length.[65, 66]

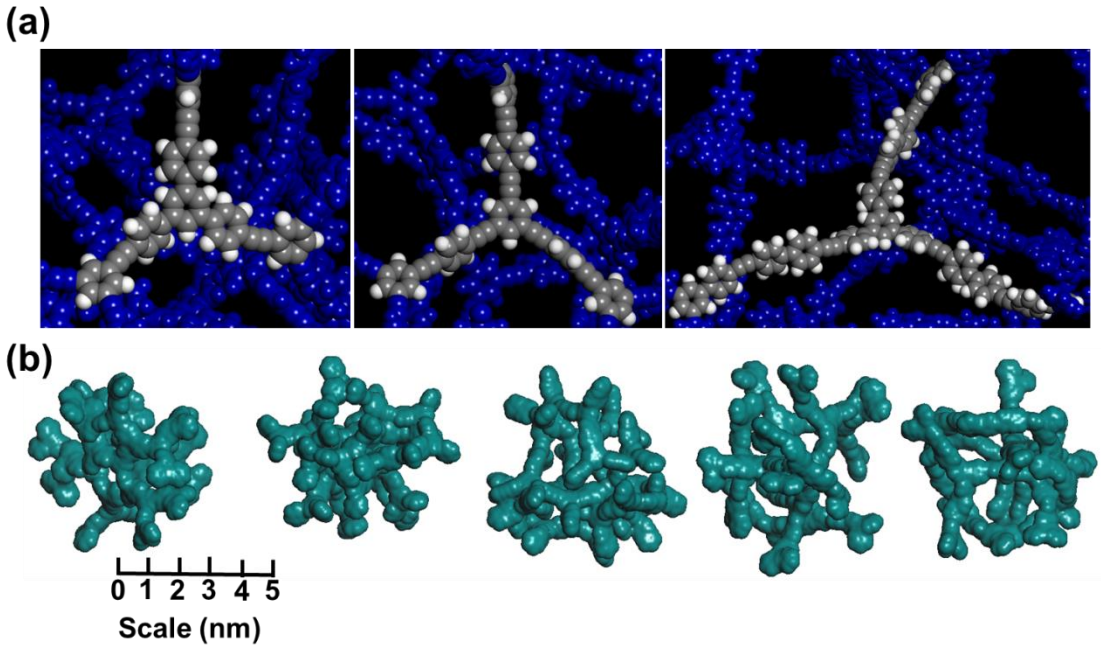

Figure 1-2: Atomistic simulations for CMP networks with different strut lengths. (a) Node-strut topology for simulated network fragments for CMP-0 (left), CMP-1 (centre), and CMP-5 (right). A benzene-node and corresponding struts are highlighted (in grey/white) in each case. (b) Atomistic simulations of network fragments for CMP-0, CMP-1, CMP-2, CMP-3, and CMP-5 (left to right). The

solvent-accessible surface is represented in green and was calculated using a solvent diameter of 0.182 nm. Figure adapted from reference [66].

Further investigations into the effect of strut lengths upon the gas sorption properties of CMPs led to the preparation of a number of co-polymer networks (CPNs), **Scheme 1-8**.[66]

Scheme 1-8: Synthetic route to CMP co-polymers. Figure adapted from reference [66].

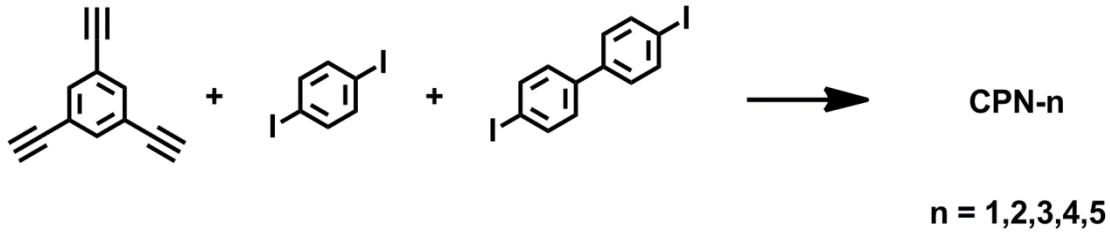

The statistical co-polymerisations further established the ability to fine-tune the gas sorption properties of these materials to a higher degree. Systematic variation of the amount of halogenated monomers led to an orderly reduction in the surface area and cumulative pore volume of the resultant materials (**Figure 1-3**).[66] Such data provided the first indication that crystallinity is not a prerequisite for control over the microporous properties of organic frameworks.

Figure 1-3: N_2 adsorption-desorption isotherms measured at 77.3 K (a) Adsorption (filled symbols), desorption (hollow symbols). For clarity, the isotherms of CPN-1, CPN-2, CPN-3, CPN-4, and CPN-5 are shifted vertically by 500, 400, 300, 200, and 100 cm^3g^{-1}, respectively. NL-DFT pore size distribution curves (b). Cumulative pore volume curve calculated using NL-DFT methods (c). Figure from reference [66].

In addition to the cross-coupled PAE networks, homocoupling routes have also been used to prepare CMP-type materials.[67] Combination of 1,3,5-triethynylbenzene and 1,4-diethynylbenzene led to the formation of poly(phenylene butadiynylene) networks (PPBs) with SA_{BET} up to 842 m^2g^{-1}.[67] The structures of these materials are more complex than those found for PAEs, as they consist of both butadiynylene and 1,3-disubstituted enyene crosslinks (**Scheme 1-9**), as evidenced by broad aromatic peaks in the NMR spectra.[67]

Scheme 1-9: Synthetic route to homocoupled CMP networks (PPB/HCMPs) showing representations of the linear butadiynylene and 1,3-disubstitued enyene cross-linked structures of HCMP-2. Scheme adapted from reference [67].

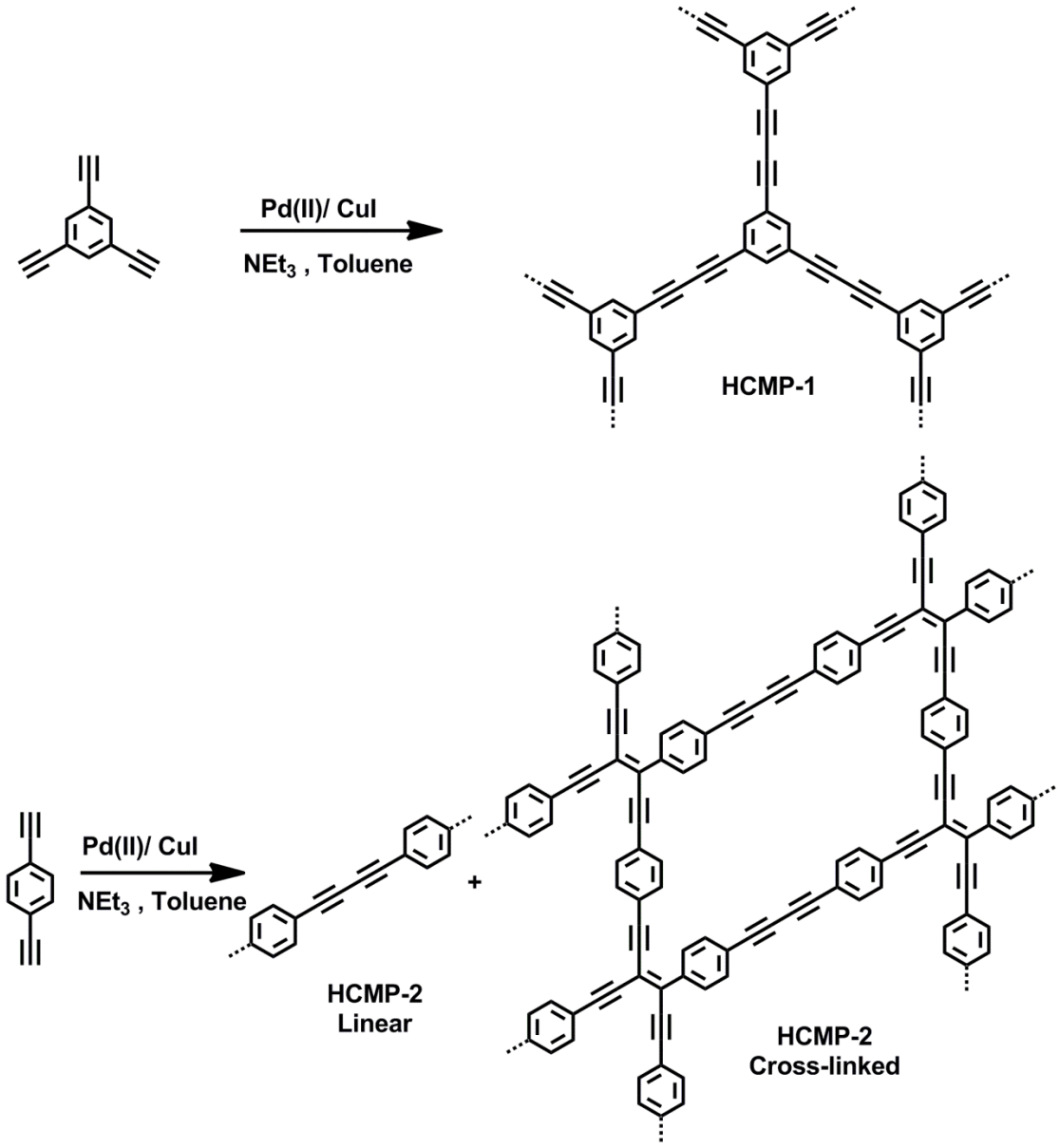

Since the first reports of CMPs, numerous variations and analogues of these materials have been synthesised *via* Sonogashira-Hagihara coupling reactions. A few examples include poly(tris(4-ethynylphenyl)amine)s,[68] spirobifluorene-containing materials,[69] triazine centred frameworks,[70] and a series of CMP networks containing different functional pendant groups.[71]

In addition to Sonogashira-Hagihara palladium coupling reactions, other metal-catalysed methods can be used to prepare CMP-like materials, such as Suzuki and Yamamoto reactions. For example, a polyphenylene-based light-

harvesting CMP network synthesised *via* the Suzuki cross-coupling route was reported by Chen and co-workers.[72] Another example includes the synthesis of a series of pyrene-based porous fluorescent CMP networks *via* Yamamoto chemistry.[73] The emission colour of this series was systematically altered by tuning the band-gap,[73] evoking the possibility of their use in organic electronics,[62, 63] optoelectronics,[74, 75] or as sensing devices.[76]

Recently, Tan *et al.* have investigated CMPs as absorbent materials for separation of organic solvents from water.[77, 78] The CMP materials studied are direct analogues to those pioneered by Cooper *et al.*[65-67] Tan and co-workers' first paper reports the uptake of various organic solvents by HCMPs[77] (for structures, see **Scheme 1-9**). Remarkable absorbencies were observed, particularly for kerosene (1500 wt%) and ethyl acetate (1400 wt%).[77] The absorbency of these materials was positively related to their total pore volumes and SA_{BET}.[77] Similar methods were applied, by the same group, to CMP-4,[78] (for structure, see **Scheme 1-7**). Once again, exceptionally high absorbencies were noted, especially for aromatic solvents, such as bromobenzene (2000 wt%), benzene (1100 wt%) and nitrobenzene (1000 wt%).[78]

A significant advancement in the area of CMP research was achieved by the use of tetrahedral monomers,[79-83] **Scheme 1-10**.[84] Such monomers gave rise to the formation of three-dimensional networks exhibiting SA_{BET} as high as 5640 m^2/g (PAF-1)[83] and 6461 m^2g^{-1} (PPN-4),[80] which is the highest reported surface area of any material to date. Both networks are synthesised *via* Yamamoto homocoupling of tetrahedral monomers, PPN-4 from tetrakis(4-bromophenyl)adamatane[80] and PAF-1 from tetrakis(4-bromophenyl)methane.[83]

Scheme 1-10: Summary of microporous CMP-type organic networks prepared using tetrahedral monomers and metal-catalysed reactions. Scheme adapted from reference [84].

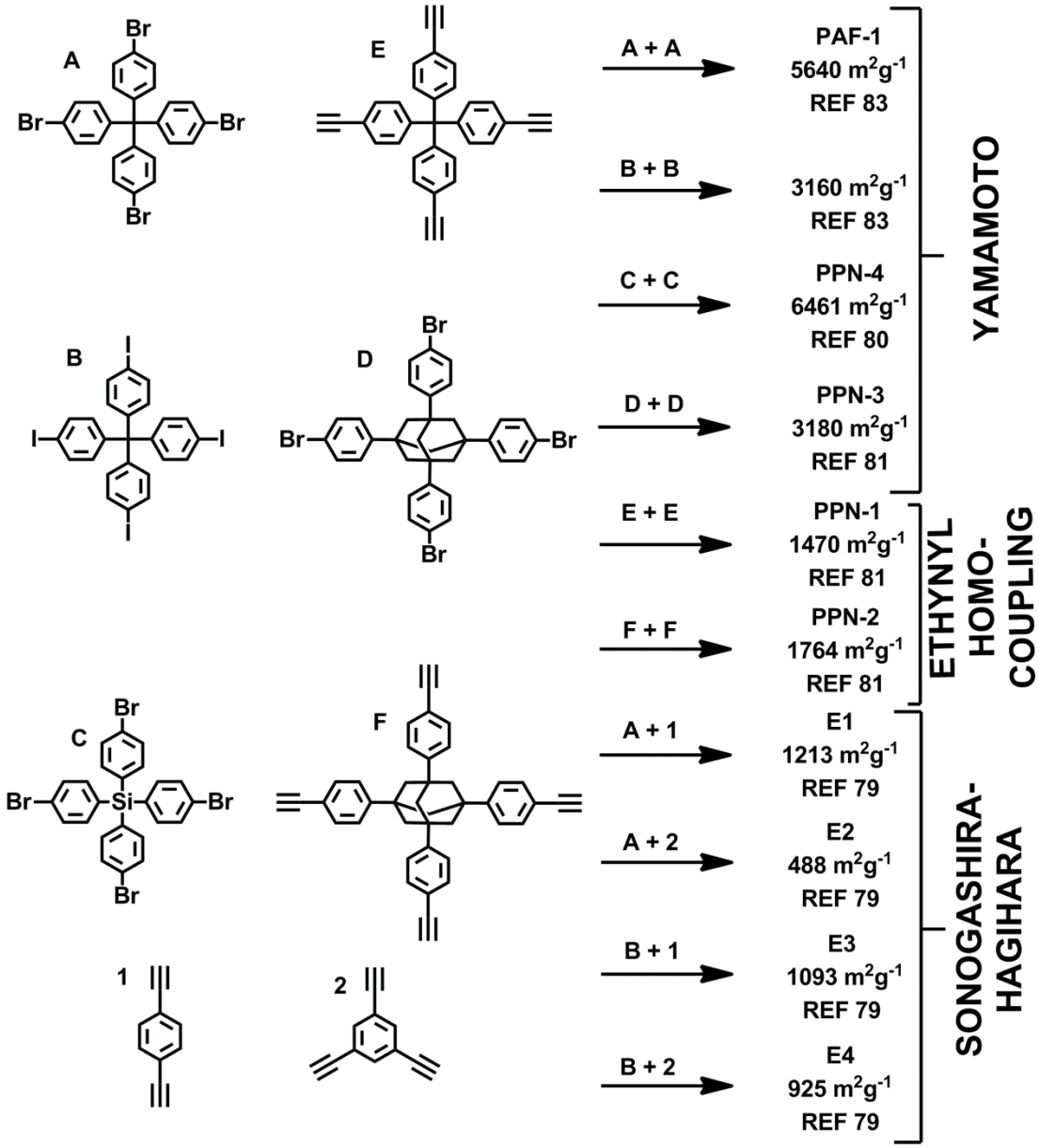

Recently, the gas storage capabilities of PAF-1 have been further improved.[85] By incorporation of lithium ions into the porous structure, enhanced adsorption enthalpies were achieved.[85] Increased gas uptakes of 22 %, 71 % and 320 % were reported for hydrogen (77 K, 1 bar), methane (77 K, 1.22 bar), and

carbon dioxide (273 K, 1.22 bar), respectively, compared with the original PAF-1 network.[85] Indeed lithiated PAF-1 currently has one of the highest CO_2 storage capacities (8.99 $mmolg^{-1}$, 273 K, 1.22 bar) reported for any material.[85-87]

So far, the preparations of CMP-type materials described here have involved the use of metal catalysts. Major disadvantages of metal-catalysed reactions include retention of heavy metals by the networks and cost. For example, CMPs obtained *via* Sonogashira-Hagihara coupling reactions use palladium and copper catalysts.[65] Similarly, the syntheses of PAF-1 and PPN-4 require stoichiometric quantities of nickel.[80, 83] Therefore, the development of alternative methods has been investigated. One promising route involves condensation reactions between aldehydes, ketones and amines. Indeed, the synthesis of CMPs *via* this pathway has been reported.[88-91] More details are given in the introduction of **Chapter 5**. However, perhaps one of the most propitious example is an aza-fused CMP synthesised by condensation of 1,2,4,5-benzenetetramine and triquinoyl hydrate.[92] The resulting network is a promising candidate for application in areas such as, porous super-capacitive energy storage and electric power supply devices.[92]

1.1.1.7.1 Future potential of CMPs and their analogues

CMPs show excellent promise as molecular sorbents and gas storage materials owing to their swelling ability and high surface areas, with some networks exhibiting the highest reported surface areas of any material to date. Moreover, fine tuning of physical properties such as pore size and surface area and absorbency has been demonstrated for CMP networks by varying the strut length and surface chemistry. A unique feature of CMPs is their extended π-conjugation, which may allow these materials to be exploited as organic sensors. A further advantage of CMPs is their high stability towards heat, air and moisture.

CMPs are typically prepared *via* metal-catalysed cross-coupling reactions.

These conditions offer two main benefits. Firstly, a wide variety of synthetic strategies can be adopted, such as reactions between functionalised monomers or post-synthetic modification of the networks. Secondly, the reactions are relatively mild compared with those used to synthesise other porous frameworks, for example CTFs, MOFs and COFs. However, a major disadvantage of the current routes to CMPs is cost. In order for CMPs to be useful for industrial applications, they will need to be synthesised in large quantities. Therefore it is vital to develop cheaper routes to CMPs.

1.1.2 Characterisation of microporous materials

It is possible to categorise microporous materials into two distinct areas, crystalline and amorphous networks.

Crystalline materials are defined as solids consisting of atoms, molecules or ions packed in an ordered manner.[93] Such materials have a unit cell that is repeated throughout the crystal lattice; **Figure 1-4 (B)**. Crystalline frameworks are generally formed during reversible reaction conditions,[38, 53] such as condensation reactions (COFs and MOFs)[10, 21, 25] and nitrile cyclisation methods (CTFs).[33] Currently, the accepted reasoning for formation of crystalline materials under reversible conditions is that crystal growth defects are re-dissolved, leading to the most thermodynamically stable structures.[25, 28, 30, 35, 53, 84, 94] However, the mechanism is poorly investigated.

Amorphous materials, on the other hand, do not possess long range order,[93] **Figure 1-4 (A, C, D)**. Such materials are often assembled under kinetic control *via* irreversible polymerisation reactions,[38, 53] for example the metal-catalysed routes used to synthesise HCPs and CMPs.[43, 65] Again the mechanism has not been investigated.

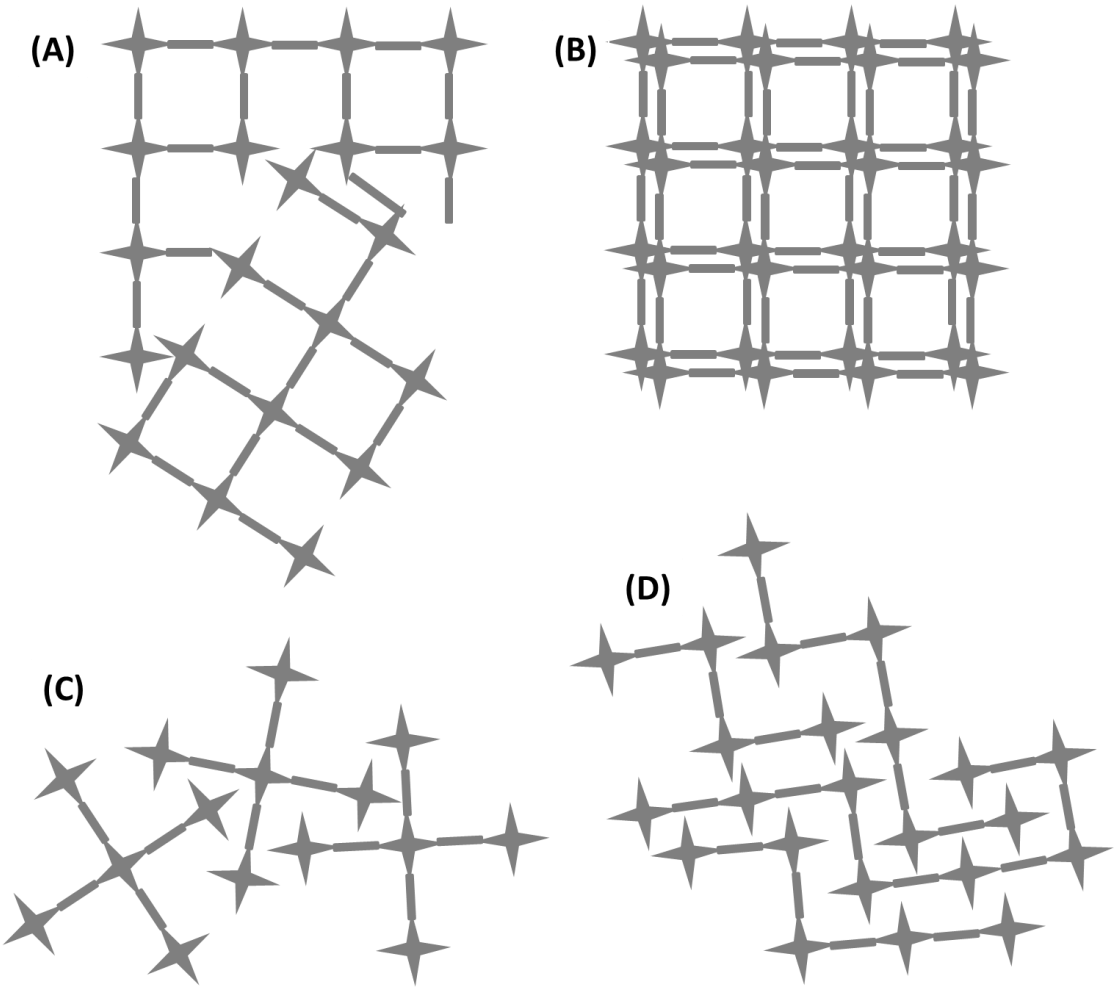

Figure 1-4: Representations of packing in microporous materials, showing 2-D amorphous structures (A, C, D) and a 3-D crystalline structure (B). Figure adapted from reference [38].

At present, there is no clear benefit for preferential synthesis of one material over the other, *i.e.* either amorphous or crystalline. Both structures can exhibit exceptionally high surface areas (*e.g.*, 6240 m^2g^{-1} for crystalline MOF-210[26] and 6461 m^2g^{-1} for amorphous PPN-4[80]). Often the synthesis strategy depends upon the desired application.[53, 84] However, a considerable challenge exists when characterising amorphous networks. Their lack of long range ordering prevents the implementation of traditional characterisation methods, such as X-ray diffraction, which is used in the characterisation of crystalline

frameworks. The insolubility of these materials (with the exception of linear PIMs),[95] also rules out the use of solution state NMR and gel permeation chromatography (GPC). Therefore, structural and molecular level characterisation of amorphous insoluble polymers, such as CMPs, are limited to solid-phase techniques, such as gas sorption for textural properties, scanning electron microscopy (SEM) for morphology and solid-state nuclear magnetic resonance (NMR) for structural elucidation.

1.1.2.1 Structural determination of porous materials by solid-state NMR

The following discussion is a brief overview of the solid-state NMR methods employed in the characterisation of amorphous microporous polymers. For further information about other polymeric systems, the reader is referred to the following four texts; Mirau[96] "Solid-state NMR of Polymers: Rapra review reports," Ando[97] "Solid-state NMR of Polymers: studies in physical and theoretical chemistry," Mathias[98] "Solid-state NMR of Polymers" and "Multidimensional Solid-state NMR and Polymers," by Schmidt-Rohr and Spiess.[99]

Understanding the molecular level structure in terms of composition and level of cross-linking is essential for the optimisation of MOPs for applications such as gas storage and heterogeneous catalysis. Structural elucidation is commonly achieved by analysis of carbon NMR spectra and many instances exist in the literature.[30, 35, 65-68, 70, 71, 79, 80, 83, 89, 90, 100] An example, from Cooper *et al.*, involves confirmation of successful cross-coupling by incorporation of functional groups into the CMP network.[71] Each functional group was identified in the NMR spectrum from its distinctive carbon chemical shifts.[71] In another report, Meilikhov *et al.* established the inclusion of a series of metallocene compounds within two MOFs, namely MIL-53(Al) and MIL-47(V), by ^{13}C NMR.[101]

Determination of the degree of polymerisation by carbon NMR also been demonstrated. In 1996, Davankov and co-workers calculated the level of cross-linking for a HCP network by spectral deconvolution of carbon NMR peaks.[102] This method was recently applied to CMP materials by the Cooper group.[65, 66] The level of polymerisation was estimated by comparison of the deconvoluted peak areas corresponding to polymeric linkages and end groups.[65, 66] Such analysis was also used to assess the effect of functional groups[71] and reaction solvent[100] upon the resultant CMP network, both of which are important factors when developing new methodologies for the synthesis of MOPs.

Several groups have also examined the swelling properties of polymers by employing ^{13}C spin-lattice (T_1) relaxation NMR.[103-105] Scott and co-workers found pH-dependent swelling behaviour for an acidic poly(ethyleneglycol) cross-linked co-block polymer.[105] Curran *et al.* used ^{13}C NMR to study the relaxation behaviour for a series of highly branched aromatic polyamide fractal polymers.[103] Their data identified a swelling mechanism dictated by hydrogen bonding. They found that breaking hydrogen bonds between two polymer segments occurs in favour of forming hydrogen bonds between the solvent and an individual polyamide chain.[103] Similar NMR methods have been applied to solvent-swollen HCPs by Davankov and co-workers.[102] Their data show an increase in polymer mobility upon swelling, leading to a reduction of cross-polarisation signal and an increase in relaxation time. Further evidence for an increase in mobility of solvent-swollen HCPs was provided by dilatometric studies.[106]

The relaxation techniques used in the literature are described in detail in **Chapter 2**.

In addition to carbon NMR, nitrogen NMR has also been used to confirm the structures of novel nitrogen-containing MOPs,[30, 90, 91] however, this is less common. The low sensitivity of nitrogen NMR means that it can take a considerable amount of time to acquire the data.[107] Cross-polarisation methods have been developed to try and overcome sensitivity issues (for further information, please see **Chapter 2**). Another possible solution is to prepare isotopically labelled MOPs, for instance imine-linked COF-300.[30] Motivation for

collecting nitrogen spectra has been to deduce polymer structure and to detect the presence of nitrogen-containing end groups.

1.1.2.1.1 Host-guest interactions by solid-state NMR

Identification of favourable interactions between porous polymers and guests is imperative for the development of MOPs in gas storage and separation technologies. Indeed many reports describe the investigation of various gas adsorptions in porous materials by solid-state NMR. Su *et al.* demonstrated the reversible hydrogen storage capabilities of a clathrate hydrate using ^{1}H NMR, by monitoring the change in ^{1}H chemical shift upon inclusion within the porous host.[108] Similarly, Sozzani *et al.* described the change in ^{13}C chemical shifts of carbon dioxide and ^{13}C and ^{1}H chemical shifts of methane upon encapsulation within a triphosphazene porous crystal.[109] By comparison of chemical shifts with other literature, the Sozzani group concluded that the guests were interacting with the aromatic groups of the porous host.[109]

Hyper-polarized xenon NMR has also been used to probe the sorption properties of various porous materials, such as mesoporous silica, porous crystals and MOFs.[110-116] Hoffman *et al.* investigated the breathing transitions of a flexible MOF by ^{129}Xe NMR.[117] As the chemical shift of ^{129}Xe is sensitive to its state of matter, the peaks in the NMR spectrum changed upon encapsulation into the MOF framework.[117] The group also demonstrated the exchange between captured and free xenon at the pore surface.[117]

Recently, Ilczyszyn and co-workers used ^{129}Xe NMR to study the H/D isotope effect upon a hydrogen bonded network of β-hydroquinone.[118] Their T_1 spin-lattice relaxation data showed that the ^{1}H-^{129}Xe dipole-dipole interactions were sensitive to hydrogen bonding and confirmed that xenon takes part in hydrogen bonding when included in the network.[118]

More recently, ^{129}Xe NMR has been used to monitor the progression of styrene polymerisation.[119] An increase in ^{129}Xe chemical shift was observed with

reaction time.[119] The data were used to find the most appropriate conditions for polymerisation by studying the effect of different initiators.[119]

Finally, deuterium NMR spectroscopy is another well-established method of probing host-guest interactions. ^{2}H NMR has been used to examine guests encapsulated in mesoporous silica,[120-122] zeolites,[123-126] polymers,[127-129] small molecules,[130-132] MOFs,[133, 134] catalysts[135] and even to investigate proton conduction.[136] This technique also provides an alternative method for determination of pore-size distributions.[137] Specific examples detailing ^{2}H NMR characterisation of porous systems are given in the introduction to **Chapter 4**.

1.1.2.1.2 Dynamics of microporous materials by solid-state NMR

In addition to structural information, ^{2}H NMR can provide details about dynamics.[99, 138] Such data can increase understanding of the origins of physical properties for a variety of different systems. A major advantage of ^{2}H NMR is the ability to examine molecular motions of specific sites. By selective deuteration, one can study either the dynamics of a guest (detailed above) or the host framework. Indeed, many hosts have been investigated, including, crystalline organic molecules,[130, 131, 139] polymers,[140-149] MOFs,[133, 150] porous silica[151] and proteins.[152-156] Furthermore, particular functional groups can be targeted, such as methyl groups,[145, 156] aliphatic chains[146, 150] and phenyl groups,[133, 141, 143, 148, 151-155] to name but a few. For detailed examples the reader is referred to the introduction of **Chapter 4**.

1.1.2.1.3 Overview of the characterisation of CMPs

Until now vast numbers of CMPs have been prepared. Indeed, much of the research in this area has focussed upon increasing functionalization of the networks rather than their characterisation. Both insolubility and the amorphous

nature of CMPs prevent structural elucidation by crystallographic and chromatographic techniques. In particular, the origins of network flexibility and porosity are poorly understood. Undoubtedly, detailed structural and dynamical analyses are essential for improving and developing CMPs for future applications.

1.2 Aims of the project

This chapter has described the different types of microporous materials and their potential employment in areas such as gas storage, molecular separations, catalysis, and in sensing technologies. In particular, CMPs have emerged as a class of materials that have advantageous properties, such as, extended π-conjugation, finely tuneable micropore size and surface area, inherent fluorescence and the ability to swell.

However, owing to their limited solubility and the amorphous nature of CMP materials, little information is known about their structure. Indeed, the characterisation of CMPs remains an arduous task. Structural analysis of CMPs is dominated by solid-state NMR. This technique is sensitive to both molecular level structure and detailed mobility. An increase in understanding of these networks is required to give an overall picture of their origins of flexibility and physical properties, ultimately leading to the design of such materials for specific applications.

In addition to the difficulties of characterisation, a considerable disadvantage of CMPs is the cost of their synthesis. Many of the current routes to CMPs involve the use of palladium, copper and nickel catalysts. It would, therefore, be advantageous to develop methodologies that use cheap monomers and do not require metal catalysts. Such improvements would increase the viability of CMPs for use in industrial applications.

Therefore, the aims of this project are split into two categories; advanced structural elucidation and investigation of the origins of physical properties (*i.e.* network flexibility, swelling and porosity) for CMP networks, specifically by solid-state NMR, and preparation of novel CMPs *via* cost-effective routes.

The characterisation part will involve two approaches. The first aims to identify a mechanism for the formation of CMP-1 networks. Products of the CMP-1 reaction shall be inspected after incremental time periods. Soluble products will be examined using solution state NMR. Insoluble products were

analysed by, FTIR, SEM and solid-state NMR, to assess composition, end groups, and efficiency of cross-linking. In particular, the evolution of porosity and morphology with increasing reaction time shall be monitored by gas sorption analysis and SEM, respectively.

The second approach aims to build upon the existing body of knowledge for CMP materials, such as carbon solid-state NMR and molecular modelling simulations, by employing advanced solid-state NMR techniques. More specifically, deuterium NMR will be used to probe the molecular motions of polymer chains for deuterated versions of CMP-1 and CMP-2. Swelling experiments of CMP-1 and CMP-2 with benzene-d_6 shall also be used to investigate changes in porosity for swollen and non-swollen networks.

Finally, a new route to CMPs will be developed by exploiting the reaction of aldehydes with amines. In particular the formation of aminal linkages shall be explored, as this would allow preparation of branched networks from bi-functional monomers. Newly synthesised materials are to be fully characterised and tested for their ability to store gas.

Chapter 2:

Characterisation Techniques

This chapter summarises the different techniques that have been used to characterise the materials investigated in this research. In particular the theoretical background and experimental configurations will be described. Such information will also be referred to in subsequent chapters.

2.1 Nuclear magnetic resonance (NMR) spectroscopy

2.1.1 Fundamentals of NMR[157-159]

NMR spectroscopy is an extremely powerful technique which is used to examine chemical structure and dynamics. NMR relies upon an intrinsic property of the nucleus, namely spin angular momentum, which is often shortened to nuclear spin. The nuclear spin is parameterised according to the spin quantum number *I*, which may have one of the following values; 0, ½, 1, 3/2, 5/2, *etc.* Nuclei with even numbers of protons and neutrons, for example ^{12}C, have a ground state nuclear spin given by $I = 0$, *i.e.* they do not possess nuclear spin. Nuclei with a non-zero quantum number have unpaired protons and/or neutrons which give rise to nuclear spin. If a nucleus possesses spin, it is able to generate a small magnetic moment. The magnetic moment (μ) is directly proportional to the spin angular momentum (*I*) with a proportionality constant known as the gyromagnetic ratio (γ), given by **Equation 2-1**.

$$\mu = \gamma I \qquad \textbf{Equation 2-1}^{159}$$

In the absence of an external magnetic field, the magnetic moments are randomly orientated and thus degenerate. However, in the presence of an external magnetic field (B_0), the magnetic moments are able to align at an angle parallel (spin up) or anti-parallel (spin down) to the B_0 field. The two states are

separated by an energy difference, ΔE, shown in **Figure 2-1**. Splitting of the energy levels is known as the Zeeman Effect.

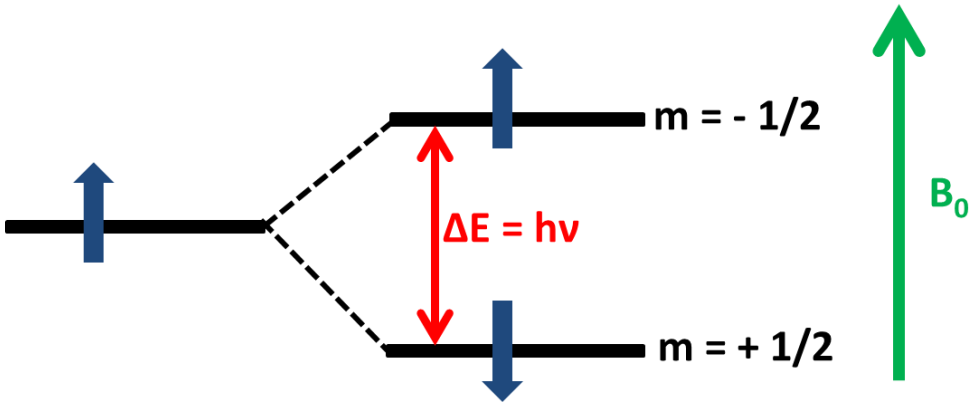

Figure 2-1: Zeeman splitting of a spin I = ½ nuclei in a magnetic field B_0. Figure adapted from reference[159].

By applying electromagnetic radiation which satisfies the condition, $\Delta E = h\nu$, (where h is Planck's constant and ν is the frequency) nuclei can be perturbed from one energy level to the other. NMR spectroscopy is measurement of the change in energy during this perturbation. The frequency, ν, also known as the Larmor frequency (ω_0), is dependent on the magnetic field and the nucleus under examination, therefore the resonance condition is given by:

$$\nu = \frac{\gamma B}{2\pi}$$ **Equation 2-2**[159]

A selection rule of $\Delta m = \pm 1$ applies; *i.e.* only transitions between adjacent energy levels are permitted.

2.1.1.1 Chemical shift[157-159]

As mentioned, the frequency at which nuclei resonate depends upon the gyromagnetic ratio and strength of the surrounding magnetic field, B_0. However, the NMR frequency is also sensitive to the position of a nucleus within a molecule due to fluctuations in the local electron distribution.

The external magnetic field causes the electrons surrounding each nucleus to circulate within their atomic orbitals, as shown in **Figure 2-2**. This induced motion is similar to an electronic current passing through a wire, and results in a small local magnetic field, B. As B occurs in the opposite direction to B_0, the nucleus is shielded by its surrounding electrons. This effect is particularly useful when studying molecular structure.

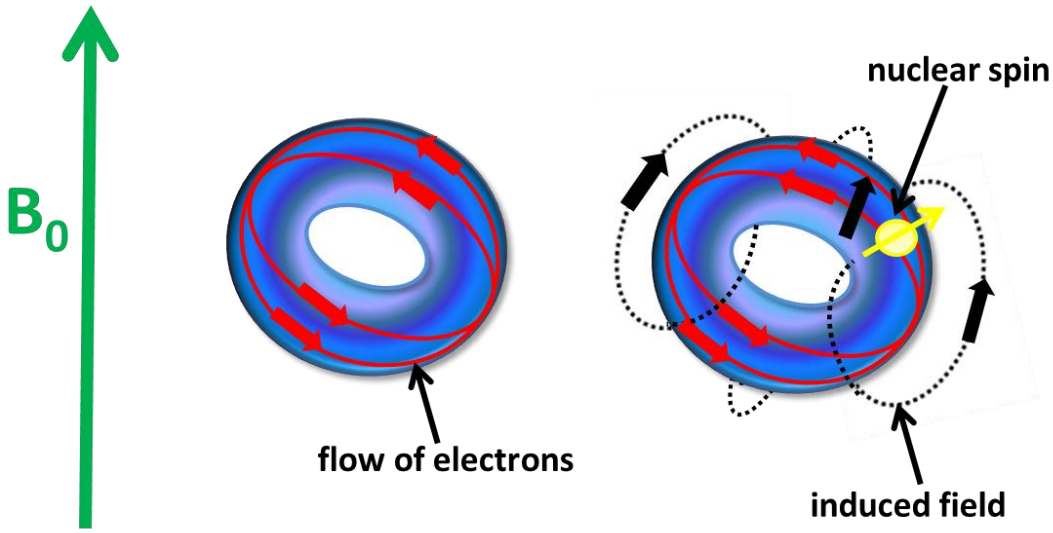

Figure 2-2: Mechanism of the chemical shift. Figure adapted from reference [158].

In molecules, nuclear shielding, and indeed de-shielding, also depends upon neighbouring atoms and is affected by many different factors, such as, hydrogen bonding, electronegativity and unpaired electrons *etc.* The shielding interaction changes the resonance frequency of the nucleus, thus giving rise to

chemical shift. Chemical shift is measured in parts per million (ppm) from a standard frequency, usually tetramethylsilane (TMS).

2.1.2 Solid state NMR[157, 158, 160-162]

Solid state NMR is a technique which is used to study the molecular structure of insoluble materials such as amorphous polymers, mesoporous silica, and heterogeneous catalysts.[96-99, 160, 163, 164]

In solution state NMR the fast motions of molecules average out many different nuclear spin interactions, leading to simplification of the spectra. The overall spin Hamiltonian (a quantum mechanical description of nuclear spin interactions) for an isotropic liquid is:

$$\hat{\mathbf{H}}_{\mathbf{total}} = \hat{\mathbf{H}}_{\mathbf{Z}} + \hat{\mathbf{H}}_{\mathbf{CS}}^{\mathbf{iso}} + \hat{\mathbf{H}}_{\mathbf{J}}^{\mathbf{iso}}$$ **Equation 2-3**[158]

The remaining interactions include the Zeeman interaction ($\hat{H}_Z$), chemical shielding ($\hat{H}_{CS}^{iso}$), and nuclear spin-spin coupling ($\hat{H}_J^{iso}$).

However, in solids, atoms and molecules are rigid and thus cannot execute random tumbling motions resulting in additional orientation dependent (anisotropic) nuclear spin interactions. The overall spin Hamiltonian for a solid powder can be represented by:

$$\hat{\mathbf{H}}_{\mathbf{total}} = \hat{\mathbf{H}}_{\mathbf{Z}} + \hat{\mathbf{H}}_{\mathbf{CSA}} + \hat{\mathbf{H}}_{\mathbf{J}} + \hat{\mathbf{H}}_{\mathbf{D}} + \hat{\mathbf{H}}_{\mathbf{Q}}$$ **Equation 2-4**[158]

The additional orientation dependent interactions include; chemical shift anisotropy ($\hat{H}_{CSA}$), dipolar coupling ($\hat{H}_D$), and quadrupolar coupling ($\hat{H}_Q$)

which is only observed for nuclei where $I > ½$. Such interactions lead to significant broadening of the solid state NMR spectral lines compared to solution NMR.

2.1.2.1 Nuclear magnetic and electric interactions[158]

In order to understand the methods of acquiring solid state NMR spectra, one must first consider the type and magnitude of interactions described by **Equation 2-3** and **2-4** which contribute to line-broadening in more depth. Therefore, a detailed description of these interactions is given in this section.

For solids, the Zeeman interaction is the same as that for liquids and both the *J*-coupling and spin-rotation (interactions of the nuclear spins with the magnetic field as a result of molecular rotation) are considerably smaller compared with other nuclear spin interactions. For these reasons, only chemical shift anisotropy, dipole-dipole coupling and quadrupolar coupling will be discussed. A summary of the interactions and their relative magnitudes is shown in **Figure 2-3**.

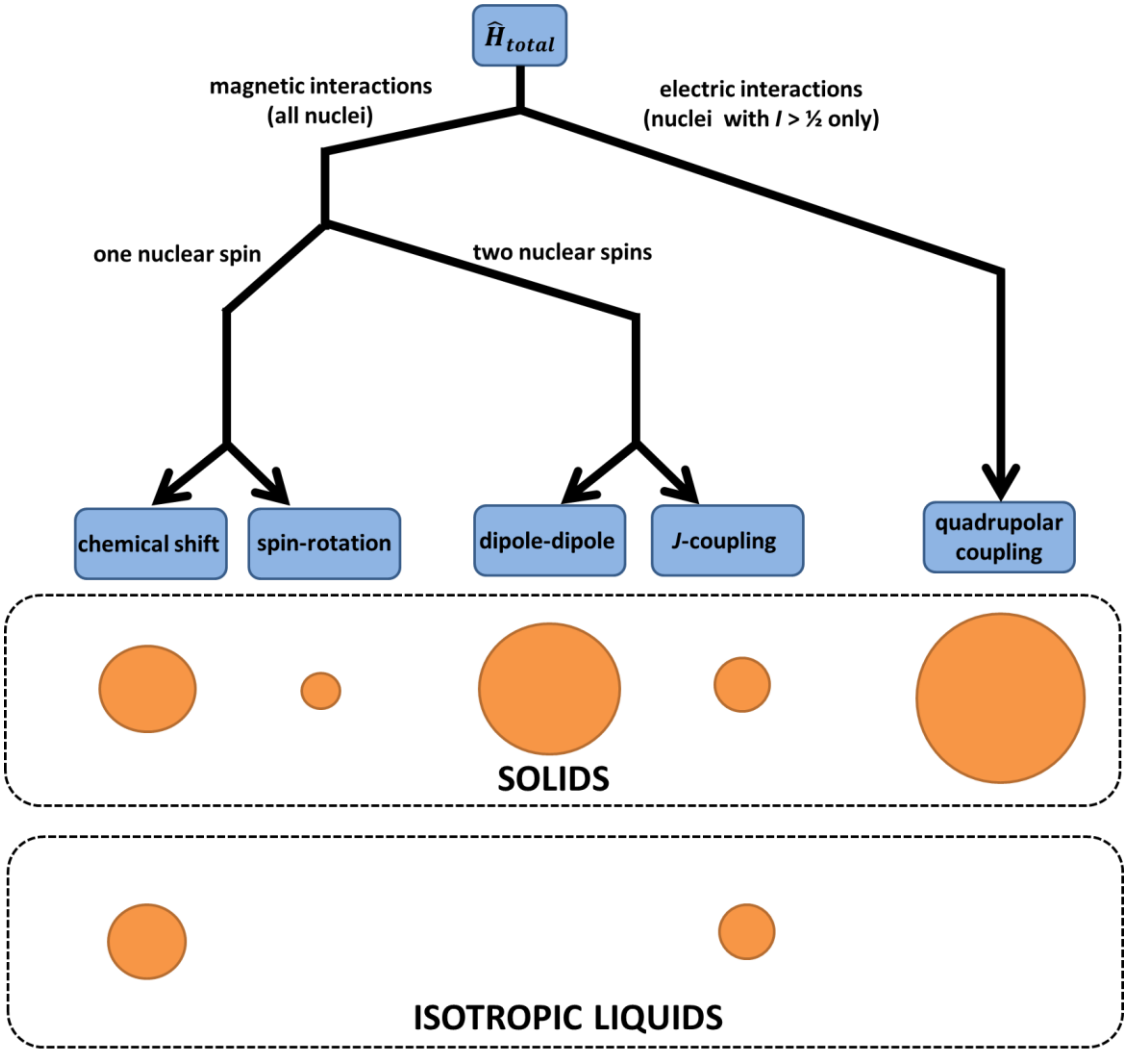

Figure 2-3: Summary of the spin Hamiltonian interactions and their rough relative magnitudes represented by circles. Quadrupolar interactions vanish for spin ½ nuclei. Figure adapted from reference [158].

2.1.2.1.1 Chemical shift anisotropy (CSA)[157, 160-162]

As mentioned in **Section 2.1.1.1**, chemical shift is the slight change in resonance frequency of a nucleus due to the presence of a local magnetic field, B. These local magnetic fields arise from induced motion of electrons by the external magnetic field, B_0.

Often the electron density surrounding the nucleus is non-spherical and can be thought of as an ellipsoid, this gives rise to chemical shift anisotropy. The electron cloud/ellipsoid is typically elongated along chemical bonds or non-bonding p-orbitals.[157] In solids, the ellipsoid can adopt many different orientations with respect to B_0. Each orientation leads to a slightly different level of chemical shielding and hence a different chemical shift, as depicted in **Figure 2-4**.

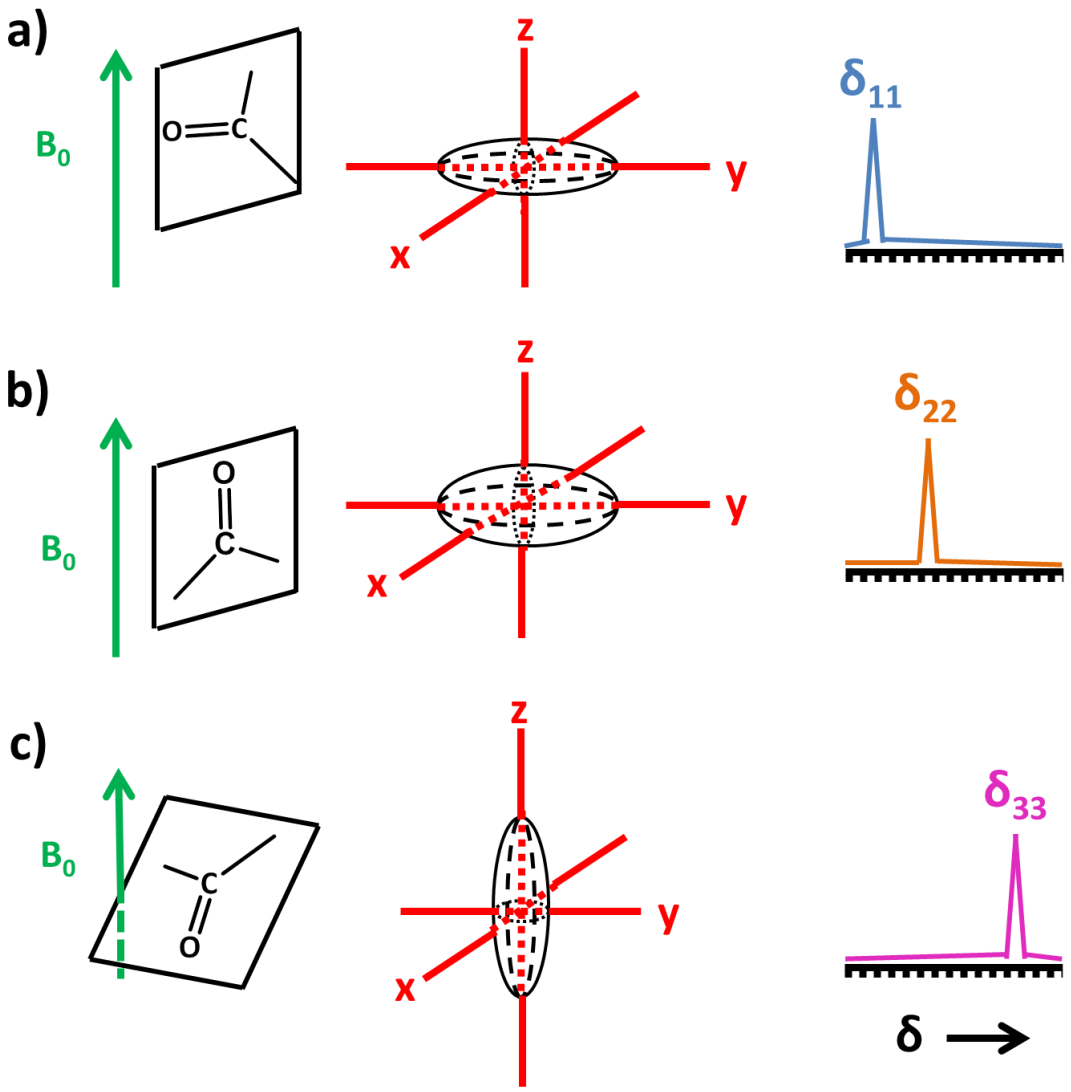

Figure 2-4: Schematic representation of the principal axis for the CSA tensor showing the chemical shift dependence on the orientation of the ellipsoid with respect to B_0. Figure adapted from reference [157].

The largest influence on the chemical shift occurs when the narrowest part of the ellipsoid is parallel to the B_0 field, this is labelled δ_{11} (**Figure 2-4 a**). The smallest chemical shift effect (δ_{33}) is observed when the widest part of the ellipsoid is parallel to B_0 (**Figure 2-4 c**). The third chemical shift (δ_{22}) is detected if the ellipsoid is orientated perpendicular to δ_{11} and δ_{33}.

However, in reality, random orientations in addition to the principal values occur in solid materials, this gives rise to a powder pattern (**Figure 2-5**).

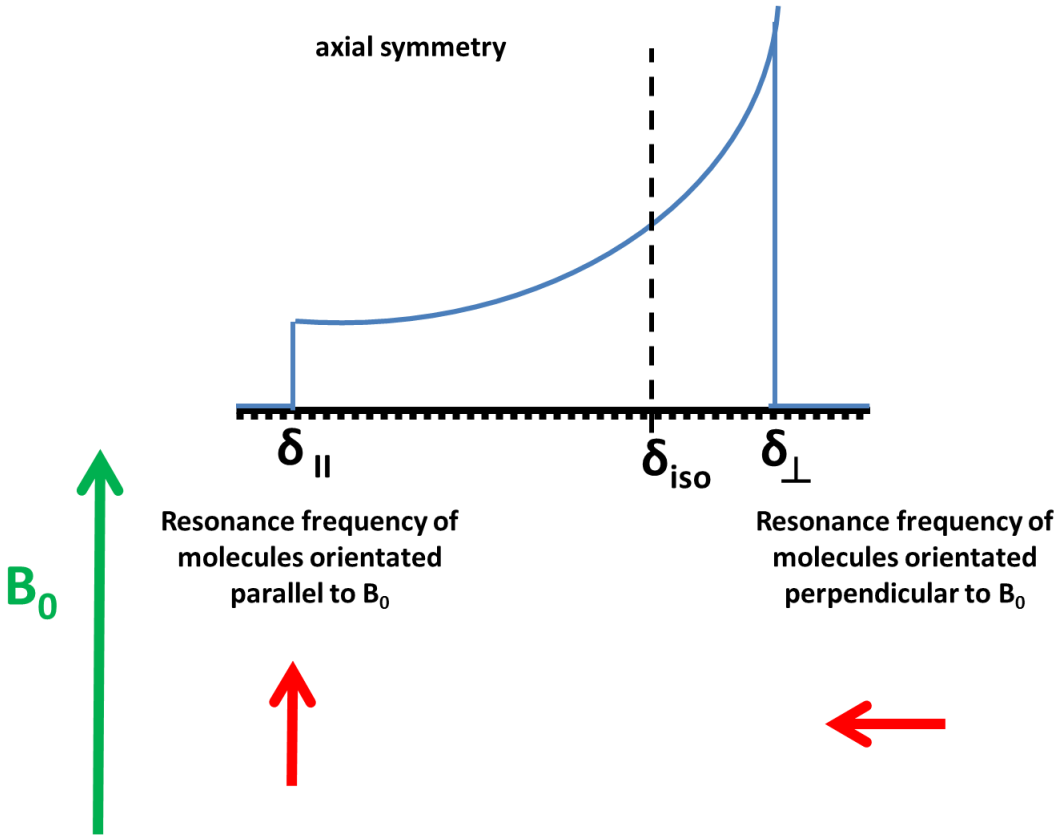

Figure 2-5: Chemical shift anisotropy powder patterns arising from randomly orientated crystallites. Figure adapted from reference [161].

In order to further understand CSA, one must consider the chemical shift Hamiltonian for an axially symmetric molecule given in **Equation 2-5**:

$$\hat{H}_{CSA} = \gamma B_0 I_Z \left[\delta_{iso} + \frac{1}{2}\delta_{CSA}(3\cos^2\theta - 1)\right] \qquad \textbf{Equation 2-5}^{157,161}$$

Where θ is angle which represents the orientation of the molecule with respect to B_0, δ_{iso} is the isotropic chemical shielding factor (*i.e.* the average of all three principal CSA values) from **Equation 2-6**, and δ_{CSA} dictates the magnitude of the CSA and is given by **Equation 2-7**.

$$\delta_{iso} = \frac{1}{3}(\delta_{11} + \delta_{22} + \delta_{33})$$ **Equation 2-6**[157,161]

$$\delta_{CSA} = \delta_{33} - \delta_{iso}$$ **Equation 2-7**[157,161]

Techniques can be applied to eliminate the effect of CSA thus allowing the isotropic chemical shift to be observed. Such techniques are discussed in **Section 2.1.2.2**.

2.1.2.1.2 **Dipole-dipole coupling**[157, 160-162]

Dipole-dipole or dipolar coupling arises from interactions between the magnetic moments of nuclear spins. This interaction takes place between nuclei with the same spin (homonuclear) and nuclei with different spin (heteronuclear). Unlike *J*-coupling, which involves indirect coupling of nuclear spins by electron clouds in chemical bonds, dipolar coupling is a through-space interaction. Thus coupling is both intra- and inter-molecular.

In solution NMR, dipolar interactions are averaged to zero as a result of molecular tumbling. However, in solid state NMR, the interaction leads to significant line-broadening. Techniques employed to reduce this broadening are detailed in **Section 2.1.2.2**.

2.1.2.1.2.1 Heteronuclear dipolar coupling[157]

Heteronuclear dipolar coupling is the result of interaction between the magnetic moments of two non-identical spins that are close in space. By convention, the spins are labelled I and S, where I represents abundant spins (such as ^{1}H) and S represents rare spins (such as ^{13}C or ^{15}N). In a magnetic field, each spin undergoes Zeeman splitting and aligns either parallel or antiparallel with respect to the B_0 field. As each spin exhibits a local magnetic field, their

magnetic moments affect the amount of external magnetic field felt by neighbouring spins. The strength of the interaction between the I and S spins is given by the Hamiltonian:

$$\widehat{H}_D^{IS} = -d\,(3\cos^2\theta - 1)I_z S_z$$ **Equation 2-8**[157]

Where d is the dipolar constant:

$$d = \left(\frac{\mu_0}{4\pi}\right)\frac{\hbar\gamma_I\gamma_S}{r_{IS}^3}$$ **Equation 2-9**[157]

Where r_{IS} is the inter-nuclear distance, μ_0 is the permeability of free space, γ_I and γ_I are the gyromagnetic ratios of the I and S spins, and I_z and S_z are the z components of the nuclear spin angular momentum operators of the I and S spins.

From the Hamiltonian (**Equation 2-8** and **2-9**), it is clear that the strength of heteronuclear dipolar coupling is dependent on the gyromagnetic ratios (*i.e.* the higher the ratio the stronger the coupling) and the coupling is inversely proportional to the distance between the spins cubed (*i.e.* as the distance increases, the coupling rapidly decreases). Another feature of heteronuclear dipolar coupling is its orientation dependency. In **Equation 2-8**, θ describes the orientation of the internuclear vector with respect the orientation of the external magnetic field (shown in **Equation 2-6**).

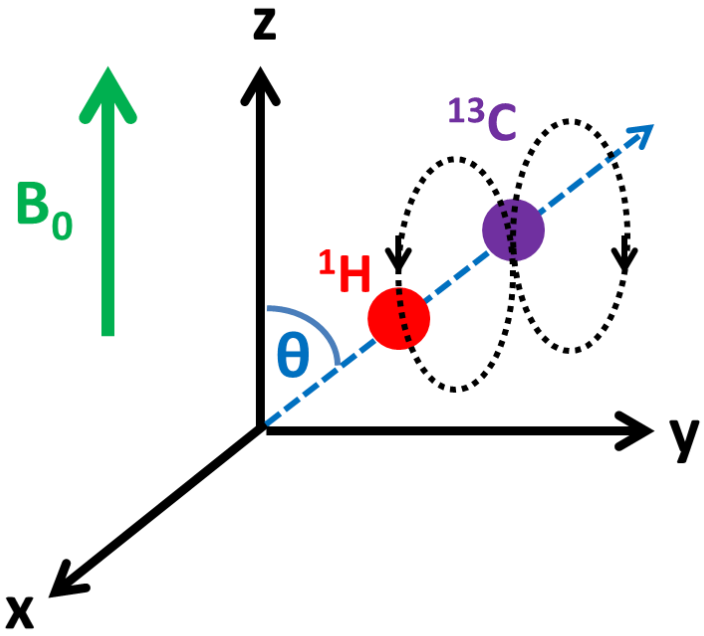

Figure 2-6: The angle between the ^{1}H and ^{13}C bond vector within the external magnetic field, B_0. Figure adapted from reference [157].

In a polycrystalline powder sample, a Pake doublet is observed in the NMR spectrum as a result of heteronuclear dipolar coupling (**Figure 2-7**). The two peaks arise from the antiparallel or parallel alignment of the I spins with respect to the S spins. The peak intensities correspond to the number of crystallites adopting a particular orientation, with the most intense peaks observed when the internuclear vector is perpendicular to B_0. When the sample is placed at the 'magic angle' (54.74°, discussed in **Section 2.1.2.2**), the resonance frequency of the crystallites is not altered by heteronuclear dipolar coupling.

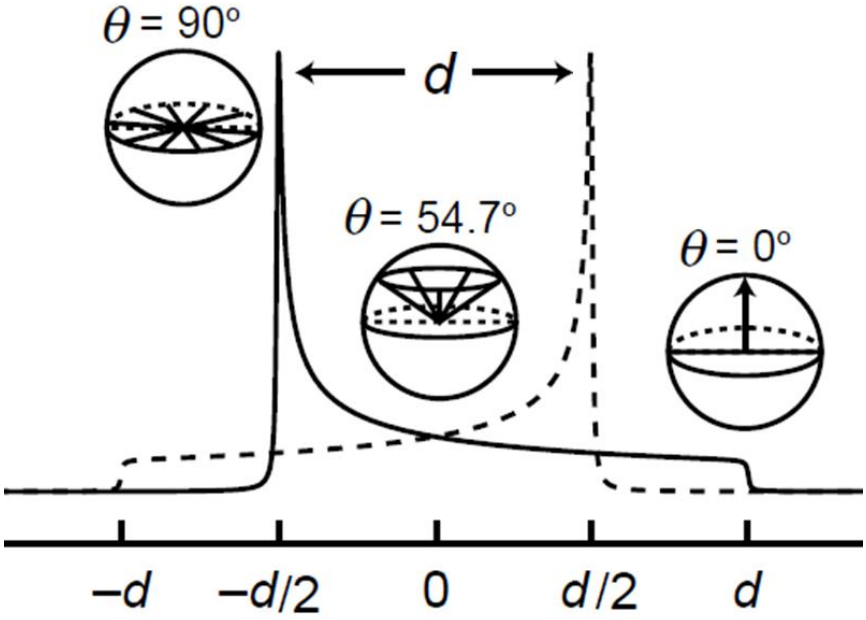

Figure 2-7: A Pake pattern resulting from heteronuclear dipolar coupling for an isolated I and S spin system. Figure adapted from reference[157]

However, in reality NMR spectra of spin ½ nuclei do not exhibit Pake patterns as each S spin couples to more than one I spin and I spins couple with each other, as discussed below.

2.1.2.1.2.2 Homonuclear dipolar coupling[157]

As with heteronuclear dipolar coupling, interactions occur between the magnetic fields of two like spins. However, as the resonance frequency of homonuclei are similar, they are able to undergo additional 'flip-flop' transitions in which one spin flips to a higher energy state while the other flips to a lower energy state (**Figure 2-8**). Such behaviour is favourable as it allows conservation of energy. These transitions do not occur between heteronuclei as their resonance frequencies are too dissimilar.

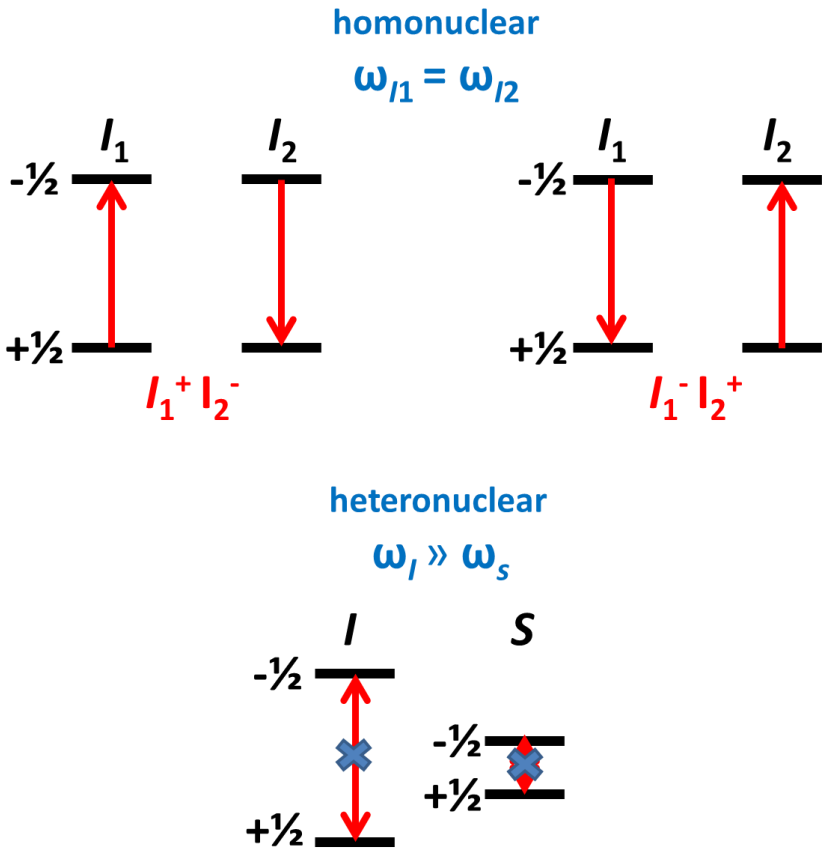

Figure 2-8: Exchange of magnetisation between homonuclear spins through energy conserving 'flip-flop' transitions. Figure adapted from reference [157].

The homonuclear dipolar Hamiltonian is given by:

$$\hat{H}_D^{II} = -d\,\frac{1}{2}(3\cos^2\theta - 1)\left(I_{1z}I_{2z} - \left(\hat{I}_1 \cdot \hat{I}_2\right)\right) \qquad \textbf{Equation 2-10}^{157}$$

Where d is the dipolar constant given by **Equation 2-9**.

Changes in magnitude of the spin operators $\hat{I}_1$ and $\hat{I}_2$ lead to alterations of the angular momentum of a spin, thus enabling a transition from spin 'up' to spin 'down' and *vice versa*.

As with heteronuclear dipolar coupling, the strength of the interaction is dependent upon the gyromagnetic ratio, therefore spin pairs such as ^{13}C and ^{29}Si only display weak homonuclear coupling. Also, homonuclear coupling between two ^{13}C spin pairs is rare as the likelihood of them being in close proximity is slim owing to their low natural abundance. However, nuclei such as ^{1}H, exhibit large homonuclear coupling owing to their large gyromagnetic ratio and a natural abundance of 100 %. Solid state NMR spectra are often broad and featureless as a consequence of ^{1}H homonuclear dipolar coupling; therefore methods have been developed to improve resolution. Such techniques are described in **Section 2.1.2.2**.

2.1.2.1.3 **Quadrupolar coupling**[157, 158, 160, 161, 165]

Around 74 % of NMR active nuclei possess a spin quantum number greater than ½ and are termed quadrupolar. Examples of quadrupolar nuclei include ^{2}H and ^{14}N (spin-1), ^{11}B and ^{23}Na (spin-3/2), ^{17}O and ^{27}Al (spin-5/2), ^{51}V (spin-7/2), and finally ^{93}Nb (spin-9/2). However, nuclei with a spin >1 are not studied in this research, therefore, only the interactions concerning spin-1 nuclei (specifically ^{2}H) shall be discussed.

Quadrupolar nuclei possess an electric quadrupole moment resulting from a non-spherical charge distribution in the nucleus. The electric quadrupole moment is able to interact with electric field gradients (EFG), which in turn arise from the distribution of electrons and nuclei surrounding the quadrupolar nucleus, as shown in **Figure 2-9**.

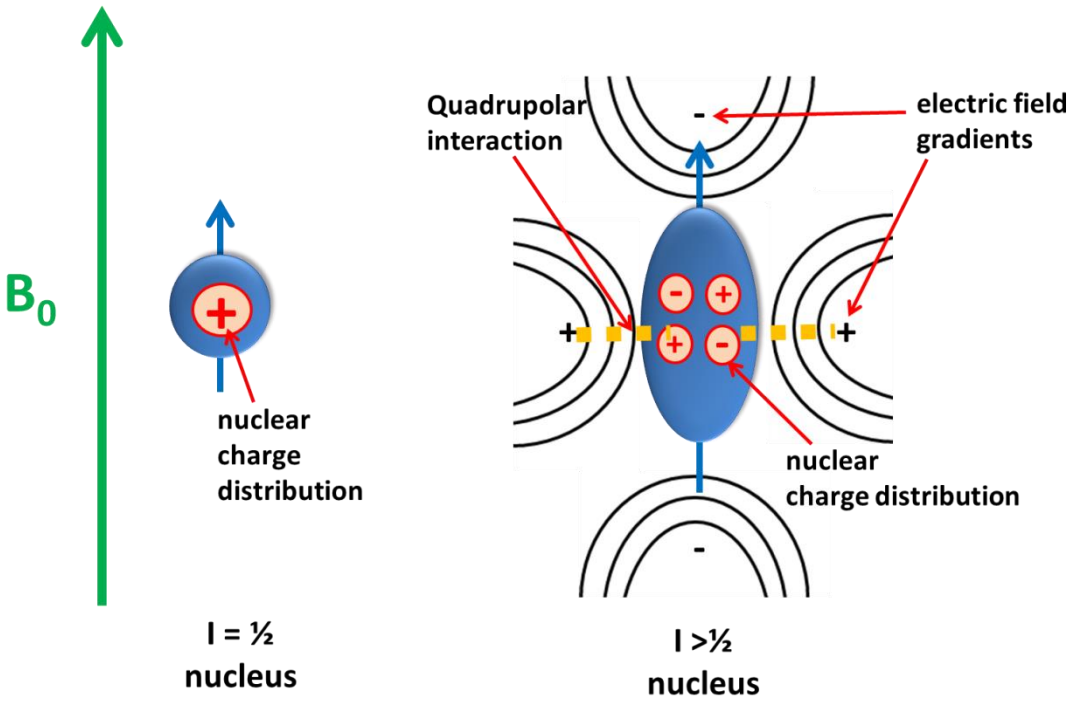

Figure 2-9: Schematic illustration of the differences between spin-½ and spin >½ nuclei. The quadrupolar coupling interaction between the spin >½ and the EFG is highlighted. Figure adapted from references [158,161,163]

The nuclear electric quadrupole moment/EFG interaction is often referred to as quadrupolar coupling and can be rather large, resulting in line widths on the order of MHz in an NMR spectrum (techniques used to acquire ^{2}H NMR spectra are discussed in **Section 2.1.2.4.1.1**). The quadrupolar interaction can be described by the quadrupolar Hamiltonian:

$$\hat{H}_Q = \frac{eQ}{2I(2I-1)\hbar}\,\hat{I}\cdot\hat{V}\cdot\hat{I}$$

Equation 2-11[161,163]

Where **e** is the proton charge, **Q** is the nuclear electric quadrupole moment (a constant for each nucleus) and **I** is the spin quantum number. $\hat{V}$ is a

second-rank Cartesian tensor used to describe the EFG in the principle axis system (PAS) given by **Equation 2-12** and $\hat{I}$ is vector used to describe the nuclear spin in the laboratory frame (LAB) given by **Equation 2-13**. Two different frames of reference (LAB and PAS) are required to describe the system as the EFG is determined by the molecular structure around the nucleus and thus has an orientation that is fixed with respect to the molecular frame of reference, whereas the nuclear spin interaction and the NMR measurements are in the laboratory frame as they are related to the external magnetic field. The relationship between the LAB frame and PAS frame is shown in **Figure 2-10**. For further discussion as to the implications of these conditions upon the NMR line shape, please see **Section 2.1.2.4.1**.

$$\hat{V} = \begin{pmatrix} V_{xx}^{PAS} & 0 & 0 \\ 0 & V_{yy}^{PAS} & 0 \\ 0 & 0 & V_{zz}^{PAS} \end{pmatrix}$$

Equation 2-12[161,163]

Where:

$$|V_{xx}| \geq |V_{yy}| \geq |V_{zz}|$$

Equation 2-13[161,163]

And:

$$\hat{I} = \begin{pmatrix} I_x^{LAB} \\ I_y^{LAB} \\ I_z^{LAB} \end{pmatrix}$$

Equation 2-14[161,163]

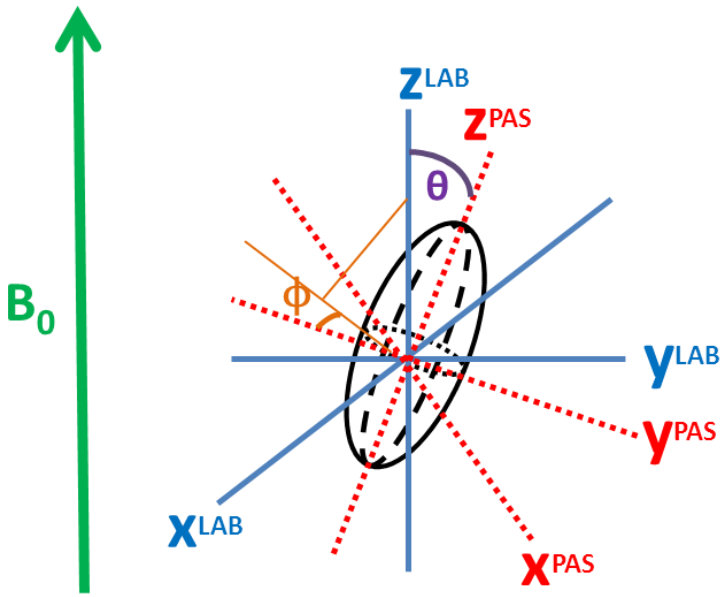

Figure 2-10: Representation of the LAB and PAS frames of reference used in **Equation 2-12** to **2-17**. **θ** and **Φ** are the angles defining the orientation of the B_0 field in the PAS frame for the EFG tensor. Figure adapted from reference[161].

Another feature of quadrupolar nuclei is that the allowed values of the spin quantum number are no longer +½ and –½, *i.e.* additional energy levels arise from the Zeeman splitting, as shown in **Figure 2-11**.

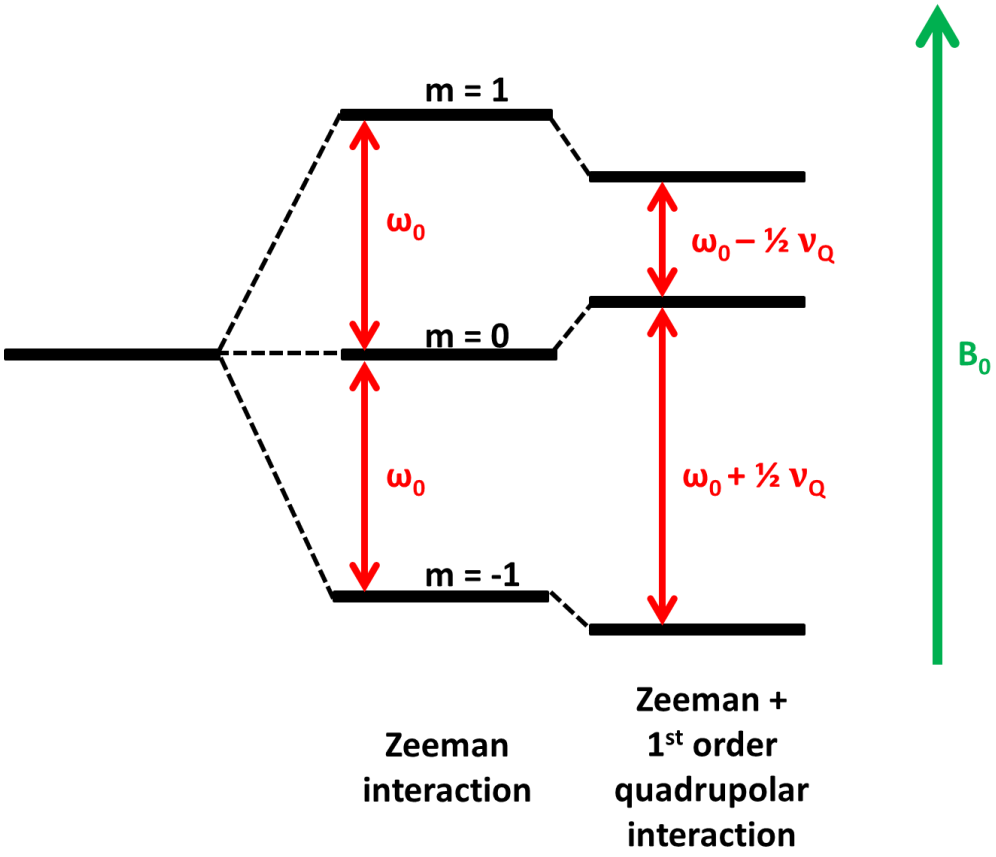

Figure 2-11: Zeeman splitting and the effect of 1st order quadrupolar interactions upon the energy levels of a spin I = 1 nuclei in a magnetic field B_0. $\boldsymbol{\omega_0}$ and $\boldsymbol{\nu_Q}$ denote the Larmor frequency and quadrupolar splitting, respectively. Figure adapted from references [157,161,163].

For spin-1 nuclei, the Zeeman energy levels are influenced by the electric quadrupolar moment/EFG interaction, or 1st order quadrupolar interaction. As the Zeeman interaction is much larger than the quadrupolar interaction, the influence of quadrupolar coupling upon the Zeeman states can be considered as a correction or perturbation of the energy levels, given by:

$$E_m = \frac{e^2 qQ}{4I(2I-1)}\left(3m^2 - I(I+1)\right)\frac{1}{2}\left[(3cos^2\theta - 1) + \eta_Q cos2\Phi sin^2\theta\right]$$

Equation 2-15[161,163]

Where m is the magnetic quantum number of the corresponding Zeeman level, I is the spin quantum number, e is the magnitude of the electron charge, q is the largest principle component of the EFG tensor (V_{zz}^{PAS}, as defined by **Equation 2-13**), Q is the quadrupolar moment, θ and Φ are the polar angles relating the LAB frame to the PAS (as shown in **Figure 2-10**). η_Q is the asymmetry parameter of the EFG tensor given by:

$$\eta_Q = \left(\frac{V_{yy}^{PAF} - V_{xx}^{PAF}}{V_{zz}^{PAF}}\right)$$

Equation 2-16[161,163]

Where:

$$0 \leq \eta_Q \geq 1$$

Equation 2-17[161,163]

Again for further discussion, please see **Section 2.1.2.4.1**.

As a result of this perturbation, the transitions between -1→0 and 0→+1 differ in energy and therefore resonate at two different frequencies; consequentially static NMR spectra consist of Pake doublets (as shown in **Figure 2-12**).

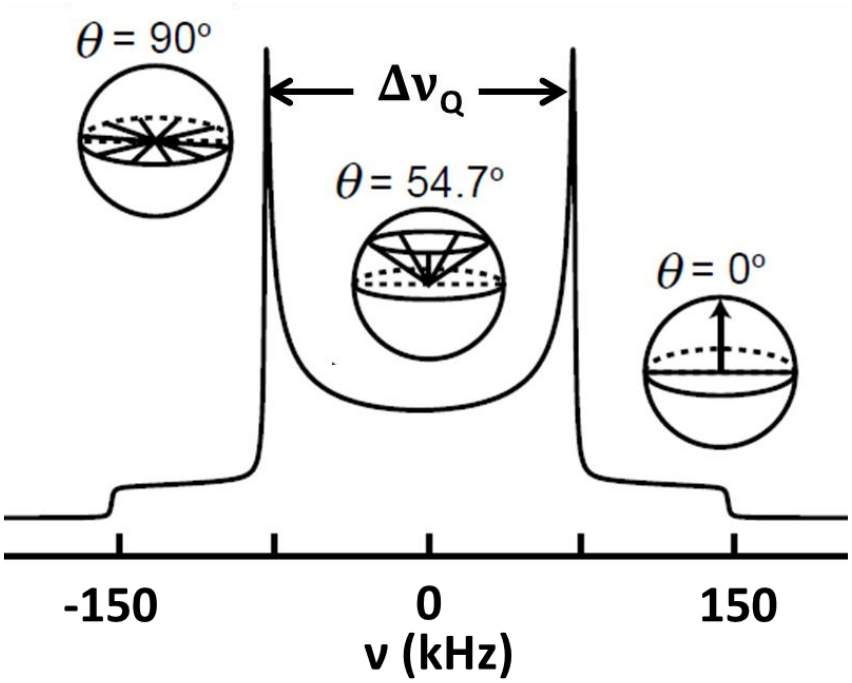

Figure 2-12: The ^{2}H quadrupole powder pattern, also referred to as the 'Pake doublet.' The doublet nature of the pattern results from the two allowed spin transitions. The distance between the 'horns' is equal to the quadrupolar frequency, ν_Q. For this particular spectrum η_Q = 0. Figure adapted from references [157, 161, 163].

The difference between the frequencies (and indeed the distance between the 'horns' of the powder pattern) is proportional to the first order quadrupolar coupling frequency, $\Delta\nu_Q$, given by:

$$\Delta\nu_Q = \frac{e^2qQ}{4I(2I-1)}\frac{1}{2}\left[(3cos^2\theta - 1) + \eta_Q cos2\Phi sin^2\theta\right]$$ **Equation 2-18**[161, 163]

As with CSA and dipolar coupling, the strength of the electric quadrupole moment is orientation dependent, thus spectral line shapes can reveal important structural information about the system under investigation. Moreover, the

NMR line shapes and relaxation measurements are particularly sensitive to molecular motions and have been extensively used to study both the materials in this research and many other host-guest systems. Line shape analysis and relaxation NMR are discussed further in **Section 2.1.2.4**.

2.1.2.2 Techniques used to improve resolution in solid-state NMR

2.1.2.2.1 Magic angle spinning (MAS)[157, 160-162]

In a polycrystalline powder, the molecular orientation dependence of the Hamiltonians for the CSA and dipolar interactions is given by: $(3cos^2\theta - 1)$, where θ is the angle which describes the orientation of the interaction. For a static powder, θ takes on all possible values, since all molecular orientations are present.

If the sample is spun rapidly about an axis inclined at an angle θ_R with respect to B_0, the interactions are averaged as the molecular orientation, and thus θ, change with time. Under these circumstances the orientation dependence of the interactions can be written as:

$$\langle 3cos^2\theta - 1\rangle = \frac{1}{2}(3cos^2\theta_R - 1)(3cos^2\beta - 1) \qquad \textbf{Equation 2-19}^{161}$$

Where the angles θ, β and θ_R are defined in **Figure 2-13**.

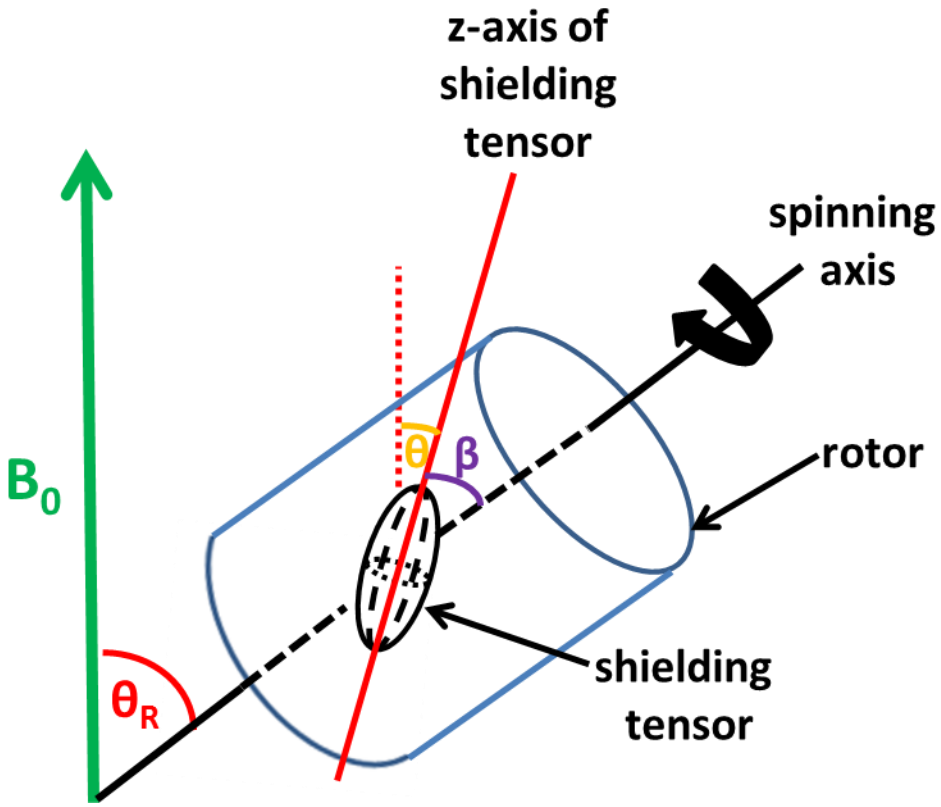

Figure 2-13: The magic angle spinning (MAS) experiment. The sample is spun rapidly in a rotor at an axis orientated by θ_R = 54.74° with respect to B_0. θ is the angle between B_0 and the z-axis of the shielding tensor. β is the angle between the z-axis of the shielding tensor and the spinning axis. Figure adapted from reference[161] .

If θ_R is set to 54.74°, the condition of $(3cos^2\theta - 1) = 0$ is satisfied, this is known as the magic angle. At this angle, the anisotropy of the interaction is averaged to zero resulting in a resonance in the NMR spectrum at the isotropic chemical shift.

2.1.2.2.2 **Decoupling**[157,160-162]

In order for MAS to average out the interactions effectively, the rate of sample spinning must be more than three times greater in magnitude than the strength of anisotropy interaction it is trying to suppress. If the interaction is particularly strong, such as that observed for homo- and hetero-nuclear coupling, decoupling is required to eliminate the interactions.

Heteronuclear decoupling involves applying a series of high-powered radiofrequency (RF) pulses close to the resonance frequency of the I spins. The irradiation causes the I spins to undergo rapid transitions between their 'spin-up and spin-down' states, thus averaging out the I-S coupling. However, this method of decoupling can cause undesirable heating of the sample, particularly if long acquisition times are required. In order to overcome these problems, alternative decoupling pulse sequences have been developed, such as Two Phase Pulse Modulation (TPPM).[166] TPPM uses two high-power pulses that differ in phase by 10 - 70°.

Homonuclear decoupling is much more complex than heteronuclear decoupling, owing to the additional spin term in the Hamiltonian **(Equation 2-10)**. For one-dimensional NMR experiments, multiple pulse sequences are often implemented. Multiple pulse sequences contain windows within the pulse sequence in which the effect of the dipolar Hamiltonian on the nuclear magnetisation is zero. If the nuclear magnetisation is detected in these windows, the effects of homonuclear dipolar coupling are removed from the spectrum.

Although a combination of MAS and decoupling leads to high resolution spectra, interactions which may give structural information such as inter-nuclear distances and molecular mobility are also eradicated. For this reason, a number of methods have been developed which reintroduce the lost interactions.

2.1.2.2.3 Cross-polarisation[157,160-162,167]

Nuclei with small gyromagnetic ratios and low natural abundance, such as ^{13}C and ^{15}N give weak NMR signals. Low abundance nuclei also tend to have long relaxation times (>10 s) owing to the absence of homonuclear dipolar interactions. For these reasons, collection of spectra can often be impractical. To overcome these problems, a technique known as cross-polarisation (CP) has been developed.

CP relies upon the tendency of magnetisation to flow from highly polarised spins (*e.g.* ^{1}H, labelled I spin) to spins with lower polarisation (*e.g.* ^{13}C or ^{15}N, labelled S spin) when the two are brought into contact. This is analogous to thermal transfer when heat flows from a hot object to a cold object when they are brought into contact. In the case of homonuclear spins, magnetisation is transferred *via* dipolar coupling and involves energy conserving 'flip-flop' interactions, however, such transitions are absent for heteronuclear spins owing to their resonance frequencies being too dissimilar (see **Section 2.1.2.1.2**). This energy gap can be bridged using RF pulses. RF pulses cause precession of magnetisation about the x-y plane. The rate of precession (or rotation frequency) is determined by the amplitude of the RF pulses. By applying two simultaneous RF pulses, one at the resonance frequency of the I spins and one at the resonance frequency of the S spins, the rates of precession can be controlled independently. Once the rotation frequencies of I and S spins are equal (as determined by the Hartmann-Hahn matching condition, **Equation 2-20**)[168], transfer of magnetisation takes place.

$$\gamma_I B_I = \gamma_S B_S \qquad \textbf{Equation 2-20}$$

Where γ_I and γ_S are the gyromagnetic ratios of the I and S spins, respectively. B_I and B_S represent the RF pulses applied to the I and S spins, respectively.

A typical CP pulse program is shown in **Figure 2-14**.

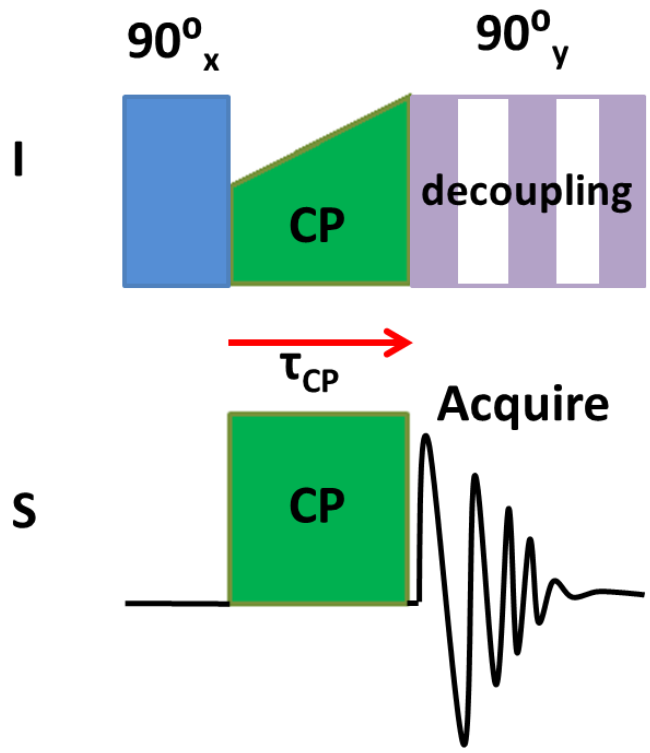

Figure 2-14: Cross polarisation pulse sequence, with a ramped amplitude CP contact pulse. I corresponds to the abundant spins, *i.e.* ^{1}H, and S corresponds to dilute spins ^{13}C or ^{15}N. Figure adapted from reference [161].

In the course of a CP experiment, the duration (or contact time, τ_{CP}, **Figure 2-14**) of the RF pulse is dependent upon the strength of the dipolar coupling. Typically contact times between 100 µs to 12 ms are required to enhance the signal of the S spins, although the signal may start to decay at longer times as a result of relaxation (discussed in **Section 2.1.2.4.2).**

It is important to note that as the signal intensities of a CP spectrum are governed by the number of local I spins, peak integrals cannot be used to determine the relative quantities of the S spin. However, CP experiments can be used to probe local structure and dynamics of the materials under investigation, since factors that affect the strength of dipolar coupling (such as inter-nuclear distance, amount of I spins and molecular motions) will also affect the rate of

transfer of magnetisation. Such information can be gathered by collecting spectra in which the length of the contact pulse is varied, this process is known as CP kinetics.

2.1.2.2.4 **Dynamics of cross-polarisation**[157,160-162,167]

The kinetics of cross-polarisation can be described by two models, depending upon the strength of the ^{1}H-^{1}H homonuclear dipolar coupling. The first, known as the classical I-S model, is most applicable to homogeneous solids. For this system, I-S heteronuclear dipolar interactions are weak, whereas I-I homonuclear interactions are strong enough to facilitate ^{1}H-^{1}H spin diffusion. The equation for the I-S model is given by:

$$I(t) = I_0\left(1 + \frac{T_{IS}}{T_{1\rho}^{S}} - \frac{T_{IS}}{T_{1\rho}^{I}}\right)^{-1}\left[exp\left(\frac{-t}{T_{1\rho}^{I}}\right) - exp\left(-t\left(\frac{1}{T_{IS}} + \frac{1}{T_{1\rho}^{S}}\right)\right)\right]$$

Equation 2-21[167]

Where I_0 is the absolute signal intensity, T_{IS} is the CP time constant (*i.e.* the time it takes to transfer magnetisation from I to S) $T_{1\rho}$ is the relaxation time in the rotating frame.

Often the relaxation time of the S spin is very long when compared to T_{IS}, *i.e.* $T_{IS}/T_{1\rho} \approx 0$, therefore **Equation 2-21** can be simplified as:

$$I(t) = I_0\left(1 - \frac{T_{IS}}{T_{1\rho}^{I}}\right)^{-1}\left[exp\left(\frac{-t}{T_{1\rho}^{I}}\right) - exp\left(-\frac{t}{T_{IS}}\right)\right]$$

Equation 2-22[167]

As the CP time constant is dependent upon the dipolar coupling, which in turn is affected by the molecular mobility number of I spins, it is characteristic for each specific functional group. $T_{1\rho}$ relaxation time is governed by ^{1}H-^{1}H

homonuclear dipolar interactions and thus provides information about the surrounding site.

The second, known as the I-I*S model, is used to explain CP kinetics of heterogeneous systems. The I-I*S model accounts for two different proton populations. I* denotes protons directly attached to the S spin and I represents protons in the areas surrounding (but not directly attached to) the S spins. In the I-I*S model, CP occurs *via* two steps. The first step involves a rapid increase in signal intensity arising from the transfer of magnetisation to the S spin from directly attached protons (I*-S). The second step involves transfer of magnetisation from I to I* *via* spin diffusion, resulting in an additional increase in signal intensity at longer contact times. The equation for the I-I*-S model is given by:

$$I(t) = I_0 \, exp\left(\frac{-t}{T_{1\rho}^{I}}\right)\left[1 - \lambda \exp\left(\frac{-t}{T_{df}}\right) - (1-\lambda) exp\left(-\frac{3/2\, t}{T_{df}}\right) exp\left(-\frac{1/2\, t^2}{T_2^2}\right)\right]$$

Equation 2-23[167]

Where T_{df} is the ^1H spin diffusion time constant which describes the strength of the homonuclear dipolar coupling and the homogeneity of the I spins and T_2 is the spin-spin relaxation time (see **Section 2.1.2.4.2**). λ is defined by: $\lambda = 1/(n + 1)$, where n is the number of I spins attached to the S spin under examination.

2.1.2.3 Quantitative analysis by ^{13}C NMR

While CP experiments have been developed to enhance signal-to-noise ratios and improve resolution, the resultant spectra are non-quantitative. As the technique relies upon the transfer of magnetisation from nearby proton sites, it relies on the strengths of ^1H-^{13}C dipolar coupling and often severely underestimates the amount of quaternary carbon atoms present within a

sample.[167] In order to overcome this problem single pulse excitation (SPE, also known as direct polarisation, DP) experiments have been developed.[169]

A typical SPE experiment is shown in **Figure 2-15**.

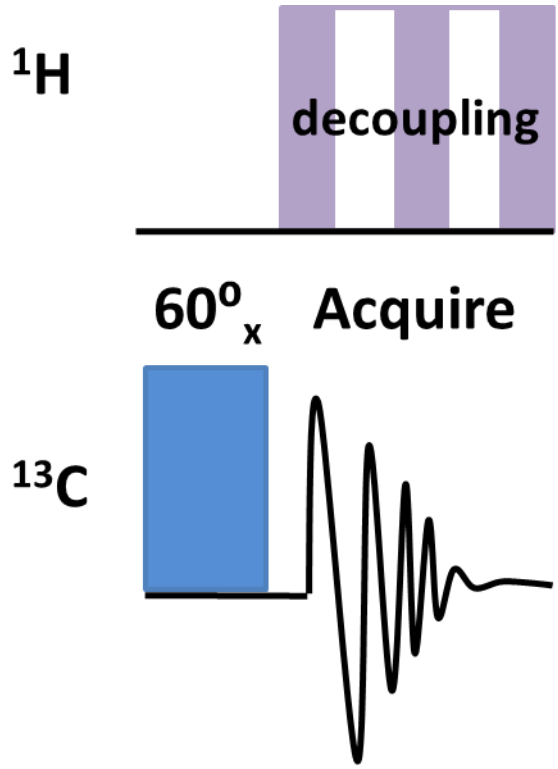

Figure 2-15: Single pulse excitation experiment used to obtain quantitative ^{13}C NMR spectra.

In the SPE experiment, an RF-pulse is applied to directly polarise the carbon nuclear spins. During the acquisition time, high power proton decoupling (HPDEC, such as two pulse phase modulation, TPPM[166]) is required to remove dipolar interactions between proton and carbon nuclear spins which significantly reduces the influence of Nuclear Overhauser Effect (NOE) exhibited by the spectra.[169] The delay between each scan of the SPE experiment should be sufficiently long enough to allow the nuclei to fully relax.[169] Providing these two conditions are met, the area under each ^{13}C resonance line is proportional to the number of nuclei in the respective molecular site when using the SPE experiment.[169-171]

Many examples of quantitative analysis by HPDEC SPE ^{13}C NMR exist in the literature covering a wide range of materials such as polyethene,[172, 173] coal tars,[174] poly(divinylbenzene) resins,[170] organic soil matter,[175] clathrates,[176] surfactants,[171] hyper-crosslinked polymers,[102] and pharmaceutical drugs.[177] The quantitative nature of ^{13}C spectra recorded in this work was also verified by full CP-kinetics analysis, leading to values of absolute intensity which do not depend on the efficiency of CP for a particular site.

2.1.2.4 Probing molecular motion and dynamics by deuterium NMR

Deuterium NMR is an exceptionally powerful technique for analysing the molecular motion and dynamics of polymeric materials. As deuterium possesses a spin of 1, the quadrupolar interaction dominates the ^{2}H NMR spectrum; therefore, the quadrupolar line shape and relaxation behaviour can reveal detailed information about the geometry and motions of the material under investigation.

Deuterium labels can be introduced into polymeric materials either by absorption of a deuterated guest or by replacing a proton for a deuteron in the polymer backbone. The labelled molecule/segment can then be analysed in terms of its structural and dynamic properties without perturbing the system.

^{2}H NMR covers an extremely wide range of motional timescales and can be used to probe motions within the timescales of seconds to picoseconds by line shape analysis or relaxation experiments (**Figure 2-16**). Such experiments provide information about motions of polymer segments (such as backbone dynamics of the polymer chains) and rate of rotation of end groups and side groups.

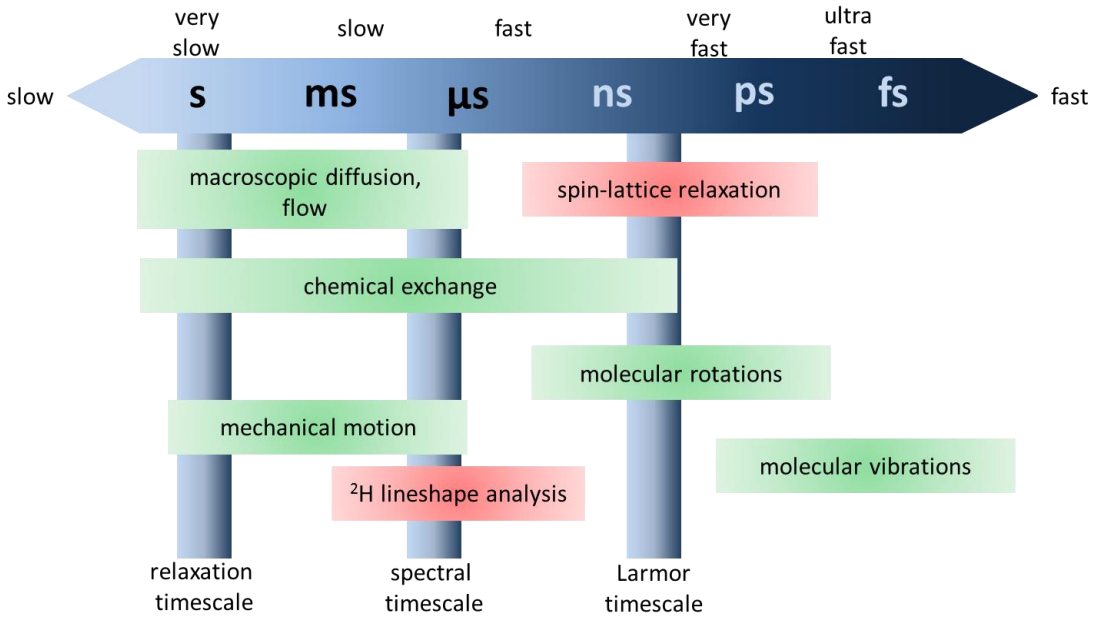

Figure 2-16: Motional timescales for physical processes. Motions probed by ^{2}H NMR are highlighted in red. Figure adapted from reference [158].

2.1.2.4.1 **Deuterium line shape analysis**

Deuterium line shape analysis involves relating the shape of the ^{2}H NMR spectral line to (a) the geometry and (b) the motions exhibited by the molecule under investigation. The ways in which information are derived from the spectra is described below:

(a) As discussed in **Section 2.1.2.1.3**, quadrupolar coupling arises from the interaction between the electric quadrupole moment and the EFG. Since EFGs are determined by the molecular structure around the nucleus, any changes in the geometry of the functional group lead to changes in the strength of the quadrupolar coupling. Changes in the quadrupolar coupling manifest in the ^{2}H NMR spectra as alterations of the distance between the 'horns' of a ^{2}H Pake doublet, owing to the splitting being

relative to the quadrupolar coupling ($\Delta\nu_Q$, **Figure 2-12**). Therefore, functional groups, exhibit a characteristic split between the horns during molecular re-orientation. For example, rotation of a methyl group around its intramolecular angle of 109.5° causes a narrowing of the static ^{2}H spectrum (**Figure 2-17 (a)**) resulting in a unique ^{2}H NMR spectrum shown in **Figure 2-17 (b)**. When reporting the effects of geometry upon the quadrupolar interaction, the quadrupolar coupling constant, Q_{cc} (where $Q_{cc} = \frac{3}{4}\nu_Q$) is often disclosed, rather than the quadrupolar frequency.

(b) For selectively deuterated materials, to good approximation, the symmetry axis of the quadrupolar interaction lies along the ^{2}H-C bond, V_{zz}. Therefore, the asymmetry parameter (η_Q), describes the magnitude of the EFG along the other two axes, V_{xx} and V_{yy} (as shown by **Equation 2-12** and **2-16**). As the magnitude of the EFG is affected by molecular reorientation, the asymmetry parameter provides information about motion. Asymmetry parameters close to one indicate fast molecular tumbling, whereas those close to zero indicate restricted motion. When a functional group undergoes complete reorientation, narrowing of the spectrum occurs. This effect is common for *para*-linked phenyl rings. Such groups are able to undergo either fast phenyl flips between two indistinguishable sites (where the residence time is long compared with the transit time, **Figure 2-17 (e)**) or continuous rotation about the *para*-axis **Figure 2-17 (c)**). However, caution must be taken when interpreting ^{2}H NMR spectra as rotation around the magic angle can lead to virtual collapse of the quadrupole splitting resulting from a geometric term (as shown in **Figure 2-17 (d)**, and should not be confused with free tumbling.

Further complications of ^{2}H line shape analysis can arise for motions on the intermediate timescale where the powder pattern is affected by relaxation processes. In the slow ($\tau_c \gg 1/\Delta\nu_Q$) and fast ($\tau_c \ll 1/\Delta\nu_Q$) limits (where τ_c is the

correlation time of the motion, see **Section 2.1.2.4.2**), the echo is completely refocused, since T_2 is comparatively slow. However, in the intermediate regime much of the signal decays as a result of T_2 relaxation leading to ^2H line shape distortion.

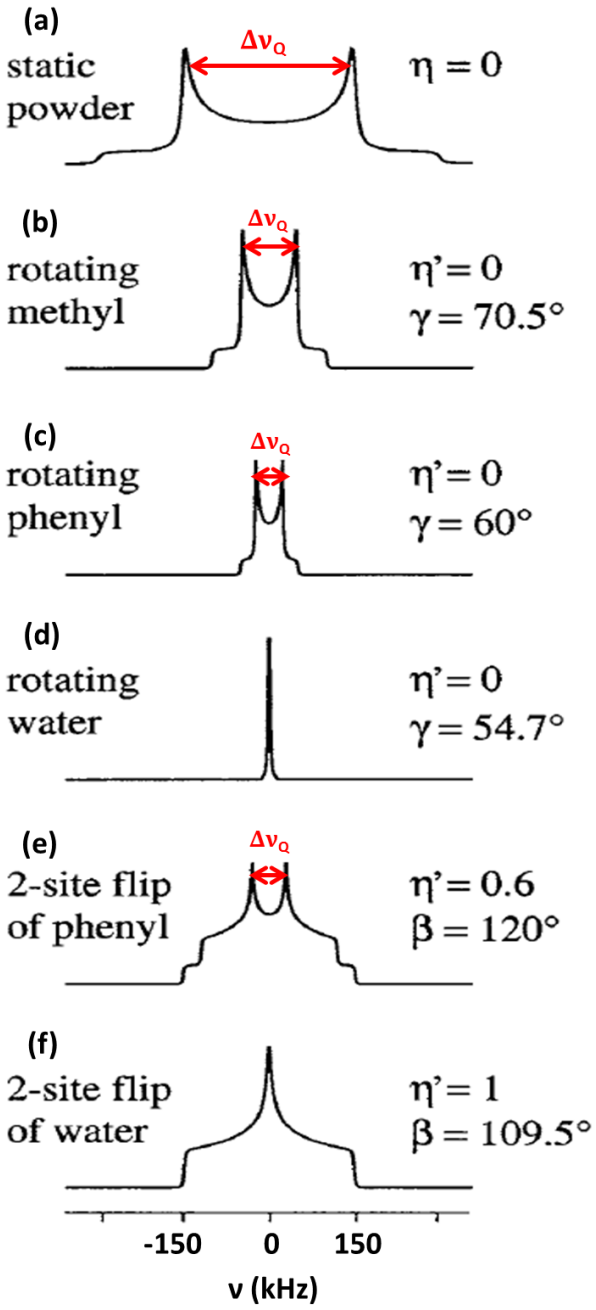

Figure 2-17: Simulated ^{2}H NMR line shapes corresponding to characteristic functional groups and their motions. In the case of fast rotation, γ represents the angle between the rotation axis and the ^{2}H-C bond. For a two-site jump, β represents the angle between the ^{2}H-C bond in the two configurations, and the effective asymmetry parameter is no longer zero, $\eta' \neq 0$. Figure adapted from reference [138].

2.1.2.4.1.1 Measuring ^{2}H NMR spectra using the quadrupole echo experiment[138, 161]

As a result of quadrupolar interactions, ^{2}H NMR spectra are very broad and have short free induction decay (FID) signals. Therefore, simple pulse-acquire experiments cannot be used to acquire ^{2}H powder patterns, as the initial part of the FID is not recorded owing to receiver dead time (the time left between a RF pulse and acquisition). These lost data contain a significant part of the total FID for ^{2}H NMR spectra and lead to distortion of the ^{2}H line shape upon Fourier transformation. To overcome this problem, ^{2}H powder patterns are recorded using a quadrupole echo pulse sequence, **Figure 2-18**. The delays τ_1 and τ_2 are adjusted so that data acquisition begins exactly at the echo maximum, resulting in the collection of un-distorted ^{2}H NMR spectra.

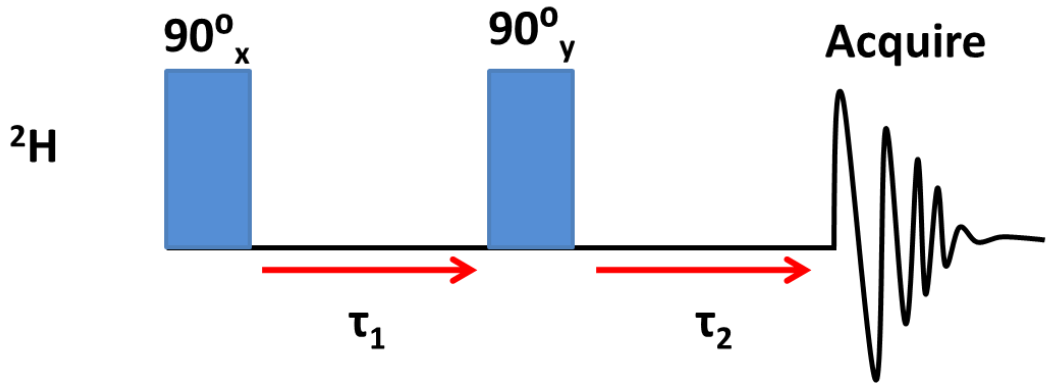

Figure 2-18: The quadrupole echo pulse sequence. Figure adapted from reference [138].

2.1.2.4.2 Deuterium relaxation NMR[158, 178, 179]

At equilibrium, nuclear spins are aligned with an external magnetic field (B_0) and the populations of energy levels are predicted by the Boltzmann distribution. When a RF pulse is applied, the equilibrium of the nuclear spin system is perturbed. As a result of this disturbance, the populations of the energy levels deviate from their thermal equilibrium values thus generating coherences. Nuclear spin relaxation is the process by which the nuclear magnetisation returns to its equilibrium configuration through interaction with the thermal molecular environment.

Relaxation processes are divided into two types. Spin lattice relaxation (also known as longitudinal or T_1 relaxation) involves the movement of spin populations back to their Boltzmann distribution values (**Figure 2-19 (b)**). Spin-spin relaxation (often referred to as transverse or T_2 relaxation) involves the decay of coherences (**Figure 2-19 (b)**).

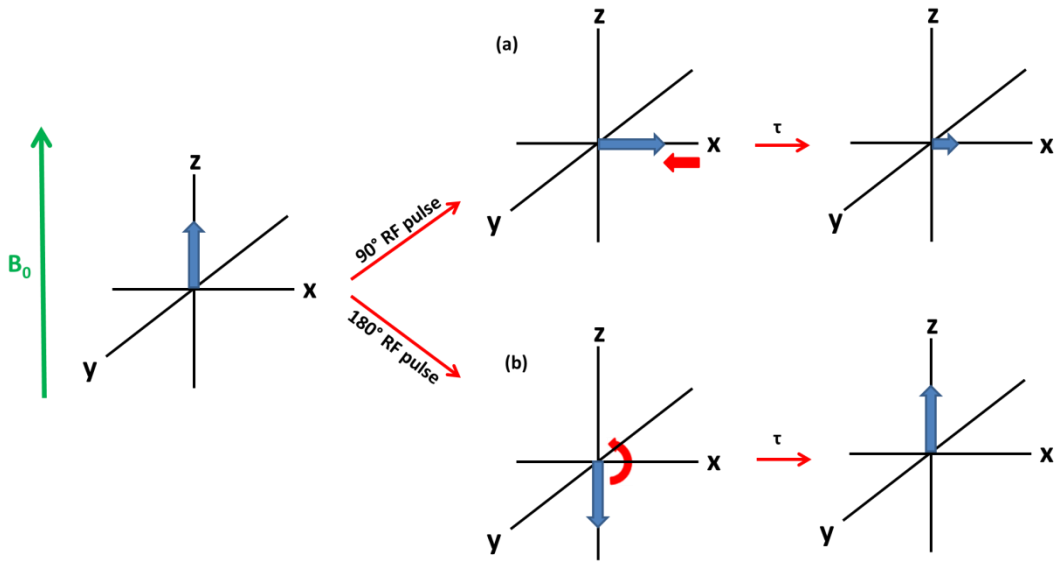

Figure 2-19: Types of relaxation represented by the vector model. **(a)** T_2 relaxation, **(b)** T_1 relaxation. Figure adapted from reference [158].

Deuterium relaxation is dominated by an intramolecular quadrupolar mechanism involving the thermal motions of molecules that give rise to local fluctuating fields at the site of nuclear spins. These motions can be described by rotational correlation times, τ_c, where the correlation time is the average time taken for a molecule to rotate through one radian. τ_c essentially provides a monitor for the speed of the motion; the smaller τ_c, the shorter the time between changes of molecular motion. The frequency distribution of the fluctuating magnetic fields associated with these motions is known as the spectral density, J(ω). The spectral density is proportional to the probability of finding a component (J) of the motion at a given frequency (ω, in rad s^{-1}). Relaxation only takes place when a suitable component exists at the Larmor frequency of a spin, therefore spectral density is given by:

$$J(\omega) = 2\frac{\tau_c}{1+\omega^2\tau^2}$$ **Equation 2-24**[167]

For deuterium, there are five different relaxation times, involving three different spectral densities $J_0(0)$, $J_1(\omega_0)$, and $J_2(2\omega_0)$, where ω_0 is the Larmor frequency of ^2H. Deuterium T_2 relaxation is used to detect slow motions near J(0), with correlation times longer than $\tau_c > 10^{-6}$ s.

^2H T_1 relaxation, however, occurs *via* three processes. The first involves recovery of the Zeeman polarisation to its equilibrium state, characterised by T_{1Z}. In order for T_{1Z} relaxation to occur, molecular tumbling must lead to modulation of electric field gradient at the Larmor frequency. If these conditions are met, relaxation is stimulated by flipping of the nuclear spin states. This process is analogous to the relaxation of spin-½ nuclei through dipolar interactions. The second route involves decay of the double quantum coherence (T_{1DQ}). The third process involves the decay of the quadrupolar polarization (T_{1q}). In this work, only T_{1Z} relaxation has been investigated.

The spectral density of T_{1Z} relaxation can be represented graphically, as shown in **Figure 2-20**.

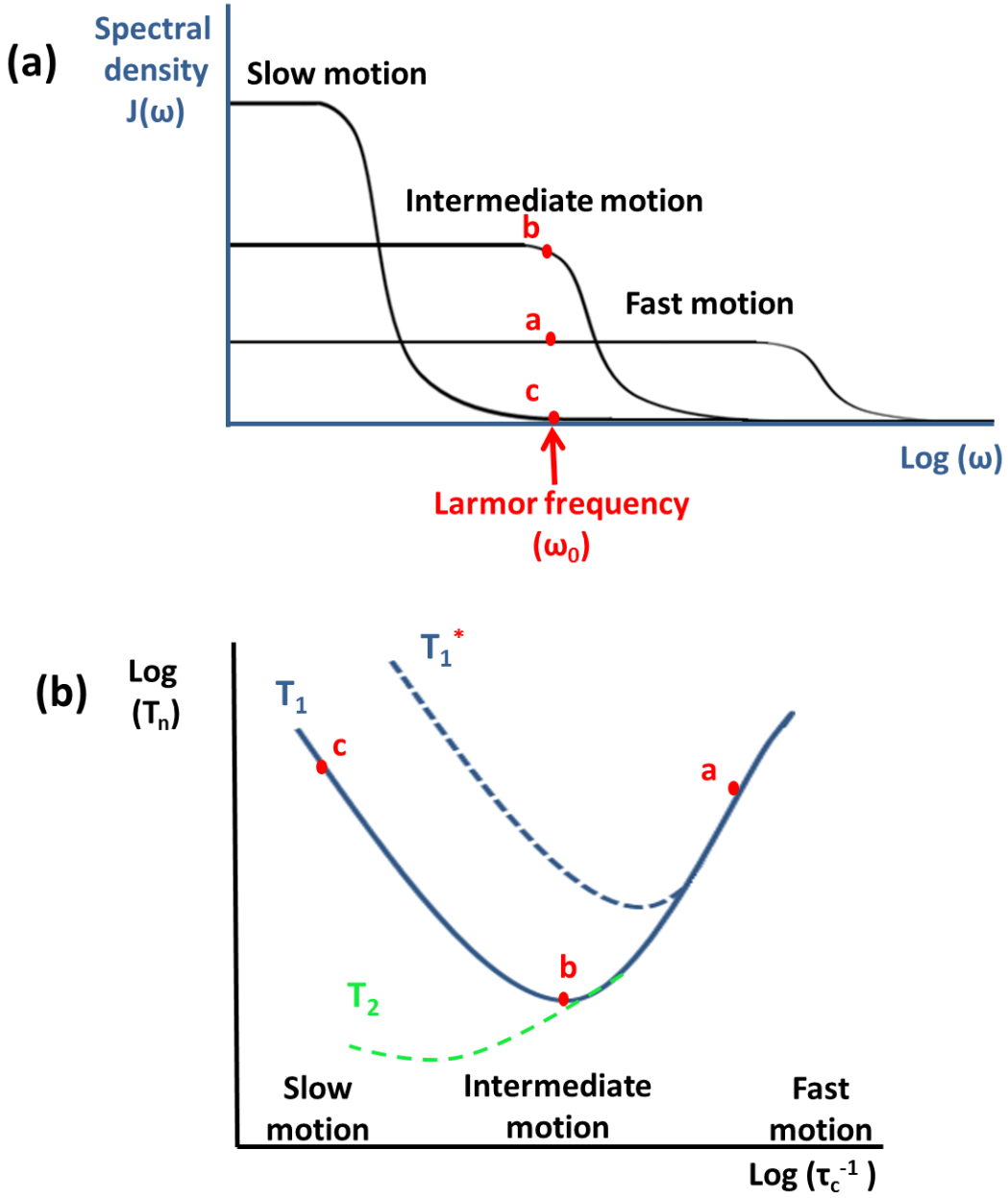

Figure 2-20: (a) Schematic representation of the spectral density, J(ω), as a function of frequency shown for molecules in three different motional regimes. For spins at the Larmor frequency, the corresponding T_1 curve is displayed in **(b)** as a function of molecular tumbling rate (*i.e.* the inverse of τ_c). As T_1 is dependent on the external magnetic field (owing to the Larmor frequency being field dependent) the T_1 minimum occurs for faster motion at higher fields, this is indicated by the dashed blue line (T_1*). Figure adapted from reference [168].

For molecules undergoing fast molecular tumbling (τ_c « $1/\Delta\nu_Q$), a small component of the spectral density occurs at the Larmor frequency (labelled 'c' on the graph in **Figure 2-20**). In this regime, the relaxation process is slow (T_1 is long). This region corresponds to small molecules in low-viscosity liquids and is known as the extreme narrowing limit.[168] As the tumbling rates decrease, the spectral density at ω_0 increases but then falls away once more at slow tumbling (τ_c » $1/\Delta\nu_Q$); hence the T_1 curve has a minimum at intermediate rates (**Figure 2-20 (b)**). Therefore, for small rapidly tumbling molecules, faster motion corresponds to slower relaxation, resulting in narrower linewidths, since longitudinal and transverse relaxation is identical (T_1 = T_2) under these conditions.[168] A reduction in tumbling rate such as an increase in solvent viscosity or reduction in sample temperature reduces the relaxation times and broadens the NMR spectrum. In the slow motion regime, energy conserving flip-flop transitions that stimulate T_2 relaxation are also present.[168] Thus for slowly tumbling molecules such as polymers, T_1 relaxation times can become long, but linewidths broaden as a result of short T_2 relaxation (**Figure 2-20 (b)**).

As molecular mobility (and thus τ_c) is affected by temperature, the fluctuating fields at the site of nuclear spins are temperature dependent. Increasing the temperature of the sample leads to an increase in field fluctuations and reduction of τ_c, whereas cooling the sample slows down the fluctuations, increasing τ_c.[158] The effect of temperature on T_1 depends on the location of τ_c with respect to the T_1 minimum. For systems with long correlation times (typically polymers and macromolecules),[158] warming the sample leads to a reduction in T_1. For systems with short correlation times (such as small molecules in low-viscosity liquids),[158] warming the sample generally increases T_1. The relationship between temperature and T_1 obeys Arrhenius behaviour, thus a plot of logT_1 *vs.* 1000/T can be used to derive the activation energy for a particular motion.[180] Therefore, variable temperature T_1 experiments are crucial for analysing molecular motion.

2.1.2.4.2.1 Measuring ^{2}H relaxation NMR by inversion recovery[138,158,167,168]

As mentioned in **Section 2.1.2.4.2**, for spin-1 nuclei T_{1Z} relaxation is the recovery of the Zeeman polarisation (z-magnetisation) to its thermal equilibrium state, where the populations are governed by the Boltzmann distribution. The relaxation behaviour of a nuclear spin in a magnetic field is described as an exponential decay by the Bloch equation:

$$\frac{dM_z(t)}{dt} = \frac{(M_z(t) - M_0)}{T_1}$$

Equation 2-25[167]

Where M_0 is the magnetisation at thermal equilibrium and T_1 is the time constant. The theory assumes that relaxation rates follow first order kinetics. After a RF pulse of 180° is applied, the T_1 time at time, t, is given by:

$$M_Z(t) = M_0\left[1 - e^{-\left(\frac{t}{T_1}\right)}\right]$$

Equation 2-26[167]

T_{1Z} relaxation can be measured using an inversion recovery pulse sequence. For deuterium, the inversion recovery pulse is followed by a quadrupole echo in order to prevent loss of data (as discussed in **Section 2.1.2.4.1.1**). As shown in **Figure 2-21**, a 180° pulse is applied to invert the magnetisation. A delay, τ_1, is allowed so that magnetisation can relax, after which a quadrupole echo is applied so that the magnetisation remaining after the delay can be measured.

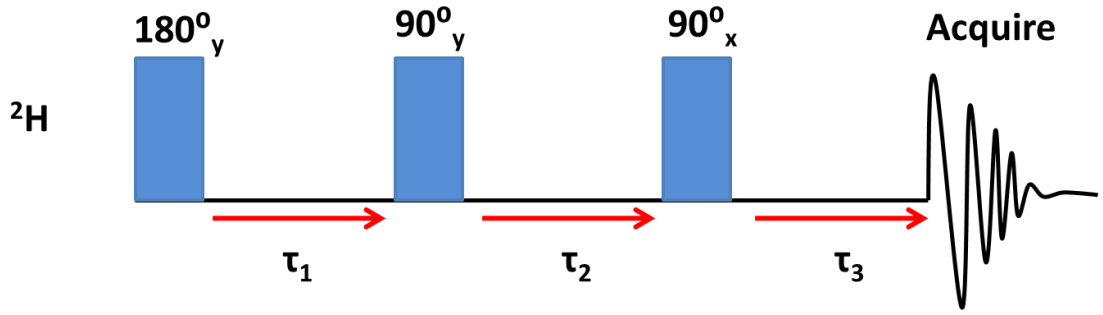

Figure 2-21: T_{1Z} inversion recovery pulse sequence with a quadrupole echo. Figure adapted from reference [138].

By varying the delay, the peak intensities can be measured as a function of τ. The changes in intensities are then fitted according to:

$$M_z(\tau_1) = M_0\left[1 - 2e^{-\left(\frac{\tau_1}{T_{1z}}\right)}\right] \qquad \textbf{Equation 2-27}^{167}$$

Where M_0 is the magnetisation recorded at τ_∞. An additional factor of two has been added to **Equation 2-26** when compared with **Equation 2-27** owing to the relaxation beginning from inverted magnetisation (as shown in **Figure 2-22**).

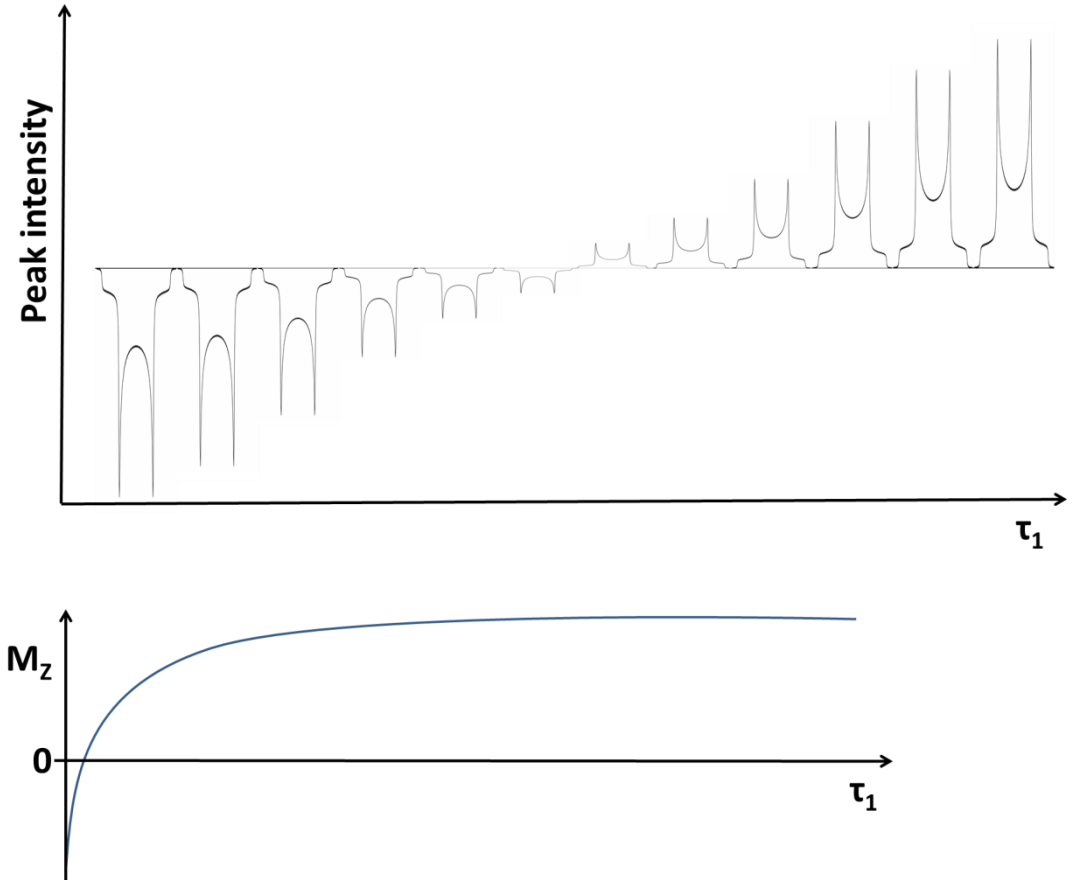

Figure 2-22: Peak intensity as a function of the delay time, τ_1, during the inversion recovery pulse sequence. As the delay time increases, the peak intensity changes from negative to positive. Figure adapted from reference [168].

Measuring T_1 relaxation times as a function of temperature enables derivation of a plot similar to that displayed in **Figure 2-20 (b)**. Interpretation of such a plot allows determination of the motional regime for the system under investigation.

2.2 Gas sorption analysis[1, 181-184]

Gas sorption is an analytical tool used to investigate porous materials. Data obtained from this method enable the elucidation of pore size, pore shape and can be used to calculate a surface area. By collecting such data, identification of the amount of accessible free space within a network and ultimately information about the structure of the network is possible.

Gas adsorption is the process in which a gas accumulates on the surface of a solid or liquid (adsorbent) forming a film of molecules or atoms (adsorbate). Adsorption is the consequence of surface energy, where the adsorbent can form weak van der Waals forces with the adsorbate, by a process called physisorption. The process is spontaneous.

2.2.1 Nitrogen adsorption isotherms[1, 181-184]

Nitrogen isotherm analysis is used to monitor the process of adsorption of nitrogen gas onto a solid. During the sorption process the temperature is kept constant at 77 K (the boiling point of nitrogen), and the volume of nitrogen is measured at increasing pressure. By plotting the volume of nitrogen adsorbed against the relative pressure ratio (P/P_0), where P_0 is the saturation vapour pressure (1 bar) of the pure nitrogen at 77 K, an adsorption isotherm can be obtained. The shape of the isotherm gives information about the nature of the porosity of the materials under examination. According to IUPAC classification,[1] six types of isotherm are possible for porous materials, however only four are exhibited by porous polymers. These are displayed in **Figure 2-23**.

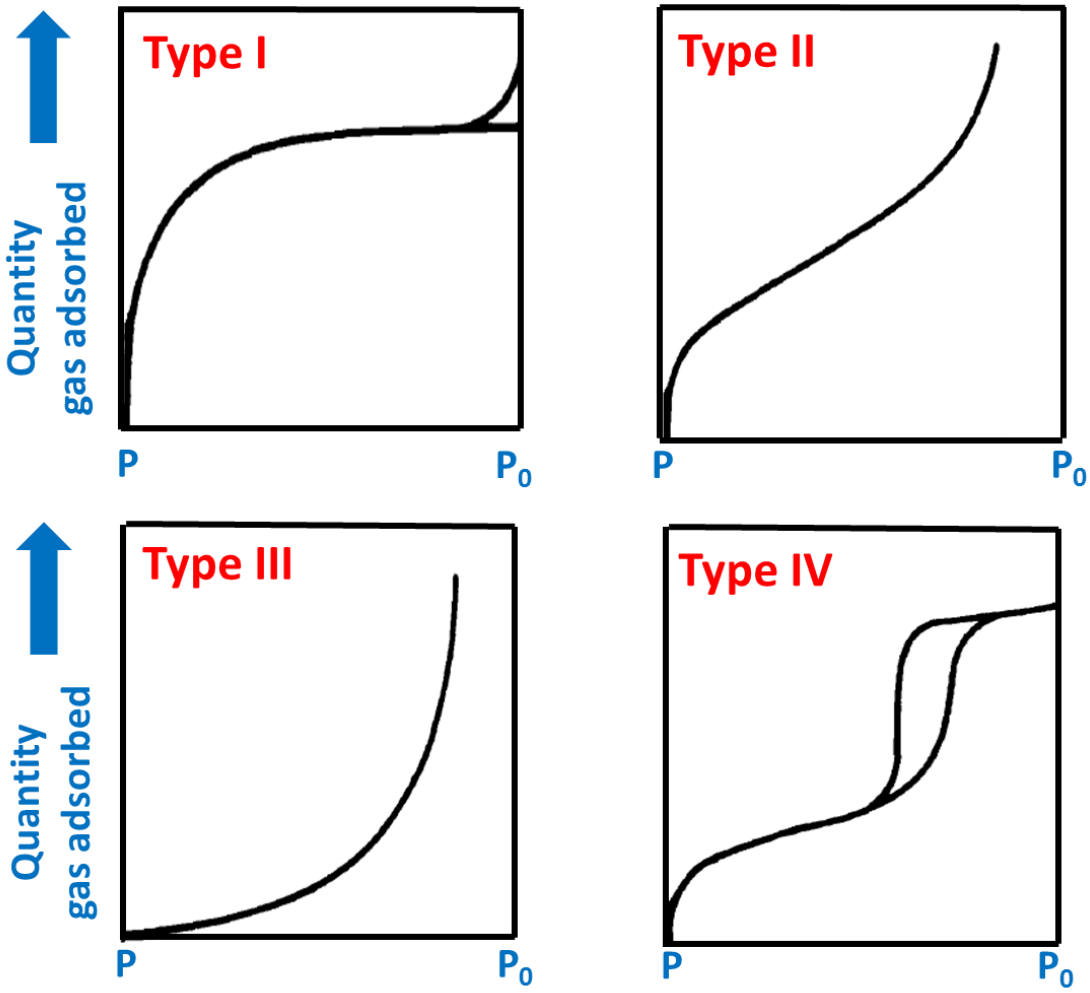

Figure 2-23: Nitrogen adsorption isotherms commonly observed in the characterisation of porous polymers.[182] Figure adapted from reference [1].

Type I isotherms are typically exhibited by microporous solids, which have pore diameters less than 2 nm.[1] At relatively low pressures a steep curve is observed as a result of nitrogen filling the micropores (as shown in **Figure 2-23**). Once all of the micropores have been filled a plateau occurs. The pressure at which the plateau is achieved is determined by the total pore volume. In some cases, a further increase in adsorption at high pressure is the result of multilayer sorption onto the external surface of the solid.

Type II isotherms are common for non-porous or macroporous solids where adsorption takes place on large external surfaces. Monolayer coverage

results in an increase in adsorption at lower partial pressures, followed by multilayer coverage at higher partial pressures (**Figure 2-23**).

Type III isotherms are rare and tend to occur when adsorbate-adsorbate interactions are stronger than adsorbent-adsorbate interactions.

Type IV isotherms are common for mesoporous solids with pore diameters in the range 2 to 50 nm.[1] The first part of the isotherm is similar to that of Type I and Type II isotherms, where monolayer formation occurs on the surface of the pore walls. At higher pressures multilayer formation takes place, resulting in a further increase in gas adsorption which gives rise to capillary condensation of gas within the mesopores. The condensed gas shows a large hysteresis upon desorption (**Figure 2-23**).

2.2.2 Desorption hysteresis[1, 181-184]

During desorption, hysteresis loops are exhibited if evaporation of the gas occurs at a pressure lower than that of capillary condensation. As the shapes of the hysteresis loops are characteristic of the pore shapes, information about pore geometry can be extracted from the desorption branches of the isotherms. Typically four types of hysteresis are observed for porous materials.[1] These are displayed in **Figure 2-24**.

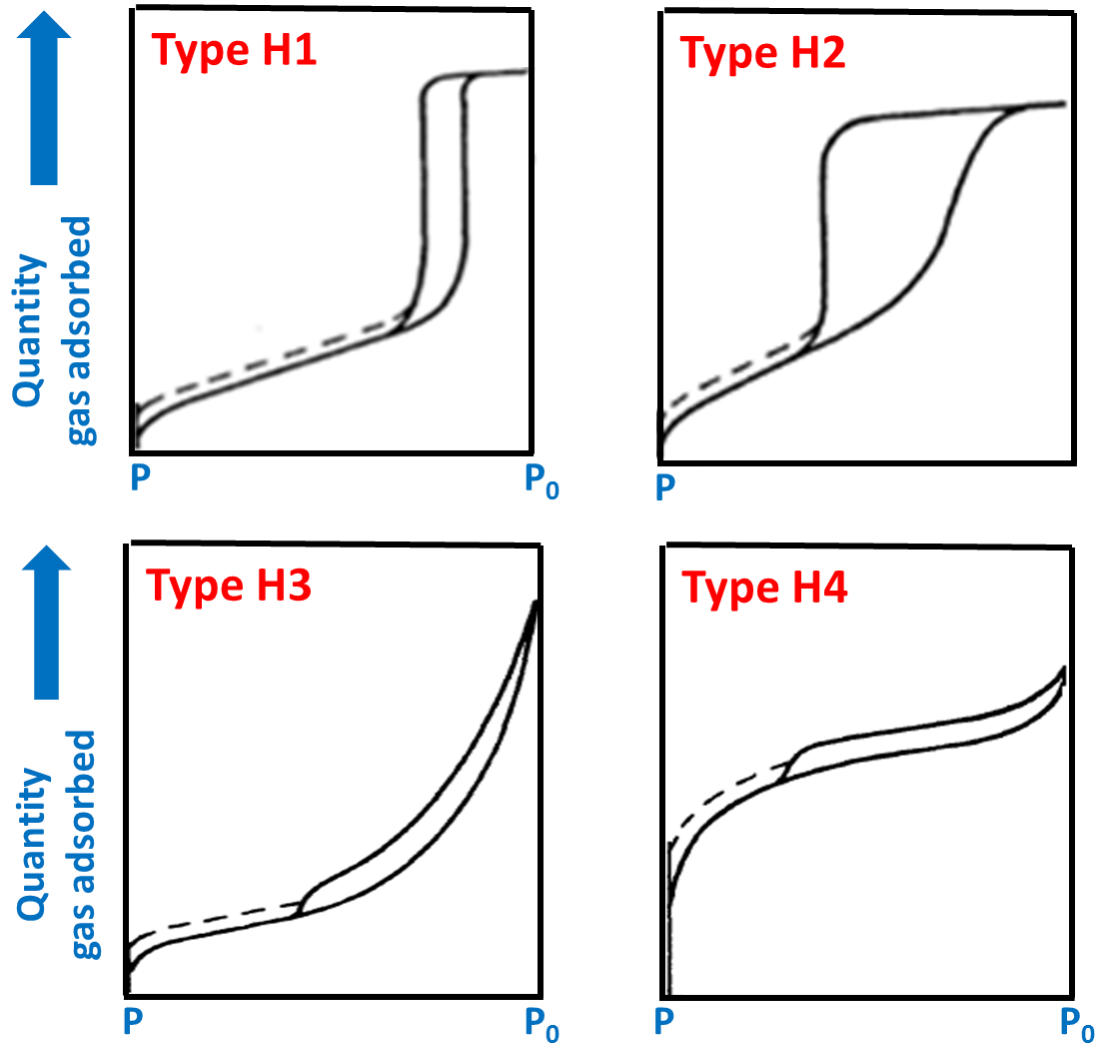

Figure 2-24: Hysteresis loops often observed in nitrogen adsorption-desorption isotherms. Figure adapted from reference [1].

H1 and H2 loops, displayed in **Figure 2-24** are usually observed for materials consisting of nearly cylindrical channels (**Figure 2-25**) or those that consist of consolidated or unconsolidated spherical particles.[182] In both cases pores can have uniform size and shape (H1) or non-uniform size or shape (H2), where ink-bottle and funnel shaped pores are non-uniform and cylindrical shaped pores are uniform (**Figure 2-25**).

H3 and H4 loops (**Figure 2-24**) are often exhibited by consolidated or unconsolidated spherical particles consisting of slit-shaped pores (**Figure 2-26**), with uniform (H4) or non-uniform (H3) pore size and/or shape.[182]

The dotted lines in **Figure 2-24** represent low-pressure hysteresis, which is thought to be associated with either the swelling of a non-rigid porous structure, or the result of adsorption of gaseous molecules with similar diameters to that of the pore entrances.[182]

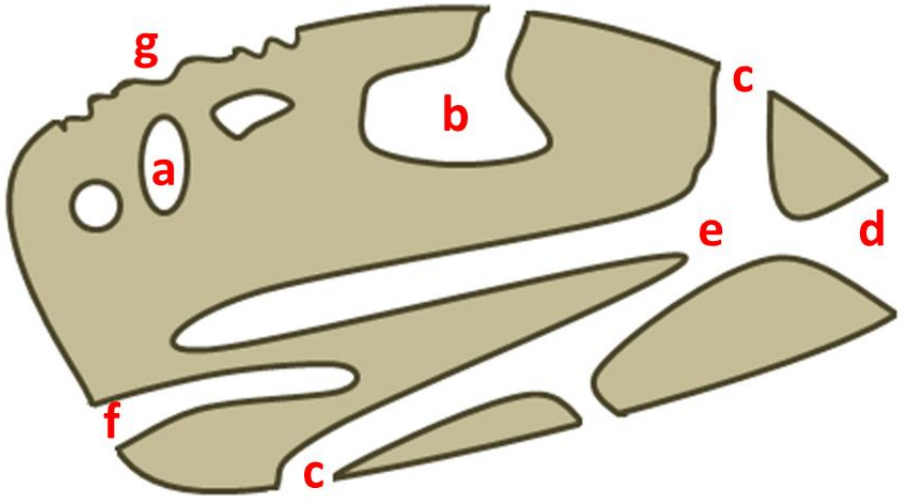

Figure 2-25: Schematic cross-section of a porous solid. Pores can be classified according to their shape, they may be cylindrical (either open (c) or dead-end (f), ink-bottle shaped (b), funnel shaped (d), or open at more than one end (e). Pores may also be slit-shaped (as shown in **Figure 2-26**). Close to, but different from porosity, is the roughness of the external surface represented by (g). Figure adapted from reference [170].

2.2.3 Pore volume and pore size distribution

The determination of pore volume and pore size distribution (PSD) of a material relies heavily upon the experimental data and models used in the calculations.[185] For crystalline materials and periodic mesoporous organosilicas, it is possible to determine the pore sizes by X-ray diffraction and then finely tune the gas sorption models to fit. However, it is particularly challenging to evaluate

pore size distributions for amorphous networks as X-ray analysis is not possible and many different pore sizes may exist within the material. In addition, the models have been developed for materials with known pore sizes, surface chemistries and gas interaction characteristics, *i.e.* zeolites, clays and activated carbons.[186-190]

The Barrett Joyner Halenda (BJH) method is based upon the Kelvin model of pore filling and applies only to the mesopore and small macropore size range. [189]

Horvath-Kawazoe (HK) technique calculates PSDs from the mathematical relationship between relative pressure and pore size using the modified Young-Laplace equation. However, the calculations are restricted to the micropore region (< 2 nm).[186, 190]

The de Boer t-plot method can be used to calculate PSDs by modelling the thickness of an adsorbate as a function of increasing relative pressure. The method relies upon the formation of multilayers during gas sorption measurements. Many data points particularly in the low and high pressure ranges are required to fit the theoretical and experimental isotherms.[187-189]

Non-local density functional theory (NL-DFT) involves construction of a 'kernel' that consists of up to 100 theoretical pore isotherms which are then compared by the software with the experimental data.[182] The theoretical isotherms take into consideration differences in pore geometry and gas-gas and gas-solid interactions. For the materials in this work, the slit pore model[191, 192] and cylindrical pore model[193] (as shown in **Figure 2-26**) are most applicable.

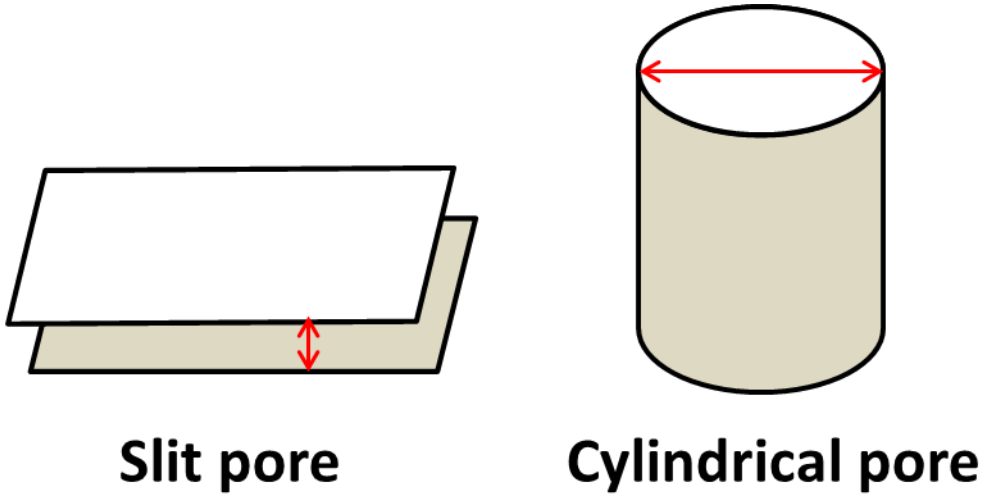

Figure 2-26: Pore models used in DFT calculations to derive the pore size and distribution. The pore size is represented by a red arrow. For cylindrical pores the pore size is given by the diameter. For slit pores the pore size is given by distance between the plates. Figure adapted from reference [182].

For pore size determination, the NL-DFT approach has no theoretical limitations.[182] In practice, its applicability ranges from ultramicropores to macropores and so comparison between materials containing these pore ranges is possible. The experimental limits are dictated by the adsorbate molecular size and the difficulty in performing precise measurements near saturation.[182] Many materials such as pillared clays, porous silica, CMPs and COFs[53, 67, 71, 100, 194, 195] have been analysed by NL-DFT.

2.2.4 Surface area determination[1, 181, 182, 184]

The Brunauer-Emmett-Teller (BET) gas sorption method is widely used to determine the surface areas of many types of porous materials, such as mesoporous silicas, COFs, MOFs and CMPs.[1, 191-193, 196]

BET theory makes the following assumptions: i) that adsorption takes place on the lattice where surface energy is uniform, ii) one monolayer is

adsorbed completely on the surface before another can start to adsorb, iii) at saturation pressure (P_0) the number of adsorbed layers is infinite (*i.e.* condensation occurs), iv) at equilibrium the rates of evaporation and condensation are equal for each layer, v) a monolayer of gas adsorbed will possess a fixed heat of adsorption (H_1) and that subsequent layers have heats of adsorption equal to the latent heat of evaporation (H_L).

The BET equation is given below:

$$\frac{P}{V(P_0-P)} = \frac{1}{V_m C} + \frac{(c-1)}{V_m C} \cdot \frac{P}{P_0}$$

Equation 2-28[171]

Where, C is a constant, V is the amount of gas adsorbed at pressure P, V_m is the amount of gas in the monolayer, P_0 is the saturation point and V tends to infinity at $P = P_0$.

According to BET theory, C is related to the heats of adsorption, given by:

$$C = exp\left[\frac{\Delta(H_1 - \Delta H_L)}{RT}\right]$$

Equation 2-29[173]

A plot of $P/V(P_0\text{-}P)$ against P/P_0 (known as a BET plot) gives a linear relationship when the BET equation is valid.[173] Both C and V_m are obtained from a BET plot, and thus the surface area can be determined. However, the linear relationship is limited to the P/P_0 range of 0.05 to 0.30 where processes such as capillary condensation and saturation are not taking place.

2.2.5 Gas selectivity[197]

Gas sorption techniques can also be used to determine the gas selectivity behaviour of a porous material. Such information is useful when developing porous materials as selective gas sorbents, for example separating carbon dioxide from nitrogen in post-combustion gases released from power stations.[86, 198]

Gas selectivities can be determined from the pure component gas isotherms using two methods. The first, and most simple method, involves calculation of the ideal selectivity by dividing the uptakes of the two gases at the same temperature and at 1 bar. The second route involves calculation of the gradient of each isotherm at low pressure. In this region the isotherms are linear and obey Henry's Law, *i.e.* the gas molecules are absorbing onto the surface of the material to form a monolayer and interactions between gas molecules are not present. Once the gradients have been calculated, they are divided so that preferential absorption between the two gases can be determined. The second method is more reliable than the first, but it requires many data points to be collected at low pressure for each gas isotherm.

2.3 Thermogravimetric analysis[199]

Thermogravimetric analysis (TGA) is a method of measuring the change in weight of a material as it is heated. A common approach involves controlled non-isothermal heating of the test material under constant gas flow. Data are plotted on a graph (called a TGA trace or thermogram) as temperature *vs.* %weight loss.

Information gathered from TGA traces can be used to determine the amount of solvent/water/monomer trapped within a polymer and the temperature in which it is released.

2.4 Scanning electron microscopy[200]

Scanning electron microscopy (SEM) is a method used for imaging the surface of a solid. The technique involves coating the surface of a sample with a conducting material, often carbon or gold, and scanning across the sample with a beam of energised electrons. The electrons that scatter on the surface of the sample are detected by the electron microscope and an image of the surface is obtained.

SEM imaging enables the topography and morphology of materials to be analysed. Information about the composition of a material such as; shape and size of particles, surface texture and presence of pores can be obtained. Often, relationships between the surface texture and morphology can be linked with other properties of the material under investigation, such as porosity.[182]

2.5 Energy-dispersive X-ray spectroscopy[200]

Energy-dispersive X-ray spectroscopy (EDX) is a technique used to determine the elemental composition of a material. During EDX analysis, a high energy beam of electrons is focused onto the analyte. The beam excites an electron from a low energy orbital resulting in ejection of the electron and generation of electron-hole. An electron from a higher energy level then fills the hole and releases the difference in energy in the form of an X-ray. The number of emitted X-rays and their associated energy is detected by an energy dispersive spectrometer. As the difference in energy levels, and thus the energy of the X-rays are unique to the atomic structure of the element from which they were emitted, the elemental composition of the material can be determined.

2.6 Fourier transform infra-red spectroscopy[93]

Fourier transform infra-red (FTIR) spectroscopy is an analytical tool that is widely used in laboratories to distinguish between different functional groups within a material. This technique involves measuring transitions between the vibrational states of a molecule using an IR spectrometer. The energy required to achieve these transitions is usually in the region of 1-100 $kJmol^{-1}$. This energy corresponds to the infra-red section of the electromagnetic spectrum.

An IR spectrometer works by measuring the amount of IR energy and the wavelength of the energy being absorbed. The change in the initial energy being passed through the sample is recorded as either an absorbance or percentage transmittance (%T). This recording often depends upon the preference of the analyst. If a sample does not absorb any IR radiation (*i.e.* the material is not being excited), it is said to have 'zero absorbance.' The corresponding transmittance would be 100 %. However, at specific frequencies, IR radiation will be absorbed by the material causing it to vibrate. In this case the transmittance will decrease. If the sample completely absorbs all of the IR radiation, then % T would be zero and absorbance would be infinite. FTIR spectrometers were developed so that all wavelengths could be measured simultaneously, dramatically reducing the analysis time.

For convenience, an IR spectrum is plotted against the wavenumber, rather than frequency or energy. Wavenumbers are the reciprocal of wavelength and have the unit cm^{-1}. Common IR spectrometers measure absorbance in the range of 200-4000 cm^{-1}. At each wavenumber, characteristic absorptions corresponding to a specific vibrational mode often occur. These absorptions allow certain functional groups to be identified or distinguished. For example, carbonyl groups absorb IR radiation between 1815 and 1550 cm^{-1}. The absorbance appears as a sharp intense peak in the IR spectrum. In contrast, an amine group absorbs IR radiation in the region of 3500 to 3300 cm^{-1} which is displayed as a broad peak in the spectrum.

2.7 Elemental analysis

Elemental analysis is a method for determining the chemical composition and purity of a material. The technique involves total combustion of a materials and analysis of the resulting combustion products by gas chromatography. The products include; carbon dioxide, water and nitric oxide. By calculating the percentage of carbon, hydrogen and nitrogen in the materials, derivation of an empirical formula is possible.

Chapter 3:

Investigation of the Reaction Pathway for CMP Networks

3.1 Introduction

CMPs, specifically poly(aryleneethynylene)s (PAEs), were first reported in 2007 by Jiang *et al.*[65] PAEs are synthesised by Sonogashira-Hagihara palladium-catalysed reactions between aromatic iodides and ethynylbenzene.[65,66] The materials have advantageous properties, such as tunable micropore size and BET surface areas (in excess of 500 m^2g^{-1}),[65,66] and the ability to swell.[78] Changes in porosity can be achieved by systematically varying the aryleneethnylene strut lengths, which may allow the networks to be used as gas storage materials.[66]

In 2009, Stöckel *et al.* reported the synthesis of PAEs from tetrahedral monomers.[79] The networks exhibited higher BET surface areas than those prepared from two-dimensional monomers.[79] In 2010, Dawson *et al.* reported the synthesis of PAE networks containing a wide range of functional pendant groups with aim of targeting selective sorption.[71] Owing to the limited commercial availability of iodinated-aromatic monomers, the functionalised CMPs were prepared from brominated-aromatic monomers.[71] A reduction in BET surface area was accompanied by a decrease in the degree of polymerisation,[71] ascribed to the lower reactivity of brominated molecules in Sonogashira-Hagihara reactions than the iodinated equivalents.[201, 202]

More recently, Dawson and co-workers investigated the effect of solvent choice upon the BET surface areas of CMP networks.[100] Various solvents were studied in order to achieve the highest surface areas. DMF, THF and 1,4-dioxane gave the highest surface area materials, while toluene led to a reduction in surface area. The effect of surface area was ascribed to solubility of the monomers and subsequent oligomers, with poor solubility leading to a reduction in polymerisation by premature precipitation of the arylene(ethynylene) oligomers.[100]

Although significant advancements have been made to improve the gas storage capabilites and increase synthetic diversity of CMPs, information about their struture remains limited. Owing to the amorphous nature of CMPs, traditional characterisation techniques such as X-ray diffraction cannot be

implemented. The insolublity of these materials also prevents the use of gel permeation chromatography. Therefore, molecular level characterisation of CMPs is limited to solid-phase methods such as gas sorption, scanning electron microscopy (SEM) and solid-state NMR.

This chapter describes investigations of the growth of CMP-1 networks during the polymerisation reaction by analysing the reaction intermediates at increasing time intervals. In this work, the brominated monomer and DMF were chosen as these conditions have previously been reported to give the greatest degree of polymerisation and the highest surface area materials.[100]

Gas sorption and SEM analyses have been used to examine the changes in textural properties and cluster size of the intermediates during the course of the reaction. The information gathered from these results has allowed a reaction mechanism for the formation of CMP-1 networks to be proposed. Validation of the mechanism was achieved by end group analysis using FTIR, EDX and ^{13}C solid-state NMR. To the best of our knowledge, this is the first proposal of a reaction mechanism for CMP network formation and highlights an alternative method for characterising such materials.

3.2 Experimental

3.2.1 Synthesis section

3.2.1.1 Materials

All chemicals and solvents were obtained from either ABCR (1,3,5-triethynylbenzene, 98 %) or Sigma-Aldrich and used as received. Anhydrous grade *N*,*N*-dimethylformamide (Aldrich) was used. All chemicals had a purity of 98 % or greater.

3.2.1.2 Preparation of glassware and equipment

All Sonogashira-Hagihara reactions were carried out in dry 2-necked round-bottomed flasks (150 mL) on a Radleys carousel, and back-filled with N_2 prior to use.

All other equipment, such as syringes, needles and magnetic stirrers, were baked for 24 h in an oven at 120 °C prior to use.

3.2.1.3 Synthesis of CMP-1 networks

Scheme 3-1: CMP-1 reaction.

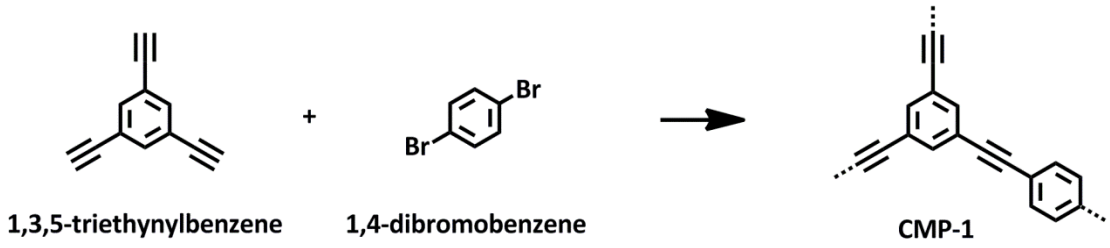

The networks were synthesised in DMF using a procedure similar to that reported for CMP-1.[100] Typically, 1,3,5-triethynylbenzene (150 mg, 1.0 mmol), 1,4-dibromobenzene (236 mg, 1.0 mmol), triethylamine (1.0 mL) and DMF (1.0 mL) were mixed under nitrogen in a 2-necked round bottomed flask (150 mL). The reaction mixture was heated to 100 °C.

Next, a slurry of the catalyst, tetrakistriphenylphosphinepalladium(0) (50 mg, 0.04 mmol) and copper (I) iodide (15 mg, 0.08 mmol) in DMF (1.0 mL), was added *via* a wide-bore needle to the flask. A stop-watch was started after all of the catalyst slurry had been added.

Each mixture was then heated under nitrogen at 100 °C for increasing time intervals of 10, 20, 30, 40, 60, 120, 300, 420, 1080 and 2520 minutes. After this time, the reaction was retarded by addition of cold methanol (*ca.* 100 mL) and filtered immediately under suction. The solid precipitate was isolated and

washed several times with methanol to remove any catalyst. The recovered solid was then Soxhlet extracted in methanol for 12 hours and dried in a vacuum oven for 24 hours prior to analysis. Yields are given in **Table 3-1**. Reactions which did not give any precipitated material upon addition of methanol (*i.e.* those collected before 40 minutes) were analysed in solution by ^{1}H NMR.

Table 3-1: Summary of the yields of reaction intermediates that gave a solid precipitate.

Reaction Time (min)	Yield (mg)	% Yield
Predicted[a]	226	100
10[b]	-	-
20[b]	-	-
30[b]	-	-
40	109.1	48.2
60	142.0	62.8
120	163.5	72.1
300	239.6	106
420	248.0	110
1080	244.9	108
2520	264.8	117

[a]Predicted values assuming 100 % reaction success and full network formation.
[b]No solid precipitate was recovered at these reaction times.

3.2.2 Characterisation conditions

3.2.2.1 Gas sorption analysis

Polymer surface areas and pore size distributions were measured by nitrogen adsorption and desorption isotherms in the range 0.01 – 0.95 P/P_0 with 98 data points at 77.3 K using a Micromeritics ASAP 2420 volumetric adsorption analyser. Gas sorption equipment was operated by either Dr. Robert Dawson or Mr. Robert Clowes.

Surface areas were calculated in the relative pressure (P/P_0) range from 0.01 to 0.10. Pore size distributions and pore volumes were derived from the adsorption branches of the isotherms using the non-local density functional theory (NL-DFT) pore model for slit pore geometry. Samples were degassed at 120 °C for 15 h under vacuum (10^{-5} bar) before analysis.

3.2.2.2 SEM and EDX

High-resolution SEM images of the network morphology were collected using a Hitachi S-4800 cold field emission scanning electron microscope (FE-SEM) by Dr. Robert Dawson. The dry samples were prepared on 15 mm Hitachi M4 aluminium stubs using either silver dag or an adhesive high-purity carbon tab. The samples were then coated with a 2 nm layer of gold using an Emitech K550X automated sputter coater. The FE-SEM measurement scale bar was calibrated using certified SIRA calibration standards. Imaging was conducted at a working distance of 8 mm and a working voltage of 3 kV using a matrix of upper and lower secondary electron detectors. Particle sizes were measured from printed copies of the expanded SEM images by hand, using a ruler. Three images were measured per sample.

An Oxford instruments 7200 EDX detector was used to characterise elemental compositions of the samples. EDX analyses were conducted at a working distance of 15 mm and a working voltage of 30 kV by Dr. Tom Hasell.

3.2.2.3 **FTIR**

IR spectra were collected as KBr pellets using a Bruker Tensor 27 spectrometer.

3.2.2.4 **TGA**

TGA analyses were carried out using a Q5000IR analyser (TA Instruments) with an automated vertical overhead thermobalance. The samples were heated at a rate of 10 °C/min under a nitrogen atmosphere to a maximum of 800 °C.

3.2.2.5 **Elemental Analysis**

All elemental analyses were carried out by the Microanalysis Department in the School of Physical Sciences, at the University of Liverpool. The conditions used to collect these data are given in **Chapter 2**, **Section 2.7**.

3.2.2.6 **Solid-State NMR**

Solid-state NMR spectra were measured at ambient temperature (unless otherwise stated) on a Bruker Avance DSX 400 spectrometer. Samples were packed into zirconia rotors 4 mm in diameter equipped with a high temperature

cap. Data were acquired using a 4 mm $^{1}H/X/Y$ probe operating at 100.61 MHz for ^{13}C and 400.13 MHz for ^{1}H.

3.2.2.6.1 ^{1}H-^{13}C CP/MAS NMR

^{1}H-^{13}C CP/MAS NMR spectra were acquired at an MAS rate of 10.0 kHz using a ^{1}H $\pi/2$ pulse of 3.6 μs and a recycle delay of 10 s. The Hartmann-Hahn condition was set using hexamethylbenzene. The spectra were measured using a contact time of 2.0 ms. Two-pulse phase modulation (TPPM) decoupling[166] was used during the acquisition. Typically, 4096 scans were accumulated. The values of chemical shifts are referred to that of TMS.

For ^{1}H-^{13}C CP/MAS kinetics experiments, various contact times were used in the range 0.01 ms to 16.0 ms. Twenty-one slices were collected. 304 scans were accumulated per slice.

3.2.2.6.2 SPE $^{13}C\{^{1}H\}$HPDEC MAS NMR

SPE $^{13}C\{^{1}H\}$ HPDEC MAS NMR spectra were acquired at an MAS rate of 10.0 kHz using a ^{13}C $\pi/3$ pulse of 2.6 μs and a recycle delay of 10 s. Two-pulse phase modulation (TPPM) decoupling[166] was used during the acquisition. Typically, 4096 scans were accumulated. The values of chemical shifts are referred to that of TMS.

3.2.2.7 Data analysis

Nitrogen adsorption isotherms were analysed using Micromeritics ASAP2420 software. All solid-state NMR spectra were acquired using

XWINNMR 3.5. All NMR spectra were processed using Bruker Topspin 2.1 software. Deconvolutions of the spectra were carried out using Origin Pro 8.5.

3.3 Results and discussion

Reactions halted before 40 minutes were analysed by solution NMR as no solid product was collected, *i.e.* the intermediates were soluble in the methanol/DMF mixture. ^{1}H NMR spectra of the soluble intermediates are given in **Figure 3-1**.

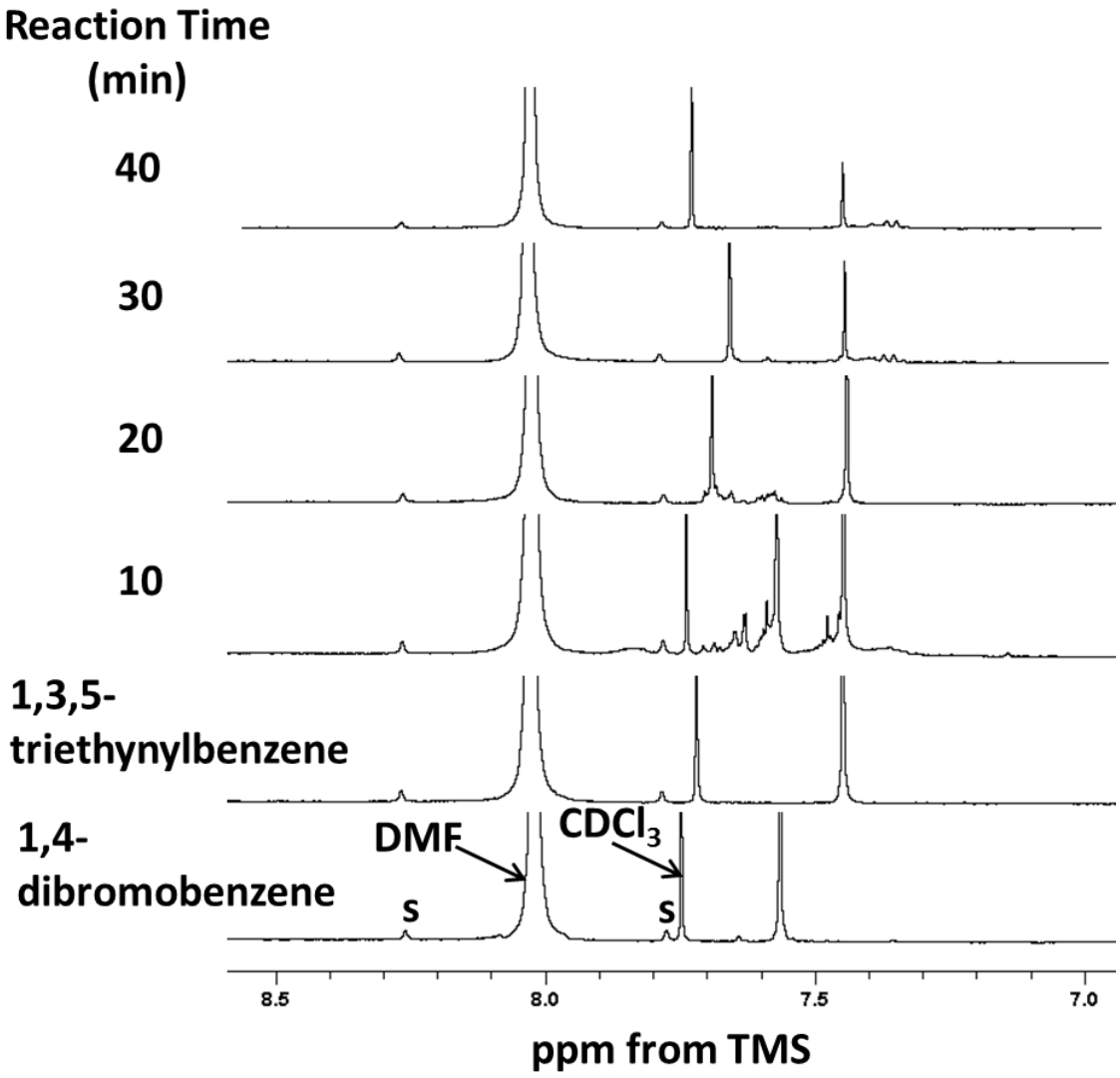

Figure 3-1: ^{1}H NMR of monomers and soluble reaction intermediates (all spectra have 8 × magnification). Spectra calibrated to DMF at 8.20 ppm. 's' denotes satellite solvent peaks.

As the reaction mixtures contain varying amounts of solvent and intermediates, their chemical shifts vary between each ^{1}H NMR spectrum. Deviations in chemical shift prevent the ability to accurately assign all of the individual peaks. Also, the alkyne peak, which would appear at *ca.* 3.1 ppm, is obscured by a solvent peak. However, the spectra can be used to show the growth and precipitation of oligomers with time.

After 10 minutes, the ^{1}H NMR spectrum consisted of peaks corresponding to soluble materials with many un-symmetrical aromatic groups, suggesting that polymerisation is taking place. After 20 minutes, fewer peaks were observed in the spectrum, suggesting that the intermediates have become more extended and precipitated out of solution. At 30 and 40 minutes even fewer aromatic peaks were detected, again this is an indication that the materials are now insoluble in the reaction mixture.

Gelation of reaction mixtures was observed after 30 minutes and upon addition of methanol, a brown solid precipitated. The brown solids were analysed by gas sorption and SEM.

3.3.1 Gas sorption

Gas sorption analysis has been used to assess the progression of porosity for the CMP-1 intermediates with increasing reaction time. The data from this chapter have also been compared with gas sorption analyses reported previously for CMP-1 networks.

Gas sorption isotherms are displayed in **Figure 3-2** and pore volume data are summarised in **Table 3-2**.

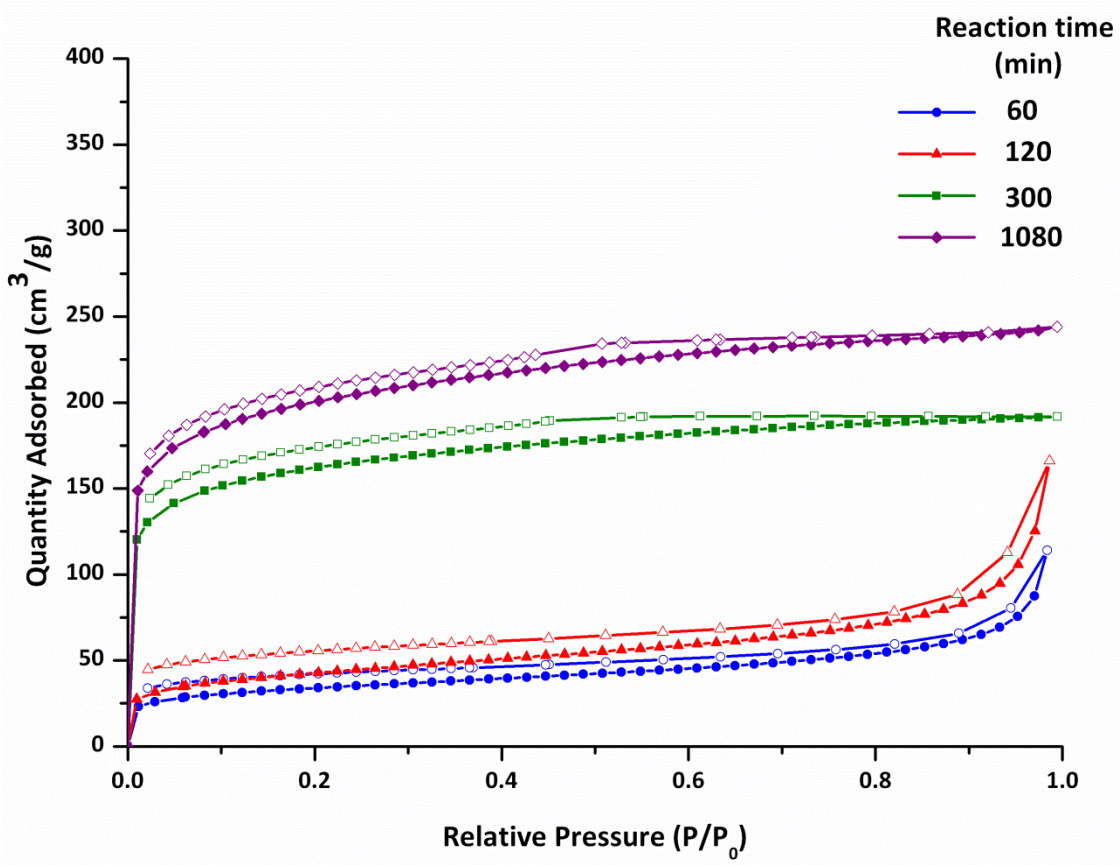

Figure 3-2: Nitrogen adsorption-desorption isotherms at 77 K for CMP-1 materials synthesised at varying reaction times (no offset). Adsorption (filled symbols), desorption (hollow symbols).

As the reaction time increases, the SA_{BET} of the material increases (from 123 m^2g^{-1} at 60 minutes, to 755 m^2g^{-1} at 300 minutes, **Table 3-2**). The SA_{BET} of the material collected at 300 minutes is comparable with other CMP-1 networks, even though the reaction times used to prepare the reported networks are in excess of 24 hours.[65, 66, 71, 100]

The shapes of the isotherms also change with increasing reaction time. Reaction intermediates collected at 60 and 120 minutes display Type I isotherms, (according to IUPAC classifications) with some Type IV character.[1] At low pressure ($P/P_0 < 0.1$) a small uptake of gas is observed, this is indicative of the filling of micropores. As the pressure increases further, the gas uptake

continues to rise, although at a slower rate. At high relative pressure (P/P_0 > 0.9) the curve steepens dramatically as a result of nitrogen filling the large mesopores and interparticular speace. H3/4 hysteresis is observed upon desorption, such behaviour is characteristic of slit shaped pores.[1] These data suggest porosity arises from inter-particulate sorption. Type I/IV isotherms have also been reported for CMP networks synthesised from the brominated monomer.[71]

At longer reaction times (*i.e.* 300 and 1080 minutes), exclusively Type I isotherms are observed, with slight hysteresis during desorption (**Figure 3-2**). For these reaction intermediates, a larger uptake of gas is observed at low pressure (P/P_0 < 0.1), compared with those collected at 60 and 120 minutes. The uptake of gas plateaus at high relative pressure (P/P_0 > 0.9). These isotherms are indicative of microporosity and are similar to those observed for CMPs synthesised from the iodinated monomer.[65, 66]

Values for $V_{0.1}/V_{Tot}$ have been used previously to estimate the level of microporosity in CMP networks.[71, 100] The ratios are calculated by dividing the pore volume at low pressure by the pore volume at high relative pressure. Porous materials with ratios close to zero denote mesoporosity. Non-porous materials *i.e.* those with SA_{BET} of *ca.* zero also display $V_{0.1}/V_{Tot}$ ratios close to zero. $V_{0.1}/V_{Tot}$ ratios that tend towards one are indicative of microporosity.

As shown in **Table 3-2**, values of less than 0.29 are found for intermediates collected before 300 minutes. Such values suggest that the majority of sorption for these materials arises from interparticulate mesoporosity. Mesoporosity is also common for polymers in which agglomerated structures are formed during liquid-liquid phase separation.[203]

A value of 0.77 is calculated for materials collected at 300 minutes and above (**Table 3-2**). These values are similar to those reported for other CMP-1 networks[65, 66, 71, 100] and confirm that the majority of sorption is due to microporosity.

Table 3-2: Summary of gas sorption data for CMP-1 materials synthesised at varying reaction times.

CMP-1 material	SA_{LANG} (m^2g^{-1})[a]	SA_{BET} (m^2g^{-1})[b]	$V_{0.1}$ (cm^3g^{-1})[c]	V_{Tot} (cm^3g^{-1})[d]	$V_{0.1}/V_{Tot}$
Intermediate at 60 min	162	123	0.04	0.18	0.22
Intermediate at 120 min	206	153	0.06	0.29	0.21
Intermediate at 300 min	593	755	0.23	0.30	0.77
Intermediate at 1080min	934	733	0.23	0.38	0.61
CMP-1-Br[e] (synthesised in DMF)[100]	1071	837	0.32	0.45	0.71
CMP-1 –Br[e] (synthesised in toluene)[71]	1046	867	0.33	0.99	0.33
CMP-1-I[f] (synthesised toluene)[65]	728	834	0.33	0.47	0.70

[a]Based on an isotherm pressure range of 0.06-0.20. [b]Based on an isotherm pressure range of 0.06-0.12. [c]Pore volume at $P/P_0 = 0.1$. [d]Total pore volume at $P/P_0 = 0.98$. Data collected at 77 K using N_2 as the sorbate. [e]Network synthesised from the brominated monomer. [f]Network synthesised from the iodinated monomer.

Non-local density functional theory (NL-DFT) has been used to calculate pore sizes and provide further confirmation of the pore shapes proposed by the gas sorption isotherms.[196, 204] NL-DFT was chosen as it can be used to calculate pores over a wide range of sizes (ultramicropore to macropores, see **Section 2.2** for further information). NL-DFT has also been used for pore size determination of similar materials such as CMPs and COFs allowing a comparison between the materials in this work with those that are published.[53, 67, 71, 100, 194, 195] The NL-DFT model for slit-shaped pores gave the best fit (the standard deviation of fit values were smaller, lower than 0.02, compared with those found for the model representing pillared clay with cylindrical pores,

higher than 0.05). As the intermediates collected at 60 and 120 minutes display H3/4 hysteresis (**Figure 3-2**), one would expect the slit-pore model to be most applicable (see **Section 2.2** for further information).

Pore size distribution curves are shown in **Figure 3-3**. The NL-DFT plots do not go below 10 Å as there is a lack of experimental points at low pressure. In order to collect low pressure data points the probe gas would also need to be changed from nitrogen to carbon dioxide or argon.

For reaction intermediates collected before 300 minutes, pore sizes of 300–450 Å were observed. These pore sizes fall within the mesoporous range. Intermediates collected after 300 minutes display pore sizes within the microporous range at *ca.* 20 Å. The pore sizes of materials collected after 300 minutes are similar to those found for other CMP-1 networks.[65, 66, 71, 100]

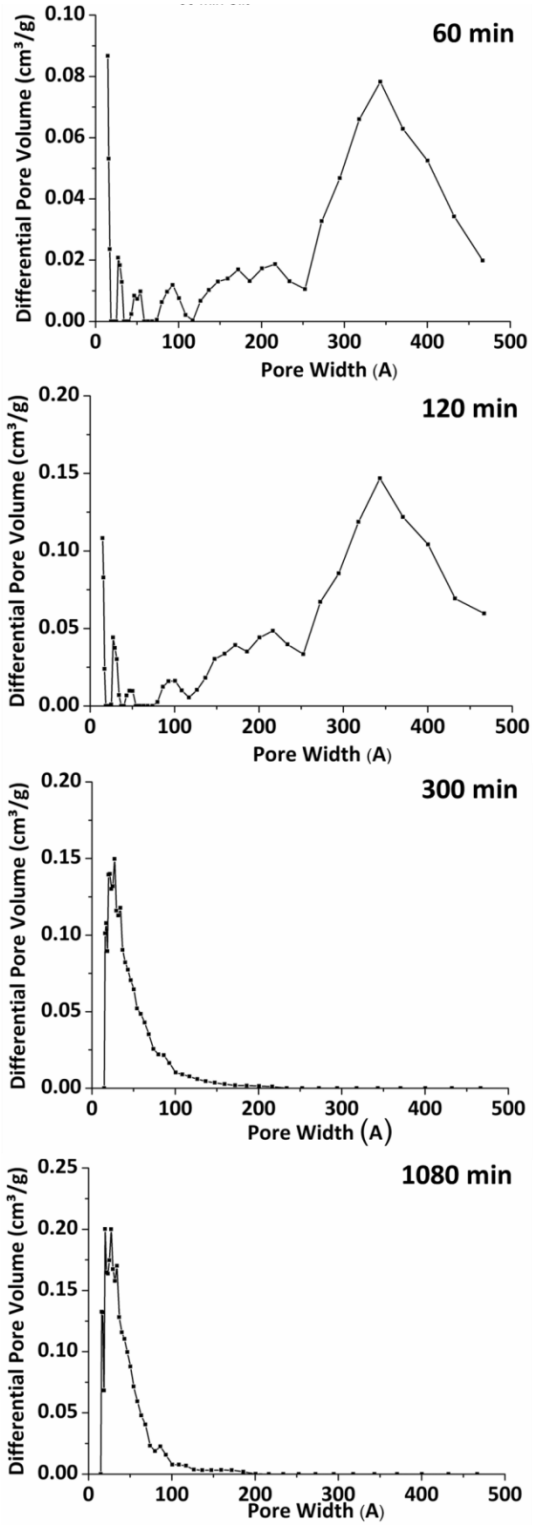

Figure 3-3: NL-DFT pore size distributions of CMP-1 intermediates synthesised at varying reaction times. NL-DFT model for slit pores was used in the calculations.

3.3.2 Morphology

A strong link between polymer morphology and gas sorption properties exists.[1,203] Materials with spherical morphologies often display mesoporosity resulting from inter-particulate sorption, while those with larger fused masses and a rough texture are generally microporous arising from intra-particulate sorption.[181]

In a paper by Dawson *et al.*[100] this link was examined for a range of functionalised CMP networks synthesised from the brominated monomer in various solvents. Networks prepared in toluene were mesoporous and exhibited smooth spherical morphologies. When synthesised in DMF, the networks were microporous and consisted of larger fused masses with rough surfaces. It was concluded that the change in morphology was a consequence of solubility of reaction intermediates in the solvent. Indeed, spherical morphologies have been reported for aromatic polymers that undergo liquid-liquid phase separation (*i.e.* premature precipitation of oligomers) during their synthesis.[203]

In this current work, intermediates collected at 60 and 120 minutes exhibit interparticulate mesoporosity and consist of fused-spherical morphologies with smooth surfaces (as shown in **Figure 3-4**). The morphologies are similar to the CMP-1 networks prepared in toluene.[71] Materials collected at 300 and 1080 minutes are microporous and display larger particles with rough surfaces (**Figure 3-4**). These results are akin to CMP-1 synthesised in DMF.[100]

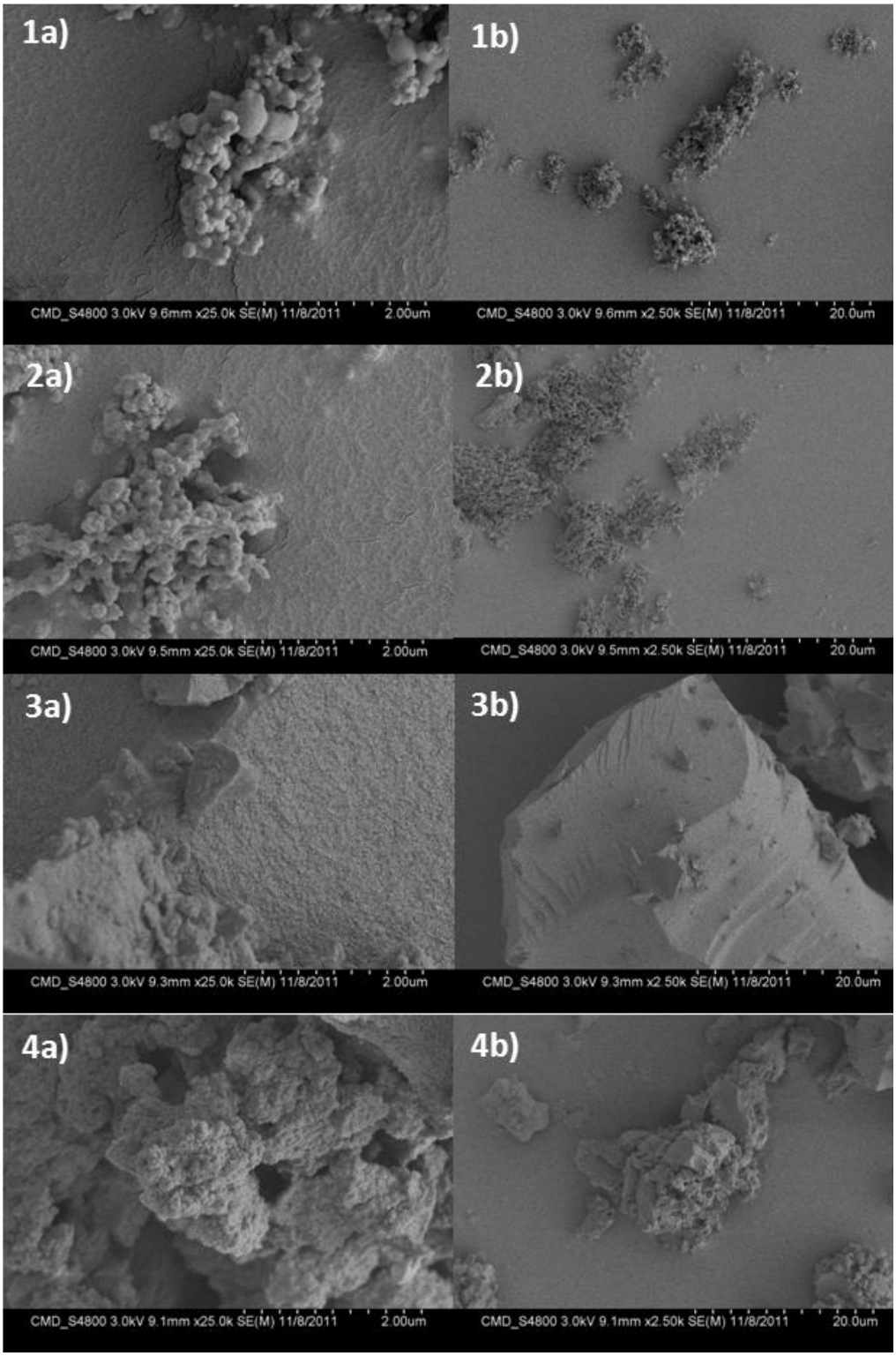

Figure 3-4: SEM images of CMP-1 materials collected at reaction times of: 1) 60 min, 2) 120 min, 3) 300 min, 4) 1080 min, with magnifications of: a) 25.0 K and b) 2.50 K.

In a related study by Trewin *et al.*,[205] computer modelling was used to propose a link between hyper-crosslinked polymer cluster sizes and their pore volume. Polymer clusters containing less than 121 monomer units (with a simulation box size of less than 3.0 nm) were calculated to have total pore volumes (V_{Tot}) of less than 0.19 cm^3g^{-1}. Larger clusters (containing *ca.* 140 monomer units, with a simulation box size of 3.15 nm) had calculated V_{Tot} values of 0.44 cm^3g^{-1}.

In this current work, a relationship between particle size and V_{Tot} can also be identified for the reaction intermediates, by comparing gas sorption data with particle sizes measured from the SEM images (**Figure 3-4**). Materials collected at short reaction times (*i.e.* 60 and 120 minutes) display particle sizes in the range 50 × 50 μm to 75 × 85 μm and V_{Tot} values of 0.18 and 0.29 cm^3g^{-1}, respectively. Materials collected at 300 min and above exhibit particle sizes in excess of 583 × 566 μm and V_{Tot} values greater than 0.30 cm^3g^{-1}. Although these results should be treated with a degree of caution (CMP materials are inhomogeneous and particle size is dependent upon sample preparation during SEM analysis, also the size of particles measured experimentally contain more than one cluster as they are 1000 times larger than the computer models), the findings show the same relationship between particle size and total pore volume as the simulated data, *i.e.* as the particle size increases, the total pore volume increases.

3.3.3 Proposal of a reaction pathway for the formation of CMP-1 networks

Combination of the gas sorption and morphology data allows a mechanism for the formation of CMP-1 networks to be postulated.

One possible reaction pathway could involve the following scenario (**Scheme 3-2**); during the initial stages of the reaction all of the starting materials are soluble (as shown by solution NMR, **Figure 3-1**). As the reaction progresses oligomers start to grow. Once the oligomers reach a specific molecular weight

gelation of the reaction mixture occurs. After gelation, further polymerisation takes place between catalyst-activated end groups in the oligomer-rich droplets, resulting in the final material.[203]

Scheme 3-2: Possible mechanism for the formation of CMP-1 networks.

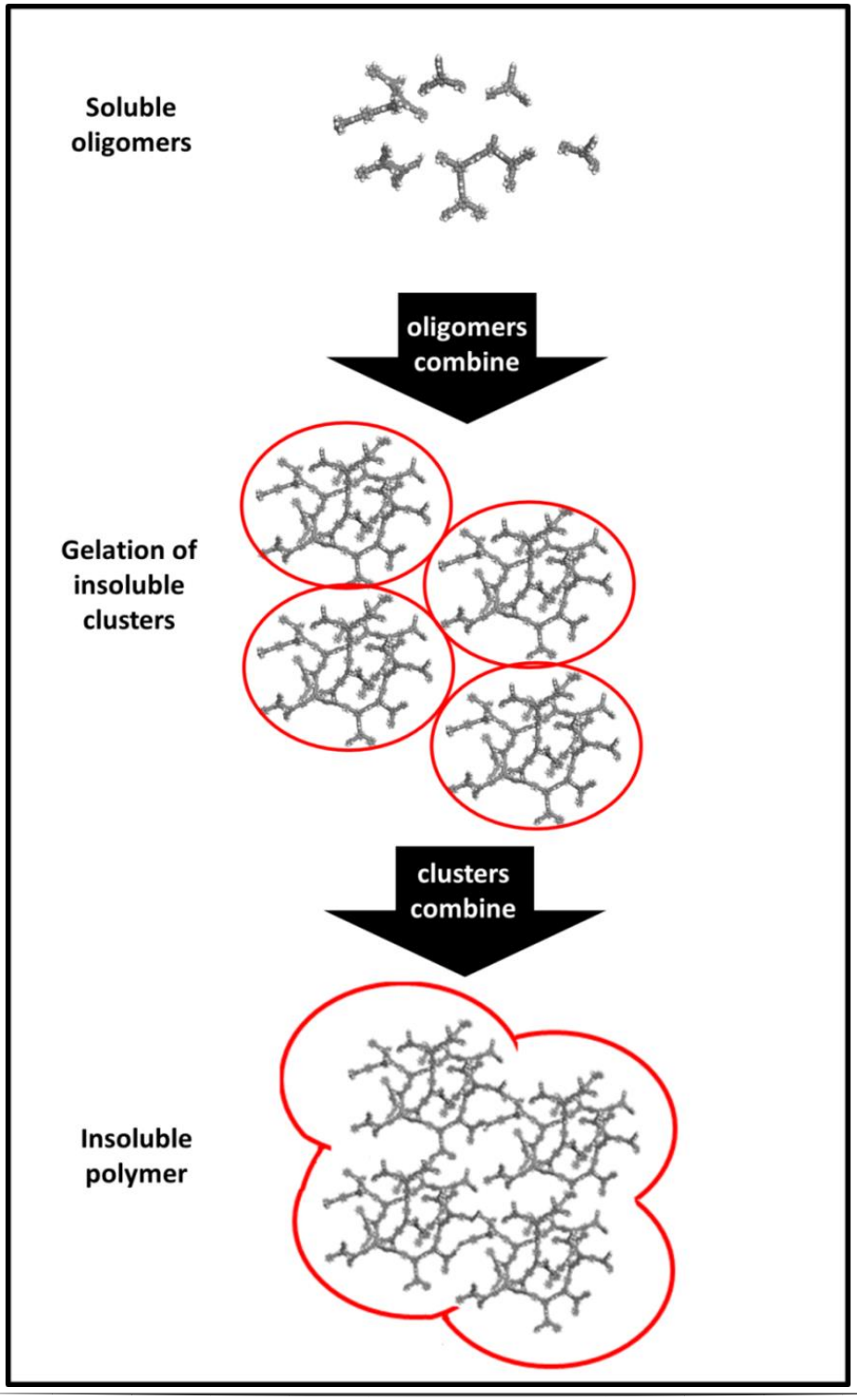

The mechanism shown in **Scheme 3-2** is strongly supported by the data discussed so far in this chapter.

Solution NMR (**Figure 3-1**) shows that the monomers are soluble in the reaction mixture. Once polymerisation begins, oligomers are formed in the reaction. The oligomers increase in size until they cause gelation of the reaction mixture. Reaction intermediates collected after short reactions times (*i.e.* 60 and 120 minutes) consist of fused spherical particles and exhibit interparticulate mesoporosity. In these cases the reaction is halted before crosslinking between oligomer clusters can take place. At longer reaction times, greater than 300 minutes, clusters are able to crosslink thus giving rise to microporosity, an increase in pore volume and a change in morphology.

The rest of this chapter discusses data reflecting the chemical and structural changes occurring at different stages of the synthesis.

3.3.4 Chemical composition

A summary of the elemental analysis data is presented in **Table 3-3**.

Table 3-3: Elemental analysis of CMP-1 intermediates at various reaction times.

CMP-1 material	Elemental analysis		
	% C	% H	% N
Predicted network[a]	95.2	4.8	0
Intermediate at 40 min	78.8	3.2	0
Intermediate at 60 min	82.0	3.2	0
Intermediate at 120 min	83.0	3.3	0
Intermediate at 300 min	84.4	3.4	0
Intermediate at 420 min	85.7	3.4	0
Intermediate at 1080 min	95.2	3.3	0
Intermediate at 2520 min	81.7	3.4	0.3
CMP-1-Br[e] **(synthesised in DMF)**[100]	82.6	3.8	0
CMP-1 –Br[e] **(synthesised in toluene)**[71]	75.3	3.7	0
CMP-1-I[f] **(synthesised toluene)**[65]	83.6	3.7	0

[a]Predicted values assuming 100 % reaction success and full network formation. Average error is ± 0.3%.

The percentage of carbon and hydrogen remain fairly consistent throughout the reaction at *ca.* 80 % and 3.3 %, respectively. These values are also in agreement with those reported previously for other CMP networks[65,71,100] (see **Table 3-3**). However, the elemental microanalysis results deviate significantly from the predicted values. In the literature,[65, 71, 79, 80, 90, 91, 100, 206-211] there are many examples of a contradiction between experimental and predicted microanalysis results for porous materials. Explanations for the disagreement include poor combustion of polymeric materials,[90, 91, 206, 207] trapped solvent and gases,[80, 207] catalyst retention[208, 209, 211] and the presence of un-reacted end groups.[71,

[100, 210] Indeed many of these explanations are possible for the materials in this work. In particular, un-reacted end groups are likely as the presence of bromine would lead to lower carbon content, specifically for the intermediates collected at short reaction times. Also, the material collected at 2520 minutes contains nitrogen (see **Table 3-3**), indicative of trapped triethylamine or DMF.

The presence of trapped solvent is further demonstrated by thermogravimetric analysis. A weight loss of *ca.* 5 % below 200 °C is exhibited by the materials, as shown in **Figure 3-5**. Trapped solvent has also been observed in many other CMP networks.[71, 79, 100, 208, 209]

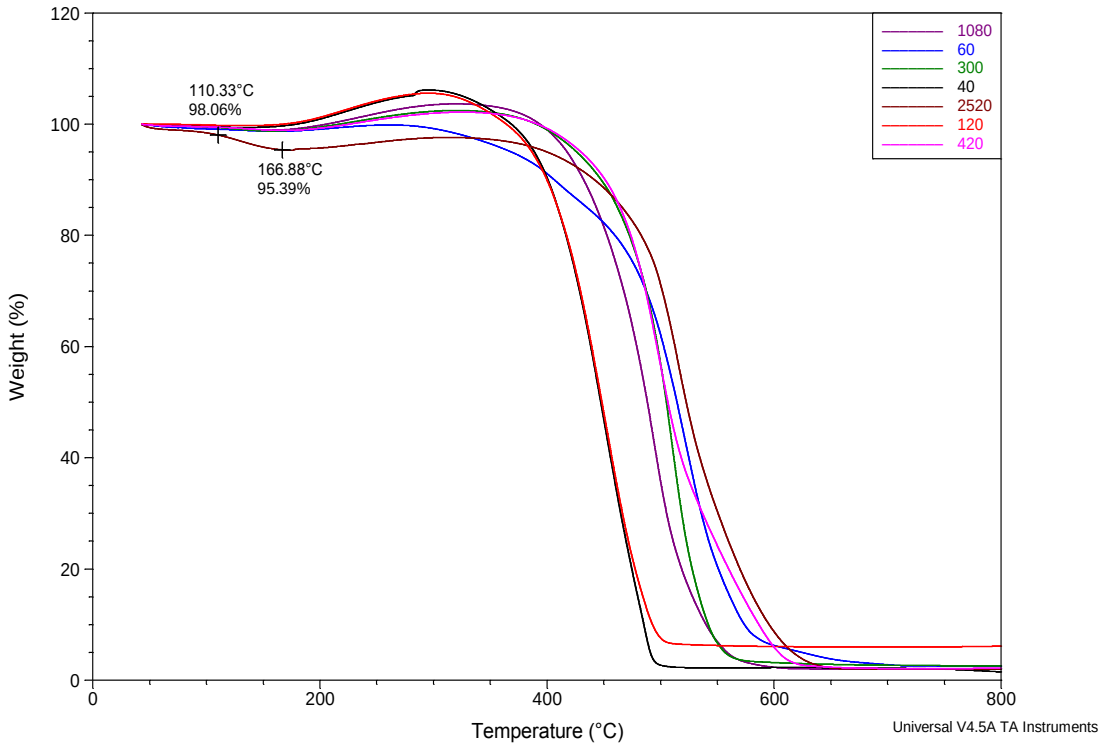

Figure 3-5: TGA curves (carried out under oxygen) for CMP-1 materials at varying reaction times. The reaction time labels are denoted in the figure legend.

Interestingly, the TGA curves also exhibit an increase in mass. Feasible explanations for this behaviour include base-line drifting (an inherent inaccuracy of the equipment) [212] or possibly oxide formation as a result of trapped catalyst. [176,177]

In order to investigate the possible presence of catalyst and bromine end groups, EDX analysis was performed. An advantage of this method is that the analyte is placed under high vacuum; therefore, removing any trapped solvent. Data are displayed in **Table 3-4** and have been compared with other CMP-1 networks.[65,71,100]

Table 3-4: Summary of EDX analyses.

CMP-1 material	wt% C	wt% halogen	wt% Pd	wt% Cu
Predicted network	100	0	0	0
60	93.4 ± 0.5	4.8 ± 0.4	1.1 ±0.2	0.4 ± 0.1
1080	95.9 ± 0.4	2.9 ± 0.3	1.0 ± 0.2	0.2 ± 0.05
CMP-1-Br[e] (synthesised in DMF)[100]	97.58	2.05	0.37	0.00
CMP-1 –Br[e] (synthesised in toluene)[71]	83.68	3.64	0.57	-
CMP-1-I[f] (synthesised toluene)[65]	95.79	2.27	1.03	-

The presence of palladium and copper indicates residual catalyst. The materials also contain bromine or iodine (depending upon the monomer used during synthesis). Halogeneted species may originate from trapped triethylamine salts, although they more likely to indicate the presence of residual end groups, as the materials are soxhlet extracted in methanol. The percentage of halogen (specifically bromine) decreases between 60 and 1080 minutes, from 4.8 % to 2.9 %, respectively. A reduction in bromine content with increasing reaction time suggests fewer end groups in the final material and therefore a more extended polymeric structure compared with materials collected at earlier stages of the reaction.

However, as the synthesis of CMP-1 involves reaction between a halogen monomer and an alkyne monomer, it is also possible for materials to contain

alkyne end groups. Indeed, alkyne end groups have been reported for CMP materials previously.[65, 66, 71, 79, 89, 100]

As alkyne moeities contain only carbon and hydrogen, they cannot be distinguished easily from the bulk polymer by chemical composition analysis. Therefore, other techniques such as FTIR and solid-state NMR were employed. Particular attention was paid to identifying and quantifying the amount of end groups in order to assess the level of poly-condensation for each material. Again, comparisons with other CMP-1 networks are made.

3.3.5 Alkyne end group analysis

The presence of alkyne functionalities was demonstrated by FTIR. All materials display two distinctive alkyne peaks. The peak at *ca.* 2200 cm^{-1} corresponds to a polymerised alkyne (R-**C**≡**C**-R)[65, 66, 71, 100, 195, 213] and the peak at *ca.* 2100 cm^{-1} can be ascribed to alkyne end groups (R-**C**≡**C**-H). [65, 66, 71, 100, 195, 213] Peaks at 1580 cm^{-1} are ascribed to aromatic (**C=C**) stretches.[71, 100]

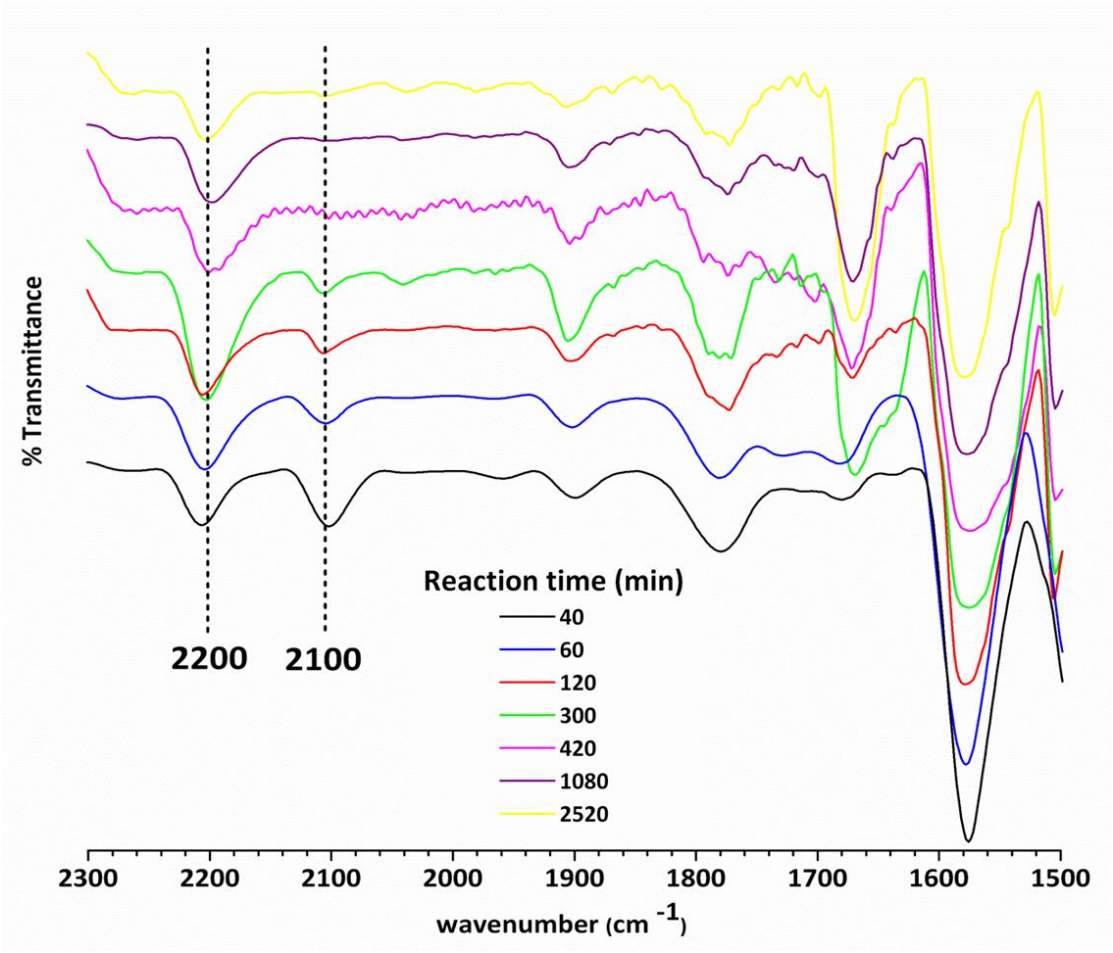

Figure 3-6: FTIR spectra of CMP-1 reaction intermediates.

A method for quantifying the amount of functional groups from FTIR spectra was demonstrated recently by Pandey *et al.*[89] This method was used to assess the extent of polymerisation for POF materials.[89]

If we apply a similar method, deconvolution of the peak due to polymerised alkyne (2200 cm^{-1}) *versus* alkyne end group peak (2100 cm^{-1}) could give an indication as to the extent of poly-condensation for each CMP-1 material. The values for deconvoluted peak areas and alkyne ratios are given in **Table 3-5**.

Table 3-5: Deconvoluted peaks corresponding to FTIR data in **Figure 3-6**.

Reaction time (min)	**Alkyne peaks**		**Ratio of Alkyne peaks**
	Polymerised alkyne peak area C≡C stretch at 2200 cm^{-1}	**End group alkyne peak area C≡C stretch at 2100 cm^{-1}**	**(2200 cm^{-1} : 2100 cm^{-1}) Polymerised alkyne : end group alkyne**
40	550	570	1 : 1.04
60	820	220	1 : 0.27
120	700	190	1 : 0.27
300	1500	110	1 : 0.07
420	750	10	1 : 0.01
1080	840	0	1 : 0
2520	430	0	1 : 0

These data show that the reaction intermediates collected at 40 minutes contain the highest amount of alkyne end groups. The largest reduction of alkyne end groups occurs between 40 and 60 minutes. Between 60 and 2520 minutes the amount of alkyne end groups in the materials continues to decrease. Materials collected at 1080 and 2520 minutes contained undetectable amounts of alkyne end groups.

A more accurate method of quantifying level of end groups involves the use of solid-state NMR. Previously, the extent of polymerisation for CMP materials was measured using single pulse excitation (SPE) ^{13}C NMR with high powered proton decoupling (HPDEC).[71, 100] The quantitative nature of these measurements for CMP networks has previously been verified by CP kinetics experiments.[214]

SPE ^{13}C NMR has also been extensively used to quantify the populations of carbon environments in materials such as coal tars,[174] poly(divinylbenzene) resins,[170] organic soil matter,[175] clathrates,[176] surfactants,[171] hyper-crosslinked polymers,[102] and pharmaceutical drugs.[177]. For further information, see **Section 2.1.2.3**. Solid-state NMR can also be used for structural elucidation of amorphous polymers and has been widely used to characterise MOPs and CMP materials.[65-67, 71, 79, 80, 89-91, 100, 195, 211, 214]

The structures of the CMP-1 intermediates were elucidated by SPE $^{13}C\{^{1}H\}$HPDEC MAS NMR (**Figure 3-7**). All materials show aromatic peaks at 131.9 ppm (-$\boldsymbol{C}_{Ar\text{-}H}$) and 123.9 ppm (-$\boldsymbol{C}_{Ar}$-C≡C-$\boldsymbol{C}_{Ar}$) and an alkyne peak at 91.5 ppm (-C_{Ar}-$\boldsymbol{C}$≡C-), confirming that polymerisation has been successful. A resonance at 82.4 ppm, ascribed to alkyne end groups (-C≡$\boldsymbol{C}$-H) is also present in the NMR spectra. All peaks are consistent with the spectra of CMP networks reported previously.[65, 66, 71, 100]

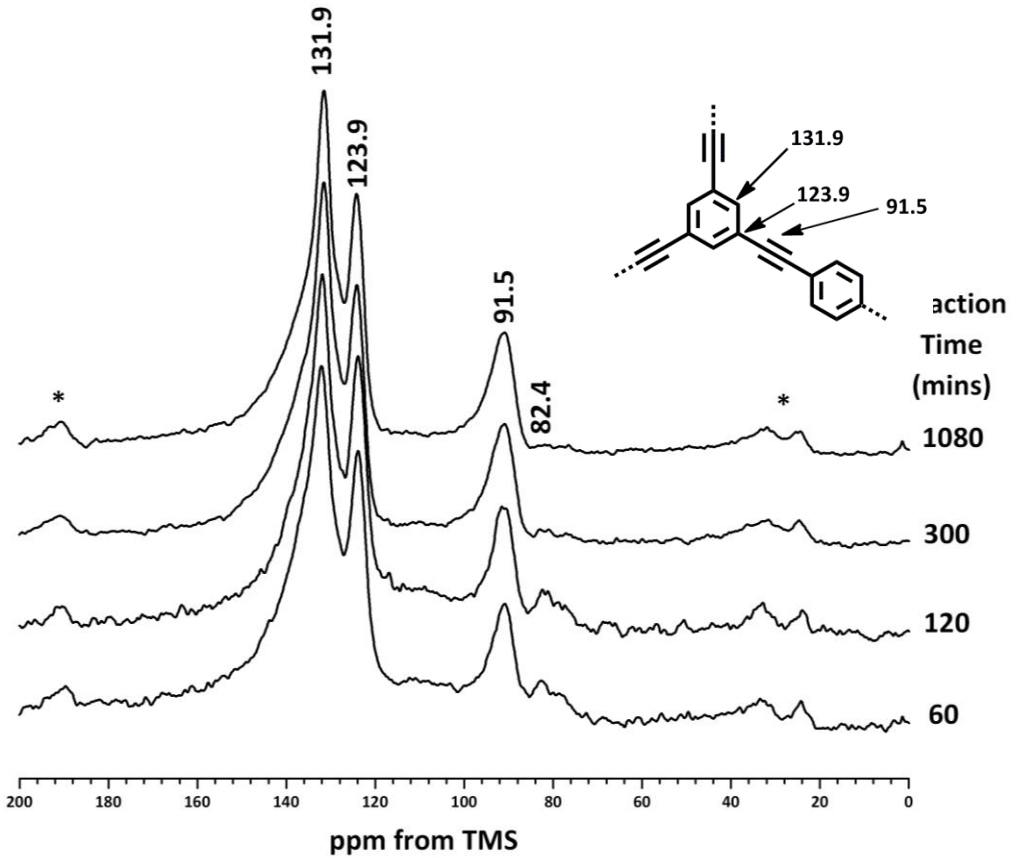

Figure 3-7: SPE ^{13}C {^{1}H}HPDEC MAS NMR spectra of CMP-1 materials recorded at an MAS rate of 10 kHz. Structure of CMP-1 labelled with peak assignments (inset). Asterisks denote spinning sidebands.

As with previous CMP networks, we also observe a large shoulder resonance *ca.* 137 ppm, which was originally ascribed to residual halogen end groups ($\boldsymbol{C}_{Ar}$-X, X= I or Br).[65, 66, 71, 79, 100] This assumption was validated by the presence of halogens in EDX data (up to 2 wt% for CMP-1 synthesised from the iodinated monomer[65] and 4 wt% for CMP-1 synthesised from the brominated monomer[71]). Analysing the monomers by NMR should allow confirmation of the NMR assignments. ^{1}H-^{13}C CP/MAS NMR spectra of the monomers are shown in (**Figure 3-8**).

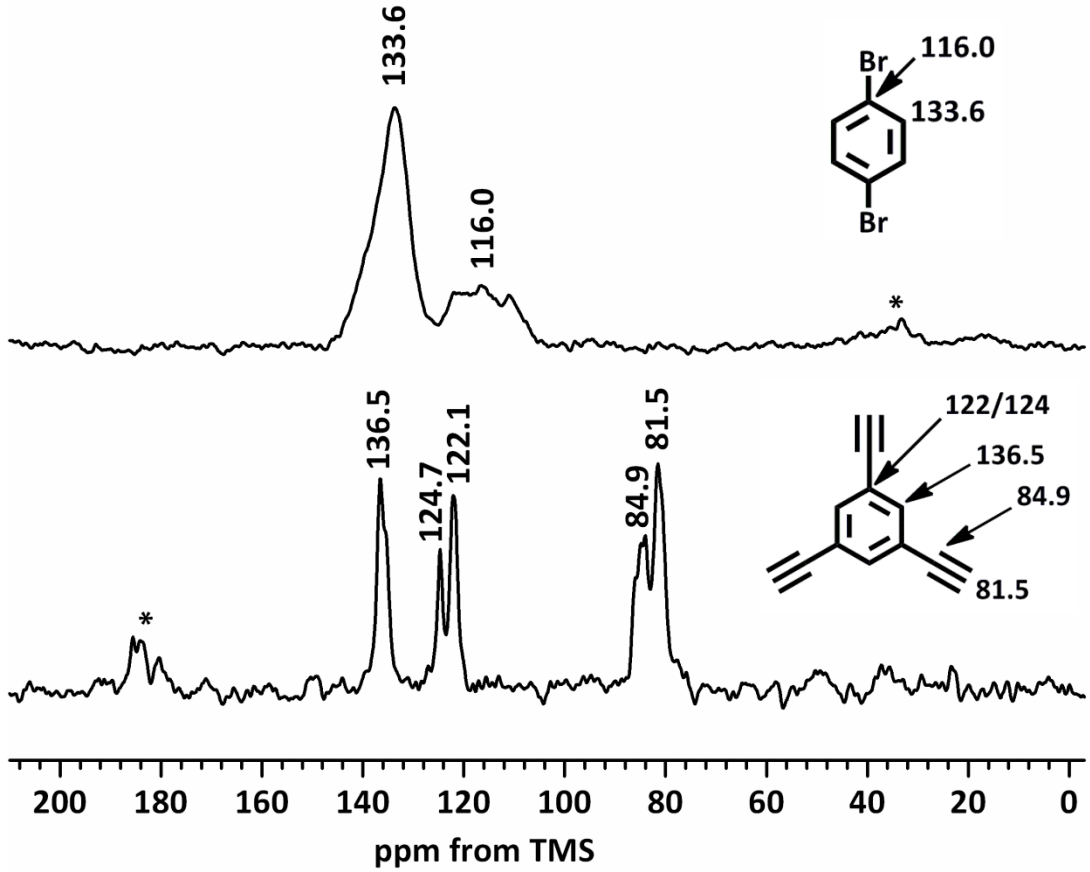

Figure 3-8: ^{1}H-^{13}C CP MAS NMR spectra of monomers recorded at an MAS rate of 10 kHz. Structure of monomers labelled with peak assignments (inset). Asterisks denote spinning sidebands. Multiple peaks at 116 and 122-124 ppm are a consequence of ^{13}C-$^{79/81}$Br residual dipolar coupling and different environments in the crystal structure, respectively.[179,180]

Both monomers exhibit aromatic peaks in the range of 122.1-133.6 ppm.[215, 216] These peaks overlap with those displayed in the NMR spectra of the polymerised networks (**Figure 3-7**). Each monomer also displays a peak at *ca.* 136 ppm. This peak is well-pronounced for the alkyne monomer and appears as only a shoulder peak for the brominated-monomer (**Figure 3-8**). Conveniently, each monomer also displays its own characteristic peak at 116.0 ppm (-$\boldsymbol{C}_{\mathrm{Ar}}$-Br)[139] for 1,4-dibromobenzene and *ca.* 83 ppm (-C≡$\boldsymbol{C}$-H) for

1,3,5-triethynylbenzene. Comparison between the spectra of the monomers and the spectra of the reaction intermediates enables unambiguous assignment of the peaks.

The CMP-1 materials in this work exhibit small peaks at 116.0 ppm in their spectra (**Figure 3-7**), therefore they contain only low amounts of halogen end groups, this is consistent with EDX analysis. The CMP-1 materials display peaks at *ca.* 83 ppm, corresponding to an alkyne end group (**Figure 3-7**). With the absence of a peak at 116.0 ppm and the presence of a peak at *ca.* 83 ppm, one can conclude that the shoulder resonance observed at 137 ppm in the spectra of the reaction intermediates (**Figure 3-7**) is a consequence of alkyne end groups and not brominated end groups.

It is possible to quantify the amount of end groups by deconvolution of the peaks from the SPE $^{13}C\{^{1}H\}$ HPDEC MAS NMR spectra, Compared with FTIR methods, determination of level of poly-condensation from SPE $^{13}C\{^{1}H\}$HPDEC MAS NMR spectra is more accurate as the area under each resonance line is proportional to the number of nuclei in the respective molecular site.

Two methods for the determination of level of poly-condensation from SPE $^{13}C\{^{1}H\}$ HPDEC MAS NMR spectra have been reported previously.[65, 66, 71, 100] The first involves calculating the ratio of peak intensities of aromatic to polymerised alkyne, (131.9 +123.9) : 91.5 ppm.[65, 66] This ratio provides information about the level of polymerisation by assessment of the populations of $-C_6H_4-$ linkages. The second method requires determination of the ratio of peak intensities for polymerised alkyne to end group alkyne, 91.5 : 82.4 ppm.[71, 100] For a fully polymerised CMP-1 network, an *aromatic : polymerised alkyne* ratio of 0.40, and *polymerised alkyne : end group alkyne* ratio of 0 would be expected.[65, 66, 71, 100]

As well as calculating the level of poly-condensation, these methods were used to determine the dominant end group. For example, some functionalised CMPs synthesised in toluene have shown *aromatic : alkyne* ratios above 0.40 and peaks at 116.0 ppm.[71] In these cases, the networks terminate preferentially at the

halogen-bearing end group. For CMP-1 networks synthesised in DMF, preferential termination occurs at the alkyne.[100] These networks do not exhibit a peak at 116.0 ppm and display *polymerised alkyne : alkyne* end group ratios which tend towards 1.0.[100]

In this work, both methods have been used to assess the level of polymerisation with reaction time. These data are summarised in **Table 3-6**.

Table 3-6: Areas of the deconvoluted peaks corresponding to SPE $^{13}C\{^{1}H\}$ HPDEC MAS NMR spectra from **Figure 3-7**.

Reaction Time (min)	**Deconvoluted Peak Area**				**Polymerised Alkyne : end group alkyne ratio 91.5 ppm : 82.4 ppm**	**Aromatic : Polymerised Alkyne Ratio (131.9 +123.9) : 91.5 ppm**
	131.9 ppm	**123.9 ppm**	**91.5 ppm**	**82.4 ppm**		
60	4.20	3.60	2.16	0.86	0.40	0.28
120	3.39	3.56	2.14	0.80	0.37	0.30
300	3.80	3.07	2.34	0.11	0.05	0.34
1080	3.02	3.22	2.33	0.03	0.01	0.37
CMP-1 Br DMF[100a]					*ca.* 0	0.17
CMP-1 Br Toluene[71a]					0.15	0.20
CMP-1 I Toluene[65, 66a]					0.14	0.27

[a]Ratios quoted from previously published results (see references).

The peak areas corresponding to alkyne end groups (82.4 ppm) decrease with increasing reaction time and the polymerised alkyne peak areas (91.5 ppm) increase with increasing reaction time (**Table 3-6**). The ratio of *polymerised alkyne: end group alkyne* is in good agreement with these observations as it

decreases significantly from 0.40 at 60 minutes to 0.013 at 1080 minutes. Also, as the reaction progresses, the *polymerised alkyne: end group alkyne* ratio becomes closer to the ideal value of zero. These data suggest that the CMP-1 materials become more polymerised as the reaction progresses.

The ratio of *aromatic : polymerised alkyne* increases from 0.28 at 60 minutes to 0.37 at 1080 minutes, becoming closer to the ideal (a ratio of 0.40) with increasing reaction time. This observation suggests that the number of -C_6H_4- linkages increase with increasing reaction time.

Combining this information shows that as the reaction progresses a reduction in the amount of end groups and an increase in the amount of polymerised groups take place. One can also conclude that the materials terminate preferentially with an alkyne group, although the amount of alkyne end group was found to be lower than that reported for other CMP-1 networks.[71, 100] Termination at the alkyne end group is expected, as the networks are synthesised with a stoichiometric excess of alkyne monomer. These data also give a strong indication that the CMP-1 networks become more polymerised with increasing reaction time.

3.3.6 Effect of end groups and molecular structure on ^{1}H-^{13}C CP/MAS kinetics

Cross-polarisation (CP) kinetics can be used to investigate polymer structures by examination of the parameters used to fit the CP kinetics curves. In particular, overall network mobility can be identified by examination of the $T_{1\rho}^{H}$ relaxation values. Descriptions of CP kinetics theory and associated models and fitting parameters are provided in greater detail in **Section 2.1.2.2.3** and **2.1.2.2.4.**

Here, CP kinetics has been used to show that intermediates collected at 60 and 1080 minutes are structurally and dynamically different as a result of differences in polymerisation and cross-linking.

In order to assess the effect of network mobility upon the kinetics parameters ^{1}H-^{13}C CP/MAS kinetics data were collected at room temperature and at 353 K for two intermediates isolated at 60 and 1080 minutes.

The CP kinetics curves and fitting parameters collected at 298 K are shown in **Figure 3-9** and **Table 3-7**. The CP kinetics curves and fitting parameters at 353 K are shown in **Figure 3-10** and **Table 3-8**, respectively. The CP kinetics of the terminal alkyne environments (137 and 82 ppm) were omitted due to poor resolution and low populations in the ^{1}H-^{13}C CP/MAS spectra.

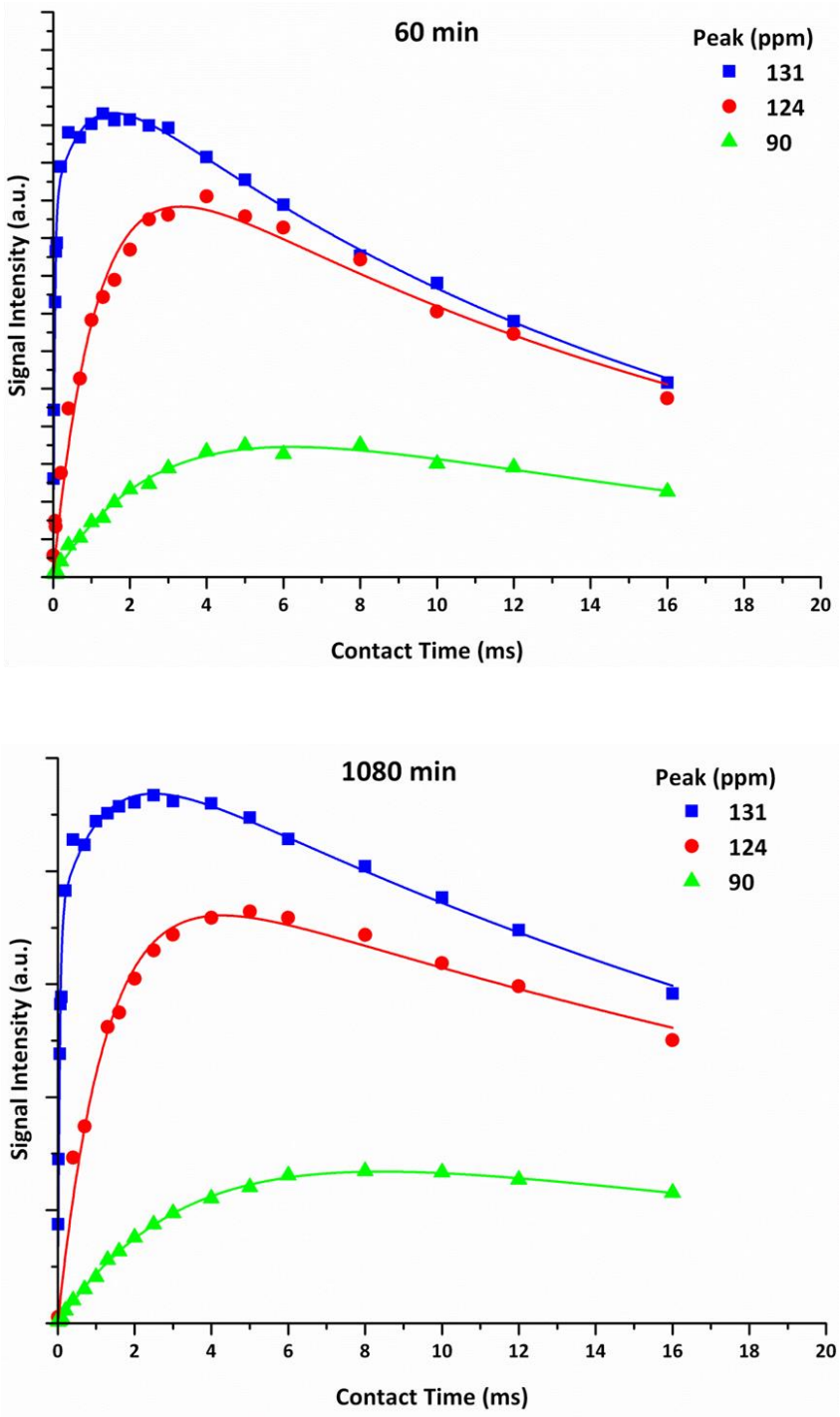

Figure 3-9: ^{1}H-^{13}C CP/MAS kinetics curves for CMP-1 reaction intermediates. Data were collected at 298 K.

Table 3-7: ^{1}H-^{13}C CP/MAS kinetics parameters derived from the Classical I-S Model and Two-Component I-S Model at 298 K.

Reaction Time (min)	^{13}C Site (ppm)	T_{IS} (ms)	$T_{1\rho}^{H}$ (ms)	R^2
60	131.9	Fast: 0.038 ± 0.003	0.82 ± 0.042	0.990
		Slow: 0.82 ± 0.035	16.03 ± 0.79	
60	123.9	1.14 ± 0.12	17 ± 2	0.970
60	91.5	3.00 ± 0.32	16 ± 2	0.993
1080	131.9	Fast: 0.049 ± 0.005	1.07 ± 0.07	0.983
		Slow: 1.10 ± 0.06	27 ± 3	
1080	123.9	1.27 ± 0.097	32 ± 5	0.984
1080	91.5	3.54 ± 0.16	29 ± 3	0.999

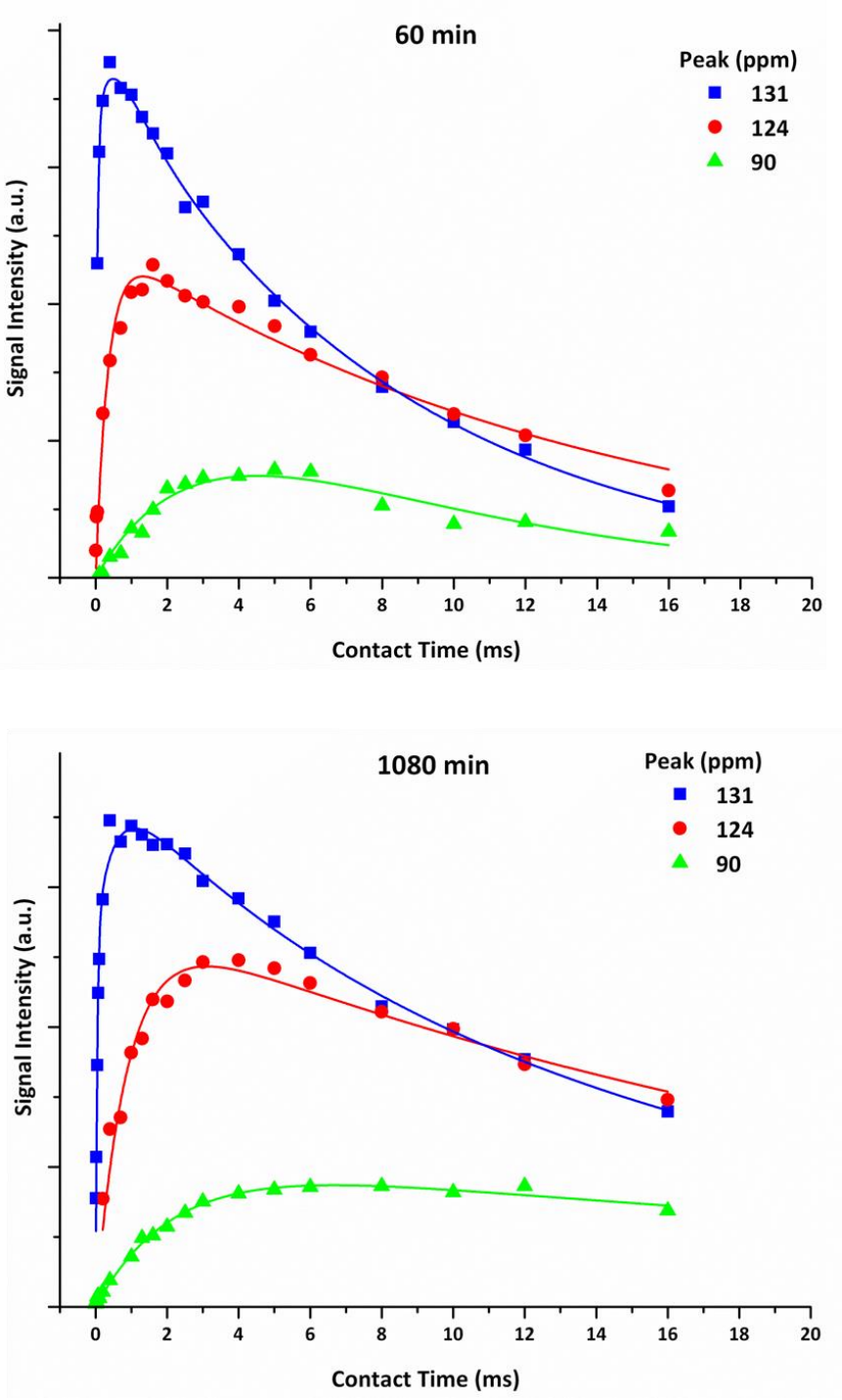

Figure 3-10: ^{1}H-^{13}C CP/MAS kinetics curves for CMP-1 reaction intermediates. Data were collected at 353 K.

Table 3-8: ^{1}H-^{13}C CP/MAS kinetics parameters derived from the Classical I-S Model and Two-Component I-S Model at 353 K.

Reaction Time (min)	^{13}C Site (ppm)	T_{IS} (ms)	$T_{1\rho}^{H}$ (ms)	R^2
60	131.9	Fast: 0.045 ± 0.006	0.6 ± 0.3	0.995
		Slow: 0.5 ± 0.2	8.2 ± 0.4	
60	123.9	0.35 ± 0.04	14.0 ± 1.4	0.959
60	91.5	3.2 ± 1.4	6.8 ± 3.2	0.924
1080	131.9	Fast: 0.046 ± 0.007	6.9 ± 4.4	0.982
		Slow: 0.5 ± 0.3	22 ± 5	
1080	123.9	0.89 ± 0.09	26 ± 4	0.932
1080	91.5	2.2 ± 0.2	40 ± 10	0.991

Both of the reaction intermediates display a reduction in the value of $T_{1\rho}^{H}$ with increasing temperature, *i.e.* as the molecular mobility of the materials increase, their relaxation times decrease. Such behaviour is characteristic of materials in the slow motional regime (*i.e.* left hand side of the T_1 minimum, see **Figure 2-20**). In this regime materials exhibiting long relaxation times are larger in structure. As the material collected at 60 minutes exhibits shorter $T_{1\rho}^{H}$ times compared with the intermediate isolated at 1080 minutes over both temperatures, one can conclude that the longer reaction time leads to more extended and motionally constrained structure. These results are in excellent agreement with the SEM data as they both show that the networks become larger with increasing reaction time.

3.4 Conclusions and outlook

In summary, a series of reaction intermediates collected during the synthesis of CMP-1 networks were investigated.

Products collected before 120 minutes are composed of spherical particles exhibiting interparticulate mesoporosity, while materials collected after this time consist of fused particles exhibiting intraparticulate microporosity. Based upon the change in textural properties, a reaction mechanism for the formation of CMP-1 networks has been suggested.

The proposed mechanism involves formation of oligomers in solution that react to give clusters. These clusters then precipitate out of solution and continue to react in the solid-state by cross-linking, ultimately leading to the formation of extended CMP-1 networks.

Validation of this mechanism has been demonstrated by chemical and structural analyses. Particular attention was paid to the identification and quantification of end groups. All materials contain alkyne end groups, as evidenced by FTIR and solid-state NMR. These data support the reaction mechanism as the amount of end groups decrease during the reaction and CP kinetics data show that the materials become more extended as the reaction progresses.

As the proposed reaction pathway involves precipitation of an intermediate, factors that influence the solubility of these species are likely to affect the final polymer network. Such factors include concentration, solvent, temperature and type of monomers. A study of these factors may lead to information which would enable control over the chemical and textural properties of the resultant polymeric materials.

While, CP kinetics has been used to confirm the structural diversity of materials at different stages of the reaction, further investigations are required to probe the various types of molecular motion exhibited by the materials. Continuation of this work may involve collection of CP kinetics data over a

range of temperatures to assess any changes in motion based upon $T_{1\rho}^{H}$ relaxation. These experiments have previously been used to probe motions of phenyl groups in poly(*p*-phenylenevinylene) networks.[157]

Another potential method of exploring the motions exhibited by the materials in this work may involve measuring $T_{1\rho}^{C}$ as a function of temperature. This technique has previously been used to examine differences between fractal polymers and rigid networks of aromatic polyamides.[158]

The porous nature of CMP-1 materials allows them to be investigated using various solvent loadings. Preliminary data show that the ability of these materials to swell in THF varies with reaction time. Previous studies based upon fractal polymers show that swelling of such materials is indeed associated with the amount of polymer defects.[158] Swelling studies using CMP-1 materials from this work could lead to the assessment of polymer defects during the reaction mechanism.

Finally, the study detailed in this chapter could be applied to other CMP materials, such as CMP-2 and CMP-3 to see if the proposed reaction mechanism is applicable for these networks.

Chapter 4:

Solid-State NMR Studies of Deuterated CMPs

4.1 Introduction to the need for deuterium NMR analysis

The design and synthesis of microporous organic polymer (MOPs) networks has attracted significant interest due to potential applications in areas such as molecular separations,[217, 218] heterogeneous catalysis,[216] and gas storage.[219] One particular type of MOP, namely conjugated microporous polymers (CMPs), have advantageous properties, such as the ability to swell and tuneable micropore size and surface area by varying the poly(aryleneethynylene) strut.[66]

Alteration of the strut length was achieved by systematically increasing the total number of benzene links. CMPs with longer struts were found to have the largest pore diameters. However, a decrease in both pore volume and SA_{BET} were observed with increasing strut length.[66] Such behaviour was ascribed to an increase in the degree of interpenetration.[66] This hypothesis was further evidenced by atomistic simulations.[66] For further information, please see **Section 1.1.1.7**.

However, owing to poor solubility and the amorphous nature of these materials, structural information is limited and characterisation is dominated by NMR. Previous CMP structure elucidation has been achieved by ^{1}H-^{13}C CP/MAS NMR,[65, 66] however very little is known about the origins of physical properties, in particular their swelling behaviour and porosity.

Deuterium NMR is a powerful technique for measuring molecular motions, and has been used to study the dynamics of a range of porous materials and encapsulated guests. Applying this method of analysis to CMPs would enable an overall picture of the origins of flexibility and physical properties for CMP networks to be developed, ultimately leading to the design of such materials for specific applications.

4.1.1 Challenges in ^{2}H NMR analysis

Currently, two methods exist for the analysis of deuterium NMR spectra. The first involves calculation of the ^{2}H NMR line shape using mathematical models using SIMPSON[220] or WEBLAB[221] programs. It is possible to calculate the spectra prior to the collection of experimental NMR data allowing a comparison to be made once the experimental data is collected. This approach requires input of parameters such as host-guest geometries and motional timescales, and thus relies heavily upon structural analysis. Often this method is adopted for crystalline materials where detailed structural information can be gathered from X-ray analysis and molecular modelling. Examples of materials analysed by this method include poly(oxyethylene),[141] crystalline poly(styrene)[127] and periodic mesoporous organosilica.[222]

The second method consists of simulating ^{2}H line shapes in the presence of the experimental data using DMFit[223] and QUADFIT[224] programs and does not require a prior knowledge of structural or dynamical information. As a result, this method is often used to analyse ^{2}H NMR spectra of amorphous and inhomogeneous materials where little information is known about the sample. Examples of materials analysed by this method include amorphous silica[225] and proteins.[226]

Each method of ^{2}H NMR line shape analysis requires comparisons between the experimental and simulated spectra, thus it is important to obtain good simulation data that closely fit the experimental results. Unfortunately the majority of simulation software available at present does not incorporate a numerical output for assessing the goodness of fit, therefore it is often based upon the users' discretion rather than a calculated error. As a consequence examples of both good (**Figure 4-1**) and poorly fitting simulations (**Figure 4-2**) exist within the literature.

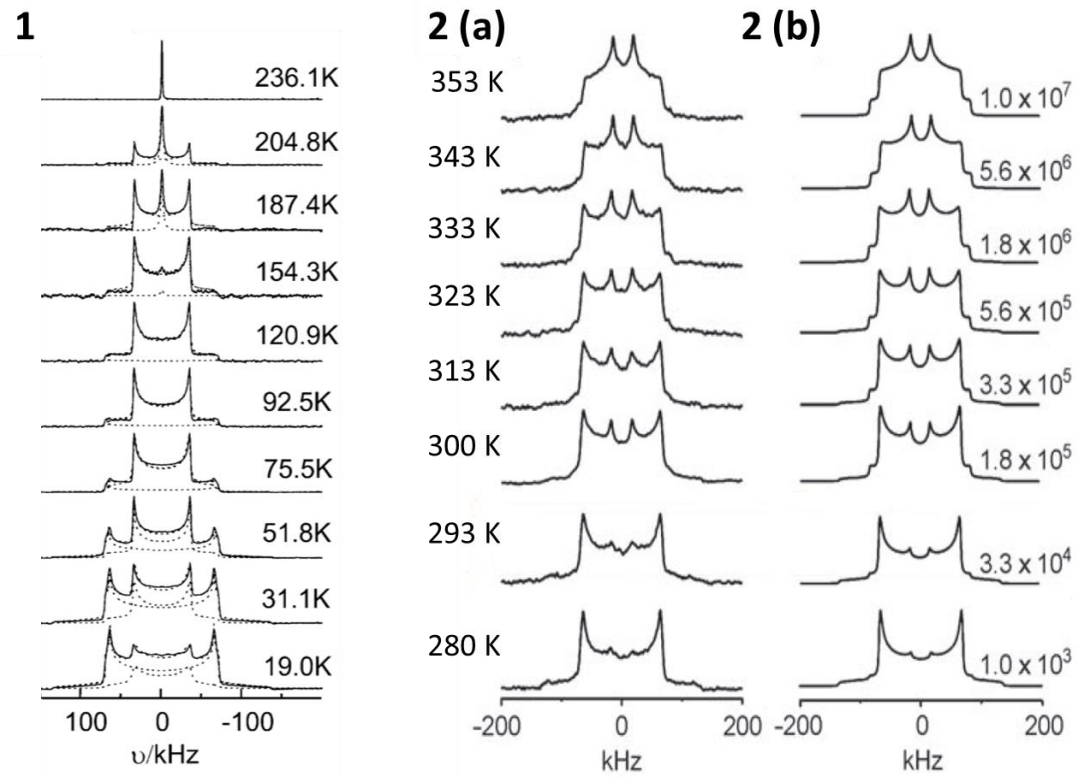

Figure 4-1: Examples of line shape analyses containing simulated data that closely resemble the experimental data. 1) ^{2}H NMR spectra of amorphous benzene-d_6 inside mesoporous silica SBA-15, with a pore diameter of 0.8 nm. Dotted lines represent the simulated spectra. Figure adapted from reference[120]. 2) ^{2}H NMR spectra of *p*-phenylenesilica-d_4 including the experimental (a) and simulated spectra (b). Values indicated on the right of 2(b) indicate the phenyl ring flipping rate in Hz. Figure adapted from reference[222].

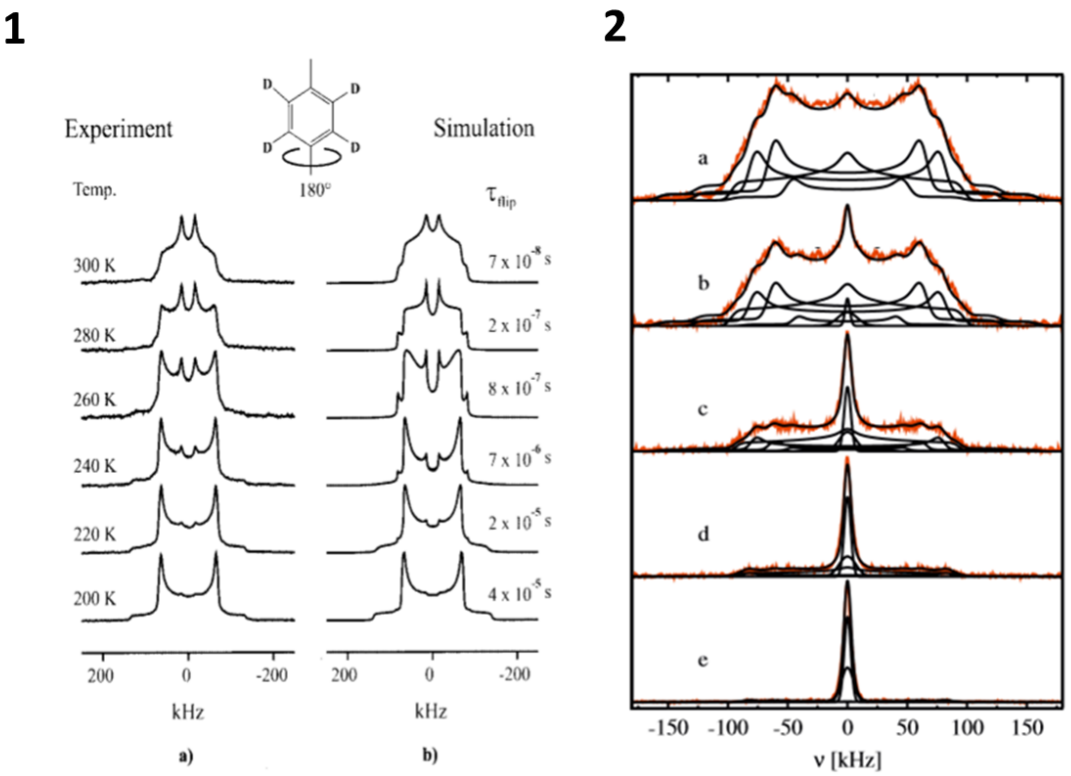

Figure 4-2: Examples of line shape analyses containing simulated data that do not closely resemble the experimental data. 1) ^{2}H NMR spectra (a) experimental and (b) simulated for a siloxane-based inorganic-organic hybrid polymer containing perdeuterated phenyl rings within the struts. Figure adapted from reference[227]. 2) ^{2}H NMR spectra of hydrated zeolite NaDY(0.8) at various temperatures (a) 50 K, (b), 70 K, (c) 100 K, (d) 140 K, and (e) 180 K. Experimental data is represented by the red line and the simulated line shapes are displayed in black. Figure adapted from reference[228].

Further complications arise during line shape simulation when multiple motions manifest in the spectra. For example, frozen and liquid-like benzene (**Figure 4-1, 1**) and zeolites containing many hydration sites (**Figure 4-2, 2**). In such cases the analyst relies upon features in the experimental line shape to determine whether additional motions/sites are present and it is easy to over-complicate the data by simulating too many lines (**Figure 4-2, 2**).

The presence of multiple motions also adds to the difficulty in examining deuterium relaxation data. In order to retrieve information from ^{2}H NMR relaxation data, such as relaxation times and activation energies, one must construct plots of peak intensity *vs.* delay time (see **Section 2.1.2.4.2.1** for further details). The plots are then fitted by the exponential function given in

$$M_z(\tau_1) = M_0\left[1 - 2e^{-\left(\frac{\tau_1}{T_{1z}}\right)}\right]$$

Equation 2-27.

For systems containing a distribution of motions, a single exponential function cannot satisfactorily describe the ^{2}H magnetisation recovery curve, therefore several functions are needed. For example, poly(oxy-1,4-phenyleneoxy-1,4-phenylenecarbonyl-1,4-phenylene) requires two exponential functions and methylated zeolite NaX[229] requires three exponential functions in order to fit the magnetisation recovery curves.[230] As with the line shape simulations, it is possible to overestimate the number of components in a multiexponential fitting protocol for the magnetisation recovery curves.

4.1.2 Previous host-guest systems analysed by deuterium NMR

One major advantage of ^{2}H NMR is the ability to study a porous system from two perspectives either by studying the molecular motions of an absorbed guest or the mobility of a host network.

Many deuterated guest molecules have been studied by ^{2}H NMR these include; benzene,[120, 127, 128, 130, 131, 133, 137], cyclohexane,[134] pyridine,[120] water,[120] and a range of aliphatic alkanes[124-126] and alcohols,[123, 231] to name a few.

One particular molecule that has received significant research interest, owing to its' six-fold symmetry, is per-deuterated benzene. In 1989, R. L Vold and co-workers[131] reported the molecular motions of pure per-deuterated benzene by ^{2}H NMR, as a function of temperature. When pure benzene-d_6 freezes, it

adopts a crystalline structure. At temperatures below 140 K, the spectra display a typical Pake doublet, with broad horns.[131] A quadrupolar coupling constant (Q_{cc}) of 183 kHz was ascribed to the benzene-d_6 molecules in solid II phase, undergoing rotations about the C_6-axis[120, 130, 131] (**Figure 4-3**), at a rate of *ca.* 1.30 $\times 10^4$ s^{-1} at 94 K.[131]

Above 140 K, Pake doublets with Q_{cc} of *ca.* 180 kHz were observed. At these temperatures, the per-deuterated benzene is in solid I phase and undergoing much faster six-fold rotations at a rate of 1.20×10^7 s^{-1}.[131]

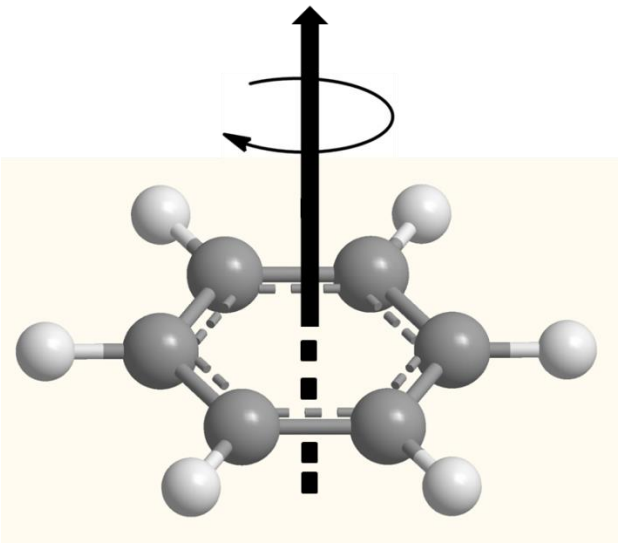

Figure 4-3: Pictorial representation of benzene-d_6 undergoing in-plane rotation about the C_6-axis.

Heating above the melting point of benzene-d_6 (*i.e.* 279.8 K) leads to a ^{2}H NMR spectrum with a single line at $\nu = 0$ kHz. This feature was ascribed to benzene undergoing fast isotropic reorientation.[120, 128, 131, 133]

The effect of encapsulation upon the motions of per-deuterated benzene has also been widely investigated by ^{2}H NMR.[120, 128, 131, 133] Often NMR measurements are verified by either molecular dynamics simulations[127, 134, 150, 151, 153, 232] or thermal analysis, such as differential scanning calorimetry.[128, 134, 153] Many factors were found to affect the motions of benzene-d_6 molecules inside the hosts. These factors include; surface interactions between the host and guest,[120,

[127, 130, 133] guest-guest interactions,[120] effect of pore fullness,[233] the effect of pore diameter,[120, 133, 233] possible swelling of the host,[232] and diffusion.[120, 232, 233] Therefore, such studies can lead to detailed structural information about the host.

A notable effect of liquid encapsulation is melting point depression.[137] Such behaviour is pore-size dependent and thus provides an alternative method of pore-size determination to gas sorption.[137] A major advantage of using liquid encapsulation to measure porosity is the ability to analyse swollen pores. Such measurements would be particularly useful in the characterisation of CMP networks, as the materials swell by up to 570 wt% and may provide a method for analysing occluded pore volumes.

In 2003, Aksnes *et al.* reported the study of benzene melting point depression and pore size determination for a series of controlled-pore glasses.[137] An inverse relationship between benzene melting point and pore size was established, *i.e.* in small pores, benzene remains as a liquid at lower temperatures than in larger pores. This behaviour was ascribed to weak interactions between the pore wall and the benzene guest.

In addition to guest mobility, it is also possible to examine the motions of a host framework. Indeed many investigations of deuterated hosts have been reported, including crystalline organic molecules,[130, 131] MOFs,[133] polymers[127, 128] and porous silicas.[120, 137] Selective deuteration enables specific framework functional groups to be considered. Such functionalities include methyl groups,[145, 156] aliphatic chains[146, 150] and phenyl groups,[133, 141, 143, 148, 151-155] to name but a few. As CMP networks are composed of aromatic linkers, studies of the mobility of phenyl groups are most relevant to the work discussed in this chapter.

In 1981, Gall and co-workers[152] proposed two motional regimes for the deuterated phenyl rings of phenylalanine-d_5. The first regime involved static C-D bonds arising from immobile phenyl rings, resulting in a simulated Pake doublet with a Q_{cc} of *ca.* 180 kHz, as shown in **Figure 4-4 (a)**. The second motion involved phenyl rings undergoing 180° flips about their C_2-axes, which gave a Pake doublet with a reduced Q_{cc} of 168 kHz **Figure 4-4 (b)**. However, the

experimental spectra collected for poly(phenylalanine)-d_5 consisted of two overlapping Pake doublets, ascribed to the presence of both mobile and immobile phenyl rings (**Figure 4-4 (c)**).

Investigations of poly(phenylalanine) carried out by Hiraoki *et al.*[153] focused upon ^{2}H T_1 relaxation data. Again two Pake doublets were observed. The Pake doublet corresponding to static C-D bonds gave a T_1 value of 1 s, whereas the inner Pake doublet (ascribed to 180 ° flips) gave a T_1 relaxation time of 10 ms. By plotting the T_1 relaxation time against temperature, Arrhenius-type behaviour was observed. Such information allowed calculation of the activation energy for ring flips, which was used to measure the steric interactions between phenyl rings. Similar techniques could be applied to assess the effect of interpenetration on the flexibility of CMP networks.

Recently, ^{2}H NMR has been used to examine the effect of guest inclusion upon host phenyl ring rotations in MOF-5[133] and *p*-phenylene organosilica.[151] In each case, the presence of a guest led to retardation of the rate of phenyl ring flips.

This chapter describes the investigation of porosity and flexibility for CMP-1 and CMP-2 by ^{2}H NMR. Porosity was examined by studying the effect of encapsulation of deuterated benzene inside the networks. The loading of benzene-d_6 was varied in order to assess the effect of swollen and non-swollen pores upon guest mobility.

In this chapter, network flexibility was examined by selective deuteration of phenyl rings within the struts of each network. T_1 relaxation times have been determined for dry CMP-1 and CMP-2 to assess the effect of interpenetration upon network mobility.

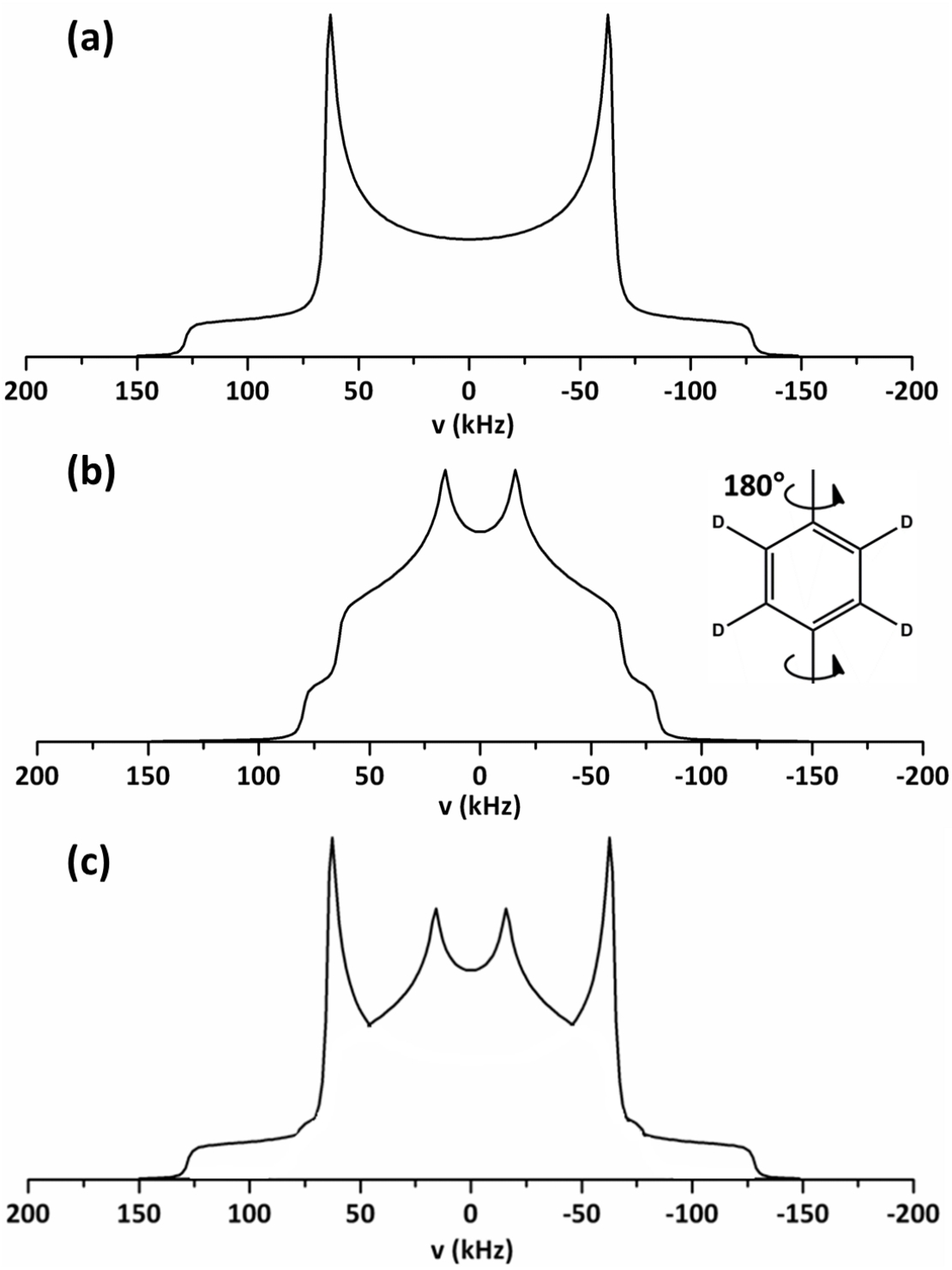

Figure 4-4: ^{2}H NMR spectra simulated using the NMR Weblab v4.0[221] for a static C-D bond (a), a phenyl ring undergoing a 180° π-flip motion around its C_2-axis (b), and a superposition of both spectra (c). Figure adapted from reference [133].

4.1.3 Experimental

4.1.3.1 Materials

All chemicals and solvents were obtained from either ABCR (1,3,5-triethynylbenzene, 98 %), QMX Laboratories Ltd (4,4'-dibromobiphenyl-d_8, 99 %) or Sigma-Aldrich and were used as received. Anhydrous grade toluene (Aldrich) was used. All chemicals had a purity of 98 % or greater.

4.1.3.2 Preparation of glassware and equipment

All Sonogashira-Hagihara reactions were carried out in dry 2-necked round-bottomed flasks (150 mL CMP-1-d_4, 50 mL CMP-2-d_8) on a Radleys carousel, and back-filled with N_2 prior to use.

All other equipment, such as syringes, needles and magnetic stirrers, were baked for 24 h in an oven at 120 °C prior to use.

4.1.3.3 Synthesis of deuterated CMP networks

Scheme 4-1: Deuterated CMP-1 reaction.

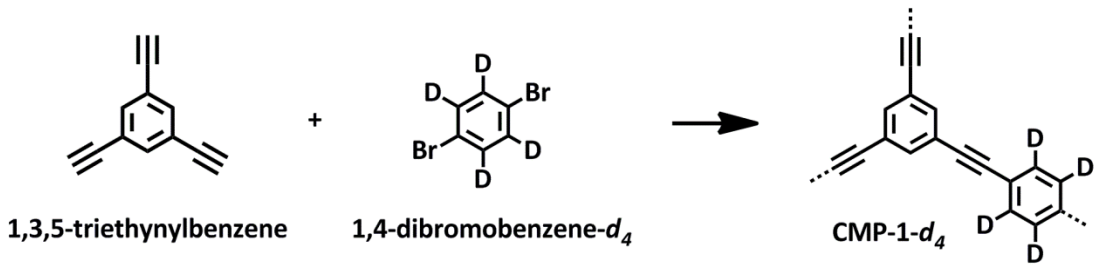

The networks were synthesised in toluene using a procedure similar to that reported for CMP-1.[65, 66] Typically, 1,3,5-triethynylbenzene (150 mg, 1.0 mmol), 1,4-dibromobenzene (236 mg, 1.0 mmol), triethylamine (1.0 mL) and

toluene (1.0 mL) were mixed under nitrogen in a 2-necked round bottomed flask (150 mL). The reaction mixture was heated to 80 °C.

Next, a slurry of the catalyst, tetrakistriphenylphosphinepalladium(0) (50 mg, 0.04 mmol) and copper (I) iodide (15 mg, 0.08 mmol) in toluene (1.0 mL), was added *via* a wide-bore needle to the flask. Each mixture was then heated under nitrogen at 80 °C overnight. After this time, methanol (*ca.* 100 mL) was added and the mixture filtered under suction. The solid precipitate was isolated and washed several times on the filter with methanol to remove any catalyst. The recovered brown solid was then Soxhlet extracted in methanol for 12 hours and dried in a vacuum oven for 24 hours prior to analysis. Yield 235 mg, 118%. Observed(%): C, 78.96; H, 3.33. $C_{20}H_7$ requires (%): C, 96.40; H, 3.60.

Scheme 4-2: Deuterated CMP-2 reaction.

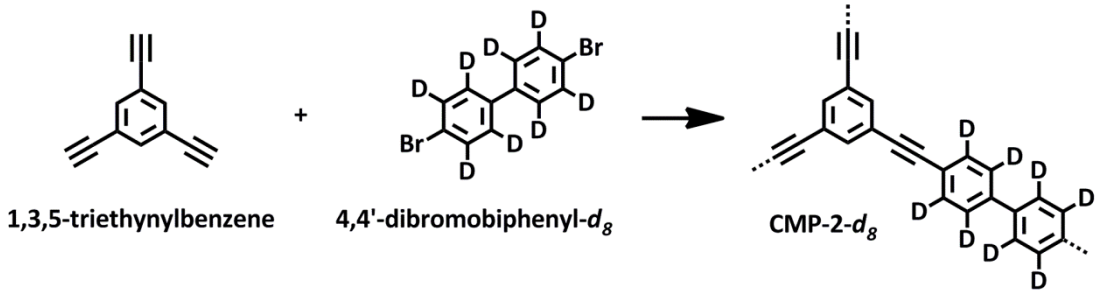

The networks were synthesised in toluene using a procedure similar to that reported for CMP-2.[65, 66] Typically, 1,3,5-triethynylbenzene (75 mg, 0.5 mmol), 4,4'-dibromobiphenyl-d_8 (160 mg, 0.5 mmol), triethylamine (0.75 mL) and toluene (0.75 mL) were mixed under nitrogen in a 2-necked round bottomed flask (50 mL). The reaction mixture was heated to 80 °C.

Next, a slurry of the catalyst, tetrakistriphenylphosphinepalladium(0) (30 mg, 0.02 mmol) and copper(I) iodide (8.75 mg, 0.04 mmol) in toluene (0.5 mL), was added *via* a wide-bore needle to the flask. Each mixture was then heated under nitrogen at 80 °C overnight. After this time, methanol (*ca.* 100 mL) was added and the mixture filtered under suction. The solid precipitate was isolated and washed several times on the filter with methanol to remove any

catalyst. The recovered brown solid was then Soxhlet extracted in methanol for 12 hours and dried in a vacuum oven for 24 hours prior to analysis. Yield 76 mg, 106%. Observed(%): C, 75.08; H, 3.26. $C_{24}H_{11}$ requires (%): C, 96.30; H, 3.70.

4.1.3.4 Impregnation of benzene in CMP networks

4.1.3.4.1 Guest/benzene mobility

For investigations of a guest within the swollen networks, the required amount of $\mathbf{C_6D_6}$ was added *via* a wide-bore needle to a vial containing the dry **non-deuterated** network (50 mg). For investigations of the effect of a guest upon the mobility of the networks, the required amount of $\mathbf{C_6H_6}$ was added *via* a wide-bore needle to a vial containing the dry **deuterated** network (50 mg). Each host-guest material was then packed immediately into an NMR rotor, sealed, and then left overnight to allow diffusion of the solvent into the network.

4.1.4 Characterisation conditions

4.1.4.1 Gas sorption analysis

Polymer surface areas and pore size distributions were measured by nitrogen adsorption and desorption isotherms in the range 0.01 – 0.95 P/P_0 with 98 data points at 77.3 K using a Micromeritics ASAP 2420 volumetric adsorption analyser. Gas sorption equipment was operated by either Dr. Robert Dawson or Mr. Robert Clowes.

Surface areas were calculated in the relative pressure (P/P_0) range from 0.01 to 0.10. Pore size distributions and pore volumes were derived from the adsorption branches of the isotherms using the non-local density functional

theory (NL-DFT) pore model for pillared clay with cylindrical pore geometry. Samples were degassed at 120 °C for 15 hours under vacuum (10^{-5} bar) before analysis.

4.1.4.2 **FTIR**

IR spectra were collected as KBr pellets using a Bruker Tensor 27 spectrometer.

4.1.4.3 **TGA**

TGA analyses were carried out using a Q5000IR analyser (TA Instruments) with an automated vertical overhead thermobalance. The samples were heated at a rate of 10 °C/min under a nitrogen atmosphere to a maximum of 700 °C.

4.1.4.4 **Elemental Analysis**

All elemental analyses were carried out by the Microanalysis Department in the School of Physical Sciences, at the University of Liverpool. The conditions used to collect these data are given in **Chapter 2**, **Section 2.7**.

4.1.4.5 **Solid-State NMR**

Solid-state NMR spectra were measured at ambient temperature (unless otherwise stated) on a Bruker Avance DSX 400 spectrometer. Samples were packed into zirconia rotors 4 mm in diameter equipped with a high temperature

cap. Data were acquired using a 4 mm $^{1}H/X/Y$ probe operating at 100.61 MHz for ^{13}C, 400.13 MHz for ^{1}H and 61.4 MHz for ^{2}H.

4.1.4.5.1 ^{1}H-^{13}C CP/MAS NMR

^{1}H-^{13}C CP/MAS NMR spectra were acquired at an MAS rate of 10.0 kHz using a ^{1}H $\pi/2$ pulse of 3.6 μs and a recycle delay of 10 s. The Hartmann-Hahn condition was set using hexamethylbenzene. The spectra were measured using a contact time of 2.0 ms. Two-pulse phase modulation (TPPM) decoupling[166] was used during the acquisition. Typically, 4096 scans were accumulated. The values of chemical shifts are referred to that of TMS.

For ^{1}H-^{13}C CP/MAS kinetics experiments, various contact times were used in the range 0.01 ms to 16.0 ms. Twenty-one slices were collected. 304 scans were accumulated per slice.

4.1.4.5.2 SPE ^{13}C {^{1}H} HPDEC MAS NMR

SPE $^{13}C\{^{1}H\}$ HPDEC MAS NMR spectra were acquired at an MAS rate of 10.0 kHz using a ^{13}C $\pi/3$ pulse of 2.6 μs and a recycle delay of 10 s. Two-pulse phase modulation (TPPM) decoupling[166] was used during the acquisition. Typically, 4096 scans were accumulated. The values of chemical shifts are referred to that of TMS.

4.1.4.5.3 ^{2}H solid echo NMR and T_1 inversion recovery

^{2}H NMR static spectra were acquired using the solid-echo pulse sequence ($90°_x - \tau_1 - 90°_y - \tau_2$ -acquire). A ^{2}H $\pi/2$ pulse of 2.6 μs and a recycle delay of 15 s (CMP-1-d_4) or 10 s (CMP-2-d_8) were used. Two-pulse phase modulation (TPPM)

decoupling[166] was used during the acquisition. Typically, 1024 scans were accumulated. The values of chemical shifts are referred to that of external D_2O.

During the initial stages of the investigation, samples were prepared either directly before, or 24 hours in advance of NMR measurements. Those prepared directly before NMR measurements were found to give inconsistent results. This effect is presumably the result of different extent of diffusion of benzene- d_6 within the polymer network. Samples prepared 24 hours in advance gave concordant spectra. In this instance, the guest was allowed time to diffuse through the network, enabling an equilibrium state to be reached. Therefore, all investigations were carried out on samples prepared a minimum of 24 hours prior to NMR measurements.

A typical temperature cycle used in these experiments was as follows:

1. Cooling from room temperature to 173 K over 1 hour
2. Equilibration for 45 minutes followed by the acquisition of spectra.
3. Heating by 10 K, equilibration for 15 minutes, and then recording of spectra.
4. Repeat step three until 373 K is reached.
5. After recording of spectra at 373 K, cool to room temperature.

Low temperature experiments were performed using cold boil-off nitrogen gas. The temperature of the material was controlled using a thermocouple on the sample chamber of the probe.

Line-shape simulations were performed using DMFit software.[223]

^2H T_1 relaxation times were measured using a solid-echo pulse sequence followed by a conventional T_1 inversion recovery pulse sequence ($180°_y - \tau_1 - 90°_y - \tau_2 - 90°_x - \tau_3$ -acquire). Either twenty-eight or fourteen different delay times (τ_3) were sampled in the range 0.01 to 6000 ms.

A typical temperature cycle used in these experiments was as follows:

1. Recording of spectrum at room temperature (293 K).
2. Heating the sample by 20 K, equilibration for 20 minutes, and then recording of spectra.
3. Repeat step two until 373 K is reached.
4. After recording of spectra at 373 K, cool to room temperature.

High temperature experiments were performed using a heater connected to the probe. The temperature of the samples was controlled using a thermocouple on the sample chamber of the probe.

The peak intensities were fitted as a function of delay time using **Equation 2-27** in **Section 2.1.2.4.2.1**.

4.1.4.6 **Data analysis**

Nitrogen adsorption isotherms were analysed using Micromeritics ASAP2420 software. All solid-state NMR spectra were acquired using XWINNMR 3.5. All NMR spectra were processed using Bruker Topspin 2.1 software. Deconvolutions of the spectra were carried out using Origin Pro 8.5.

4.2 Results and Discussion

The sorption properties of CMP-1 and CMP-2 have been previously examined by Cooper and co-workers[65, 66, 71, 100] using gas sorption analysis and molecular simulations.[65,66,71,100] Their results are summarised in **Table 4-1**.

Table 4-1: Physical properties of CMP networks.

	Ethynyl monomer	Bromo monomer	SA_{BET} (m^2g^{-1})[a]	V_{Tot} (cm^3g^{-1})[b]	$V_{0.1}/V_{0.99}$[c]	Average strut length (nm)[d]	Average cluster size (nm)[e]
CMP-1	1,3,5-triethynyl benzene	1,4-dibromo benzene	867	0.99	0.33	1.11	6.6
CMP-2	1,3,5-triethynyl benzene	4,4'-dibromo biphenyl	204	0.43	0.21	1.53	7.0

[a]Based on full isotherm pressure range 0.05-0.15 [b]Total pore volume at P/P_0 = 0.99 [c]$V_{0.1}$ is the pore volume at P/P_0 = 0.1. Gas sorption data are from references[71, 100]. [d]Average node-to-node strut length measured between connected quaternary carbons derived from polymer fragment models.[65, 66] [e]Average overall fragment diameter derived from polymer fragment models.[65, 66]

Two important observations were noted. The first is a shift in micropore size distribution to larger pore diameters from CMP-1 to CMP-2, ascribed to the effect of increasing the average strut length. The second is a decrease in BET surface area and total pore volume as the monomer strut length increases, attributed to interpenetration of the network by the longer struts. However, their data do not provide details about the origins of porosity nor do they explain why the networks are able to swell.

This work examines the structures and physical properties of CMP-1 and CMP-2 by ^{2}H NMR. The study is divided into two sections. The first section describes investigation of the porosity and swelling of the networks by

examination of molecular dynamics of a deuterated guest. The second section examines the mobility of deuterated analogues of CMP-1 and CMP-2.

4.2.1.1 ^{2}H NMR of an adsorbed guest inside CMP networks

Per-deuterated benzene was chosen as the probe for a number of reasons. Benzene-d_6 molecules exhibit six-fold symmetry; therefore, it should be relatively straightforward to assign the ^{2}H NMR spectra. Also, as CMP networks are composed of aromatic groups, favourable interactions may occur between the CMP host and benzene-d_6 guest. CMP networks swell significantly in aromatic solvents, thus enabling examination of pores in the swollen-state. Finally, benzene has been used widely to investigate other porous materials and so a large body of data is available as a comparison.

Three benzene-d_6 loadings (48, 190 and 570 wt%) were chosen so that the effect of different levels of swelling on porosity and dynamics of the host-guest system could be analysed. 570 wt% represents the maximum capacity of benzene inside CMP-1 and CMP-2. Addition of further benzene to the networks leads to visible free liquid in the sample vial. 48 wt% represents the lowest practical loading of benzene that can be added to each network.

Variable temperature ^{2}H NMR spectra of benzene-d_6 inside CMP-1 and CMP-2 with increasing loadings of 48, 190 and 570 wt% are shown in **Figures Figure** 4-5 to **Figure** 4-7 and **Figures Figure** 4-8 to **Figure** 4-10, respectively. In order to understand the corresponding types of motions, line shape analysis was performed using DMFit simulation software.[223] Fitting parameters used to produce the simulated spectra for each loading are given after their corresponding spectra in **Tables** Table 4-2: Parameters corresponding to simulated 2H NMR **spectra** from **Figure 4-5.** to **Table 4-7**. The data are discussed collectively, beginning on page 156.

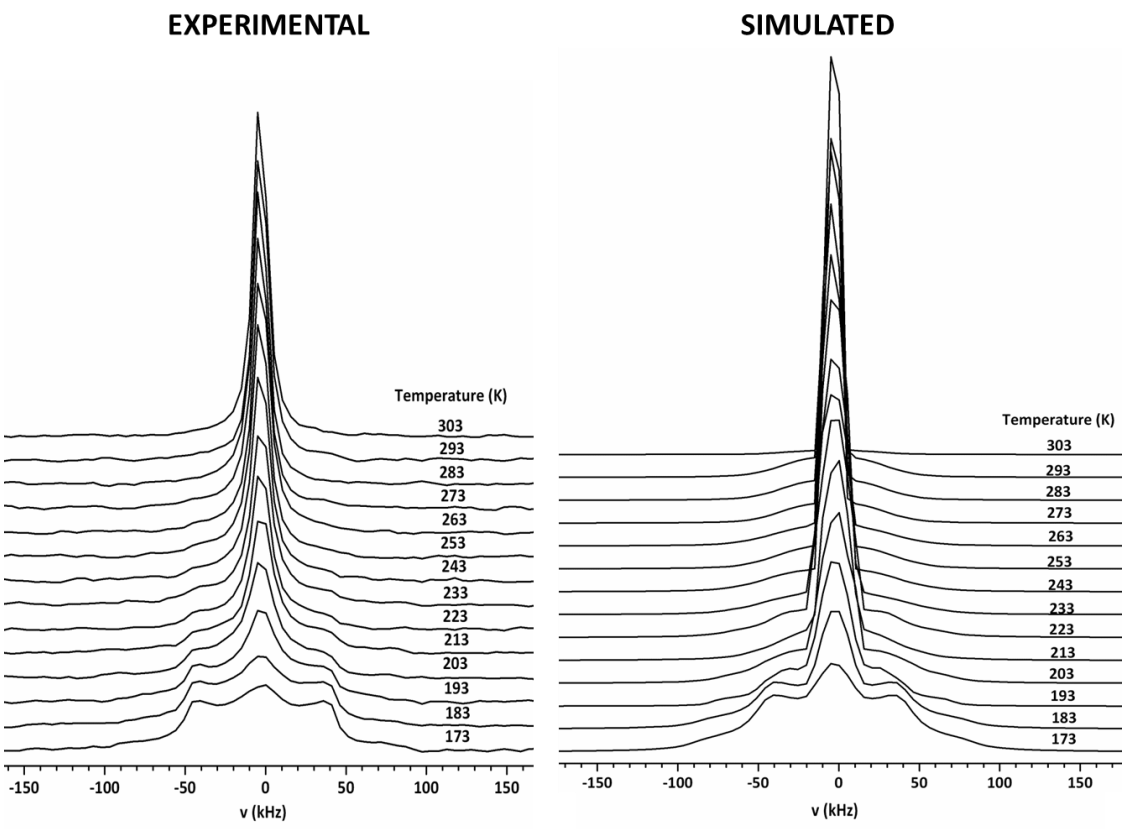

Figure 4-5: Variable temperature ^{2}H NMR spectra of benzene-d_6 inside CMP-1 with 48 wt% loading level.

Table 4-2: Parameters corresponding to simulated ^{2}H NMR spectra from **Figure 4-5**.

Temperature (K)	Integral of components (%)		Q_{cc} (kHz)		η_Q	
	Outer	Inner	Outer	Inner	Outer	Inner
173	65	13	178	27	0.02	1.0
183	54	24	173	25	0.01	1.0
193	24	55	153	25	0.2	1.0
203	25	54	151	27	0.3	1.0
213	22	57	115	25	0.3	1.0
223	18	61	141	26	0.2	1.0
233	9	70	139	26	0.4	1.0
243	11	68	128	18	0.4	1.0
253	10	69	112	17	0.4	1.0
263	6	73	117	17	0.4	1.0
273	3	76	98	15	0.4	1.0
283	3	76	98	15	0.4	1.0
293	3	79	98	15	0.4	1.0
303	0	79	0	15	0	1.0

Integral for the surface confined layer (SCL) was calculated as 22 % at 293 K. The contribution of the SCL to the line shape was assumed to be constant at all temperatures, as the surface area of the network does not change with temperature, for further discussion please see page 158 onwards. SCL quadrupolar coupling constant (Q_{cc}) was calculated as 49 kHz at 293 K.

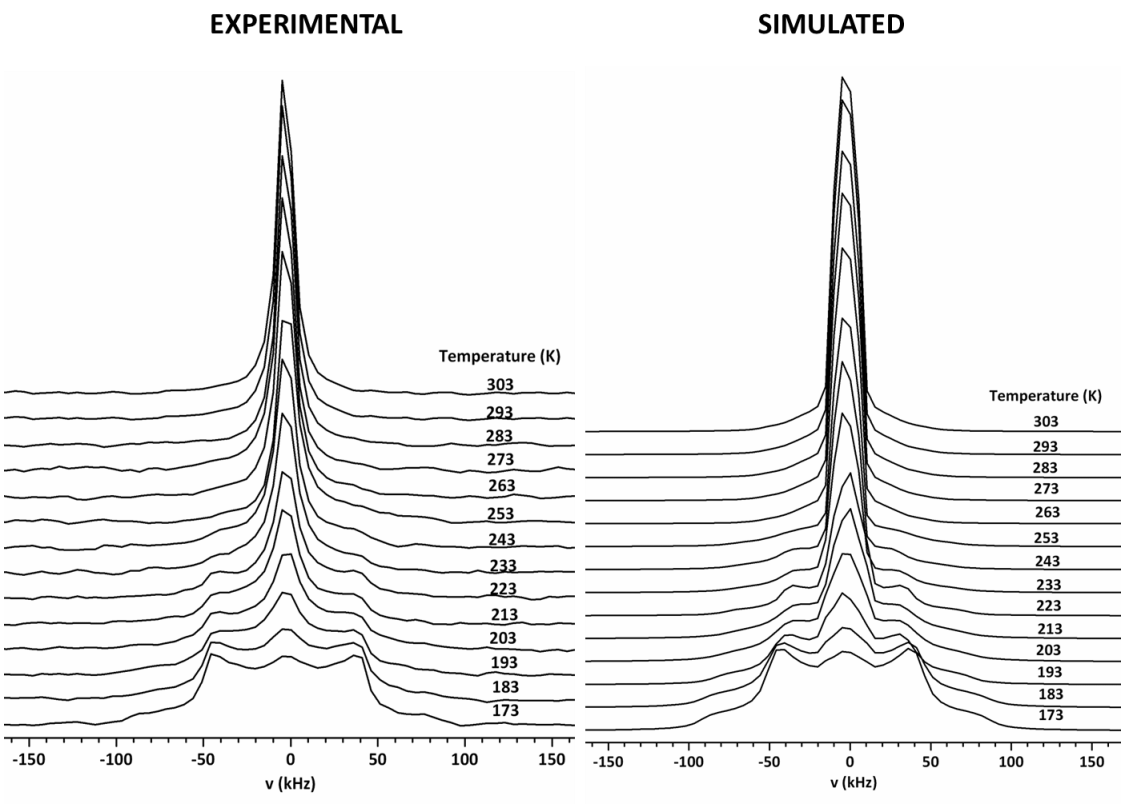

Figure 4-6: Variable temperature ^{2}H NMR spectra of benzene-d_6 inside CMP-1 with 190 wt% loading level.

Table 4-3: Parameters corresponding to simulated ^{2}H NMR spectra from **Figure 4-6.**

Temperature (K)	Integral of components (%)		Q_{cc} (kHz)		η_Q	
	Outer	Inner	Outer	Inner	Outer	Inner
173	76	5	183	28	0.06	1.0
183	71	10	181	29	0.04	1.0
193	62	20	163	29	0.1	1.0
203	54	28	157	28	0.1	1.0
213	44	37	150	26	0.01	1.0
223	33	48	154	26	0.01	1.0
233	23	58	146	24	0.01	1.0
243	18	63	139	22	0.01	1.0
253	14	68	140	21	0.3	1.0
263	4	77	108	21	0.3	1.0
273	2	79	108	21	0.3	1.0
283	1	80	108	21	0.3	1.0
293	0	81	0	21	0	1.0
303	0	81	0	21	0	1.0

Integral for the surface confined layer (SCL) was calculated as 19 % at 293 K. The contribution of the SCL to the line shape was assumed to be constant at all temperatures, as the surface area of the network does not change with temperature, for further discussion please see page 158 onwards. . SCL Q_{cc} was calculated as 54 kHz at 293 K.

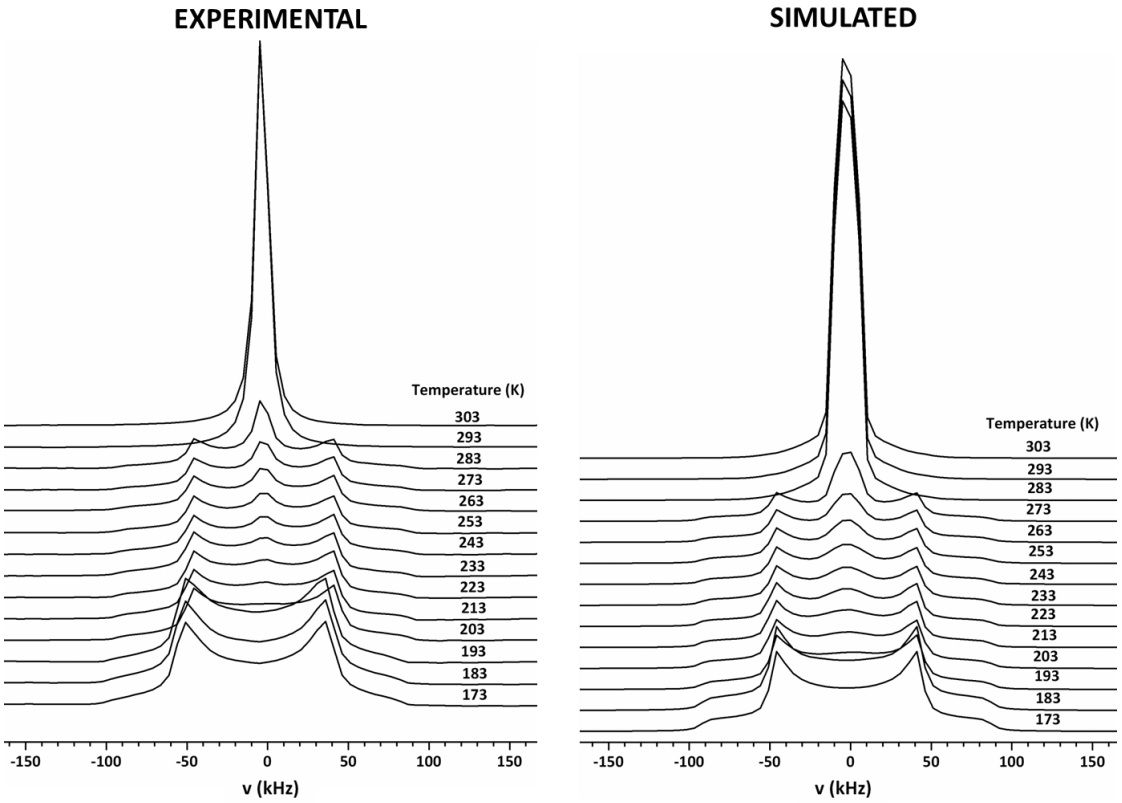

Figure 4-7: Variable temperature ^{2}H NMR spectra of benzene-d_6 inside CMP-1 with 570 wt% loading level.

Table 4-4: Parameters corresponding to simulated ^{2}H NMR spectra from **Figure 4-7**.

Temperature (K)	Integral of components (%)		Q_{cc} (kHz)		η_Q	
	Outer	Inner	Outer	Inner	Outer	Inner
173	86	0	184	-	0.02	-
183	82	4	184	69	0.02	0.02
193	78	8	184	87	0.02	1.0
203	78	8	185	87	0.04	1.0
213	75	11	185	68	0.03	1.0
223	75	11	185	30	0.03	1.0
233	74	12	184	20	0.02	1.0
243	71	15	184	12	0.02	1.0
253	70	16	184	12	0.02	1.0
263	66	20	184	12	0.02	1.0
273	56	30	184	12	0.02	1.0
283	0	86	0	9	0	1.0
293	0	86	0	7	0	1.0
303	0	86	0	20	0	1.0

Integral for the surface confined layer (SCL) was calculated as 14 % at 293 K. The contribution of the SCL to the line shape was assumed to be constant at all temperatures, as the surface area of the network does not change with temperature, for further discussion please see page 158 onwards. . SCL Q_{cc} was calculated as 54 kHz at 293 K.

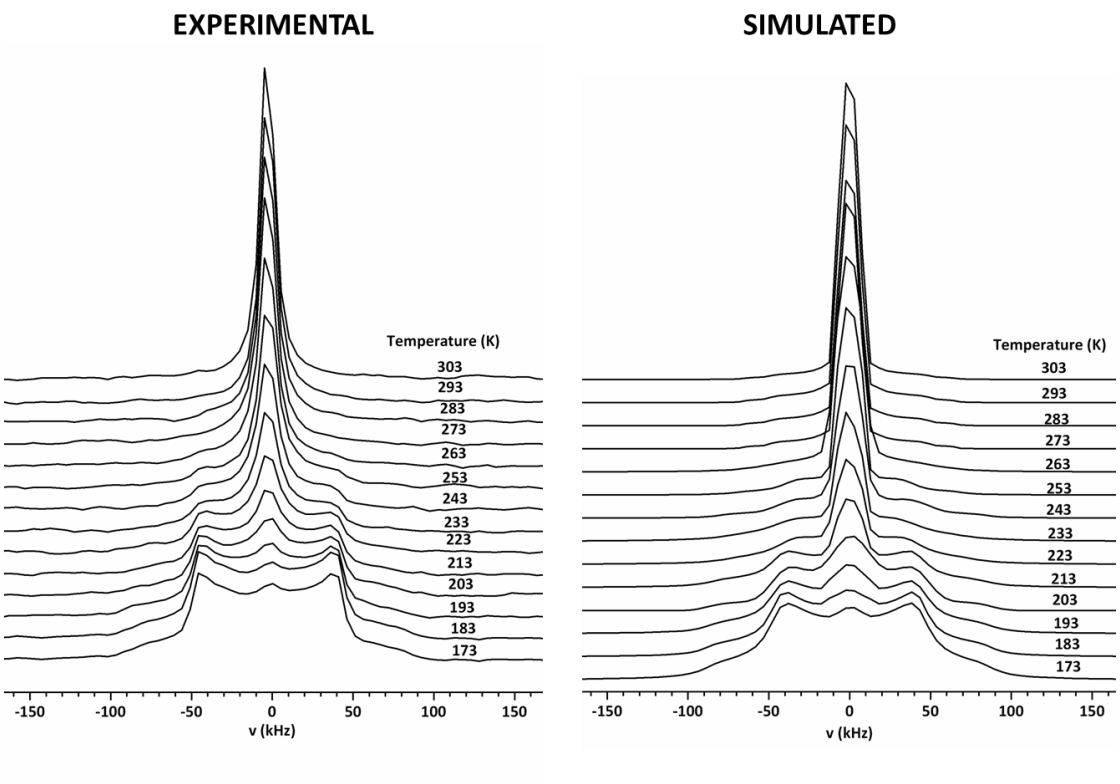

Figure 4-8: Variable temperature ^{2}H NMR spectra of benzene-d_6 inside CMP-2 with 48 wt% loading level.

Table 4-5: Parameters corresponding to simulated ^{2}H NMR spectra from **Figure 4-8**.

Temperature (K)	Integral of components (%)		Q_{cc} (kHz)		η_Q	
	Outer	Inner	Outer	Inner	Outer	Inner
173	83	2	180	19	0.03	0.8
183	80	6	181	29	0.04	1.0
193	76	10	179	28	0.09	1.0
203	58	27	180	26	0.1	1.0
213	63	23	176	24	0.04	1.0
223	52	33	155	24	0.08	1.0
233	45	41	150	22	0.1	1.0
243	28	57	171	20	0.2	1.0
253	18	67	144	21	0.2	1.0
263	12	73	134	25	0.5	1.0
273	11	75	134	25	0.5	1.0
283	8	78	134	17	0.5	1.0
293	0	85	0	17	0	1.0
303	0	85	0	17	0	1.0

Integral for the surface confined layer (SCL) was calculated as 15 % at 293 K. The contribution of the SCL to the line shape was assumed to be constant at all temperatures, as the surface area of the network does not change with temperature, for further discussion please see page 158 onwards. . SCL Q_{cc} was calculated as 67 kHz at 293 K.

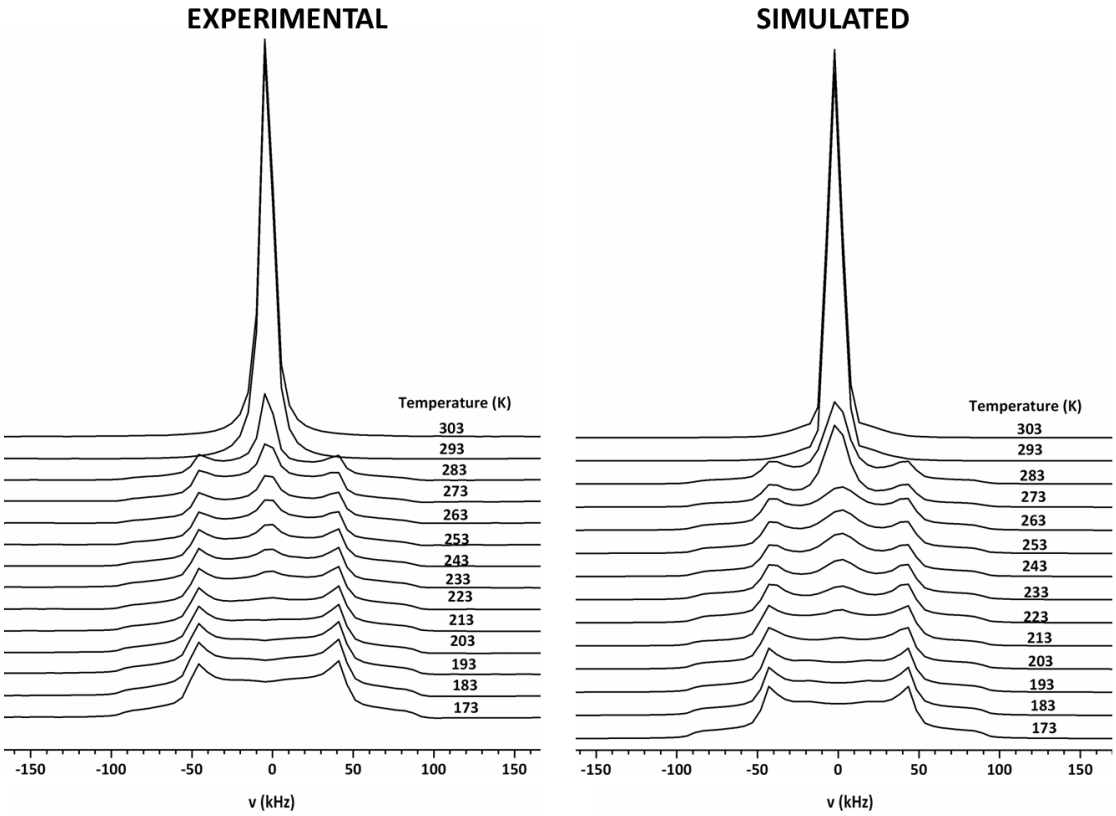

Figure 4-9: Variable temperature ^{2}H NMR spectra of benzene-d_6 inside CMP-2 with 190 wt% loading level.

Table 4-6: Parameters corresponding to simulated ^{2}H NMR spectra from **Figure 4-9**.

Temperature (K)	Integral of components (%)		Q_{cc} (kHz)		η_Q	
	Outer	Inner	Outer	Inner	Outer	Inner
173	70	12	185	87	0.02	0.02
183	69	13	185	87	0.02	0.02
193	68	14	185	87	0.02	0.02
203	69	13	185	85	0.04	1.0
213	49	33	185	105	0.04	1.0
223	74	8	182	12	0.07	1.0
233	70	12	182	112	0.07	1.0
243	64	19	182	17	0.07	1.0
253	59	23	182	17	0.07	1.0
263	55	28	182	15	0.07	1.0
273	45	37	182	10	0.07	1.0
283	0	82	0	20	0	1.0
293	0	82	0	20	0	1.0
303	0	82	0	20	0	1.0

Integral for the surface confined layer (SCL) was calculated as 18 % at 293 K. The contribution of the SCL to the line shape was assumed to be constant at all temperatures, as the surface area of the network does not change with temperature, for further discussion please see page 158 onwards. SCL Q_{cc} was calculated as 41 kHz at 293 K.

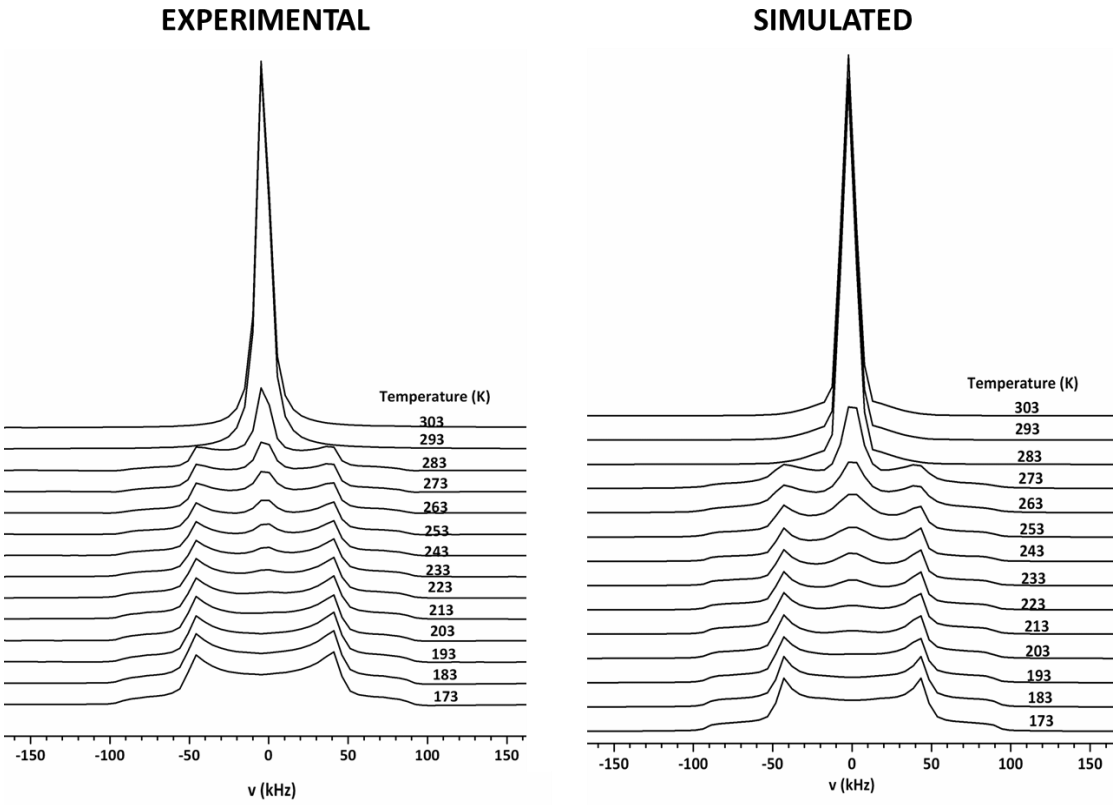

Figure 4-10: Variable temperature ^{2}H NMR spectra of 570 wt% benzene-d_6 inside CMP-2, experimental (left) and simulated (right).

Table 4-7: Parameters corresponding to simulated ^{2}H NMR spectra from **Figure 4-10**.

Temperature (K)	Integral of components (%)		Q_{cc} (kHz)		η_Q	
	Outer	Inner	Outer	Inner	Outer	Inner
173	75	8	187	87	0.02	0.02
183	75	8	187	87	0.02	0.02
193	75	7	185	68	0.05	1.0
203	78	4	185	3	0.03	1.0
213	76	6	185	20	0.03	1.0
223	74	7	185	12	0.03	1.0
233	71	10	185	12	0.03	1.0
243	66	16	185	12	0.03	1.0
253	64	18	185	12	0.03	1.0
263	64	18	185	9	0.03	1.0
273	53	28	185	7	0.03	1.0
283	0	82	0	20	0	1.0
293	0	82	0	20	0	1.0
303	0	82	0	20	0	1.0

Integral for the surface confined layer (SCL) was calculated as 18 % at 293 K. The contribution of the SCL to the line shape was assumed to be constant at all temperatures, as the surface area of the network does not change with temperature, for further discussion please see page 158 onwards. . SCL Q_{cc} was calculated as 41 kHz at 293 K.

As indicated in the introduction (**Section 4.1.1**), it is difficult to assess the accuracy of the simulated data, therefore the following discussion is based upon a largely qualitative analysis of the results. Graphs and tables have been included in order to identify trends in the data.

At first glance, all spectra are composed of two superimposed spectral features, a narrow central peak and a Pake doublet. A gradual decrease in intensity of the Pake doublet and an increase in intensity of the central peak are observed with increasing temperature (**Figure 4-5** to **Figure** 4-10). Assignment of the peaks was carried out by comparing the experimental and simulation data with that reported for similar systems in the literature, *i.e.* benzene-d_6 encapsulated inside a porous host.[120, 127, 130, 131, 133, 137]

As the central line is most prominent at higher temperatures, this line shape was examined at 293 K. At this temperature, quadrupolar coupling constants (Q_{cc}) in the range from 7 to 21 kHz and a η_Q of 1.0 were calculated for the central line, over the three different loading levels in both CMP-1 and CMP-2. These values correspond to unrestricted benzene-d_6 executing isotropic reorientation.[120, 128, 131, 133] In this motional regime, the benzene-d_6 molecules are liquid-like and can be considered as 'melted.'[120]

However, upon closer inspection of the central peak, two components were found to contribute to the experimental line shape. The two components are present in the spectra for all benzene-d_6 loadings in both networks, as shown in **Figure 4-11**.

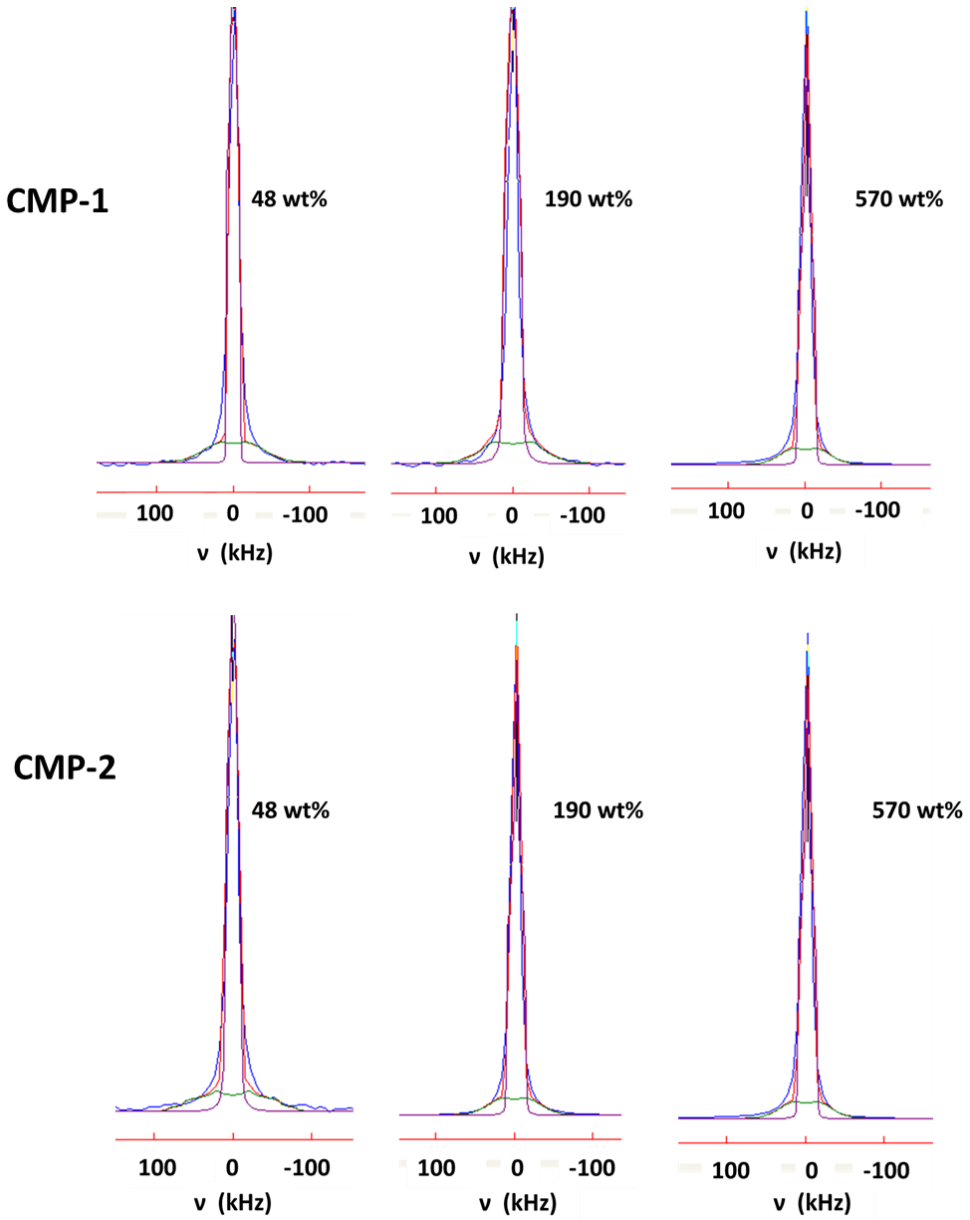

Figure 4-11: ^{2}H NMR spectra of benzene-d_6 inside CMP-1 and CMP-2 at 293 K for each loading. The extra component is represented by a green line. Experimental spectra (blue line). Simulated spectra, isotropic benzene (purple line). Sum of the simulated components (red line).

The central peak (purple) is the dominant feature and corresponds to isotropic motion of the bulk benzene-d_6 molecules at the middle of the pore.[120] A less intense broader component, which causes widening at the base of the

experimental peak is also displayed (green). The ratio of integrals of the central peak and broad component were calculated from the peak area integrals, these data are summarised in **Table 4-8**.

Table 4-8: Summary of the ratios of % integrals for benzene-d_6 inside CMP networks.

Network	Ratio of bulk : broader component for each loading of benzene-d_6 (wt%)		
	48	**190**	**570**
CMP-1	1 : 0.27	1 : 0.23	1 : 0.16
CMP-2	1 : 0.18	1 : 0.22	1 : 0.22

For CMP-1, these data show that the ratio of bulk to surface benzene decreases with increasing loading. For CMP-2, the trend in the ratio of bulk to surface benzene indicates that there is much less variation of the pore filling. These data suggest that for CMP-1 benzene is being absorbed inside the pores of the network at all loadings. However, for CMP-2, absorption is occurring on the outer surface at loadings of 190 and 570 wt%, as the pores are completely filled. This observation is a possible consequence of the increased external porosity (see **Table 4-1**) and lower pore volume of CMP-2 when compared with CMP-1.[*1]

In order to confirm whether the broad component is indeed surface confined layer of benzene, it is necessary to examine the Q_{cc} of the two components at 293 K and compare them with those reported previously in the literature. As mentioned earlier, the peak corresponding to bulk benzene exhibits Q_{cc} values in the range from 7 to 21 kHz over the three different loading

*[1] From gas sorption data, the total pore volumes of CMP-1 and CMP-2 are 0.99 and 0.43 cm^3g^{-1}. For 50 mg material the total pore volume is calculated as 0.05 and 0.02 cm^3 for CMP-1 and CMP-2, respectively. Benzene loadings of 48, 190 and 570 wt% correspond to 0.03, 0.1 and 0.3 cm, therefore the loadings represent 50, 200 and 610 % of the total pore volume of CMP-1 and 90, 460 and 1460 % of the total pore volume of CMP-2, respectively, in comparison with the UNSWOLLEN networks.

levels in both CMP-1 and CMP-2. The broader component displays Q_{cc} values in the range from 41 to 67 kHz over the three different loading levels in both CMP-1 and CMP-2. A higher Q_{cc} value suggests that the broader component corresponds to less mobile species than those represented by the narrower central peak.[232] Therefore, the broad peak can be ascribed to benzene-d_6 molecules at the surface of the pore wall (**Figure 4-12**).[120] Such results are in excellent agreement with those proposed by molecular dynamics (MD) simulations, *i.e.* slow benzene molecules at the pore surface and fast unbound solvent molecules in the centre of the pore.[232]

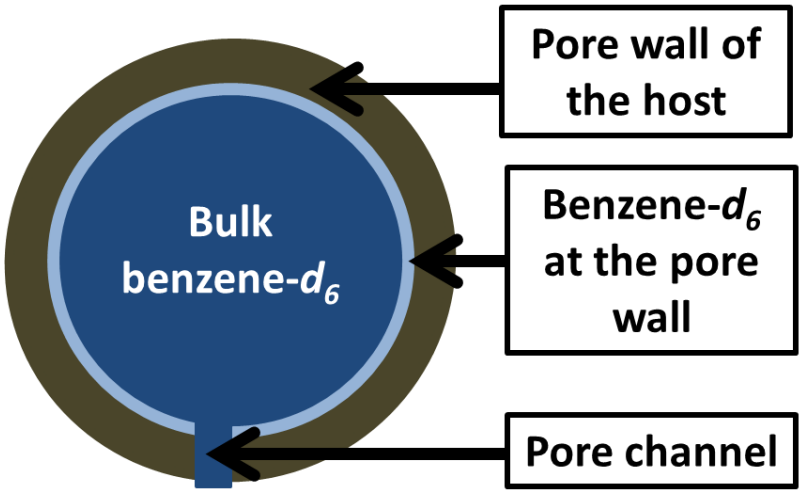

Figure 4-12: Representation of benzene-d_6 encapsulated inside a pore.

These bulk/surface observations are also comparable with other experimental data for host-guest systems such as benzene-d_6 inside polystyrene[127] and porous glasses,[137] and pyridine-d_5 and water guests inside mesoporous silica exhibiting hydrogen-bonding interactions with silanol groups on the silica pore surface.[120]

In the case of benzene inside CMP networks, two possible interactions may exist between the pore wall and the guest. The first is a T-shaped interaction, where benzene is orientated 90° with respect to the pore wall. In this case, the C-H bond of benzene interacts with the centre of the phenyl group in

the network,[232, 234] (**Figure 4-13a**). The second is a co-planar interaction where benzene π-stacks with the phenyl group and is orientated 180° with respect to the pore wall,[232, 234] (**Figure 4-13b**).

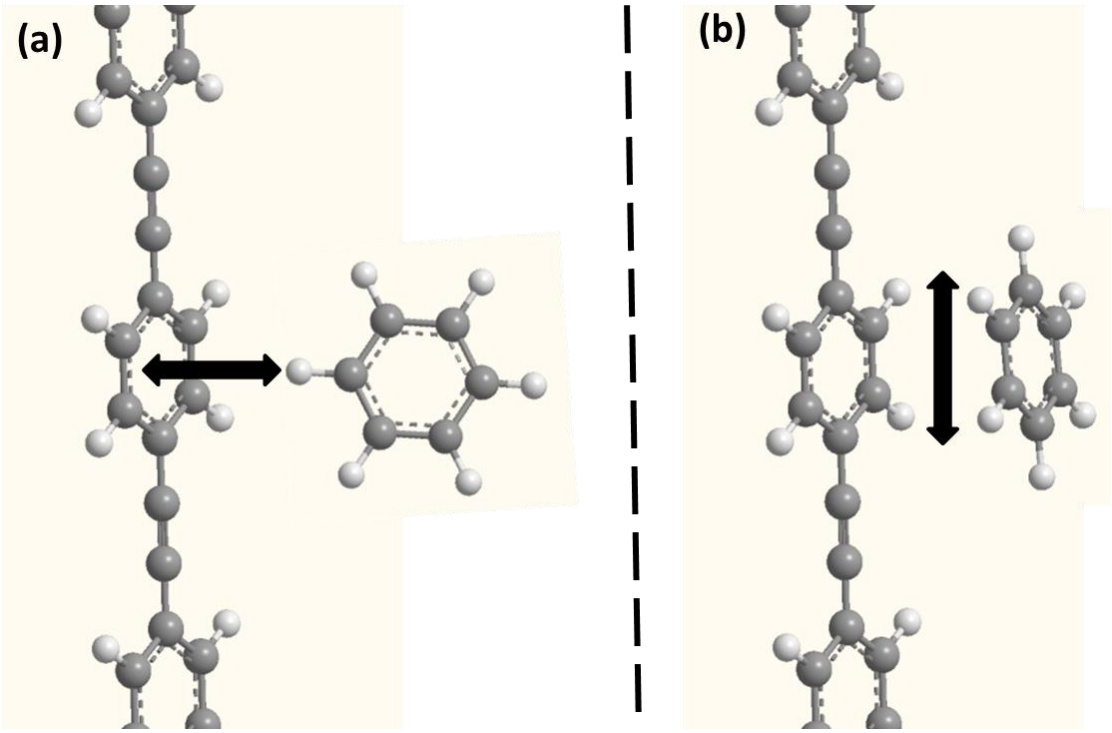

Figure 4-13: Possible interactions of benzene at the CMP-1 pore wall. (a) T-shaped interaction with 90° orientation and (b) π-stacking with 180° orientation.

These interactions were proposed previously based on Monte Carlo simulation methods for benzene-polystyrene[232] and benzene-aromatic[234] systems. Interestingly, the orientation of benzene inside polystyrene was predicted to change from the T-shaped orientation to a co-planar position with increasing benzene loading.[232]

Experimentally, it is difficult to distinguish between T-shaped and π-stacking interactions by motional studies, as both orientations exhibit C_6-axis rotation.[127] Additionally, the surface layer and bulk benzene are exchanging constantly.[232] Another problem also exists in that the ^{2}H NMR powder spectra result from a distribution of molecules adopting all possible orientations.[138, 160, 161]

Possible solutions involve analysis of a guest within specifically oriented materials, such as a stretched polymer film or drawn fibre. In this case it is possible to separate the interactions of an aligned guest based upon the differences in geometry.[127, 138] However, owing to their insolubility, it is impractical to prepare oriented films of CMP networks.

Another feasible route for identifying the benzene-pore interface could involve determination of guest mobility and internuclear distances between the pore wall and the guest by ^{1}H-^{2}H CP/MAS NMR and 2D ^{1}H-^{2}H heteronuclear correlation (HETCOR) NMR. These experiments have been used previously for analysing host-guest interactions in zeolites.[235] However, identification of the interactions at the pore walls of CMP materials by ^{2}H NMR is yet to be achieved.

Next the Pake doublet shall be considered. As the Pake doublet is most prominent at lower temperatures, this line shape was examined at 173 K. At this temperature, Q_{cc} values in the range from 178 to 187 kHz and η_Q values of 0.02 to 0.06 were calculated over the three different loading levels in both CMP-1 and CMP-2. Such values are associated with benzene-d_6 molecules undergoing fast in-plane rotations about the C_6-symmetry axis[120, 130, 131] (see **Figure 4-3**). In this motional regime, the benzene-d_6 molecules are in solid II phase (rotating slowly compared to the NMR timescale) and can be considered as 'frozen.'[120]

At temperatures below 183 K, the ^{2}H NMR spectra of benzene inside CMP-2 with loadings of 190 and 570 wt% exhibit an additional doublet, as indicated in the representative spectrum displayed in **Figure 4-14**.

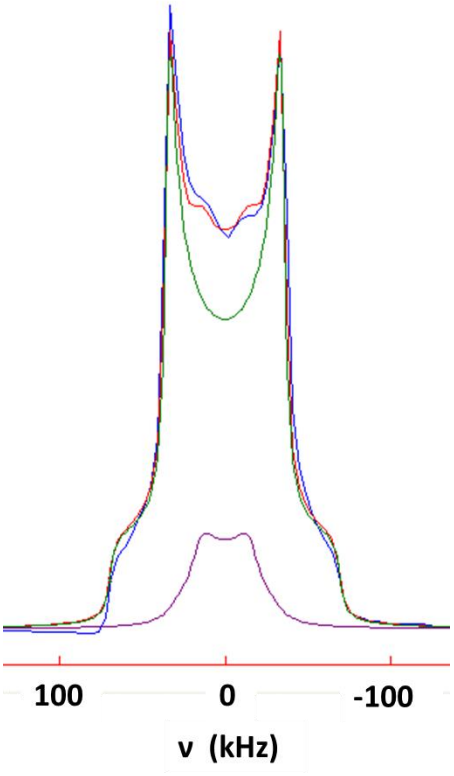

Figure 4-14: ^{2}H NMR spectrum of benzene-d_6 inside CMP-2 with 190 wt% loading level, at 173 K. Experimental spectra (blue line). Simulated spectra, Pake doublet corresponding to benzene in solid II phase (green line), the central peak is a doublet at low temperature (purple line). Sum of the simulated components (red line).

The doublet (represented by the purple line) is much narrower than the more dominant Pake doublet (green line) and exhibits Q_{cc} values *ca.* 87 kHz and a η_Q value of 0.02. These values correspond to benzene-d_6 molecules in solid I phase (benzene molecules rotating fast on the NMR timescale) and have been reported previously for benzene encapsulated inside mesoporous silica.[120]

Unfortunately, it is not possible to identify benzene-d_6 molecules in solid I phase inside CMP-1 by line shape analysis as the spectra are completely dominated by the Pake doublet, particularly in the ^{2}H NMR spectrum of benzene inside CMP-1 with a loading of 570 wt% at 173 K. As the rate of molecular motion exhibited by benzene-d_6 molecules in the surface confined

layer, liquid phase, solid II phase and solid I phase are very different; it may be possible to detect the presence of these components at each temperature and loading by measuring their relaxation behaviour. Relaxation experiments have been used previously to distinguish between surface confined benzene and bulk benzene adsorbed inside four controlled pore glasses with various pore diameters.[137] The results enabled an estimation of the thickness of the surface layer.

So far, assignment of the peaks displayed in the ^{2}H NMR spectra of benzene-d_6 loaded inside CMP-1 and CMP-2 networks has been accomplished. From the data, the following conclusions can be made; the spectra are composed of features attributed to both solid-like and liquid-like benzene-d_6 molecules. The ratios of these molecules vary with temperature. The resonance corresponding to liquid-like benzene-d_6 molecules is composed of a surface layer and bulk benzene inside the pores of the network. Finally, at temperatures below 183 K, a fourth component corresponding to benzene in solid I phase has been identified in the ^{2}H NMR spectra of CMP-2 with loadings of 190 and 570 wt%.

In order to investigate the host-benzene systems more closely, careful examination of the trends in ^{2}H NMR simulation parameters is required. Analysis of these parameters can provide information about the pores of the networks in swollen and non-swollen conditions.

Firstly, changes in peak area integrals of the Pake doublet and narrow peak with temperature and loading level are considered (see **Table 4-2** to **Table 4-7**). These data show that an increase in percentage integration of the inner components (central peak) is mirrored by a reduction in integration of the outer component (Pake doublet), *i.e.* the benzene molecules in the Pake doublet move to the central peak with increasing temperature. The changes in integrals are gradual for all of the ^{2}H NMR spectra of benzene-d_6 inside both CMP-1 and CMP-2. Such behaviour is indicative of changes in pore size distributions as a result of swelling.

In the temperature range 273–283 K (roughly the same temperature as the melting point of neat benzene-d_6), the spectra of CMP-1 with a loading of

570 wt% benzene and CMP-2 with loadings of 190 and 570 wt% benzene, exhibit large changes in peak integral. These large changes are indicative of benzene melting in the inter-pore areas and external surfaces of the network. Such a result is characteristic of non-encapsulated benzene and suggests that benzene is present on the outer surfaces of the networks.[137] As this occurs at 190 wt% for CMP-2, it shows that less benzene is required to fill the pores of CMP-2 in comparison to CMP-1. Such results are a consequence of the lower pore volume of CMP-2 (total pore volume is 0.43 cm^3g^{-1}, see page 159),[100] *i.e.* there is less pore space to fill than CMP-1 (0.99 cm^3g^{-1})[100]

Each loading also contains a surface confined layer of benzene. The amount of benzene in the surface confined layer changes with loading, as derived from the simulation data at 293 K (**Figure 4-11**). However, at temperatures below 293 K, the peak corresponding to surface confined layer is masked by the Pake doublet, therefore it is not possible to simulate the peak directly from the experimental data. As the surface areas of the networks are constant for each individual loading, it is reasonable to estimate that the surface confined layer contributes to the line shape by the same amount at low temperatures as it does at high temperatures.

In order to examine the effect of loading upon benzene-d_6 mobility (*i.e.* their ability to execute C_6-axis rotation, the simulated Q_{cc} values from **Table 4-2** to **Table 4-7** were plotted as a function of temperature for both networks in **Figure 4-15**.

For both networks, an increase in benzene loading leads to an overall consistent rise in Q_{cc} for the outer Pake doublet, *i.e.* the benzene-d_6 molecules are becoming more restricted (**Figure 4-15**). Restriction in mobility at higher loadings is a consequence of steric hindrance and increased guest-guest interactions, owing to the benzene molecules being closer in space.

Each loading of benzene inside CMP-2 shows consistently higher Q_{cc} values than those exhibited by the same loadings of benzene inside CMP-1. Such behaviour indicates that the mobility of benzene is much more restricted at all loadings inside CMP-2, compared with CMP-1 (**Figure 4-15**). A decrease in

benzene mobility inside CMP-2 is the result of a lower pore volume and increased interpenetration.

At loadings of 48 and 190 wt% for CMP-1 and 48 wt% for CMP-2, an increase in temperature results in a reduction of the Q_{cc} value for the outer Pake doublet (**Figure 4-15**). This shows that the benzene molecules are able to rotate more freely around the C_6-axis at higher temperatures. At loadings of 570 wt% for CMP-1 and 190 and 570 wt% for CMP-2, the Q_{cc} values are constant for the Pake doublet over all temperatures (*ca.* 180 kHz). This indicates that the pores are completely filled at these loading levels.

A reduction in Q_{cc} values for the inner peak with increasing temperature is observed at loadings of 570 wt% for CMP-1 and 190 and 570 wt% for CMP-2 (**Figure 4-15**). This is indicative of melting on the outer surfaces of the networks.

In the temperature range 203-220 K, a large spike is observed in the Q_{cc} values of the inner peaks in the spectra of CMP-2 with loadings of 190 and 570 wt% benzene (**Figure 4-15**), this a consequence of increased mobility of benzene-d_6 in solid I phase.

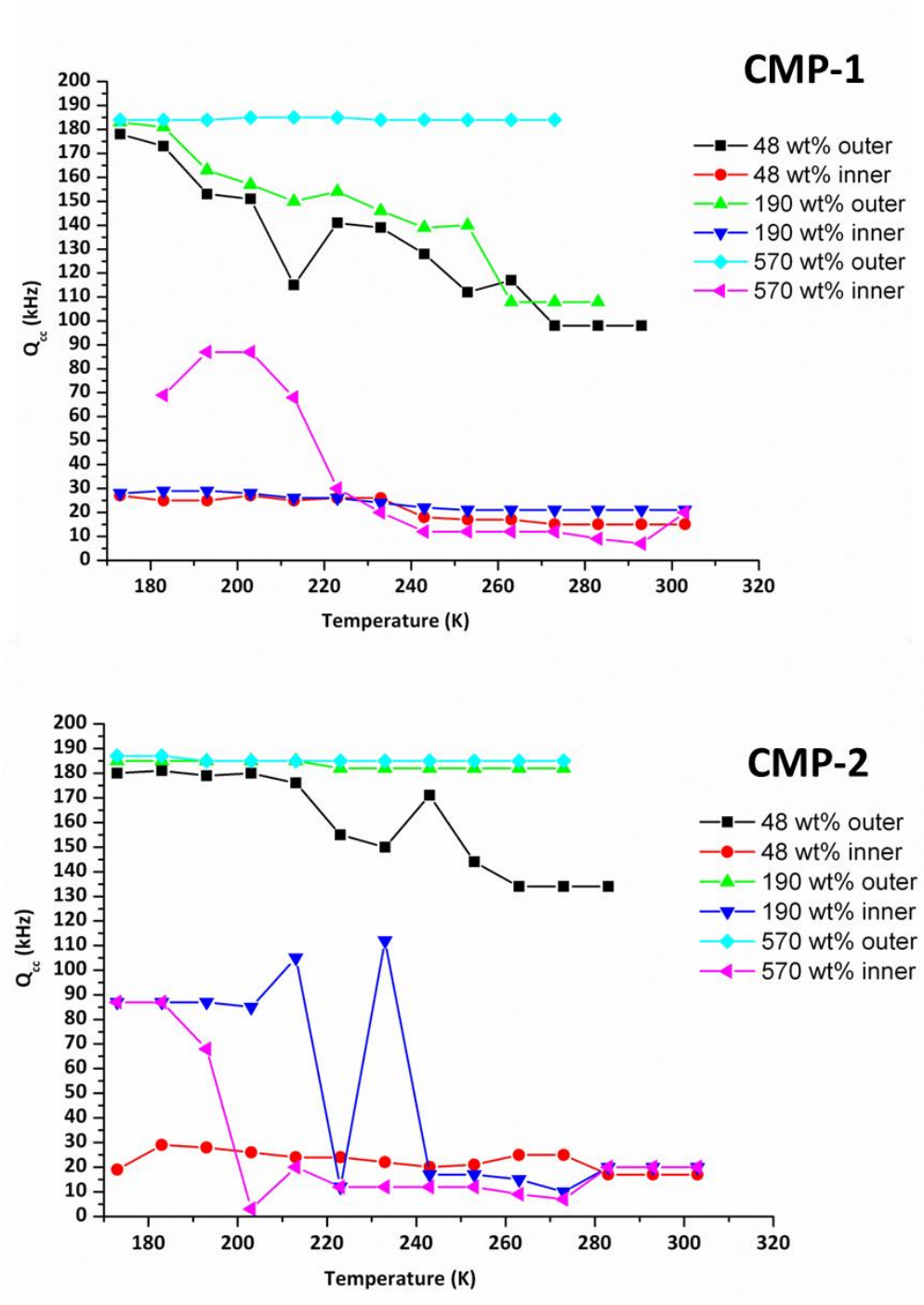

Figure 4-15: Effect of temperature on Q_{cc} derived from ^{2}H NMR spectra for benzene-d_6 inside CMP-1 (top) and CMP-2 (bottom) at three loadings. The large spike in the line corresponding to CMP-2 with a loading of 570 wt% benzene is a result of the transition of benzene molecules from solid I phase to the liquid phase.

The asymmetry parameter (η_Q) also provides further information about guest mobility. The simulated η_Q values from **Table 4-2** to **Table 4-7** were plotted as a function of temperature for both networks in **Figure 4-16**.

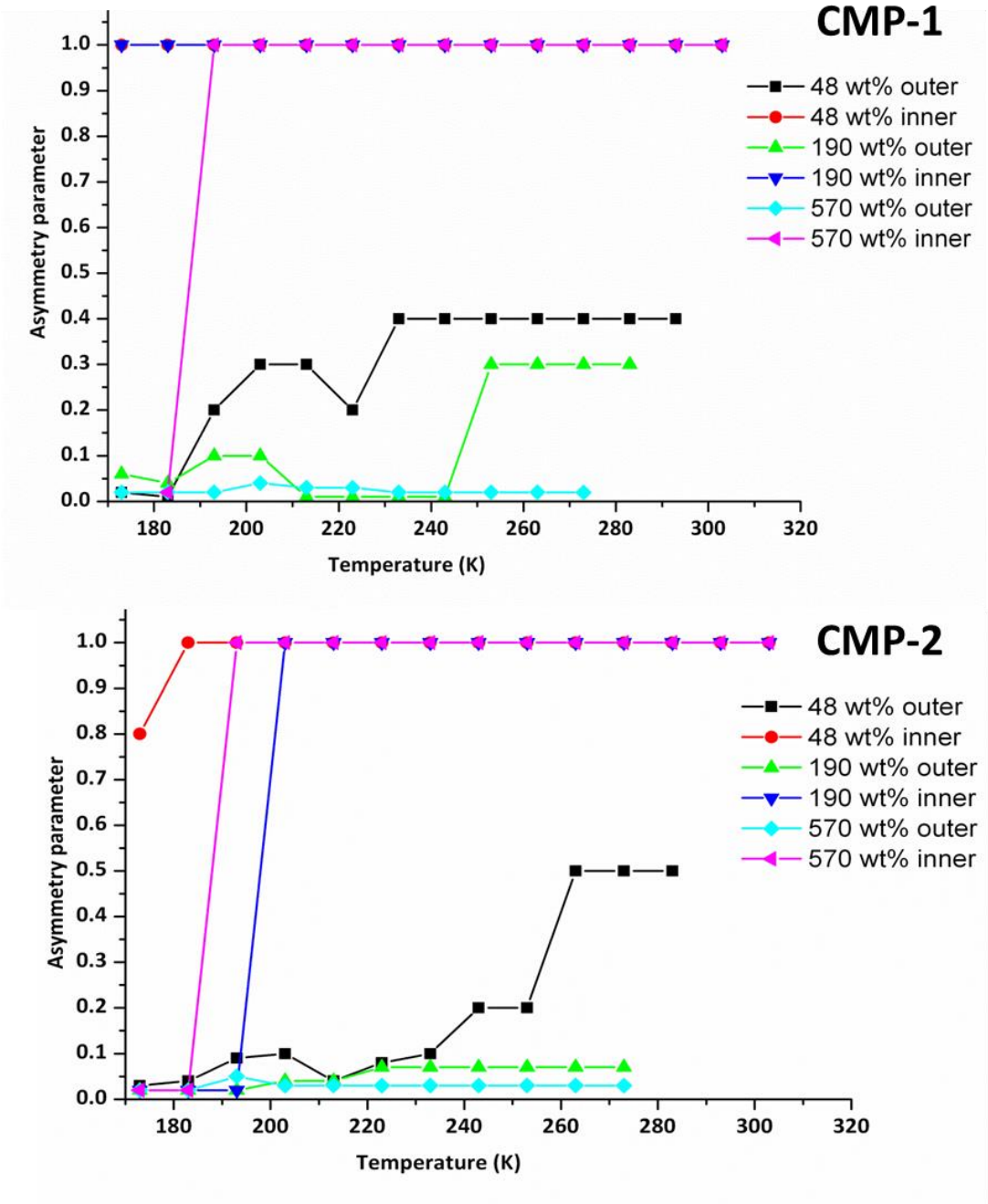

Figure 4-16: Effect of temperature on η_Q derived from ^{2}H NMR spectra for benzene-d_6 inside CMP-1 (top) and CMP-2 (bottom) at three loadings.

At temperatures above 193 K, the inner peak displays a η_Q value of 1.0 for all loadings inside CMP-1 and CMP-2 (**Figure 4-16**). This value is characteristic of benzene molecules undergoing isotropic motion.[120] At temperatures below 193 K, the inner peak of CMP-2 with benzene-d_6 loadings of 190 and 570 wt% displays a η_Q value of *ca*. zero (**Figure 4-16**). This is a consequence of in-plane rotation exhibited by benzene molecules in solid I phase.[120]

For each network and loading, an increase in temperature leads to an increase in η_Q for the outer Pake doublet (**Figure 4-16**). An increase in η_Q can be ascribed to fluctuations or tilting about the benzene ring normal, which are often referred to in the literature as 'wobbling.'[120, 127, 128, 130, 131] Such motions are shown in **Figure 4-17**. Interestingly, for both networks the degree of 'wobbling' is dependent on loading level, *i.e.* as the loading level increases the smaller the 'wobble.' This is a consequence of increased steric hindrance and increased guest-guest interactions, owing to higher occupation of the pores.

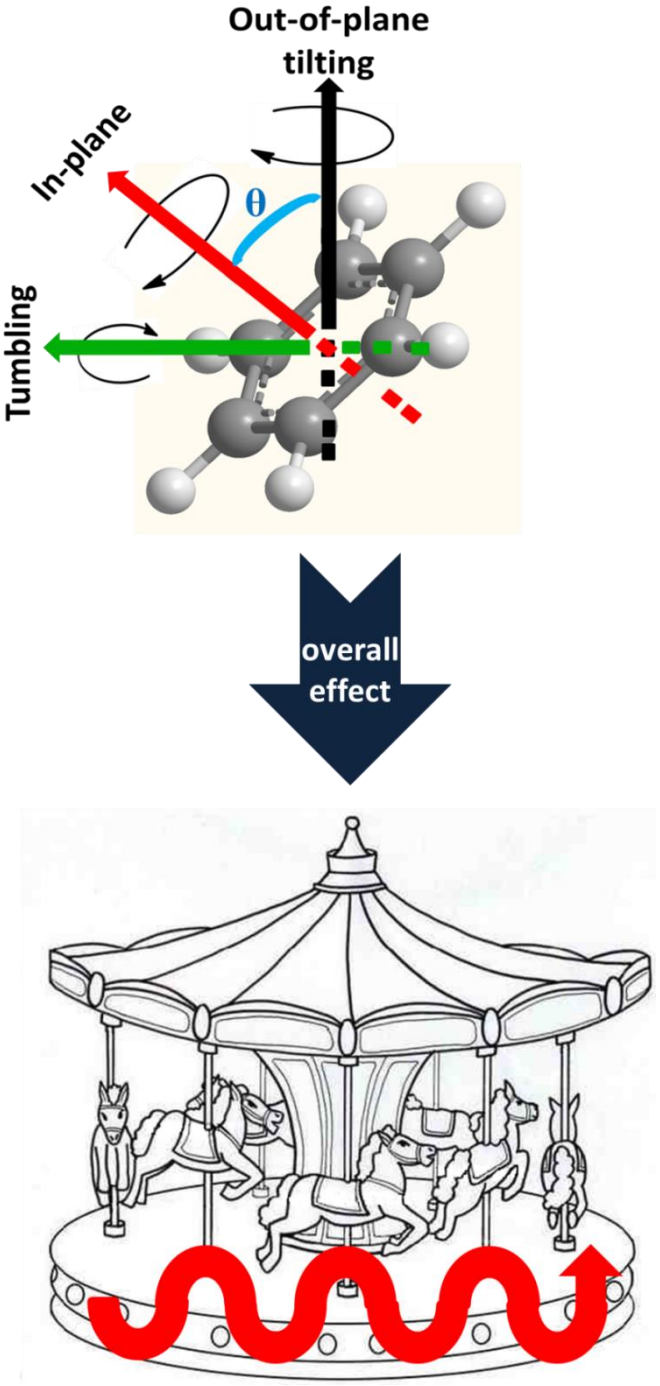

Figure 4-17: Possible orientation vectors for benzene-d_6. In-plane motions involve rotation about the C_6-axis. Out-of-plane tilting occurs when there are slight fluctuations around the ring normal (top). Overall motions exhibited by benzene if $\eta_Q > 0$ (bottom).

4.2.1.2 Summary of the investigation of an adsorbed guest inside CMP networks

In summary, the pore structures of CMP-1 and CMP-2 have been investigated by simulation of ^{2}H NMR spectra of a per-deuterated benzene guest at three loadings.

For each network, a surface confined layer, liquid phase and solid II phase benzene were found to exist within the pores. For CMP-1, an increase in loading level led to a decrease in the ratio of bulk to surface benzene. Such observations are consistent with non-uniform pore filling where a surface layer of benzene is put down across the whole surface of the material before the pores begin to fill. Much less variation was observed in the pore filling of CMP-2, indicative of swollen pores.

Closer inspection of the ^{2}H NMR line shape corresponding to benzene inside CMP-2 with loadings of 190 and 570 wt% revealed the presence of a fourth component ascribed to benzene in solid I phase at temperatures below 183 K. It was not possible to identify benzene-d_6 molecules in solid I phase inside CMP-1 by line shape analysis as the spectra are completely dominated by the Pake doublet.

Analysis of the peak integrals indicates that as the temperature increases the benzene-d_6 molecules are lost from the Pake doublet site and move to the narrow line site. Changes in the peak integrals are gradual, suggesting that the pores of each network are no-longer discrete. It is assumed that the surface confined layer remains constant with temperature for each individual loading as the surface area is constant.

For both networks, the Q_{cc} and η_Q values from the NMR simulation data indicate that the benzene molecules become less mobile with increasing loading level, owing to higher occupation of the pores. These data also show that the mobility of benzene is much more restricted at all loadings inside CMP-2,

compared with CMP-1, as a result of a lower pore volume and increased network interpenetration.

4.2.2 Deuterated CMP networks

By Sonogashira-Hagihara coupling of a commercially available deuterated monomer, it is possible to selectively deuterate two separate sections of a CMP polymer. The first is deuteration of the polymer core (**Route (a)**, **Scheme 4-3**). The second is a deuterated strut (**Route (b)**, **Scheme 4-3**).

Scheme 4-3: Possible routes for CMP deuteration of either the core (a) or the strut (b).

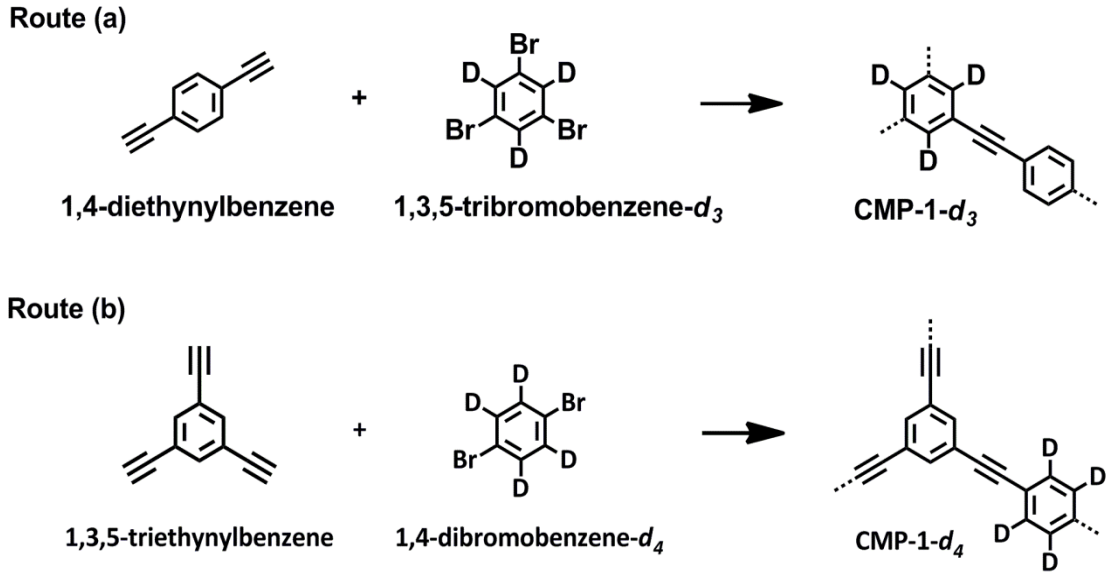

This study focuses upon two CMP networks with a deuterated strut, namely CMP-1-d_4 and CMP-2-d_8 (**Scheme 4-4**). This particular section of the network was deuterated as our previous studies suggest that variation of the strut length affects the sorption properties of these materials.[66]

Scheme 4-4: Structures of deuterated CMP-1 and CMP-2 networks.

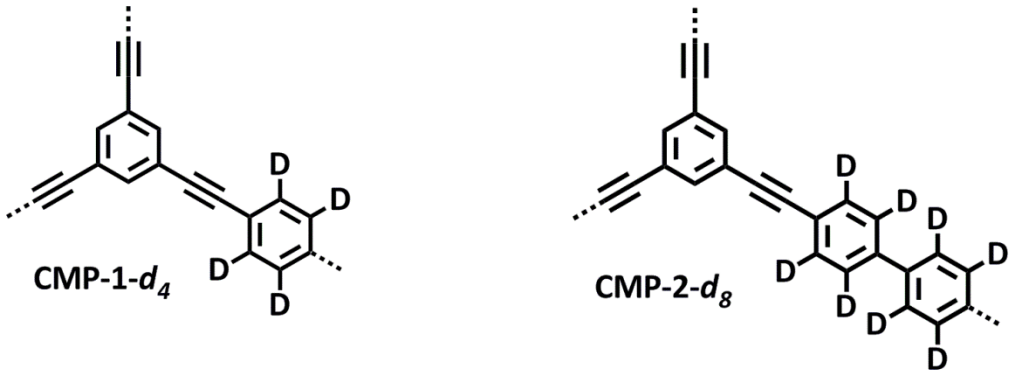

As the deuterated networks are analogues of the original CMP materials, comparisons between the structures and textural properties of deuterated and non-deuterated versions are important.

4.2.3 Structural comparison between deuterated and non-deuterated networks

4.2.3.1 Infra-red spectroscopy

Successful polymerisation was demonstrated by FTIR, as both networks display a polymerised alkyne stretch (R-**C≡C**-R) at approximately 2200 cm^{-1}. Peaks at 1580 cm^{-1} can be ascribed to aromatic (**C=C**) stretches, (**Figure 4-18**). Unreacted alkyne end groups (R-**C≡C**-H) at 2100 cm^{-1}, were also detected in agreement with the original CMP networks.

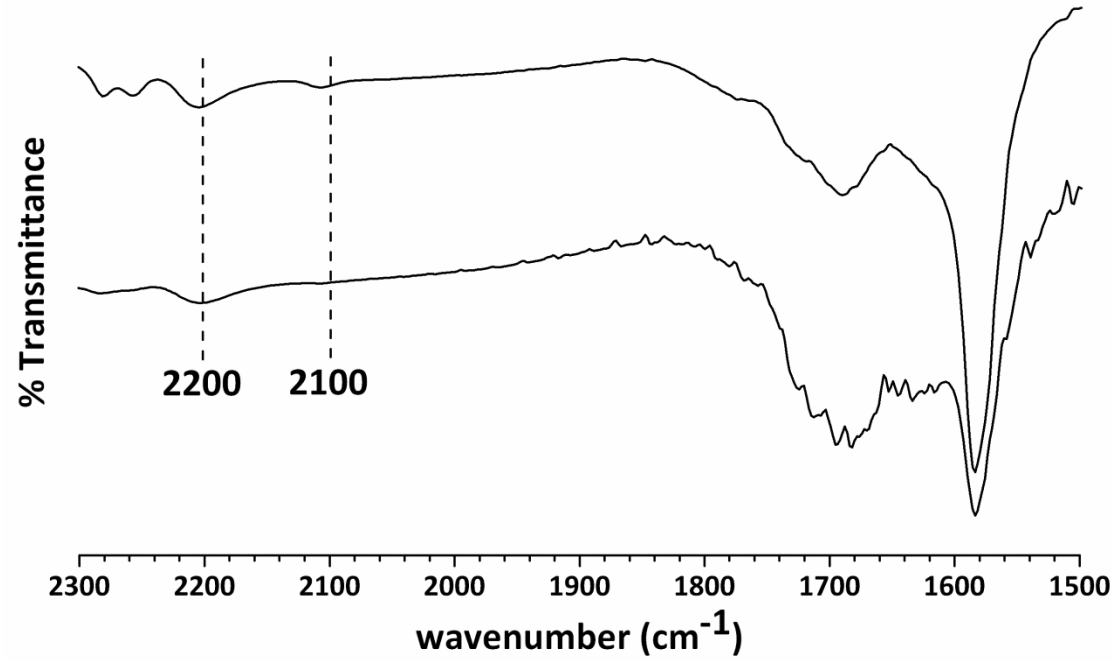

Figure 4-18: FTIR spectra of CMP-1-d_4 (bottom) and CMP-2-d_8 (top).

4.2.4 Solid state NMR

The deuterated materials were analysed at the molecular level using solid-state NMR to confirm network formation and incorporation of the deuterated monomer. The SPE $^{13}C\{^{1}H\}$ MAS NMR spectra are shown in **Figure 4-19**.

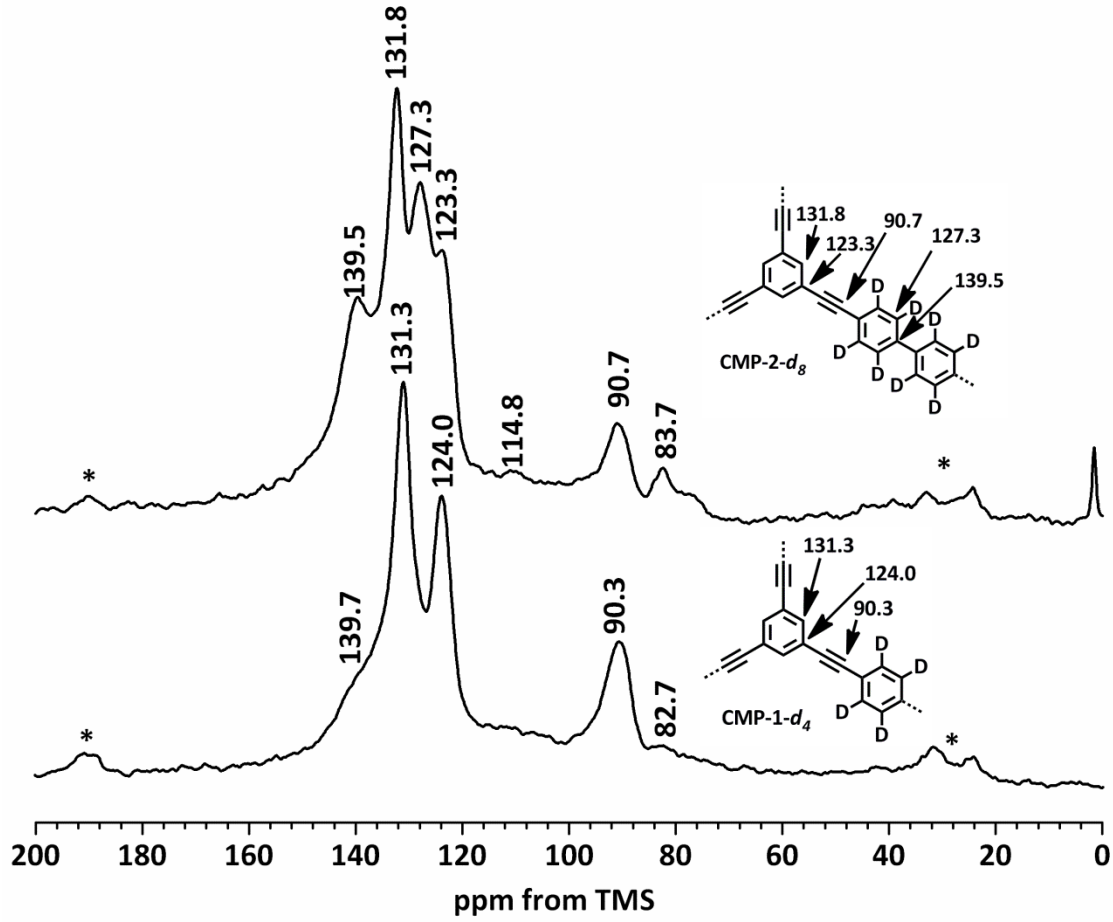

Figure 4-19: SPE $^{13}C\{^1H\}$ MAS NMR spectra of CMP-1-d_4 (bottom) and CMP-2-d_8 (top). Spectra recorded at an MAS rate of 10 kHz. Structures of the networks labelled with peak assignments (inset). Asterisks denote spinning sidebands.

Both networks display peaks corresponding to the aromatic core *ca.* 131 ppm (-$\boldsymbol{C}_{\text{Ar-H}}$) and *ca.* 124 ppm (-$\boldsymbol{C}_{\text{Ar}}$-C≡C-$\boldsymbol{C}_{\text{Ar}}$). An alkyne peak, observed at *ca.* 90 ppm, confirms that polymerisation has been successful. This is in agreement with the FTIR spectra. Resonances at 82.7 and 139.7 ppm in the spectrum of CMP-1-d_4 can be ascribed to alkyne end groups (-C≡$\boldsymbol{C}$-H). Peaks in the spectrum of CMP-2-d_8 at 82.7 and 114.8 ppm, correspond to alkyne and bromine (-$\boldsymbol{C}_{\text{Ar}}$-Br) end groups, respectively. All peaks are consistent with CMP networks synthesised previously.[71]

Energy dispersive X-ray analysis provided further confirmation of the presence of end groups, as levels of 4 and 7 wt% of bromine were found for CMP-1-d_4 and CMP-2-d_8, respectively.

The ^{1}H-^{13}C CP/MAS kinetics curves and fitting parameters (**Figure 4-20** and **Table 4-9**, respectively) of the CMP networks highlight the presence of deuterons within the polymer structures.

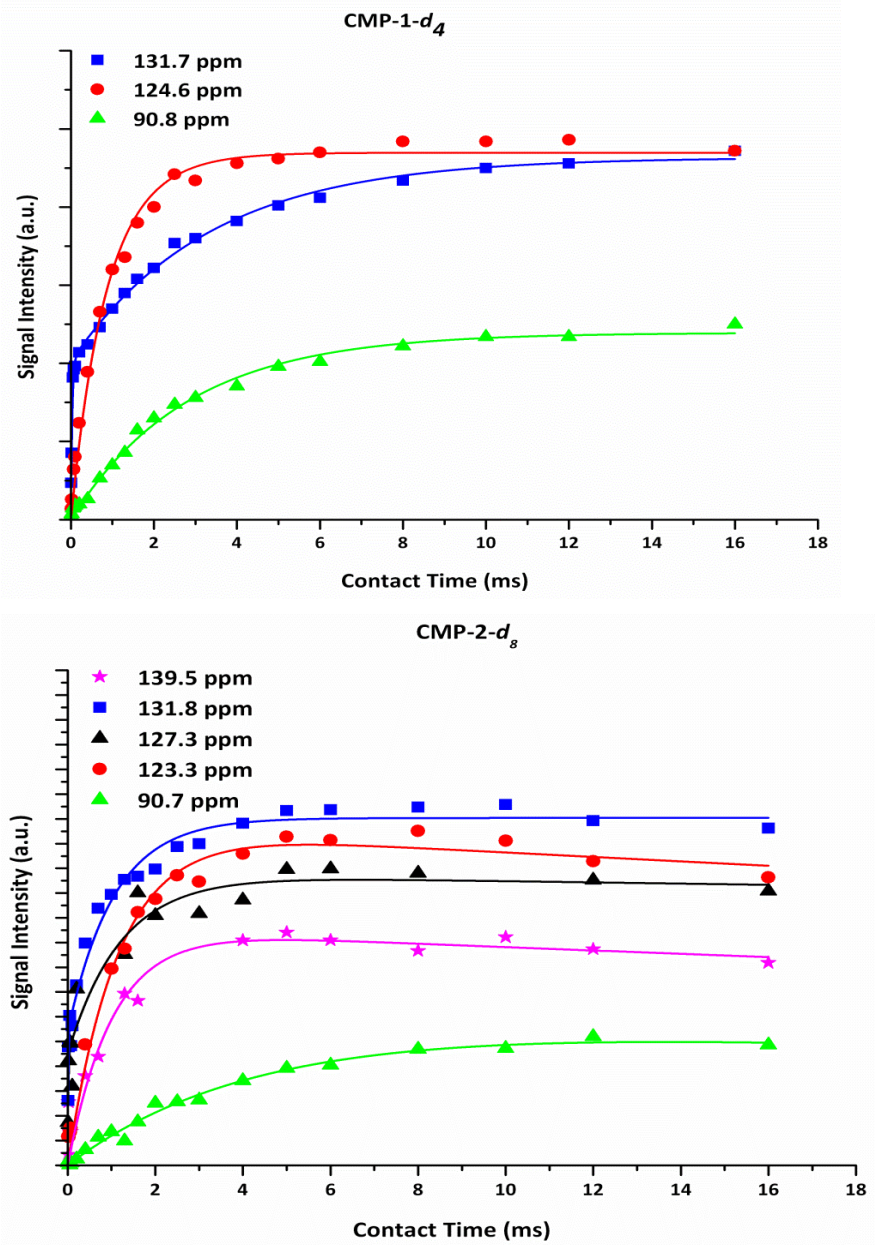

Figure 4-20: ^{1}H-^{13}C CP/MAS kinetics curves for deuterated networks. Corresponding fitting parameters are given in **Table 4-9**.

Table 4-9: ^{1}H-^{13}C CP/MAS kinetics parameters derived from the Classical I-S Model and Two-Component I-S Model used to fit CP kinetics curves in **Figure 4-20**.

Network	^{13}C Site (ppm)	T_{IS} (ms)	$T_{1\rho}^{H}$ (ms)	R^2
CMP-1-d_4	131.8	Fast: 0.03 ± 0.003	3.31 ± 0.02	0.995
		Slow: 3.31 ±0.09	>50	
	124.0	0.88 ± 0.05	>50	0.990
	90.3	2.8 ± 0.1	>50	0.993
CMP-2-d_8	139.5	1.0 ± 0.2	>50	0.936
	131.3	Fast: 0.01 ± 0.003	1.1 ± 0.2	0.974
		Slow: 1.1 ± 0.06	>50	
	127.3	Fast: 0.01 ± 0.007	1.2 ± 0.4	0.915
		Slow: 1.2 ± 0.3	>50	
	123.3	1.1 ± 0.1	>50	0.982
	90.7	4 ± 1	>50	0.988

Non-protonated sites at around 139, 124 and 90 ppm all exhibit a slower CP 'build up' and much longer $T_{1\rho}^{H}$ times compared with the CP kinetics data of the original non-deuterated CMP networks reported by Jiang *et al.*[65, 66, 214] This is consistent with a reduction in the amount of protons within the networks. The carbon site at *ca.* 131 ppm, which is the only site to retain an attached proton in the deuterated networks, only gave satisfactory fittings with a two-component I-S model. This is representative of an inhomogeneous carbon site, in which magnetisation is transferred from protons directly attached to the carbon and protons from areas surrounding the site. As with the other carbon sites, the component corresponding to transfer of magnetisation from surrounding protons has a significantly longer $T_{1\rho}^{H}$ time.

4.2.5 Comparison of textural properties for non-deuterated and deuterated CMP networks

Since the aim of this work is to explore the origins of the physical properties of CMP materials by analysis of deuterated analogues, it is important to assess whether the deuterated networks have the same textural properties.

4.2.5.1 **Thermal stability**

Both deuterated networks exhibited good thermal stability with onset of decomposition above 300 °C as measured by TGA under nitrogen (**Figure 4-21**).

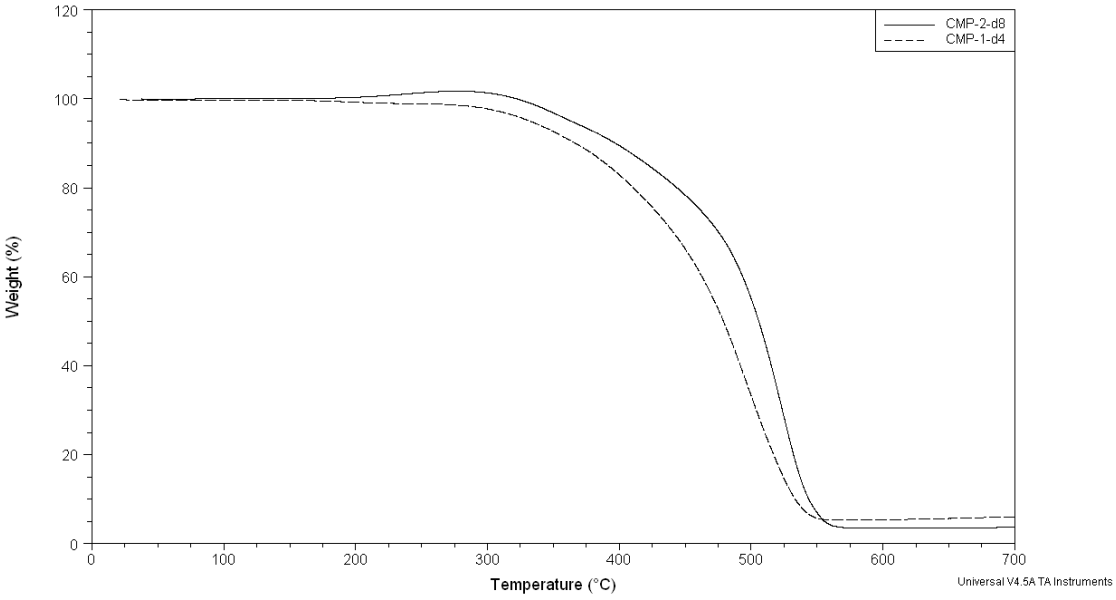

Figure 4-21: TGA curve of CMP-1-d_4 (dotted line) and CMP-2-d_8 (filled line).

The decomposition temperatures are similar to other CMP networks.[65, 66]

4.2.5.2 **Gas sorption properties**

The gas sorption properties were investigated by nitrogen gas adsorption analysis. The gas sorption isotherms are given in **Figure 4-22**.

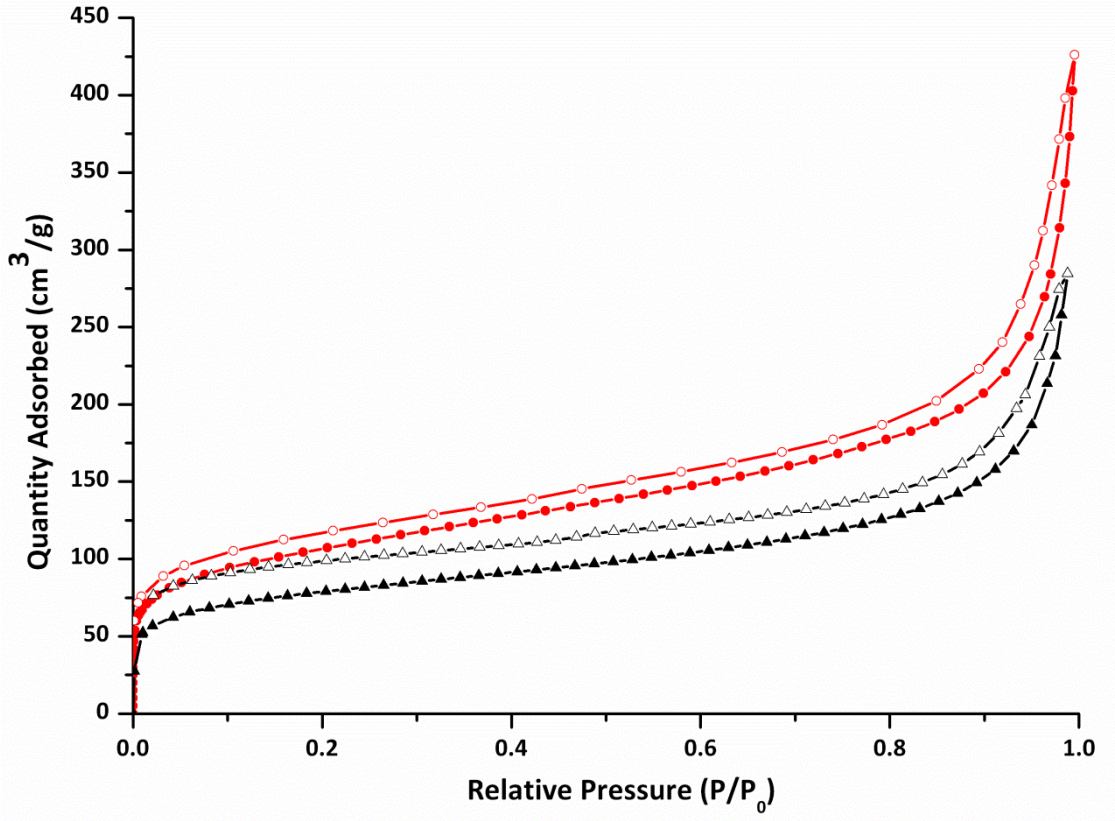

Figure 4-22: Nitrogen adsorption-desorption isotherms collected at 77 K for deuterated networks. CMP-1-d_4 (red) and CMP-2-d_8 (black). Adsorption branch (filled symbols), desorption branch (hollow symbols).

Both networks exhibit Type I isotherms with significant Type IV character, *i.e.* mesoporous characteristics at high relative pressures (**Figure 4-22**), according to IUPAC classifications.[1] The networks also display H4 hysteresis upon desorption. These isotherms are comparable with those reported for other CMP networks synthesised from the bromo-monomers.[71, 100]

The BET surface areas were calculated as 385 and 282 m^2g^{-1} for CMP-1-d_4 (red) and CMP-2-d_8, respectively. The deuterated analogue of CMP-1 also has much more Type IV gas sorption behaviour, indicating a slight difference in microstructure which may possibly be the result of a difference in reactivity or solubility between the non-deuterated and deuterated monomer. Also there is a slight increase of trapped catalyst (EDX analysis of CMP-1-d_4 shows *ca*. 1 wt% trapped catalyst compared to 0.4 wt% for non-deuterated CMP-1).[100] However, the surface area for the deuterated analogue of CMP-2 is in excellent agreement with that reported previously. The pore properties and surface areas of the networks are summarised in **Table 4-10**. Pore size distribution curves of CMP-1-d_4 and CMP-2-d_8 are given in **Figure 4-23** and **Figure 4-24**, respectively.

Table 4-10: Summary of gas sorption data for CMP materials.

Network	SA_{LANG} (m^2g^{-1})[a]	SA_{BET} (m^2g^{-1})[b]	$V_{0.1}$ (cm^3g^{-1})[c]	V_{Tot} (cm^3g^{-1})[d]	$V_{0.1}/V_{Tot}$
CMP-1 brominated[71]	1046	867	0.33	0.99	0.33
dCMP-1	503	385	0.15	0.67	0.22
CMP-2 brominated[71]	231	204	0.28	0.67	0.41
dCMP-2	378	282	0.11	0.44	0.25

[a]Based on full isotherm pressure range 0.02-0.23. [b]Based on full isotherm pressure range 0.05-0.15 [c]Pore volume at $P/P_0 = 0.1$. [d]Total pore volume at $P/P_0 = 0.99$. Data collected at 77 K using N_2 as the sorbate.

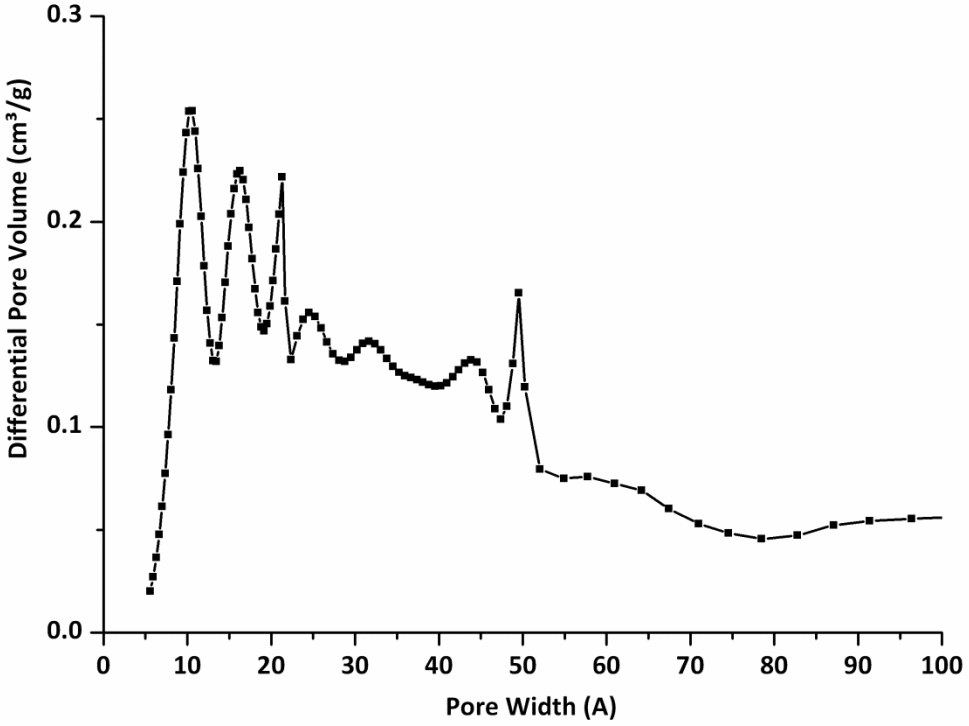

Figure 4-23: NL-DFT pore size distribution curve for CMP-1-d_4. Plotted using the NL-DFT for pillared clay. A limited number of points below 10 Å is the result of a lack of experimental data points at low relative pressure.

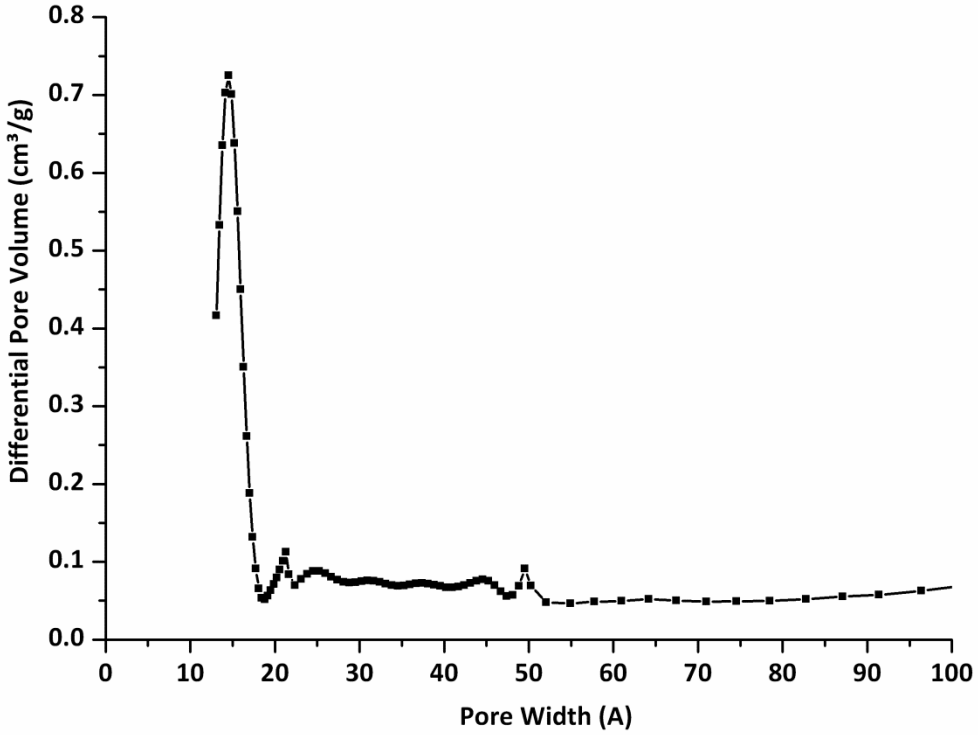

Figure 4-24: NL-DFT pore size distribution curve for CMP-2-d_8. Plotted using the NL-DFT model for pillared clay. A limited number of points below 10 Å is the result of a lack of experimental data points at low relative pressure.

4.2.6 Dynamics of host CMP networks

This section discusses the investigation of network mobility by advanced solid-state NMR techniques.

4.2.6.1 **Solid state deuterium NMR of network motions**

As mentioned in **Section 4.2.2**, this work examines the molecular motions of two CMP networks with a deuterated strut by ^{2}H NMR, with the aim

of giving an overall picture of the origins of flexibility and physical properties for CMPs.

Initially, we focused our study upon the interpretation of static ^{2}H NMR spectra by line-shape analysis (**Figure 4-26** and **Figure 4-27**). A similar method to that used earlier for studying encapsulated deuterated benzene was adopted. All spectra were simulated using DMFit software[223] and found to consist of three Pake doublets, labelled A, B and C according to the representative spectra displayed in **Figure 4-25**.

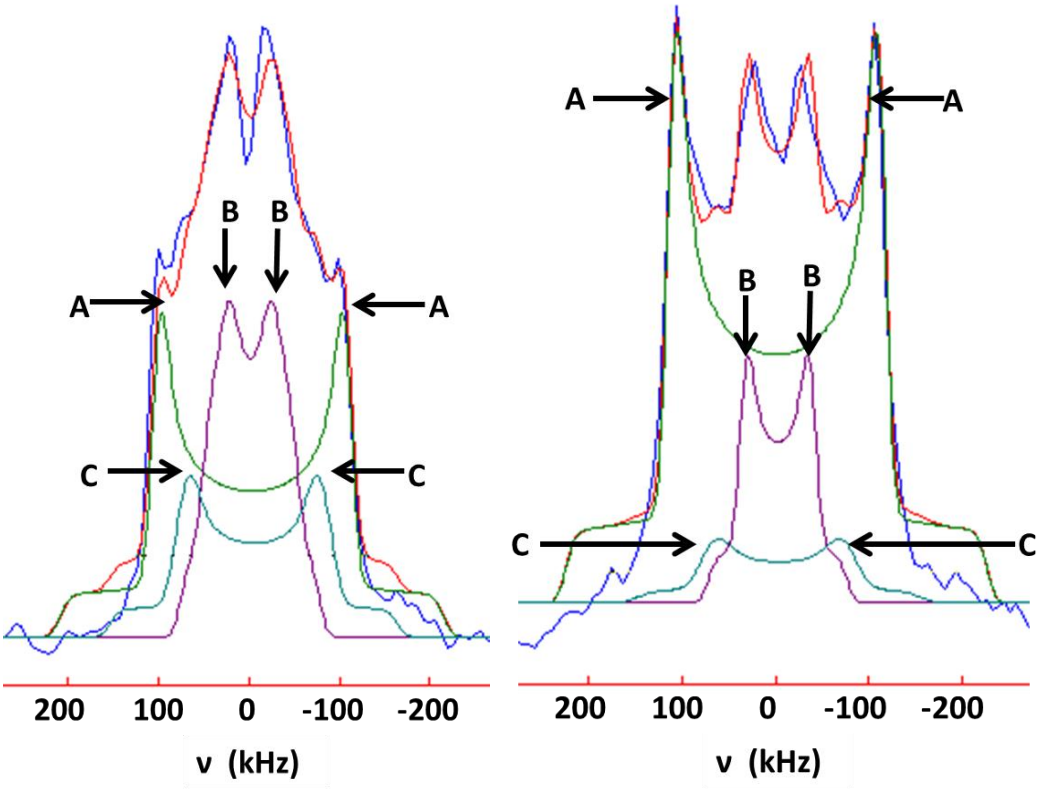

Figure 4-25: ^{2}H NMR spectra of CMP-1-d_4 at 263 K (left) and CMP-2-d_8 at 223 K (right) showing three Pake doublets for the simulated spectra. The Pake doublets, A (green), B (purple), and C (light blue) correspond to the simulated data in **Table 4-11** and Table 4-12 for CMP-1-d_4 and CMP-2-d_8, respectively. Experimental spectrum (dark blue line). Sum of the simulated Pake doublets (red line).

Deuterium NMR spectra containing multiple Pake doublets have been reported previously for phenyl rings in periodic mesoporous organosilica (PMO), a tetraphenylethylene-bridged MOF, poly(phenylalanine), MOF-5, MOCP-L, MIL-47 and MIL-53 (for more information, please see **Table 4-13**).[133, 151-154, 236-239] The presence of multiple Pake doublets in ^{2}H NMR spectra is often dictated by the complexity of the system under investigation. For example MOPC-L materials (with internal defects in their structure due to rapid precipitation of the network during synthesis) display a greater variation in phenyl ring mobility compared to the phenyl groups of MOF-5.[133]

In order to examine the effect of temperature upon the three Pake doublets, variable temperature ^{2}H spectra were collected. The experimental and simulated spectra are shown in **Figure 4-26** and **Figure 4-27**, for CMP-1-d_4 and CMP-2-d_8, respectively. Fitting parameters for the simulated data sets are given after their corresponding spectra in **Table 4-11** and **Table 4-12**.

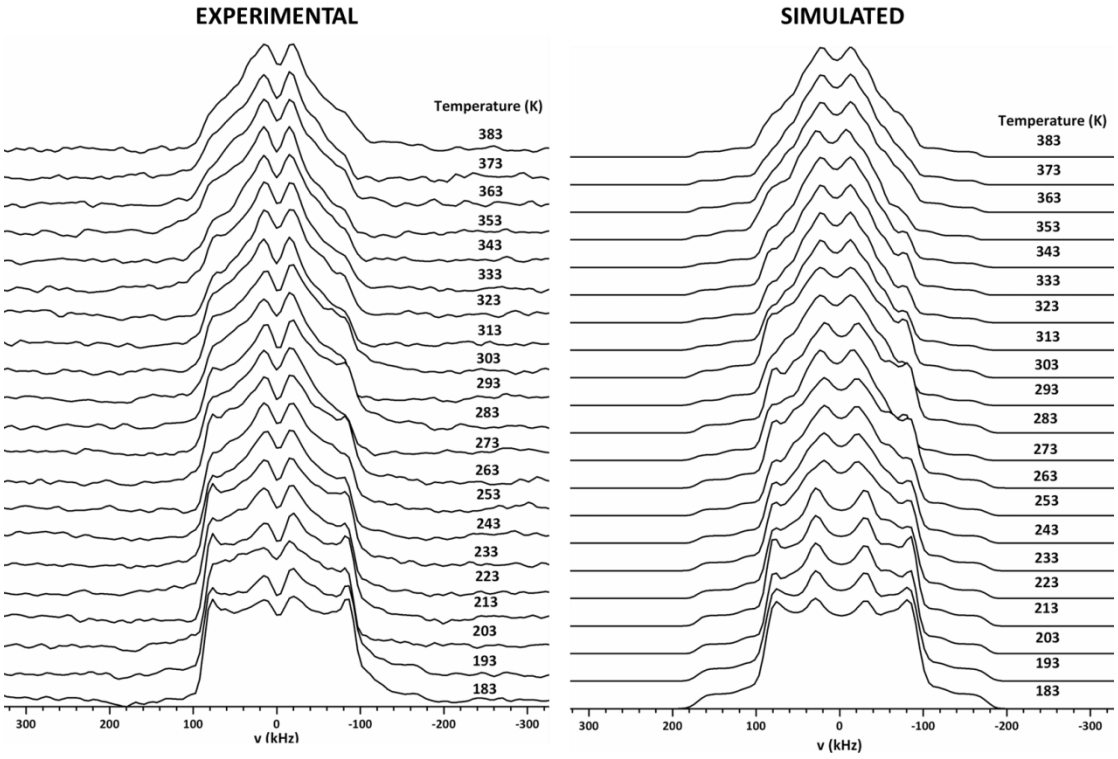

Figure 4-26: Variable temperature ^{2}H NMR spectra of CMP-1-d_4 network.

Table 4-11: Parameters corresponding to simulated ^{2}H NMR spectra for CMP-1-d_4 from **Figure 4-26.**

Temperature (K)	Q_{cc} (kHz)			η_Q		
	Pake doublet			Pake doublet		
	A	B	C	A	B	C
183	173	69	124	0.0	0.2	0.2
193	173	69	124	0.0	0.2	0.2
203	173	69	124	0.0	0.2	0.2
213	173	69	124	0.0	0.2	0.2
223	173	69	124	0.0	0.2	0.2
233	173	64	124	0.0	0.4	0.2
243	173	64	124	0.0	0.4	0.2
253	173	64	129	0.0	0.4	0.1
263	173	64	129	0.0	0.4	0.1
273	171	64	130	0.0	0.4	0.1
283	171	64	130	0.0	0.4	0.1
293	171	64	131	0.0	0.4	0.1
303	171	64	131	0.0	0.4	0.1
313	171	64	131	0.0	0.4	0.1
323	171	64	131	0.0	0.4	0.1
333	171	64	131	0.0	0.4	0.1
343	171	64	131	0.0	0.4	0.1
353	170	64	131	0.1	0.4	0.1
363	170	64	131	0.1	0.4	0.1
373	170	64	131	0.1	0.4	0.1
383	170	64	131	0.1	0.4	0.1

NB: Deconvolution of the peak areas was not carried out as the intensities are misrepresented (see page 190).

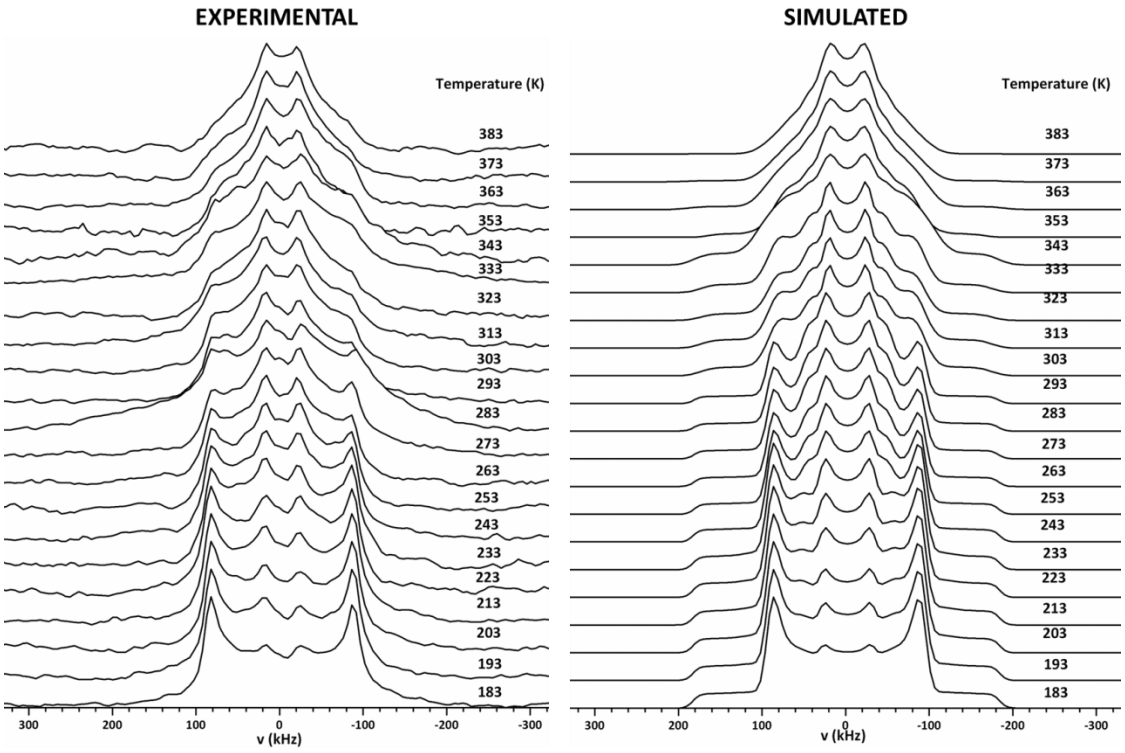

Figure 4-27: Variable temperature ^{2}H NMR spectra of CMP-2-d_8 network.

Table 4-12: Parameters corresponding to simulated ^{2}H NMR spectra for CMP-2-d_8 from **Figure 4-27**.

Temperature (K)	Q_{cc} (kHz)			η_Q		
	Pake doublet			Pake doublet		
	A	B	C	A	B	C
183	182	-	61	0.0	-	0.05
193	184	123	61	0.0	0.05	0.05
203	184	123	61	0.0	0.05	0.05
213	184	123	61	0.0	0.05	0.05
223	184	123	61	0.0	0.05	0.05
233	184	123	61	0.0	0.05	0.05
243	184	97	57	0.0	0.05	0.05
253	182	97	57	0.0	0.05	0.05
263	182	97	57	0.0	0.05	0.05
273	182	97	57	0.0	0.05	0.05
283	182	97	57	0.0	0.05	0.05
293	182	97	57	0.0	0.05	0.05
303	174	97	51	0.0	0.05	0.05
313	174	97	51	0.0	0.05	0.05
323	174	97	51	0.0	0.05	0.05
333	174	97	51	0.0	0.05	0.05
343	182	99	52	0.2	0.3	0.3
353	163	100	52	0.01	0.5	0.3
363	189	100	52	0.10	0.5	0.3
373	189	100	52	0.10	0.5	0.3
383	189	100	52	0.10	0.5	0.3

NB: Deconvolution of the peak areas was not carried out as the intensities are misrepresented (see page 190).

For both networks Pake doublet A displays the largest distance between the horns with quadrupolar coupling constants in the range of 173-170 and 163-189 kHz for CMP-1-d_4 (**Figure 4-26**, **Table 4-11**) and CMP-2-d_8 (**Figure 4-27**, **Table 4-12**), respectively. Such values have been reported in the literature and are attributable to phenyl rings in which the C-D bonds are static[133, 151-153, 236-239] (see **Table 4-13**).

Pake doublet B shows Q_{cc} values in the range 69-63 and 51-60 kHz, for CMP-1-d_4 (**Figure 4-26**, **Table 4-11**) and CMP-2-d_8 (**Figure 4-27**, **Table 4-12**), respectively. Pake doublet C has Q_{cc} values of 124-131 kHz and 96-123 kHz for CMP-1-d_4 and CMP-2-d_8, respectively. The quadrupolar coupling constants for Pake doublets B and C represent rotating phenyl rings. The Q_{cc} values for B and C are lower than that for Pake doublet A owing to averaging of the quadrupolar interaction. However, Q_{cc} values such as those calculated here for B and C are larger than those reported in the literature (see **Table 4-13**), suggesting that the phenyl ring flips of CMP-1 and CMP-2 are more restricted than those exhibited by other porous materials.

Table 4-13: Deuterium NMR parameters for porous and polymeric biological materials.

Phenyl-ring containing system	Q_{cc} (kHz)	Temperature observed (K)	Assignment
$Zn_4O(BDC^*)_3$ (MOF-5)[133]	180	≥173	static C-D
	43	≥173	180° π-flip
MOCP-L[133]	180	≥173	static C-D
	43	≥173	180° π-flip
$VO(BDC^*)$ (MIL-47(V))[237, 238]	170	< 483	static C-D (< 1 kHz flip rate)
$Cr(OH)(BDC^*)(BDC^*)_x(H_2O)_y$ (MIL-53(Cr))[237, 239]	170	≥373	static C-D (< 1 kHz flip rate)
Periodic mesoporous organosilica (PMO)[151]	180	≤353	static C-D
	170	≤353	slow phenyl ring (14 kHz flip rate)
	44	≥216	180° π-flip (10^7 kHz flip rate)
Tetraphenylethylene-bridged MOF[236]	171	≤300	static C-D
	43	≥321	180° π-flip (270 kHz flip rate)
Poly(phenylalanine)[152, 153]	168	≤338	static C-D
	43	≥173	180° π-flip

*BDC = 1,4-benzenedicarboxylate

Another approach for identifying molecular motions involves understanding NMR relaxation times. T_1 relaxation times can provide information about the motional regimes of the system under investigation, such as network rigidity and rate of molecular reorientation (namely correlation time, τ_c). In particular, activation energies can be determined from the Arrhenius equation by plotting the inverse spin lattice relation time as a function of temperature. Once derived, activation energies could be compared with those reported in the literature. Such information could facilitate assignment of the motions corresponding to the Pake doublets in the ^{2}H NMR spectra of CMP-1-d_4 and CMP-2-d_8. For further information on relaxation NMR topics, the reader is referred to **Chapter 2**, **Section 2.1.2.4.2**.

Upon data collection, the T_1 relaxation times were significantly longer than first anticipated. Unfortunately, the variable temperature static ^{2}H NMR spectra were also affected by this result, as the experiments were carried out under similar conditions to the relaxation measurements. Consequently, the static ^{2}H NMR spectra (**Figure 4-26** and **Figure 4-27**) considerably misrepresent the amplitudes of the three different Pake doublets; particularly Pake doublet A, as it corresponds to the motion with the slowest relaxation time. This underestimation is further exaggerated at temperatures below 293 K. Fortunately, both the quadrupolar coupling constants and asymmetry parameters remain unaffected and thus these values are still reliable. In light of this information, T_1 relaxation data for both networks were re-collected under revised conditions.

For both networks, Pake doublets A and B only gave satisfactory fittings with a model containing three different relaxation times (see **Appendix I**), suggesting that each doublet has three different T_1 relaxation components associated with it. Large errors in the data confirm the dispersive nature of the relaxation times and are representative of an inhomogeneous deuterium site in which multiple motions are occurring at the same temperature. As a result of the errors, these data should be treated in a semi-quantitative manner. The presence of multiple relaxation species is not uncommon and has been reported previously

for aromatic polymers and zeolites.[229, 230] The three relaxation times have been labelled T_{1a}, T_{1b} and T_{1c}. The T_1 relaxation data for Pake doublet C are omitted due to poor resolution of ^2H NMR spectra.

Examination of the pre-exponential factors (see **Appendix I**) highlights the contributions of each of the three relaxing species to the overall relaxation curve. The dominant relaxation species fluctuates between T_{1a} and T_{1b} with temperature. While T_{1c} contributes the least amount to the T_1 relaxation curve, it still represents a significant proportion of the networks.

Relaxation times for T_{1a} were found to be remarkably short for both Pake doublet A and B, with values in the range of 0.001 to 0.01 ms (**Appendix I**). Such values would correspond to exceptionally fast motions and thus seem somewhat unrealistic. However T_{1a} may be a consequence of residual quadrupolar relaxation leading to the presence of artefacts in the NMR spectrum.[138] Artefacts can arise when a motion is between the slow and fast limits, where $1/\Delta\nu_Q << \tau_c >> 1/\Delta\nu_Q$.[138] At this intermediate timescale, the NMR signal is not completely averaged (as with the fast and slow limits), resulting in line-shape distortion from spin-spin relaxation (T_2). Distortion is especially prominent if different orientations of the molecule or chain decay with different T_2 rates.[163, 164, 240-245]

The other two relaxation times, T_{1b} and T_{1c} (**Table 4-14**), represent relaxation times over realistic ranges (*i.e.* similar to those reported in the literature)[99, 120, 140, 152-154, 163] and so will be examined in greater detail for both networks. The effect of temperature upon the relaxation values of both networks is shown in **Figure 4-28** and **Figure 4-29**, for T_{1b} and T_{1c}, respectively.

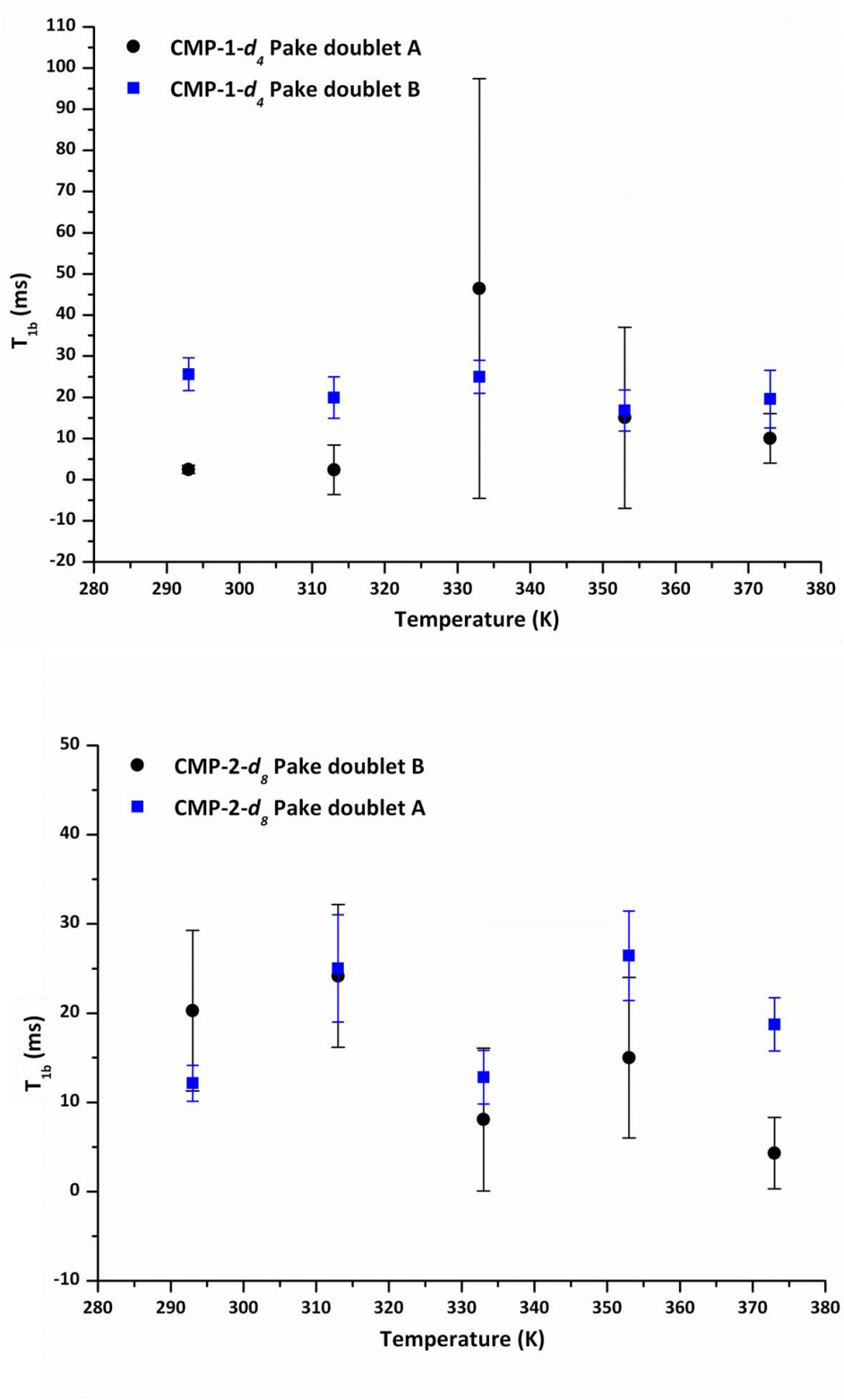

Figure 4-28: ^{2}H T_1 relaxation curves of T_{1b} for networks CMP-1-d_4 (top) and CMP-2-d_8 (bottom) with associated error bars.

Both networks exhibit T_{1b} relaxation times over the range 2 to 46 ms, which correspond to motions with short relaxation times. Such relaxation times are exhibited by discrete molecules[158, 179] and may correspond to mobile aromatic end groups in the CMP network. T_{1b} fluctuates with temperature; however, no correlation between temperature and T_{1b} relaxation time was found (**Figure 4-28**), this might be a consequence of their random orientation within the networks.

T_{1c} displays a much longer relaxation time (in excess of 200 ms) which is comparable to that reported for poly(phenylalanine) (1 second).[133] Unlike T_{1b}, a clear relationship between temperature and T_{1c} relaxation time exists (**Figure 4-29**), *i.e.* as the temperature increases, the relaxation time decreases. Furthermore, the T_{1c} relaxation times of CMP-2-d_8 are approaching the T_1 minimum. The T_1 minimum corresponds a region in between fast and slow motion (a region in which $1 >> \omega_0\tau_c^2$ and $1 << \omega_0\tau_c^2$) on the frequency scale of NMR (for more details, please see **Section 2.1.2.4.2**).[215] The trend in T_{1c} relaxation times displayed in **Figure 4-29** is consistent with a system exhibiting 'solid-like' behaviour (*i.e.* these materials are in the 'slow regime' on the T_1 curve) which is typical of slow tumbling polymers and large biological molecules.[158, 179]

Both CMP-1-d_4 and CMP-2-d_8 show similar T_{1c} relaxation values for Pake A (the outer doublet) in the range 300 - 1300 ms (**Figure 4-29**). Interestingly, the T_{1c} relaxation times of Pake B (inner most doublet) for each network are very different, 340–1400 ms and 220-350 ms, for CMP-1-d_4 and CMP-2-d_8, respectively. These data show that the relaxation times corresponding to the phenyl ring flipping motions of CMP-1-d_4 are longer than those exhibited by CMP-2-d_8. This behaviour suggests the structure of CMP-1 is more extended and thus motionally constrained than that of CMP-2 (the materials are in the slow motional regime where longer relaxation times represent larger polymeric structures, see **Figure 2-20**). These results are in good agreement with those reported previously where CMP-1 was found to be more poly-condensed than

CMP-2 as a result of greater solubility of starting monomers in the reaction solvent.[71, 100]

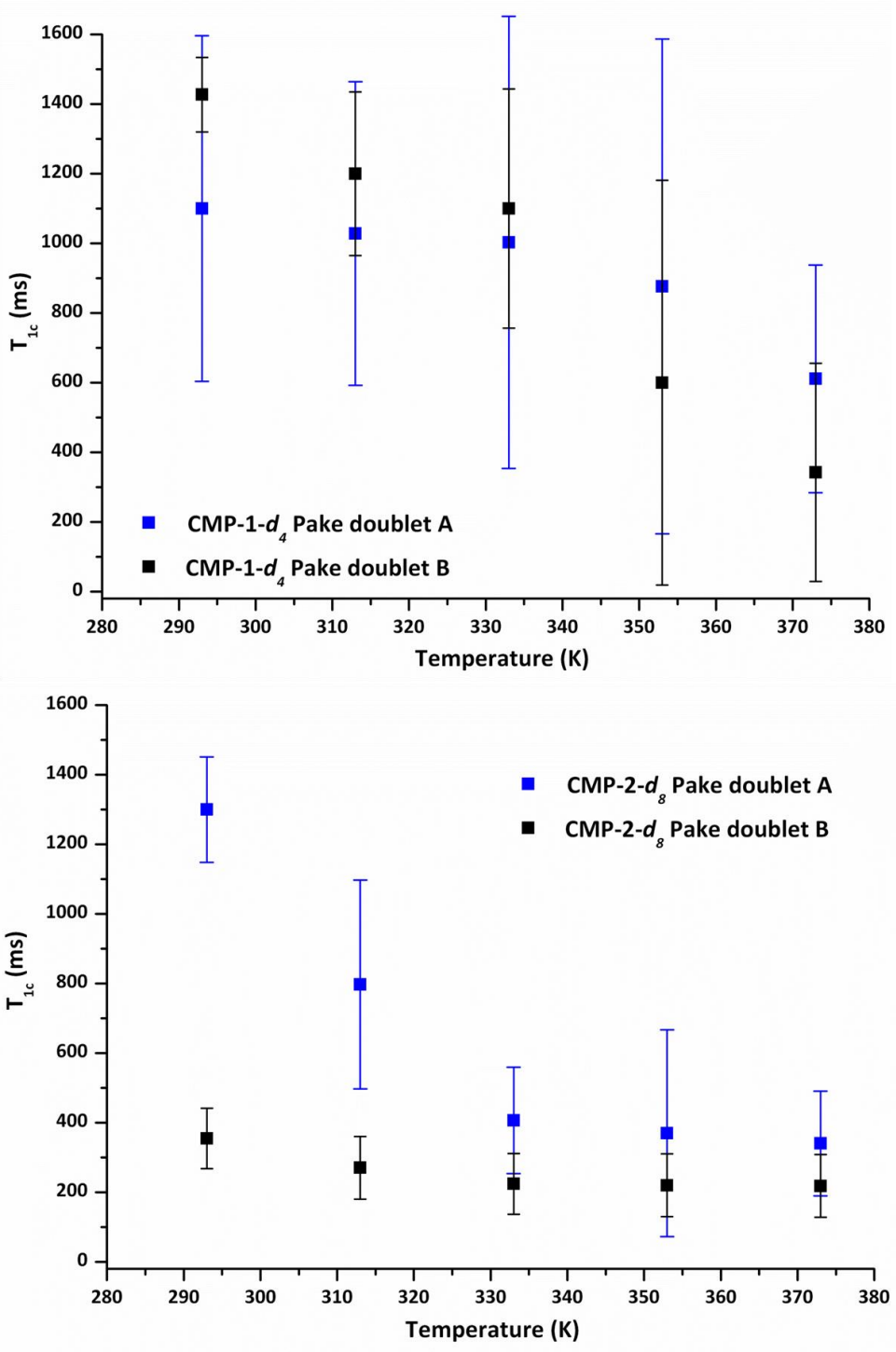

Figure 4-29: ^{2}H T_1 relaxation curves of T_{1c} for networks CMP-1-d_4 (top) and CMP-2-d_8 (bottom) with associated error bars.

As mentioned earlier, additional information can be gathered from relaxation data, particularly activation energies. Such information could be used to explain the differences between the relaxation times of the networks and would enable a comparison with the literature. However, in order to derive a realistic Arrhenius plot, relaxation parameters are required at many temperature intervals. Additionally, the errors associated with the T_1 relaxation behaviour should be minimal as any discrepancies in the fitting parameters are magnified on the logarithmic scale. Unfortunately, the errors calculated in the T_1 relaxation data for deuterated CMP-1 and CMP-2 networks are well above the 4 % margin recommended in the literature.[229] Furthermore, as the relaxation times for these networks are so long, they are beyond the limits of reasonable measurement, as a consequence reliable Arrhenius plots are yet to be achieved for these materials.

4.2.6.1.1 **Solid state deuterium NMR of swollen CMP-1**

In order to examine the effect of swelling upon the motions of CMP-1, variable temperature ^{2}H spectra were collected for CMP-1-d_4 with 570 wt% absorbed benzene. The experimental and simulated spectra are shown in **Figure 4-30**. Fitting parameters for the simulated data are given in **Table 4-14**.

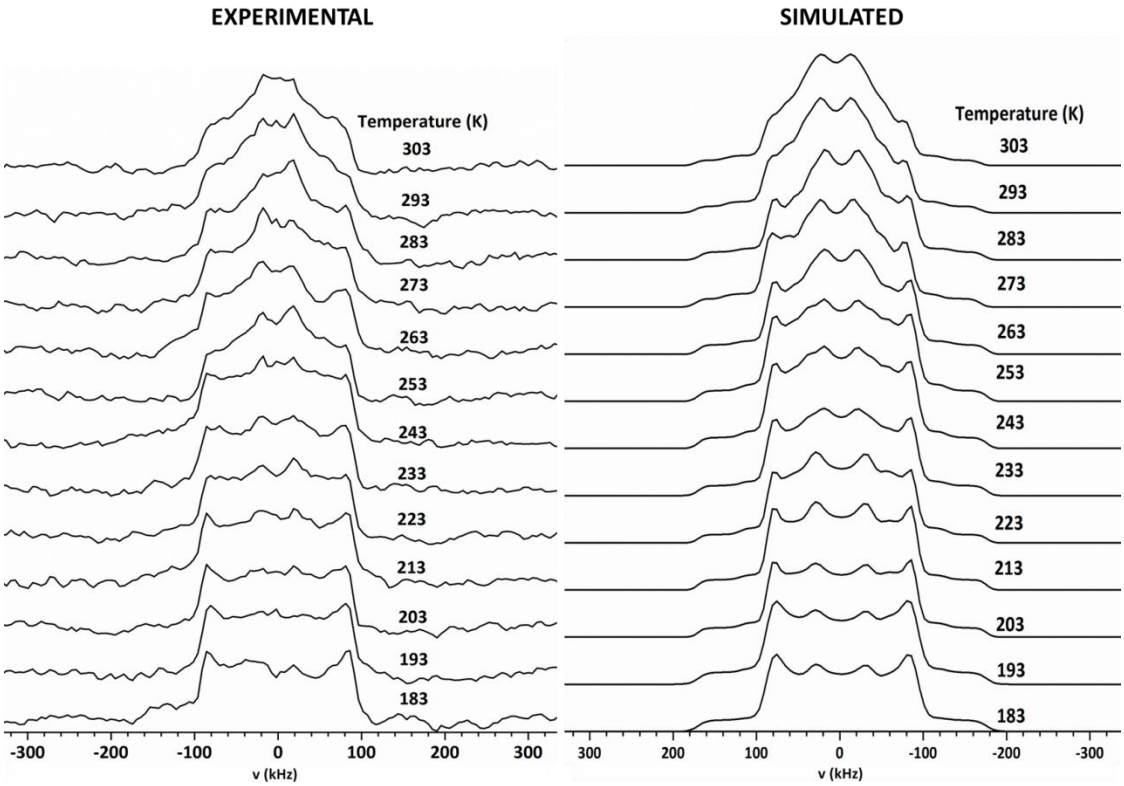

Figure 4-30: Variable temperature ^{2}H NMR spectra of CMP-1-d_4 network containing 570 wt% benzene.

Table 4-14: Parameters corresponding to simulated ^{2}H NMR spectra for swollen CMP-1-d_4 from **Figure 4-30**.

Temp. (K)	Q_{cc} (kHz)			η_Q		
	Pake doublet			Pake doublet		
	A	B	C	A	B	C
183	173	69	124	0.0	0.2	0.2
193	173	69	124	0.0	0.2	0.2
203	173	69	124	0.0	0.2	0.2
213	173	69	124	0.0	0.2	0.2
223	173	69	124	0.0	0.2	0.2
233	173	64	124	0.0	0.4	0.2
243	173	64	124	0.0	0.4	0.2
253	173	63	130	0.0	0.4	0.1
263	173	63	130	0.0	0.4	0.1
273	171	63	130	0.0	0.4	0.1
283	171	63	130	0.0	0.4	0.1
293	171	63	131	0.0	0.4	0.1
303	171	63	131	0.0	0.4	0.1

The variable temperature static ^{2}H NMR spectra of swollen CMP-1-d_4 (**Figure 4-30**) were collected prior to the realisation of the considerably long relaxation times exhibited by the network. Unfortunately, due to time restrictions these data could not be re-collected. Therefore, the static ^{2}H NMR spectra displayed in **Figure 4-30** misrepresent the intensities of the Pake doublets; hence these data have been omitted from **Table 4-14**.

However, as with the previous spectra of CMP-1-d_4, the quadrupolar coupling constants and asymmetry parameters are unaffected, therefore comparisons between these parameters for the non-swollen (**Figure 4-26** and **Table 4-11**) and swollen network (**Figure 4-30** and **Table 4-14**) are still possible. Interestingly, the quadrupolar coupling constant and asymmetry parameters

displayed by the non-swollen and swollen CMP-1 networks are very similar. These results indicate that the presence of benzene guest has no effect upon the type of motions exhibited by the CMP-1 network. Such behaviour is consistent with that reported for phenyl groups in periodic mesoporous organosilica[151] and MOF-5. However, the ratio of peak intensities corresponding to static and mobile phenyl groups within the PMO material were greatly affected by the presence of guests. Therefore, in order to fully assess the effect of swelling upon the motions of CMP networks, examination of the ratio of peak intensities of the Pake doublets is required.

4.3 Conclusions and outlook

In summary, the origins of network flexibility, swelling and porosity for CMP-1 and CMP-2 were investigated using solid state deuterium NMR.

The pore structures of CMP-1 and CMP-2 were examined by simulation of ^{2}H NMR spectra of an adsorbed per-deuterated benzene guest at three loadings. At all low loadings the pores of CMP-1 and CMP-2 are swollen and the mobility of benzene is restricted. For each network, a surface confined layer, liquid phase and solid II phase benzene were found to exist within the pores. Closer inspection of the ^{2}H NMR line shape corresponding to benzene inside CMP-2 with loadings of 190 and 570 wt% revealed the presence of a fourth component ascribed to benzene in solid I phase at temperatures below 183 K.

Framework flexibility was investigated by selective deuteration of phenyl rings within the struts of each network. Deuterium line shape analysis revealed the presence of three Pake doublets corresponding to static phenyl rings and two mobile phenyl rings undergoing 180° π-flips. The quadrupolar coupling constants associated with these Pake doublets were larger than those reported for phenyl groups in other porous frameworks, suggesting that the rate of flipping motion is much slower in the CMP networks. Relaxation NMR provided information about the motional regimes of the networks. Both materials exhibit

long relaxation times (up to 1.3 s) which decrease with increasing temperature. This behaviour corresponds to the slow motional regime and is characteristic of polymeric frameworks and large biological molecules.[158, 179] A faster component was also identified which may correspond to mobile end groups.

Further investigations of the benzene-CMP host-guest system could involve collection of benzene-d_6 deuterium relaxation NMR data. Relaxation data can be used to derive activation energies for melting of benzene within the pores of CMP-1 and CMP-2 and would enable a comparison with similar systems in the literature.

During the ^{2}H NMR analysis, a surface-confined layer, liquid benzene and bulk benzene were found to exist within the pores. Potential methods of identifying the proximity and interactions between the surface confined layer of benzene and polymer pore wall may include triple resonance (^{1}H-^{13}C-^{2}H) NMR or ^{1}H-^{2}H CP/MAS NMR. This information would be useful in developing CMP networks as selective sorbents by chemical modification of the pore wall.

The study detailed in this work could be repeated for the adsorption of other deuterated guest molecules, such as toluene, chloroform and methanol. Such information would allow examination of the effect of guest polarity and structure upon the swelling capabilities of CMP-1 and CMP-2.

In order to provide further information on the effect of benzene upon network mobility, analysis of the ratio of peak integrals in the deuterium NMR spectra of the swollen networks could be carried out. However, owing to the long relaxation times, data collection would be time-consuming.

Finally, additional investigations of un-swollen network motions could involve collecting deuterium spectra at higher temperatures as the CMP networks exhibit high thermal stability. High temperature NMR work would provide two main advantages, relaxation times decrease with increasing temperature enabling faster collection of data, and an increase in the number of data points may allow Arrhenius plots to be derived.

Chapter 5:

Microporous Organic Polymers from Di-functional Monomers

This work has been published in Polymer Chemistry as, "Branching out with aminals: microporous organic polymers from di-functional monomers" Andrea Laybourn, Robert Dawson, Rob Clowes, Jonathan A. Iggo, Andrew I. Cooper, Yaroslav Z. Khimyak and Dave J. Adams, *Polymer Chemistry*, **2012**, *3*, 533-537.

5.1 Introduction to imine and aminal-containing microporous organic polymers

A considerable disadvantage of MOPs is the cost of their synthesis. For example, the first CMPs were obtained *via* Sonogashira-Hagihara coupling reactions using palladium and copper catalysts.[65] Similarly, the syntheses of PAF-1 and PPN-4 require stoichiometric quantities of nickel.[80, 83] It would therefore be advantageous to develop methodologies that use cheap monomers and do not require metal catalysts. A potential cost-effective route to MOPs is the use of amines and aldehydes as monomers.[90] Indeed, the synthesis of MOPs *via* the poly-condensation of aldehydes and amines has been demonstrated. In 2009, Yaghi *et al.* reported a polyimine (or poly(azomethine)) network, COF-300, synthesised from the reaction between terephthaldehyde and tetra(4-anilyl) methane, *i.e.* an $A_2 + B_4$ monomer combination.[30] COF-300 exhibited a SA_{BET} of 1360 m^2/g and was found to be crystalline. Crystallinity was ascribed to the formation of imine bonds under reversible reaction conditions. Recently, Pandey *et al.* reported the synthesis of imine-linked microporous polymer frameworks (POFs) with SA_{BET} up to 1521 m^2/g.[89] Various solvents were studied in order to achieve the highest surface areas. *N*-Methyl-2-pyrrolidone (NMP), DMF and DMSO were reported to give the highest surface area materials, while mesitylene and 1,4-dioxane led to a reduction in surface area. The effect on surface area was ascribed to the polarity of the solvent, with low polarity solvents leading to premature precipitation of the imine oligomers before cross-linking could occur.[246] More recently, porphyrin-[247] and furan-based[88] imine-linked polymers and have been reported. Another route to MOPs by exploiting the reaction of aldehydes with amines is the synthesis of Schiff base networks, from reaction between melamine and various aldehydes ($A_3 + B_3$ or $A_3 + B_4$ monomer combinations) in DMSO.[90] The resulting networks, with SA_{BET} of up to 1377 m^2/g, did not contain any imine bonds, but were instead linked by aminal

moieties. Aminal formation resulted from secondary attack of the imine bonds that were formed by melamine.

A different route to reduce the cost of MOPs is to use only A_2 and B_2 monomer combinations, since these are commercially available and often cheaper. However, synthesis of polymers from A_2 + B_2 combinations usually results in the formation of linear structures. Linear polymers are predominantly non-porous, as they do not possess permanent free space between their chains. Linear polymers of intrinsic microporosity (PIMs), are an exception here, since they can be microporous (SA_{BET} of up to 1064 m^2/g).[7, 248-250] For PIMs, porosity arises as a result of inefficient packing of the polymers in the solid-state. For badly packing microporous linear polymers, rigid monomers are essential, and monomers with permanently twisted geometries, such as spiro-linkages, are often chosen.[95, 251]

This study shows that by taking advantage of aminal formation, it is possible to synthesise MOP networks *via* one-pot poly-condensation reactions between A_2 + B_2 aldehyde and amine monomers.

5.2 Experimental

5.2.1 Synthesis section

5.2.1.1 Materials

All chemicals and solvents were obtained from Sigma-Aldrich and used as received. Anhydrous grade 1,4- dioxane (Aldrich) was used. All chemicals had a purity of 97 % or greater.

5.2.1.2 Preparation of glassware and equipment

All reactions were carried out in sealed dry thick-walled vials (40 mL) in an oven.

5.2.1.3 Synthesis of PI networks

The networks were synthesised using a procedure similar to that reported for COF-300.[30] Typically, terephthaldehyde (134 mg, 1.0 mmol), 2,6-diaminopyridine (109 mg, 1.0 mmol), and anhydrous 1,4-dioxane (10.0 mL) were mixed in a thick-walled (40 mL) sample vial. The contents of the vial were swirled to promote the monomer dissolution. Next, acetic acid (2.0 mL, 3 M) was added. The sealed container was placed in an oven and heated to 120°C for 72 hours. After cooling, the solid residue was removed by filtration and washed sequentially on the filter with 1,4-dioxane (20 mL), methanol (20 mL) and THF (20 mL). The solid was then Soxhlet extracted using THF for 12 hours and dried in a vacuum oven for 24 hours to afford the final polymer network. Example data for network **PI-1** (see **Scheme 5-1**). Average yield: 195 mg (94.0 %, assuming only imine formation). Elemental Analysis: Observed (%): C, 61.62; H, 4.96; N, 17.59. Assuming an ideal polyimine network (see Scheme 2), $C_{13}H_9N_3$ requires (%): C, 75.35; H, 4.38; N, 20.27. Assuming an ideal polyaminal network (see Scheme 2), $C_{18}H_{16}N_6$ requires (%): C, 68.34; H, 5.10; N, 26.56. Discrepancies between predicted and actual values are common for porous materials due to the presence of end groups and adsorbed water and gases.[90]

5.2.1.3.1 **Synthesis of small molecule analogue**

Scheme 5-1: Reaction used to synthesise small molecule analogue **A-1** of **PI-1.**

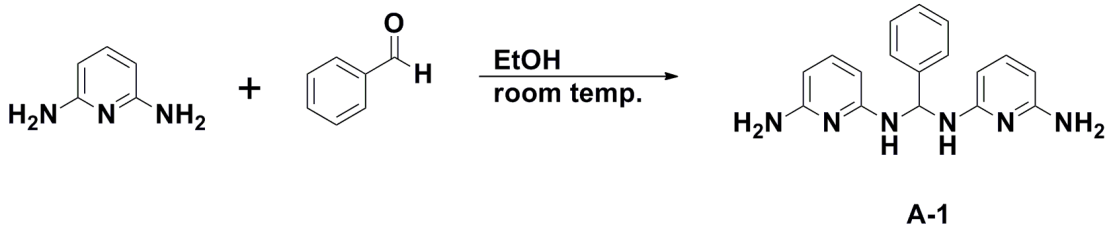

A-1

The small molecule analogue **A-1** (**Scheme 5-1**) was synthesised using a similar procedure to that reported previously.[252] To a stirred solution of 2,6-diaminopyridine (109 mg, 1.0 mmol) in ethanol (anhydrous, *ca.* 10 mL) was added drop-wise a solution of benzaldehyde (0.20 mL, 2.0 mmol) in ethanol (anhydrous, 13.0 mL). The reaction mixture was heated to 80 °C for 3 hours. After this time, the solvent was removed *in vacuo* and the crude product was recrystallised. Compound **A-1** was obtained as a dark yellow solid. Yield: 152.8 mg, 49.9 %. Dissolution of **A-1** in $CDCl_3$ led to hydrolytic cleavage of the aminal bond, resulting in peaks corresponding to the amine and aldehyde starting materials in solution NMR. Elemental Analysis: Observed (%):C, 74.67; H, 5.58; N, 15.58. Required C, 66.65; H, 5.92; N, 27.43 (assuming only aminal formation occurs). Required C, 79.98; H, 5.30; N, 14.73 (assuming only imine formation occurs). FTIR (KBr discs) cm^{-1}: 3449 (-N-H amine, broad), 3385 (-N-H aminal, broad), 1630 (-C=N- imine, sharp).

5.2.2 Characterisation conditions

5.2.2.1 Gas sorption analysis

Polymer surface areas and pore size distributions were measured by nitrogen adsorption and desorption at 77.3 K using a Micromeritics ASAP 2420 volumetric adsorption analyser. Data were collected either by Dr. Robert Dawson or Mr. Robert Clowes. The surface areas were calculated in the relative pressure (P/P_0) range from 0.01 to 0.10. Pore size distributions and pore volumes were derived from the adsorption branches of the isotherms using the non-local density functional theory (NL-DFT) pore model for pillared clay with cylindrical pore geometry, as these were found to give the best fit. Samples were degassed at 120 °C for 15 h under vacuum (10^{-5} bar) before analysis.

Carbon dioxide isotherms at 273 K were measured using a Micromeritics ASAP 2050 while carbon dioxide and nitrogen isotherms at 298 K were measured using a Micromeritics ASAP 2020. Data were collected by either Dr. Robert Dawson or Mr. Robert Clowes. Both analysers were fitted with a chiller/circulator to maintain a constant temperature. Carbon dioxide isosteric heats were calculated using the DataMaster 4.03 software provided by Micromeritics.

5.2.2.2 FTIR

IR spectra were collected as KBr pellets using a Bruker Tensor 27 spectrometer.

5.2.2.3 **SEM**

High-resolution imaging of the network morphology was collected using a Hitachi S-4800 cold field emission scanning electron microscope (FE-SEM) by Dr. Robert Dawson. The dry samples were prepared on 15 mm Hitachi M4 aluminium stubs using either silver dag or an adhesive high-purity carbon tab. The samples were then coated with a 2 nm layer of gold using an Emitech K550X automated sputter coater. The FE-SEM measurement scale bar was calibrated using certified SIRA calibration standards. Imaging was conducted at a working distance of 8 mm and a working voltage of 3 kV using a matrix of upper and lower secondary electron detectors.

5.2.2.4 **Solid-state NMR**

The spectra were measured on a Bruker Avance DSX 400 spectrometer operating at 100.61 MHz for ^{13}C, 400.13 MHz for ^{1}H and 40.54 MHz for ^{15}N. Samples were packed into zirconia rotors 4 mm in diameter.

5.2.2.4.1 **^{1}H-^{13}C CP/MAS NMR**

^{1}H-^{13}C cross-polarization magic angle spinning (CP/MAS) NMR experiments were carried out at an MAS rate of 10.0 kHz. The ^{1}H $\pi/2$ pulse was 3.4 μs and two-pulse phase modulation (TPPM) decoupling[166] was used during the acquisition. The Hartmann-Hahn condition was set using hexamethylbenzene. The spectra were measured using a contact time of 2.0 ms and a relaxation delay of 10.0 s. Typically, 600 scans were accumulated. The values of the chemical shifts are referred to that of TMS.

5.2.2.4.2 ^{1}H-^{15}N CP/MAS NMR

^{1}H-^{15}N CP/MAS NMR experiments were carried out at an MAS rate of 5.0 kHz. The ^{1}H $\pi/2$ pulse was 3.4 μs and two-pulse phase modulation (TPPM) decoupling[166] was used during the acquisition. The Hartmann-Hahn condition was set using ^{15}N-labelled glycine. The spectra were measured using a contact time of 5.0 ms and a relaxation delay of 5.0 s. Typically, 48,000 scans were accumulated (as the spectra were acquired without isotopic enrichment of ^{15}N). Chemical shifts are calibrated to that of liquid $^{15}NH_3$ (at 0 ppm), using ^{15}N-enriched glycine at 35.1 ppm as a secondary reference.

5.2.2.5 TGA

TGA analysis was carried out using a Q5000IR analyser (TA Instruments) with an automated vertical overhead thermobalance. The samples were heated at a rate of 10 °C/min under nitrogen atmosphere to a maximum of 700 °C.

5.2.2.6 Elemental analysis

All elemental analyses were carried out by the Microanalysis Department in the School of Physical Sciences, at the University of Liverpool. The conditions used to collect these data are given in **Chapter 2**, **Section 2.7**.

5.2.2.7 Data analysis

Nitrogen adsorption isotherms were analysed using Micromeritics ASAP2420 software. All solid-state NMR spectra were acquired using

XWINNMR 3.5. All NMR spectra were processed using Bruker Topspin 2.1 software. Deconvolution of the spectra was carried out using Origin Pro 8.5.

5.3 Results and discussion

5.3.1 Choice of monomers and reaction conditions

Two types of porous polymers can be synthesised from poly-condensation reactions between amines and aldehydes using A_x + B_y monomers, **Scheme 5-2**. The first type of polymer consists of imine linkages (COF-300, POFs, ANWs).[30, 246] The second is built from aminal linkages (SNWs).[90, 253]

Scheme 5-2: Possible polymer structures linked by either imines (PI-1/2a) or aminals (PI-1/2b).

As mentioned in the introduction, the porosity of these materials is greatly dependent upon the conditions of their synthesis. Therefore, preliminary work involved finding the conditions that gave the highest surface areas for our PI networks *i.e.* the reaction of terephthaldehyde with one of two A_2 monomers – 2,6-diaminopyridine and 2,4-diaminotoluene. Reactions were conducted with and without the presence of an acid catalyst. Various solvents, including DMF, 1,4-dioxane, and DMSO, were also screened. The highest BET surface areas were achieved in 1,4-dioxane/acetic acid, following a procedure analogous to that used for COF-300,[30] to give **PI-1** and **PI-2** respectively, **Scheme 5-2**.

Scheme 5-3: Monomers used in the synthesis of PI-1 and PI-2.

In both cases, an insoluble solid was recovered in good yield (over 90 %). **PI-1** was a yellow/brown solid, whilst **PI-2** was bright yellow

5.3.2 Investigation of polymer structures

In order to investigate the formation of imine and aminal linkages within the networks, FTIR and solid-state NMR were employed.

5.3.2.1 Infrared spectroscopy

The presence of imine and aminal bonds, **Scheme 5-2**, within the networks was demonstrated by FTIR. Both networks display an imine (-C=N-) stretch at *ca.* 1630 cm^{-1} and a broad peak at 3380 cm^{-1}, corresponding to an aminal (-N-H) stretch (**Figure 5-1**). Unreacted end groups (aldehyde at *ca.* 1690 cm^{-1}, amine at 3000 cm^{-1}, overlapping with the aminal peak) were also detected. For materials reported in the literature, the level of end groups varies significantly. COF-300[30] and ANWs[91] have very little unreacted groups, whereas SNWs,[90] furan-based imines,[88] and POFs[89] exhibit intense peaks in their FTIR spectra for both aldehyde and amine end groups.

Figure 5-1: IR spectra of **PI-1** (black line) **PI-2** (red line).

5.3.2.2 Solid-state NMR

The networks were studied at the molecular level using solid-state NMR to confirm the presence of imine and aminal groups and to assess the end-group content. The ^{1}H-^{13}C CP/MAS NMR spectra are shown in **Figure 5-2**. The NMR spectra exhibit a peak at 155-160 ppm, ascribed to imine (-H***C***=N-)[30, 91] and pyridyl[20] units and a peak at *ca.* 45 ppm resulting from aminal linkages (-HN-***C***H-NH-).[90] A distinct carbonyl peak (-***C***=O) at 192-196 ppm indicated the presence of residual aldehyde end groups. Unreacted end groups have been previously reported for furan-based imines and POFs.[88, 89]

This text box is where the unabridged thesis included the following third party copyrighted material:

"Branching out with aminals: microporous organic polymers from di-functional monomers" Andrea Laybourn, Robert Dawson, Rob Clowes, Jonathan A. Iggo, Andrew I. Cooper, Yaroslav Z. Khimyak and Dave J. Adams, *Polymer Chemistry*, **2012**, *3*, 533-537.

Figure 5-2: ^{1}H-^{13}C CP/MAS NMR spectra of networks **PI-1** (top) and **PI-2** (bottom). Spectra were recorded at an MAS rate of 10 kHz and a contact time of 2 ms. Asterisks denote spinning sidebands. 's' denotes residual solvent.

However, it is difficult to quantify the extent of polymerisation and the level of end groups accurately. The peaks corresponding to both the imine (C=N-) and heterocyclic (-C=N-) bonds overlap in both IR and ^{1}H-^{13}C CP/MAS NMR spectra. ^{1}H-^{15}N CP/MAS NMR spectra are capable of distinguishing between imine and heterocyclic (-C=N-) bonds as their respective ^{15}N chemical shifts are very different.

Although, ^{1}H-^{15}N CP/MAS NMR spectra have been reported for similar materials, such as COF-300, ANWs and SNWs,[90, 91, 254] discrepancies exist between the assignment of ^{15}N environments. These discrepancies arise from research groups using different ^{15}N references to calibrate the NMR spectra.[107, 206]

Traditionally, liquid ammonia has been used as an external reference for biochemical materials, such as proteins.[107, 206] Indeed, the ^{15}N spectrum of COF-

300 is referenced to liquid ammonia.[254] However, following IUPAC recommendations in 2001,[107, 206] most solid-state NMR groups also reference to nitromethane. Referencing to nitromethane results in negative chemical shifts, such is the case for ANWs and SNWs.[90, 91]

To overcome the referencing problem, collection of ^{1}H-^{15}N CP/MAS NMR spectra for a series of model small molecule analogues was required so that ^{15}N chemical shifts could be assigned unambiguously for the **PI** networks. Conveniently, imine-containing porous organic cage materials are currently the focus of research within Prof. Cooper's group and these materials were readily available for analysis. **Cage 1β R3** and **Reduced Cage 3** were provided by Drs. James T. A. Jones and Tom Hasell. Details of the synthesis of **A-1** (small molecule analogue of **PI-1**) is given in **Section 5.2.1.3.1**. ^{1}H-^{15}N CP/MAS NMR spectra of the model compounds are shown **Figure 5-3** and structures and chemical shifts are detailed in **Table 5-1**.

Figure 5-3: ^{1}H-^{15}N CP/MAS NMR spectra of **PI** networks and model compounds. Asterisks denote spinning sidebands. An MAS rate of 5 kHz and a contact time of 5 ms were used.

Table 5-1: Structures of model compounds and summary of nitrogen assignments.

Name of Compound	Structure	^{15}N chemical shift (ppm)	Type of nitrogen environment
2,4-diaminotoluene (Aldrich)	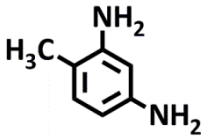	57	Primary amine ($R\text{-}NH_2$)
Reduced Cage 3 (ref. [207])	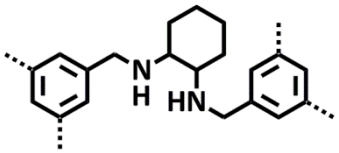	47	Secondary amine (R-NH-R)
Cage 1β R3 (ref. [207])	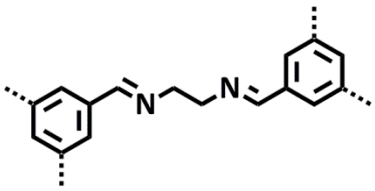	336	Imine (R-C=N-R) (split into 3 peaks due to R3 symmetry)[207]
A1 (for synthesis see **Section 5.2.1.3.1**)	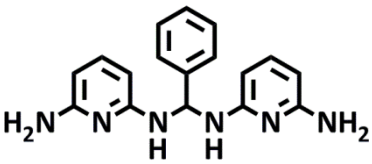	32	Primary amine ($R\text{-}NH_2$)
		60 to 90	Secondary amine (R-NH-R)
		227	Pyridine heterocyclic nitrogen

A comparison of the ^{1}H-^{15}N CP/MAS NMR spectra for **PI-1** and **PI-2** is shown in **Figure 5-4**.

Figure 5-4: ^{1}H-^{15}N CP/MAS NMR spectra of **PI-1** (bottom) and **PI-2** (top). Spectra were recorded at an MAS rate of 5 kHz and a contact time of 5 ms.

The peaks at 32 ppm for both networks (**Figure 5-4**) can be ascribed to terminal amine end groups.[30] The NMR spectrum of **PI-1** also exhibits peaks at *ca*. 224 ppm, corresponding to the heterocyclic nitrogen from the pyridine ring.[107] Interestingly, **PI-2** displays clear peaks for both imine (327 ppm)[30] and aminal (50 ppm),[90] whereas **PI-1** displays a clear aminal peak at 66 ppm. The imine peak for **PI-1** (which would be predicted at *ca.* 339 ppm) is just detectable above the level of noise. The intensity of the centre band of the imine peak is reduced due to the presence of strong spinning sidebands, which are also observed for **PI-2** and the model imine materials (**Cage 1β R3**). However, for **PI-1**, the imine group is clearly detectable using IR and ^{1}H-^{13}C CP/MAS NMR techniques. It is therefore possible to conclude that **PI-1** is mainly connected by aminal linkages, whereas **PI-2** comprises of both imine and aminal linkages. These data are

consistent with those reported elsewhere for pyridyl-amines.[255] Owing to their basicity, pyridyl-amines were found to preferentially attack imine bonds, leading to formation of the aminal.[255]

5.3.3 Textural properties of the polymers

Since possible applications of MOPs include gas storage and molecular separations, good thermal stability and gas selectivity would be highly desirable for such materials. Therefore, investigation of the textural properties of **PI** networks is required. A comparison of such properties was made with current imine and aminal-containing MOPs.

5.3.3.1 **Thermal stability**

Both networks exhibited good thermal stability with onset of decomposition above 350 °C as measured by TGA under nitrogen (**Figure 5-5** and **Figure 5-6**).

This text box is where the unabridged thesis included the following third party copyrighted material:

"Branching out with aminals: microporous organic polymers from di-functional monomers" Andrea Laybourn, Robert Dawson, Rob Clowes, Jonathan A. Iggo, Andrew I. Cooper, Yaroslav Z. Khimyak and Dave J. Adams, *Polymer Chemistry*, **2012**, *3*, 533-537.

Figure 5-5: TGA curve of **PI-1** including starting monomers.

This text box is where the unabridged thesis included the following third party copyrighted material:

"Branching out with aminals: microporous organic polymers from di-functional monomers" Andrea Laybourn, Robert Dawson, Rob Clowes, Jonathan A. Iggo, Andrew I. Cooper, Yaroslav Z. Khimyak and Dave J. Adams, *Polymer Chemistry*, **2012**, *3*, 533-537.

Figure 5-6: TGA curve of **PI-2** including starting monomers.

The T_{dec} are comparable to other porous polymers, such as CMPs, COFs, and POFs.[30, 65, 246] A weight loss of up to 12 % was observed in the TGA data below 100 °C, ascribed to residual solvent (also detected by solid state NMR, **Figure 5-2**). Solvent can be trapped within the networks during Soxhlet extraction in THF and is not uncommon.[246]

5.3.3.2 Gas sorption and N_2/CO_2 selectivities

Firstly, the pore structures and gas sorption properties of these networks were investigated by nitrogen gas sorption analysis. The results are summarised in **Table 5-2**. The BET surface areas were around 500 m^2/g, lower than found for COF-300 (SA_{BET} = 1360 m^2/g)[30] and POFs (SA_{BET} of up to 1521 m^2/g),[246] but comparable with many other materials, such as furan-based imines and melamine resins.[88, 208]

Table 5-2: Summary of N_2 gas sorption data for **PI-1** and **PI-2**, including pore properties and surface areas.

Network	SA_{BET} (m^2/g)[a]	SA_{Lang} (m^2/g)[b]	$V_{0.1}$ (cm^3/g)[c]	V_{Tot} (cm^3/g)[d]	$V_{0.1}/V_{Tot}$
PI-1	506	643	0.20	0.50	0.40
PI-2	568	710	0.22	0.38	0.58

[a]Based on full isotherm pressure range 0.01-0.10 P/P_0. [b]Based on full isotherm pressure range 0.06-0.20 P/P_0. [c]Pore volume at P/P_0 = 0.10. [d]Total pore volume at P/P_0 = 0.97. Data collected at 77 K using N_2 as the sorbate.

Both networks exhibit Type I nitrogen isotherms (according to IUPAC classification) with some Type IV character,[1] *i.e.* mesoporous characteristics at high relative pressures (**Figure 5-7**). As with POFs,[246] the networks display only slight adsorption hysteresis, indicating that adsorption and desorption are equally facile.

Figure 5-7: N_2 sorption at 77 K for **PI-1** (a) and **PI-2** (b). Adsorption (filled symbols, desorption (hollow symbols).

Figure 5-8: Pore size distribution curve for **PI-1** (a) and **PI-2** (b). Pore sizes calculated using NL-DFT model for pillared clay, as this was found to give the best fit.

The pore size distributions of **PI-1** and **PI-2** are relatively narrow (**Figure 5-8**), compared with other CMP materials.[65, 66, 71]

The amorphous nature of the PI networks is in stark contrast to the crystalline structure of COF-300, despite their similar reaction conditions. As the crystallinity of COFs (and MOFs) arises from their ability to self-repair by reversible disassembly/reassembly,[13] one can assume that the conditions required for the PI networks to undergo such processes is not met under the same conditions as those for COF-300. Indeed, many factors affect the reversibility of imine and aminal formation, such as the presence of catalyst, rate of reaction, stability of resulting networks and solvent interactions, to name but a few.[209, 210]

Recent literature indicates that porous materials containing a high amount of nitrogen in their structure have a high carbon dioxide gas uptake.[38, 53, 87, 198, 211, 256-268] As the PI networks contain a significant amount of nitrogen, they were evaluated for CO_2 uptake and N_2/CO_2 gas selectivity.

Carbon dioxide isotherms were measured up to 1 bar at 273 and 298 K, and are shown in **Figure 5-9**. These particular conditions were chosen as they allow identification of good overall CO_2 adsorbents and can be used to assess CO_2 capture under post-combustion conditions.[86, 198]

Figure 5-9: CO_2 isotherms at 273 K (red circles) and 298 K (black circles) and N_2 isotherms at 298 K (black squares) for **PI-1** (a) and **PI-2** (b). Adsorption (filled symbols, desorption (hollow symbols).

PI-1 showed an uptake of 1.41 mmol/g, substantially higher than that of **PI-2** (1.00 mmol/g). The CO_2 uptakes for **PI-1** and **PI-2** at 1 bar and 298 K are similar to a number of other microporous polymer networks.[269] However, the sorption values are around half that measured for the best-performing networks in this class thus far, such as BILP-1 (benzimidazole-linked polymer, 2.98 mmol/g)[270] or the PECONF (porous covalent electron-rich organonitridic frameworks) materials (PECONF-3, 2.47 mmol/g).[271] Both BILPs and PECONFs are synthesised from *ortho*-amine poly-condensation reactions with hexachlorotriphosphazene[271] and aromatic aldehydes,[270] respectively.

In order to try to rationalise the higher CO_2 uptake observed for **PI-1** compared with **PI-2**, the isosteric heats of adsorption were measured for both networks, **Figure 5-10**. A summary of these data are given in **Table 5-3**.

Figure 5-10: Isosteric heats of adsorption of CO_2 for **PI** networks.

Interestingly, **PI-1** not only shows the highest uptake of the two materials, but also the highest isosteric heat, **Table 5-3**. The isosteric heat of **PI-1** is also amongst the highest reported for other microporous polymers and is similar to

that of CMPs[272] and PECONFs.[271] The isosteric heat of **PI-1** is close to the range required for carbon dioxide capture using pressure swing adsorption.[273] The improved isosteric heat value for CO_2 in **PI-1** can be attributed to the higher micropore volume and the high density of nitrogen in the network, arising from both the pyridine and the imine/aminal linkages. Both factors have previously been found to improve the uptake of CO_2 in porous networks.[86, 198]

In order to further assess the PI networks for post-combustion CO_2 capture (where carbon dioxide is often mixed with nitrogen), the CO_2/N_2 selectivities were determined. The selectivities were calculated using the Henry Law constants from the pure N_2 and CO_2 component isotherms in the linear low pressure (< 0.1 bar) range at 298 K. (**Figure 5-11** and **Figure** 5-12). A summary of these data are given in **Table 5-3**.

Figure 5-11: CO_2/N_2 gas selectivity at 298 K for **PI-1**.

Figure 5-12: CO_2/N_2 gas selectivity at 298 K for **PI-2**.

Table 5-3: Summary of carbon dioxide uptakes and selectivity.

Network	CO_2 uptake (mmol/g)[a]		N_2 uptake (mmol/g)[b] 298 K	Heat of adsorption for CO_2 (kJ/mol)[c]	CO_2/N_2 selectivity[d]	
	273 K	298 K			Ideal selectivity	Henry Law constants
PI-1	2.00	1.41	0.15	34	9.5	27:1
PI-2	1.51	1.00	0.15	27	6.7	12:1

[a]CO_2 uptake at 1 bar. [b]N_2 uptake at 1 bar. [c]Calculated from CO_2 isotherms collected at 273 and 298 K at low coverage. [d]CO_2:N_2 selectivity at 298 K calculated from Henry law constants.

PI-2 showed a selectivity of 12:1 while **PI-1** was calculated to be more than twice as selective (27:1). While these values are low in comparison to PECONFs,[271] they are comparable to many other types of polymer network[269] including melamine resins[208] and furan-based imine networks,[88] as well as porous organic cages.[274]

5.3.3.3 **Polymer Morphology**

Polymer morphology can also be used to rationalise gas sorption properties. Polymers with spherical morphologies are often mesoporous and have BET surface areas less than 200 m^2/g, while those with larger fused masses and rough surfaces have higher surface areas and are generally microporous[181] (see **Section 3.3.2**). For these reasons, polymer morphology was probed by SEM analysis (**Figure 5-13**).

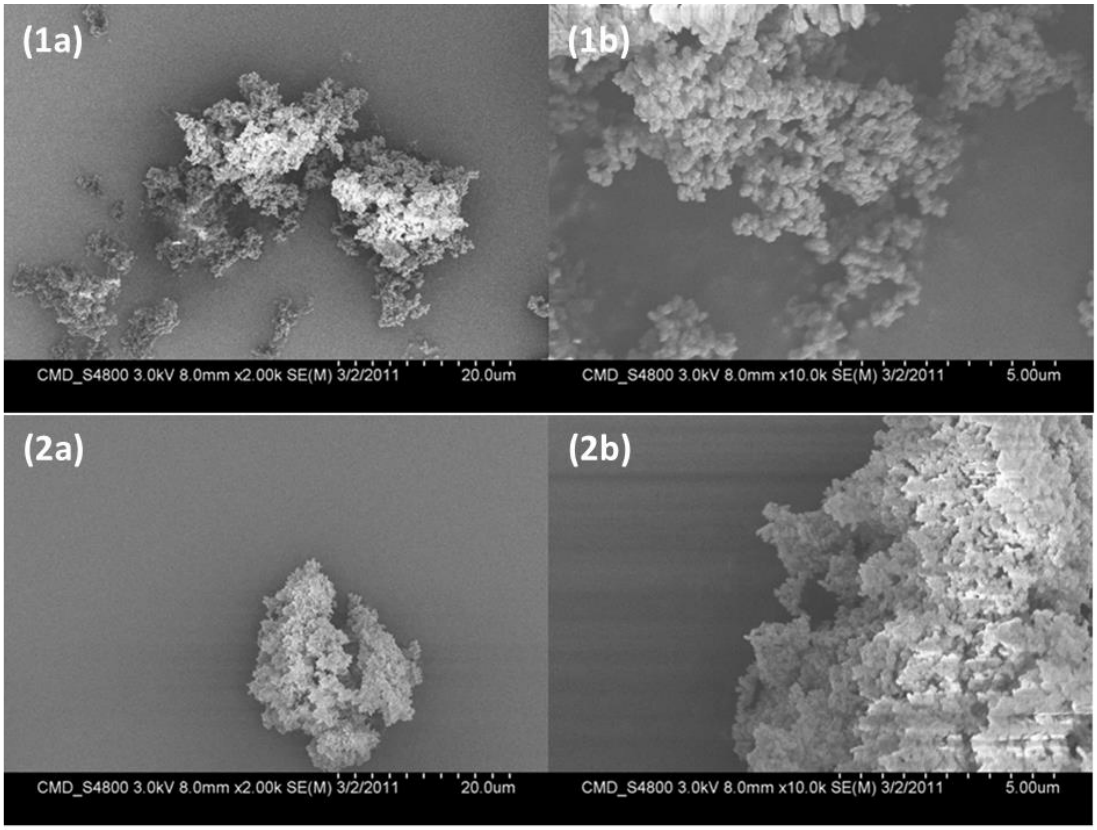

Figure 5-13: SEM images of **PI-1** (1a, 1b) and **PI-2** (2a, 2b) with magnifications of (a) 2.50 K and (b) 6.25 K (scale bars inset).

Both networks display similar morphologies to that reported for other porous imine[89] and aminal[90] materials. **PI-1** consists of smooth fused spheres, whereas **PI-2** comprises of less-defined rough spheres. Interestingly, these observations correlate well with the gas sorption properties, *i.e.* **PI-1** exhibits greater type IV mesoporosity than **PI-2**.

5.4 Conclusions and outlook

In summary, the possibility of introducing branching (and thus porosity) into networks that would otherwise consist of linear imine-linked chains by taking advantage of aminal formation has been demonstrated. Although the

level of aminal formation/branching has proven difficult to quantify, the pyridyl monomer was found to form aminal bonds preferentially, while the less basic amine monomer forms both imine and aminal linkages with equal ease.

An increased isosteric heats of adsorption and an improved CO_2 uptake and N_2/CO_2 selectivity was found for **PI-1**. A higher affinity for CO_2 is the result of a high density of nitrogen in the network.

One potential (and indeed expensive) method for quantifying the amount of aminal branching would be to synthesise the networks from ^{15}N enriched amine monomers and collect ^{15}N $\{^1H\}$ MAS NMR spectra. Deconvolution of each spectrum would allow quantification of ^{15}N sites. However, this study shows that the even though the level of branching remains unknown it is sufficient to achieve permanently porous networks with surface areas of over 500 m^2/g.

Continuation of this work could involve trying to control the level of branching by altering the reaction conditions. As formation of the imine is dependent on the initial protonation of the aldehyde, a possible study could involve altering the pH of the reaction mixture as one would expect preferential formation of the imine at low pH.

Another possible study of these materials could involve chelation of metals to the nitrogen atoms in the polymer back-bone, which may allow these materials to be used as solid-catalyst supports.

Ultimately, this chemistry presents an alternative strategy for the synthesis of microporous polymers based on A_2 and B_2 monomers. The ready accessibility of many functionalised di-amines or di-nitro compounds (which can be easily reduced) means that this could be an attractive means for preparing microporous materials containing a range of functional groups.

Overall Conclusions and Outlook

In this work the structure and dynamics of conjugated microporous polymers were investigated. Advanced structural elucidation and examination of network flexibility and porosity was achieved using two approaches.

The first approach involved analysis of a series of intermediates collected at incremental time periods during the synthesis of CMP-1. Products collected at early reaction times (*i.e.* before 120 minutes) are composed of spherical particles exhibiting interparticulate mesoporosity, whereas materials collected after this time consist of fused particles that exhibit intraparticulate microporosity. Based upon the changes in textural properties, a mechanism for the formation of CMP-1 networks was suggested. The mechanism involves formation of oligomers which react to form insoluble clusters. The clusters precipitate out of solution and crosslink in the solid state to form extended CMP-1 networks. Validation of the reaction mechanism was achieved by analysing changes in the amount of end groups and the molecular mobility.

The second approach involved probing the origins of network flexibility, swelling and porosity for CMP networks using deuterium NMR. Firstly, the pore structures of CMP-1 and CMP-2 were investigated by simulation of deuterium NMR spectra of an adsorbed deuterated benzene guest. At all benzene loadings, the pores of CMP-1 and CMP-2 are swollen and the mobility of benzene is restricted.

Secondly, framework flexibility was investigated by selective deuteration of the phenyl rings within the struts of CMP-1 and CMP-2. Deuterium line shape analysis revealed the presence of static and mobile phenyl groups, undergoing 180° π-flips, over a large temperature range. Results show that the rate of ring flipping motion is much slower than those reported for other porous networks and that the dynamics of the struts are in the slow motional regime, corresponding to polymeric frameworks and large biological molecules.

Finally, a new synthetic route to CMPs was developed by reactions between aldehydes and amines. Introduction of branching (and thus porosity) into networks that would otherwise consist of linear imine-linked chains was achieved by taking advantage of aminal formation. This chemistry presents an alternative strategy for the preparation of microporous polymers from bi-functional monomers and does not require the use of metal catalysts, thus increasing the potential of CMPs for use in industrial applications.

The research presented here highlights significant advances in the preparation and detailed structural characterisation of complex amorphous microporous materials by solid-state NMR. We have shown that the porosity of amorphous materials can be probed by studying the motions of a guest within the network. This method has a major advantage over traditional gas sorption analysis as the properties of swollen networks can be investigated. We have also shown that the levels of polymerisation for amorphous materials can be qualitatively derived from a combination of carbon and deuterium solid-state NMR. However, additional NMR experiments and molecular simulations are needed to accurately derive the motional energy barriers and to fully uncover the effect of swelling upon network mobility. Solid-state NMR was also used to confirm the presence of key functional groups within newly synthesised CMP networks.

Ultimately a combination of solid-state NMR and molecular simulations are required to fully understand the structure and properties of new and existing amorphous microporous materials. Such information is essential for the development of new materials for specific applications.

References

1. Sing, K.S.W., *Pure & Appl. Chem.* **1982**, 54(*11*), 2201-2218.
2. Budd, P.M., Butler, A., Selbie, J., Mahmood, K., McKeown, N.B., Ghanem, B., Msayib, K., Book, D., Walton, A., *Phys. Chem. Chem. Phys.* **2007**, *9*, 1802.
3. Furukawa, H., Yaghi, O.M., *J. Am. Chem. Soc.* **2009**, *131*, 8875.
4. Wood, C.D., Tan, B., Trewin, A., Niu, H.J., Bradshaw, D., Rosseinsky, M.J., Khimyak, Y.Z., Campbell, N.L., Kirk, R., Stockel, E., Cooper, A.I., *Chem. Mater.* **2007**, *19*, 2034.
5. Svec, F., Germain, J., Frechet, J.M.J., *Small* **2009**, *5*, 1098.
6. McKeown, N.B., Budd, P. M., *Chem. Soc. Rev.* **2006**, *35*, 675.
7. McKeown, N.B., Budd, P.M., *Chem. Soc. Rev.* **2006**, *35*, 675-683.
8. Ghanem, B.S., McKeown, N.B., Budd, P.M., Al-Harbi, N.M., Fritsch, D., Heinrich, K., Starannikova, L., Tokarev, A., Yampolskii, Y., *Macromolecules* **2009**, *42*, 7881.
9. Schmidt, J., Weber, J., Epping, J.D., Antonietti, M., Thomas, A., *Adv. Mater.* **2009**, *21*, 702.
10. Li, H., Eddaoudi, M., O'Keeffe, M., Yaghi, O.M., *Nature* **1999**, *402*, 276-279.
11. Zhou, H.-C., Long, J.R., Yaghi, O.M., *Chem. Rev.* **2012**, *112*, 673-674.
12. Stock, N., Biswas, S., *Chem. Rev.* **2012**, *112*, 933-969.
13. Eddaoudi, M., Kim, J., Rosi, N., Vodak, D., Wachter, J., O'Keeffe, M., Yaghi, O.M., *Science* **2002**, *295*, 469-472.
14. Cohen, S.M., *Chem. Rev.* **2012**, *112*, 970-1000.
15. Furukawa, H., Ko, N., Go, Y.B., Aratani, N., Choi, S.B., Choi, E., Yazaydin, A.O., Snurr, R.Q., O'Keeffe, M., Kim, J., Yaghi, O.M., *Science* **2010**, *329*, 424-428.
16. Allendorf, M.D., Bauer, C.A., Bhakta, R.K., Houk, R.J.T., *Chem. Soc. Rev.* **2009**, *38*, 1330.
17. Sumida, K., Rogow, D.L., Mason, J.A., McDonald, T.M., Bloch, E.D., Herm, S.R., Bae, T.-H., Long, J.R., *Chem. Rev.* **2012**, *112* 724–781.
18. McKinlay, A.C., Morris, R.E., Horcajada, P., Ferey, G., Gref, R., Couvreur, P., Serre, C., *Angew. Chem. Int. Ed.* **2010**, *49*, 6260.
19. Ma, L.Q., Abney, C., Lin, W.B., *Chem. Soc. Rev.* **2009**, *38*, 1248.
20. Lee, J., Farha, O.K., Roberts, J., Scheidt, K.A., Nguyen, S.T., Hupp, J.T., *Chem. Soc. Rev.* **2009**, (*38*), 1450.
21. Phan, A., Doonan, C.J., Uribe-Romo, F.J., Knobler, C.B., O'Keeffe, M., Yaghi, O.M., *Accounts of Chemical Research* **2010**, *43*(1), 58-67.
22. Tian, Y.-Q., Cai, C.-X., Ji, Y., You, X.-Z., Peng, S.-M., Lee, G.-H., *Angew. Chem. Int. Ed.* **2002**, (*41*), 1384–1386.
23. Park, K.S., Ni, Z., Cote , A.P., Choi, J.Y., Huang, R., Uribe-Romo, F.J., Chae, H.K., O'Keeffe, M., Yaghi, O.M., *Proc. Natl. Acad. Sci.* **2006**, (*103*), 10186-10191.

24. Maesen, T.L.M., Marcus, B.I., van Bekkum, H., Flanigen, E.M., Jacobs, P.A., Jansen, J.C., *Introduction to Zeolite Science and Practice*. 2nd Edition edn., *Elsevier*. Amsterdam, **2001**.
25. Cote, A.P., Benin, A.I., Ockwig, N.W., O'Keeffe, M., Matzger, A.J., Yaghi, O.M., *Science* **2005**, *310*, 1166.
26. Furukawa, H., Yaghi, O.M., *J. Am. Chem. Soc.* **2009**, *131*, 8875–8883.
27. Mastalerz, M., *Angew. Chem. Int. Ed.* **2008**, *47*, 445 – 447.
28. El-Kaderi, H.M., Hunt, J.R., Mendoza-Cortes, J.L., Cote, A.P., Taylor, R.E., O'Keeffe, M., Yaghi, O.M., *Science* **2007**, *316*, 268.
29. Wan, S., Guo, J., Kim, J., Ihee, H., Jiang, D., *Angew. Chem. Int. Ed.* **2009**, *48*, 1-5.
30. Uribe-Romo, F.J.H., J. R.; Furukawa, H.; Klock, C.; O'Keeffe, M.; Yaghi, O. M., *J. Am. Chem. Soc.* **2009**, *131*, 4570-4571.
31. Kuhn, P., Forget, A., Su, D., Thomas, A., Antonietti, M., *J. Am. Chem. Soc.* **2008**, (*130*), 13333 – 13337.
32. Kuhn, P., Thomas, A., Antonietti, M., *Macromolecules* **2009**, (*42*), 319 – 326.
33. Kuhn, P., Antonietti, M., Thomas, A., *Angew. Chem., Int. Ed.* **2008**, (*47*), 3450 – 3453.
34. Bojdys, M.J., Jeromenok, J., Thomas, A., Antonietti, M., *Adv. Mater.* **2010**, (*22*), 2202 – 2205.
35. Ren, S., Bojdys, M.J., Dawson, R., Laybourn, A., Khimyak, Y.Z., Adams, D.J., Cooper, A.I., Adv. Mater. **2012**, (*24*), 2357–2361.
36. McKeown, N.B., Makhseed, S., Budd, P.M., *Chem. Commun.* **2002**, 2780.
37. McKeown, N.B., Hanif, S., Msayib, K., Tatershall, C.E., Budd, P.M., *Chem. Commun.* **2002**, 2782.
38. McKeown, N.B., Budd, P.M., *Macromolecules* **2010**, (*43*), 5163–5176.
39. McKeown, N.B., Budd, P.M., Msayib, K., Ghanem, B.S., Kingston, H.J., Tattershall, C.E., Makhseed, S., Reynolds, K.J., Fritsch, D., *Chem. Eur. J.* **2005**, (*11*), 2610.
40. Budd, P.M., Ghanem, B., Makhseed, S., McKeown, N.B., Msayib, K., Tattershall, C.E., *Chem. Commun.* **2004**, 230.
41. Budd, P.M., Elabas, E.S., Ghanem, B.S., Makhseed, S., McKeown, N.B., Msayib, K.J., Tattershall, C.E., Wang, D., *Adv. Mater.* **2004**, (*16*), 456.
42. Budd, P.M., McKeown, N.B., Fritsch, D., *J. Mater. Chem.* **2005**, (*15*), 1977.
43. Davankov, V.A., Rogozhin, S.V., Tsyurupa, M.P., US Pat., **1971**; Vol. 3.729.457.
44. Tsyurupa, M.P., Maslova, L.A., Andreeva, A.I., Mrachkovskya, T.A., Davankov, D.A., *React. Polym.* **1995**, (*25*), 69.
45. Davankov, V.A., Tsyurupa, M.P., Rogozhin, S.V., *J. Polym. Sci., Polym. Symp.* **1974**, (*47*), 95.
46. Davankov, V.A., Tsyurupa, M.P., Rogozhin, S.V., *Angew. Makromol. Chem.* **1976**, (*53*), 19.

47. Tsyurupa, M.P., Volynskaya, A.I., Belchich, L.A., Davandov, V.A., *J. Appl. Polym. Sci.* **1983**, (*28*), 685.
48. Krauss, D., Popov, G., Schwachula, G., *Plaste. Kautschuk* **1977**, (*24*), 545.
49. Ahn, J.-H., Jang, J.-E., Oh, C.-G., Ihm, S.-K., Cortez, J., Sherrington, D.C., *Macromolecules* **2006**, (*39*), 627.
50. Law, R.V., Sherrington, D.C., Snape, C.E., Ando, I., Kurosu, H., *Macromolecules* **1996**, (*29*), 6284.
51. Hradil, J., Kralova, E., *Polymer* **1998**, (*39*), 6041.
52. Schwab, M.G., Senkovska, I., Rose, M., Klein, N., Koch, M., Pahnke, J., Jonschker, G., Schmitz, B., Hirscherd, M., Kaskel, S., *Soft Matter* **2009**, (*5*), 1055–1059.
53. Jiang, J.-X., Cooper, A.I., *Topics in Current Chemistry* **2010** *293*, 1-33.
54. Penner, N.A., Nesterenko, P.N., Rybalko, M.A., *J. Anal. Chem.* **2001**, (*56*), 934.
55. Fontanals, N., Manesiotis, P., Sherrington, D.C., Cormack, P.A.G., *Adv. Mater.* **2008**, (*20*), 1298.
56. Podlesnyuk, V.V., Hradil, J., Kralova, E., *React. Funct. Polym.* **1999**, (*42*), 181.
57. Veverka, P., Jerabek, K., *React. Funct. Polym.* **2004**, (*59*), 71.
58. Nesterenko, P.N., Kebets, P.A., Volgin, Y.V., *J. Anal. Chem.* **2001**, (*56*), 715.
59. Wood, C.D., Tan, B., Trewin, A., F., S., Rosseinsky, M.J., Bradshaw, D., Sun, Y., Zhou, L., Cooper, A.I., *Adv. Mater.* **2008**, (*20*), 1916.
60. Rose, M., Bohlmann, W., Sabo, M., Kaskel, S., *Chem. Commun.* **2008**, 2462.
61. Germain, J., Frechet, J.M.J., Svec, F., *J. Mater. Chem.* **2007**, (*17*), 4989.
62. Mullen, K., Scherf, U., *Organic Light Emitting Devices: Synthesis, Properties and Applications*. *Wiley*. New York, **2006**.
63. Friend, R.H., Gymer, R.W., Holmes, A.B., Burroughes, J.H., Marks, R.N., Taliani, C., Bradley, D.C.C., Dos Santos, D.A., Bredas, J.L., Loglund, M., Salaneck, W.R., *Nature* **1999**, (*397*), 121.
64. Skotheim, T.A., Reynolds, J.R., *Conjugated Polymers: Theory, Synthesis, Properties, and Charaterisation.* 3rd Edition, *CRC Press*. Florida, **2007**.
65. Jiang, J.X., Su, F., Trewin, A., Wood, C.D., Campbell, N.L., Niu, H., Dickinson, C., Ganin, A.Y., Rosseinsky, M.J., Khimyak, Y.Z., Cooper, A.I., *Angew. Chem. Int. Ed.* **2007**, 46, 8574-8578.
66. Jiang, J.X., Su, F., Trewin, A., Wood, C.D., Niu, H., Jones, J.T.A., Khimyak, Y.Z., Cooper, A.I., *J. Am. Chem. Soc.* **2008**, 130(24), 7710-7720.
67. Jiang, J.-X., Su, F., Niu, H., Wood, C.D., Campbell, N.L., Khimyak, Y.Z., Cooper, A.I., *Chem. Commun.* **2008**, 486-488.
68. Jiang, J.-X., Trewin, A., Su, F., Wood, C.D., Niu, H., Jones, J.T.A., Khimyak, Y.Z., Cooper, A.I., *Macromolecules* **2009**, (*42*), 2658-2666.
69. Weber, J., Thomas, A., *J. Am. Chem. Soc.* **2008**, (*130*), 6334.

70. Ren, S., Dawson, R., Laybourn, A., Jiang, J.-X., Khimyak, Y.Z., Adams, D.J., Cooper, A.I., *Polym. Chem.* **2012**, (*3*), 928-934.
71. Dawson, R., Laybourn, A., Clowes, R., Khimyak, Y.Z., Adams, D.J., Cooper, A.I., *Macromolecules* **2009**, *42*, 8809-8816.
72. Chen, L., Honsho, Y., Seki, S., Jiang, D., *J. Am. Chem. Soc.* **2010**, (*132*), 6742–6748.
73. Jiang, J.-X., Trewin, A., Adams, D.J., Cooper, A.I., *Chem. Sci.* **2011**, (*2*), 1777–1781.
74. Weder, C., Wrighton, M.S., *Macromolecules* **1996**, (*29*), 5157.
75. Schmitz, C., Posch, P., Thelakkat, M., Schmidt, H.W., Montali, A., Feldman, K., Smith, P., Weder, C., *Adv. Funct. Mater.* **2001**, (*11*), 41.
76. Swager, T.M., *Acc. Chem. Res.* **1998**, (*31*), 201.
77. Tan, D., Fan, W., Xiong, W., Sun, H., Li, A., Deng, W., Meng, C., *Eur. Polym. J.* **2012**, *48*, 705–711.
78. Tan, D., Fan, W., Xiong, W., Sun, H., Cheng, Y., Liu, X., Meng, C., Li, A., Deng, W.-Q., *Macromol. Chem. Phys.* **2012**, ASAP.
79. Stockel, E., Wu, X., Trewin, A., Wood, C.D., Clowes, R., Campbell, N.L., Jones, J.T.A., Khimyak, Y.Z., Adams, D.J., Cooper, A.I., *Chem. Commun.* **2008**, 212-214.
80. Yuan, D., Lu, W., Zhao, D., Zhou, H.-C., *Adv. Mater.* **2011**, *23*, 3723-3725.
81. Lu, W., Yuan, D., Zhao, D., Schilling, C.I., Plietzsch, O., Muller, T., Braïse, S., Guenther, J., Blüimel, J., Krishna, R., Li, Z., Zhou, H.-C., *Chem. Mater.* **2010**, *22*(21), 5964–5972.
82. Holst, J.R., Stöckel, E., Adams, D.J., Cooper, A.I., *Macromolecules* **2010**, *43*, 8531–8538.
83. Ben, T., Ren, H., Ma, S., Cao, D., Lan, J., Jing, X., Wang, W., Xu, J., Deng, F., Simmons, J.M., Qiu, S., Zhu, G., *Angew. Chem. Int. Ed.* **2009**, *48*, 9457-9460.
84. Dawson, R., Cooper, A.I., Adams, D.J., *Prog. Polym. Sci.* **2012**, (*37*), 530–563.
85. Konstas, K., Taylor, J.W., Thornton, A.W., Doherty, C.M., Lim, W.X., Bastow, T.J., Kennedy, D.F., Wood, C.D., Cox, B.J., Hill, J.M., Hill, A.J., Hill, M.R., *Angew. Chem. Int. Ed.* **2012**, *51*, 1-5.
86. D'Alessandro, D.M., Smit, B., Long, J.R., *Angew. Chem.* **2010**, *122*, 6194 – 6219.
87. D'Alessandro, D.M., Smit, B., Long, J.R., *Angew. Chem. Int. Ed.* **2010**, *49*, 6058 – 6082.
88. Ma, J., Wang, M., Du, Z., Chen, C., Gao, J., Xu, J., *Polym. Chem.* **2012**, *3*, 2346-2349.
89. Pandey, P.K., Katsoulidis, A.P., Eryazici, I., Wu, Y., Kanatzidiz, M.G., Nguyen, S.T., *Chem. Mater.* **2010**, *22* ((17)), 4974–4979.
90. Schwab, M.G., Fassbender, B., Spiess, H.W., Thomas, A., Feng, X., Mullen, K., *J. Am. Chem. Soc.* **2009**, *131*, 7216-7217.

91. Schwab, M.G., Hamburger, M., Feng, X., Shu, J., Spiess, H.W., Wang, X., Antonietti, M., Mullen, K., *Chem. Commun.* **2010**, ***46***, 8932-8934.
92. Kou, Y., Xu, Y., Guo, Z., Jiang, D., *Angew. Chem. Int. Ed.* **2011**, *50*, 8753 –8757.
93. Housecroft, C.E., Constable, E.C., CHEMISTRY. 2nd Edition., *Pearson Education Limited*. **2002**.
94. Weber, J., Schmidt, J., Thomas, A., Bohlmann, W., *Langmuir* **2010**, *26*(19), 15650-15656.
95. Budd, P.M., Ghanem, B.S., Makhseed, S., McKeown, N.B., Msayib, K.J., Tattershall, C.E., *Chem. Commun.* **2004**, (230–231.).
96. Mirau, P., *"Solid State NMR and Polymers: Rapra review reports"* **2004**.
97. Ando, I.T.A., *"Solid State NMR of Polymers: studies in physical and theoretical chemistry" Elsevier Science*, The Netherlands, **1998**.
98. Mathias, L.J., *"Solid State NMR of Polymers" Plenum Press*, New York, **1991**.
99. Schmidt-Rohr, K., Spiess, H.W., *"Multidimensional Solid State NMR and Polymers" Academic Press Ltd*. **1994**.
100. Dawson, R., Laybourn, A., Khimyak, Y.Z., Adams, D.J., Cooper, A.I., *Macromolecules* **2010**, *43*, 8524-8530.
101. Meilikhov, M., Kirill Yusenko, K., Fischer, R.A., *Dalton Trans.* **2010**, *39*, 10990–10999.
102. Joseph, R., Ford, W.T., Zhang, S., Tsyurupa, M.P., Pastukhov, A.V., Davankov, V.A., *J. Polym. Sci. A: Polym. Chem.* **1997**, *35*, 695-702.
103. Curran, S.A., LaClair, C.P., Aharoni, S.M., *Macromolecules* **1991**, *24*, 5903-5909.
104. Davankov, V.A., Pastukhov, A.V., Tsyurupa, M.P., *J. Polym. Sci. B: Polym. Phys.* **2000**, *38*, 1553-1563.
105. Scott, R.A., Cowans, B.A., Peppas, N.A., *J. Polym. Sci. B: Polym. Phys.* **1999**, *37*, 1953–1968.
106. Davankov, V.A., Pastukhov, A.V., Tsyurupa, M.P., *J. Polym. Sci. B: Polym. Phys.* **2000**, *38*(11), 1553-1563.
107. Webb, G.A., *"Annual Reports on NMR Spectroscopy"* Volume 11B, *Academic Press*, **1981**.
108. Su, F., Bray, C.L., Carter, B.O., Overend, G., Copper, C., Iggo, J.A., Khimyak, Y.Z., Fogg, A.M., Cooper, A.I., *Adv. Mater.* **2009**, *21*, 2382-2386.
109. Sozzani, P., Bracco, S., Comotti, A., Ferretti, L., Simonutti, R., *Angew. Chem. Int. Ed.* **2005**, *44*, 1816 –1820.
110. Raftery, D., Long, H., Meersmann, T., Grandinetti, P.J., Reven, L., Pines, A., *Phys. Rev. Lett.* **1991**, *66*, 584.
111. Ripmeester, J.A., Ratcliffe, C.I., *J. Phys. Chem.* **1990**, *94*, 7652.
112. Barrie, P.J., Klinowski, J., *Prog. Nucl. Magn. Res. Spectrosc.* **1992**, *24*, 91.
113. Sozzani, P., Comotti, A., Simonutti, R., Meersmann, T., Logan, J.W., Pines, A., *Angew. Chem. Int. Ed.* **2000**, *39*, 2695.

114. Comotti, A., Bracco, S., Valsesia, P., Ferretti, L., Sozzani, P., *J. Am. Chem. Soc.* **2007**, *129*, 8566.
115. Cheng, C.-Y., Bowers, C.R., *J. Am. Chem. Soc.* **2007**, *129*, 13997.
116. Cheng, C.-Y., Stamatatos, T.C., Christou, G., Bowers, C.R., *J. Am. Chem. Soc.* **2010**, *132*, 5387.
117. Hoffmann, H.C., Assfour, B., Epperlein, F., Klein, N., Paasch, S., Senkovska, I., Kaskel, S., Seifert, G., Brunner, E., *J. Am. Chem. Soc.* **2011**, *133*, 8681–8690.
118. Ilczyszyn, M., Marcin Selent, M., Ilczyszyn, M.M., *J. Phys. Chem. A.* **2012**, *116*, 3206−3214.
119. Duewel, M., Vogel, N., Weiss, C.K., Landfester, K., Spiess, H.W., Mu¨nnemann, K., *Macromolecules* **2012**, *45*, 1839−1846.
120. Buntkowsky, G., Breitzke, H., Adamczyk, A., Roelofs, F., Emmler, T., Gedat, E., Grunberg, B., Xu, Y., Limbach, H.-H., Shenderovich, I., Vyalikh, A., G., F., *Phys. Chem. Chem. Phys.* **2007**, *9*, 4843-4853.
121. Hassan, J., Reardon, E.H., Peemoeller, H., *Micro. Meso. Mater.* **2009**, *122*, 121–127.
122. Vyalikh, A., Emmler, T., Shenderovich, I., Zeng, Y., Findenegg, G.H., Buntkowsky, G., *Phys. Chem. Chem. Phys.* **2007**, *9*, 2249–2257.
123. Stepanov, A.G., Alkaev, M.M., Shubin, A.A., *Journal of Physical Chemistry B* **2000**, 104(32), 7677-7685.
124. Stepanov, A.G., Alkaev, M.M., Shubin, A.A., Luzgin, M.V., Shegai, T.O., Jobic, H., *Journal of Physical Chemistry B* **2002**, 106(39), 10114-10120.
125. Stepanov, A.G., Shegai, T.O., Luzgin, M.V., Jobic, H., *European Physical Journal E* **2003**, 12(1), 57-61.
126. Stepanov, A.G., Shubin, A.A., Luzgin, M.V., Shegai, T.O., Jobic, H., *Journal of Physical Chemistry B* **2003**, 107(29), 7095-7101.
127. Albunia, A.R., Graf, R.G., A., Guerra, G., Spiess, H.W., *Macromolecules* **2009**, *42*, 4929-4931.
128. Schulz, M., Van Der Est, A., Rossler, E., Kossmehl, G., Vieth, H.-M., *Macromolecules* **1991**, *24*, 5040-5045.
129. Albunia, A.R., Graf, R., Guerra, G., Spiess, H.W., *Macromolecular Chemistry and Physics* **2005**, 206(7), 715-724.
130. Albunia, A.R., Gaeta, C., Neri, P.G., A., Milano, G., *J. Phys. Chem. B.* **2006**, (*110*), 19207-19214.
131. Ok, J.H., Vold, R.R., Vold, R.L., *J. Phys. Chem.* **1989**, *93*, 7618-7624.
132. Villanueva-Garibay, J.A., Muller, K., *Phys. Chem. Chem. Phys.* **2006**, *8*, 1394–1403.
133. Gonzalez, J., Devi, R.N., Tunstall, D.P., Cox, P.A., Wright, P.A., *Micro. Meso. Mater.* **2005**, *84*, 97-104.
134. Ueda, T., Kurokawa, K., Omichi, H., Miyakubo, K., Eguchi, T., *Chem. Phys. Lett.* **2007**, *443*, 293-297.
135. Dickinson, L.M., Harris, R.K., Shaw, J.A., Chinn, M., Norman, P.R., *Mag. Reson. Chem.* **2000**, 38(11), 918-924.

136. Taylor, J.M., Mah, R.K., Moudrakovski, I.L., Ratcliffe, C.I., Vaidhyanathan, R., Shimizu, G.K.H., *J. Am. Chem. Soc.* **2010**, *132*, 14055–14057.
137. Aksnes, D.W., Kimtys, L., *Solid State Nuclear Magnetic Resonance* **2004**, *25*, 146-152.
138. Ulrich, A.S., Grage, S.L., Solid State NMR of Polymers. Elsivier Science. **1998**.
139. Aliev, A.E., Harris, K.M., *J. Chem. Soc. Faraday Trans.* **1993**, *89*(20), 3797-3800.
140. Simpson, J.H., Rice, D.M., Karasz, F.E., Polymer **1991**, *32*(13), 2340-2344.
141. Girardeau, T.E., Leisen, J., Beckham, H.W., *Macromolecular Chemistry and Physics* **2005**, 206(10), 998-1005.
142. Tajouri, T., Hommel, H., *Magn. Reson. Chem.* **2007**, *45*, 488–495.
143. Kreger, K., Loffler, C., Walker, R., Wirth, N., Bingemann, D., Audorff, H., Rossler, E.A., Kador, L., Schmidt, H.W., *Macromol. Chem. Phys.* **2007**, *208*, 1530–1541.
144. Cao, H., Lin, G., Jones, A.A., *J. Polym. Sci. B: Polym. Phys.* **2005**, *43*, 2433–2444.
145. Wei, Y., Graf, R., Sworen, J.C., Cheng, C.-Y., Bowers, C.R., Wagener, K.B., Spiess, H.W., *Angew. Chem. Int. Ed.* **2009**, *48*, 4617 - 4620.
146. Nakajima, T., Akiyama, T., Furuya, H., *Polym. J.* **2001**, *33*(10), 825-829.
147. Horike, S., Matsuda, R., Tanaka, D., Matsubara, S., Mizuno, M., Endo, K., Kitagawa, S., *Angew. Chem. Int. Ed.* **2006**, *45*, 7226-7230.
148. Henrichs, P.M., Nicely, V.R., Fagerburg, D.R., *Macromolecules* **1991**, *24*(14), 4033-4037.
149. Simpson, J.H., Liang, W., Rice, D.M., Karasd, F.E., *Macromolecules* **1992**, *25*, 3068-3074.
150. Kolokolov, D.I., Arzumanov, S.S., Stepanov, A.G., Jobic, H., *Journal of Physical Chemistry C* **2007**, 111(11), 4393-4403.
151. Comotti, A., Bracco, S., Valsesia, P., Beretta, M., Sozzani, P., *Angew. Chem. Int. Ed.* **2010**, *49*, 1760-1764.
152. Gall, C.M., DiVerdi, J.A., Opella, S.J., *J. Am. Chem. Soc.* **1981**, *103*, 5039-5043.
153. Hiraoki, T., Kogame, A., Nishi, N., Tsutsumi, A., *J. Mol. Struct.* **1998**, *441*, 243-250.
154. Sarkar, S.K., Young, P.E., Torchia, D.A., *J. Am. Chem. Soc.* **1986**, *108*, 6459-6464.
155. Gall, C.M., Cross, T.A., DiVerdi, J.A., Opella, S.J., *Proc. Natl. Acad. Sci.* **1982**, *79*, 101-105.
156. Xue, Y., Pavlova, M.S., Ryabov, Y.E., Reif, B., Skrynnikov, N.R., *J. Am. Chem. Soc.* **2007**, *129*, 6827-6838.
157. Laws, D.D., L., B.H.-M., Jerschow, A., *Angew. Chem. Int. Ed.* **2002**, *41*, 3096-3129.

158. Levitt, M.H., *"spin dynamics: Basics of Nuclear Magnetic Resonance"* 2nd Edition, *Wiley*. UK, **2008**.
159. Hore, P.J., "*Nuclear Magnetic Resonance*" *Oxford University Press*. New York, **1995**.
160. Duer, M.J., *"Solid-State NMR Spectroscopy - principles and applications" Blackwell Science,* **2002**.
161. Duer, M.J., *"Introduction to Solid-State NMR Spectroscopy" Blackwell Publishing Ltd.*, **2004**.
162. Borisov, A.S., Hazendonk, P., *J. Inorg. Organomet. Polym.* **2010**, *20*, 183-212.
163. Colletti, R.F., Mathias, L.J., *"Solid State NMR of Polymers" Plenum Press*, New York, **1991**.
164. Jelinski, L.W., *Ann. Rev. Mater. Sci.* **1985**, *15*, 359.
165. Ashbrook, S.E., Duer, M.J., *Concepts in Magnetic Resonance Part A* **2006**, *28A*(3), 183-248.
166. Bennett, A.E., Rienstra, C.M., Auger, M., Lakshmi, K.V., Griffin, R.G., *J. Chem. Phys.* **1995**, *103*, 6951-6958.
167. Kolodziejski, W., Klinowski, J., Chemical Reviews **2002**, *102*(3), 613-628.
168. Hartmann, S.R., Hahn, E.L., *Phys. Rev. A* **1962**, *128*, 2042.
169. Harris, R.K., *Analyst* **1985**, (*110*), 649.
170. Law, R.V., Sherrington, D.C., Snape, C.E., *Macromolecules* **1997**, (*30*), 2868-2875.
171. Nowacka, A., Mohr, P.C., Norrman, J., Martin, R.W., Topgaard, D., *Langmuir* **2010**, *26*, 16848-16856.
172. Fyfe, C.A., Lyerla, J.R., Volksen, W., Yannoni, C.S., *Macromolecules* **1979**, *12*, 757.
173. Earl, W.L., VanderHart, D.L., *Macromolecules* **1079**, *12*, 762.
174. Andresen, J.M., Dennison, P.R., Maroto-Valer, M.M., Snape, C.E., Garcia, R., Moinelo, S.R., *Fuel* **1996**, 75(15), 1721–1726.
175. Schilling, M. *"Characterisation of soil organic matter by high resolution solid state carbon-13 nuclear magnetic resonance spectroscopy"* PhD. Florida State University, **2004**.
176. Moudrakovski, I., H., L., Ripmeester, J.A., *"Experimental solid state NMR of gas hydrates: problems and solutions"* Proceedings of the 6th International Conference on Gas Hydrates (ICGH 2008),, Vancouver, British Columbia, Canada, **2008**.
177. Silvestre, V., Mboula, V.M., Jouitteau, C., Akoka, S., Robins, R.J., Remaude, G.S., *Journal of Pharmaceutical and Biomedical Analysis* **2009**, (50), 336–341.
178. Canet, D., *Advances in Inorganic Chemistry* **2005**, *57*, 3-40.
179. Claridge, T.D.W., *"High Resolution NMR Techniques in Organic Chemsistry"*. *Elsevier*. Amsterdam, The Netherlands, **1999**.
180. Imanari, M., Uchida, K., Miyano, K., Seki, H., Nishikawa, K., *Phys. Chem. Chem. Phys.* **2010**, *12*, 2959.

181. Rouquerol, J., Avnir, D., Fairbridge, C.W., Everett, D.H., Haynes, J.H., Pernicone, N., Ramsay, J.D.F., Sing, K.S.W., Unger, K.K., *Pure and Appl. Chem.* **1994**, *66*(8), 1739-1758.
182. Leofanti, G., Padovan, M., Tozzola, G., Venturelli, B., *Catalysis Today* **1998**, *41*, 207-219.
183. Unger, K.K., Reichert, H., *Trends in Analytical Chemistry* **1991**, *10*(2), 44-48.
184. Attard, G., Barnes, C., *"Surfaces" Oxford University Press Inc.* New York, USA, **1998**.
185. Sing, K.S.W., *Pure & Appl. Chem.* **1982**, *54*(11), 2201-2218.
186. Dombrowski, R.J., Lastoskie, C.M., *Surface Science and Catalysis* **2002**, 144, 99-106.
187. Kluson, P., Scaife, S.J., *Chem. Biochem. Eng. Q.* **2001**, 15, 117-125.
188. Lastoskie, C.M., Gubbins, G.E., Quirke, N., *J. Phys. Chem.* **1993**, (97), 4786-4796.
189. Groen, J.C., Peffer, L.A.A., Perez-Ramirez, J., *Micro. Meso. Mater.* **2003**, (60), 1-17.
190. Zhu, H.Y., Maes, N., Molinard, A., Vansant, E.F., *Micro. Mater.* **1994**, 3, 235-243.
191. Olivier, J.P., *J. Porous. Mater.* **1995**, *2*, 9-17.
192. Maddox, M.W., Olivier, J.P., Gubbins, K.E., *Langmuir* **1997**, *13*, 1737-1745.
193. Occelli, M.L., Olivier, J.P., Perdingon-Melon, J.A., Auroux, A., *Langmuir* **2002**, *18*, 9186-9283.
194. Cote, A.P., El-Kaderi, H.M., Furukawa, H., Hunt, J.R., Yaghi, O.M., *J. Am. Chem. Soc.* **2007**, 129, 12914.
195. Jiang, J.X., Trewin, A., Su, F., Wood, C.D., Niu, H., Jones, J.T.A., Khimyak, Y.Z., Cooper, A.I., *Macromolecules* **2009**, *42*, 2658-2666.
196. Maddox, M.W., Olivier, J.P., Gubbins, G.E., *Langmuir* **1997**, *13*, 1737-1745.
197. Dawson, R., Cooper, A.I., Adams, D.J., Submitted **2012**.
198. Du, N., Park, H.B., Dal-Cin, M.M., Guiver, M.D., *Energy. Environ. Sci.* **2012**, *5*, 7306-7322.
199. http://www.tainstruments.com/lpage.aspx?n=1&id=9&siteid=11.
200. Goldstein, J., Newbury, D.E., Joy, D.C., Lyman, C.E., Echlin, P., Lifshin, E., Sawyer, L., Michael, J.R., *"Scanning Electron Microscopy and X-ray Microanalysis"*. 3rd Edition, *Springer Science and Business Media Inc.* USA, **2003**.
201. Chinchilla, R., Najera, C., *Chem. Rev.* **2007**, *107*, 874.
202. Bunz, U.H.F., *Chem. Rev.* **2000**, *100*, 1605.
203. Kimura, K., Kohama, S.-I., Yamazaki, S., *Polym. J.* **2006**, *38*(10), 1005-1022.
204. Tarazona, P., *Molecular Physics* **1984**, *52*(1), 81-96.
205. Trewin, A., Willock, D.J., Cooper, A.I., *J. Phys. Chem. C.* **2008**, *112*, 20549-20559.

206. Harris, R.K., Becker, E.D., Cabral de Menezes, S.M., Goodfellow, R., Granger, P., *Solid State Nuclear Magnetic Resonance* **2001**, *22*, 458-483.
207. Tozawa, T., Jones, J.T.A., Swamy, S., Jiang, S., Adams, D.A., Shakespeare, S., Clowes, R., Bradshaw, D., Hasell, T., Chong, S.Y., Tang, C., Thompson, S., Parker, J., Trewin, A., Bacsa, J., Slawin, A.M.Z., Steiner, A., Cooper, A.I., *Nat. Mat.* **2009**, *8*, 973-978.
208. Wilke, A., Weber, J., *J. Mater. Chem.* **2011**, *21*, 5226-5229.
209. Duncan, N.C., Hay, B.P., Hagaman, E.W., Custelcean, R., *Tetrahedron* **2012**, *68*, 53-64.
210. Layer, R.W., *Chem. Rev.* **1963**, *63*(5), 489-510.
211. An, J., Geib, S.J., Rosi, N.L., *J. Am. Chem. Soc.* **2010**, *132*, 38-39.
212. http://mailman.egr.msu.edu.mailman/public/thermal/2005/April/002684.html
213. Dawson, R., Su, F.B., Niu, H.J., Wood, C.D., Jones, J.T.A., Khimyak, Y.Z., Cooper, A.I., Macromolecules 2008, 41, 1591-1593.
214. Jones, J.T.A. *Synthesis and Characterization of Porous Organic/ Inorganic Hybrid Materials*. PhD. Liverpool, **2009**.
215. Bakhmutov, V.I., "*Practical NMR Relaxation for Chemists*" *Wiley*. **2004**.
216. Mackintosh, H.J., Budd, P.M., McKeown N.B., *J. Mater. Chem.* **2008**, (*18*), 573.
217. Park, H.B., Jung, C.H., Lee, Y.M., Hill, A.J., Pas, S.J., Mudie, S.T., Van Wagner, E., Freeman, B.D., Cookson, D.J., *Science* **2007**, *318*, 254-258.
218. McKeown, N.B., *J. Mater. Chem.* **2000**, *10*, 1979.
219. Banerjee, R., Phan, A., Wang, B., Knobler, C., Furukawa, H., O'Keeffe, M., Yaghi, O.M., *Science* **2008**, *319*, 939.
220. Bak, M., Rasmussen, J.T., Neilsen, N.C., *J. Magn. Reson.* 2000, 147, 296-330.
221. Macho, V., Brombacher, L., Spiess, H.W., *Appl. Magn. Reson.* **2001**, *20*, 405-432.
222. Comotti, A., Bracco, S., Valsesia, P., Beretta, M., Sozzani, P., *Angew. Chem. Int. Ed.* **2010**, *49*, 1760-1764.
223. Massiot, D., Fayon, F., Capron, M., King, I., Le Calvé, S., Alonso, B., Durand, J.O., Bujoli, B., Gan, Z., Hoatson, G., *Magn. Reson. Chem.* **2002**, *40*, 70-76.
224. Kemp, T.F., Smith, M.E., *Solid State Nuclear Magnetic Resonance* **2009**, *35*, 243-252.
225. Demyanova, l.P., Tressaud, A., J-Y., B., Martineau, C., Legein, C., Malovitsky, Y.N., Rimkevich, V.S., *Inorganic Materials* 2009, *45*(2), 151-156.
226. Abu-Baker, S., Lorigan, G.A., *Open Journal of Biophysics* 2012, *2*(4), 109-116.
227. Lidner, E., Hoehn, F., Salesch, T., Mayer, H.A., Singh, S., Muller, K., *Z. Anorg. Allg. Chem.* **2002**, (628), 1124-1131.

228. Lalowicz, Z.T., Stoch, G., Birczynski, A., Punkkinen, M., Krzystyniak, M., Gora-Marek, K., Datka, J., *Solid State Nuclear Magnetic Resonance* **2010**, 37, 91-100.
229. Stoch, G., Ylinen, E.E., Birczynski, A., Lalowicz, Z.T., Gora-Marek, K., Punkkinen, M., *Solid State Nuclear Magnetic Resonance* **2013**, http://dx.doi.org/10.1016/j.ssnmr.2012.11.004.
230. Clayden, N.J., *Polymer* **2000**, (41), 1167-1174.
231. Nishchenko, A.M., Kolokolov, D.I., Stepanov, A.G., *J. Phys. Chem. A.* **2011**, *115*, 7428-7436.
232. Muller-Plathe, F., *Macromolecules* **1996**, *29*, 4782-4791.
233. Jackson, C.L., B., M.G., *J. Chem. Phys.* **1990**, *93*(12), 9002-9011.
234. Jorgensen, W.L., Severance, D.L., *J. Am. Chem. Soc.* **1990**, *112*, 4768.
235. Shantz, D.F., Lobo, R.F., *J. Phys. Chem. B.* **1999**, *103*, 5920-5927.
236. Shustova, N.B., Ong, T.-A., Cozzolino, A.F., Michaelis, V.K., Griffin, R., Dinca, M., *J. Am. Chem. Soc.* **2012**, ASAP.
237. Kolokolov, D.I., Jobic, H., Stepanov, A., Guillerm, V., Devic, T., Serre, C., Ferey, G., *Angew. Chem. Int. Ed.* **2010**, *49*, 4791-4794.
238. Meilikhov, M., Yusenko, K., Torrisi, A., Jee, B., Mellot-Draznieks, C., Peoppl, A., Fischer, R.A., *Angew. Chem. Int. Ed.* **2010**, *49*, 6212-6215.
239. Serre, C., Millange, F., Thouvenot, C., Nogues, M., Marsolier, G., Louer, D., Ferey, G., *J. Am. Chem. Soc.* **2002**, *124*, 13519-13526.
240. Rice, D.M., *"NMR Spectroscopy of Polymers" Blackie Academic and Professional*, Glasgow, **1993**.
241. Speiss, H.W., Sillescu, H., *"Chem. Phys. Macromol.". CH*, Weinheim, **1991**.
242. Griffin, R.G., Beshah, K., Ebelhauser, R., Huang, T.S., Olejniczak, E.T., Rice, D.M., Siminovitch, D.J., Wittebort, R.J., *"The Time Domain in Surfaces and Structural Dynamics" Kluwer*, Dordrecht, **1988**.
243. Speiss, H.W., *Advances in Polymer Science* **1985**, *66*, 23.
244. Speiss, H.W., *Colloid & Polymer Sci.* **1983**, *261*, 193.
245. Sillescu, H., *Pure & Appl. Chem.* **1982**, *54*, 619.
246. Pandey, P.K., Katsoulidis, A. P., Eryazici, I., Wu, Y., Kanatzidiz, M. G., Nguyen, S. T., *Chem. Mater.* **2010**, *22*(17), 4974-4979.
247. Wan, S., Gandara, F., Asano, A., Furukawa, H., Saeki, A., Dey, S.K., Liao, L., Ambrogio, M.W., Botros, Y.Y., Duan, X., Seki, S., Stoddart, J.F., Yaghi, O.M., *Chem. Mater.* **2011**, DOI: 10.1021/cm201140r.
248. McKeown, N.B., Msayib, K., Tattershall, C. E., Budd, P. M., *Chem. Commun.* **2002**, 2782-2783.
249. Ghanem, B.S.M., N. B.; Budd, P. M.; Fritsch, D., *Macromolecules* **2008**, *41*, 1640-1646.
250. Carta, M.M., K. J.; Budd, P. M.; McKeown, N. B., *Org. Lett.* **2008**, *10*, 2641-2643.
251. Budd, P.M., Elabas, E.S., Ghanem, B.S., Makhseed, S., McKeown, N.B., Msayib, K.J., Tattershall, C.E., Wang, D., *Adv. Mater.* **2004**, *16*, 456–459.

252. Miao, Z., Fu, Y., Xu, Z., Li, G., Jiang, J., *Mendeleev Commun.* **2009**, *19*, 270-271.
253. Yang, G., Han, H., Du, C., Luo, Z., Wang, Y., *Polymer* **2010**, *51*, 6193-6202.
254. Uribe-Romo, F.J., Hunt, J.R., Furukawa, H., Klock, C., O'Keeffe, M., Yaghi, O.M., *J. Am. Chem. Soc.* **2009**, *131*, 4570–4571.
255. Suggs, J.W., *J. Am. Chem. Soc.* **1979**, *101*, 489-489.
256. Vaidhyanathan, R., Iremonger, S.S., Dawson, K.W., Shimizu, G.K.H., *Chem. Commun.* **2009**, 5230-5232.
257. Guerrero, R.S., Da'na, E., Sayari, A., *Ind. Eng. Chem. Res.* **2008**, *47*, 9406-9412.
258. Kim, S.N., Son, W.J., Choi, J.S., Ahn, W.S., *Micro. Meso. Mater.* **2008**, *115*, 497-503.
259. Zukal, A., Dominguez, I., Mayerova, J., Cejka, J., *Langmuir* **2009**, *25*, 10314-10321.
260. Harlick, P.J.E., Sayari, A., *Ind. Eng. Chem. Res.* **2007**, *46*, 446-458.
261. Tang, Y., Landskron, K., *J. Phys. Chem. C.* **2010**, *114*, 2494-2498.
262. Farha, O.K., *et al.*, *Chem. Mater.* **2009**, *21*, 3033-3035.
263. Ben, T., *et al.*, *Angew. Chem. Int. Ed.* **2009**, *48*, 9457-9460.
264. Rochelle, G.T., *Science* **2009**, (*325*), 1652.
265. Demessence, A., D'Allessandro, D.M., Foo, M.L., Long, J.R., *J. Am. Chem. Soc.* **2009**, *131*, 8784.
266. Caskey, S.R., Wong-Foy, A.G., Matzger, A.J., *J. Am. Chem. Soc.* **2008**, *130*(10870.).
267. Dawson, R., Stockel, E., Holst, J.R., Adams, D.J., Cooper, A.I., *Energy. Environ. Sci.* **2011**, *4*, 4239.
268. Rabbani, M.G., El-Kaderi, H.M., *Chem. Mater.* **2011**, *23*, 1650.
269. Dawson, R., Stöckel, E., Holst, J.R., Adams, D.J., Cooper, A.I., *Energy & Environmental Science* **2011,** *4*, 4239-4245
270. Rabbani, M.G., El-Kaderi, H.M., *Chem. Mater.* **2011**, 23(7), 1650-1653.
271. Mohanty, P., Kull, L.D., Landskron, K., *Nat Commun.* **2011**, 2, 401.
272. Dawson, R., Adams, D.J., Cooper, A.I., *Chemical Science* **2011**, 2, 1173-1177.
273. Simmons, J.M., Wu, H., Zhou, W., Yildirim, T., *Energy & Environmental Science* **2011**, 4(6), 2177-2185.
274. Jiang, S., Bacsa, J., Wu, X., Jones, J.T.A., Dawson, R., Trewin, A., Adams, D.J., Cooper, A.I., *Chem. Commun.* **2011**, 47(31), 8919-8921.

Appendix I

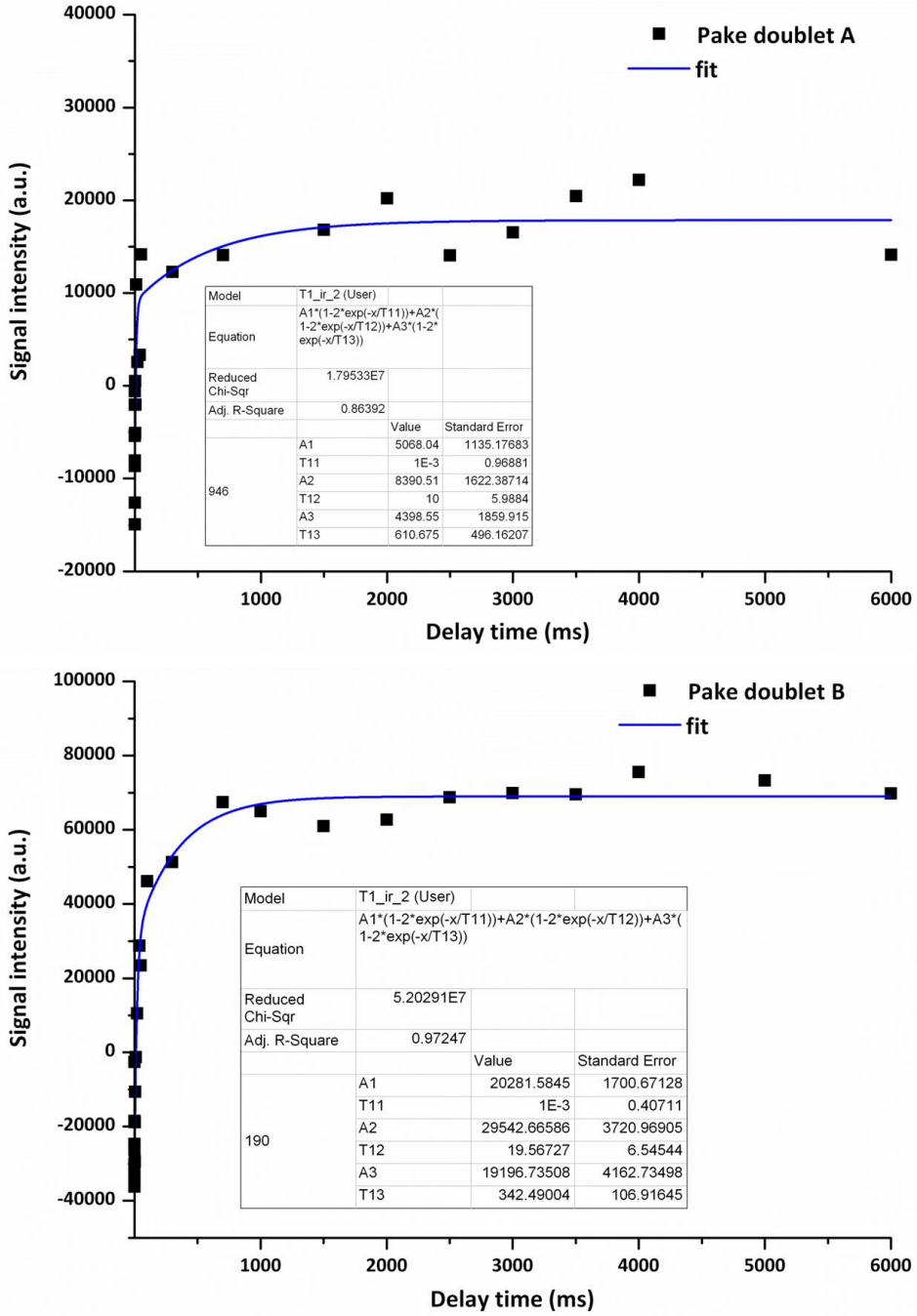

A1: Representative T_1 curves for CMP-1-d_4. Pake doublet A (top), Pake doublet B (bottom). Fitting parameters (inset) are summarised in **A3**.

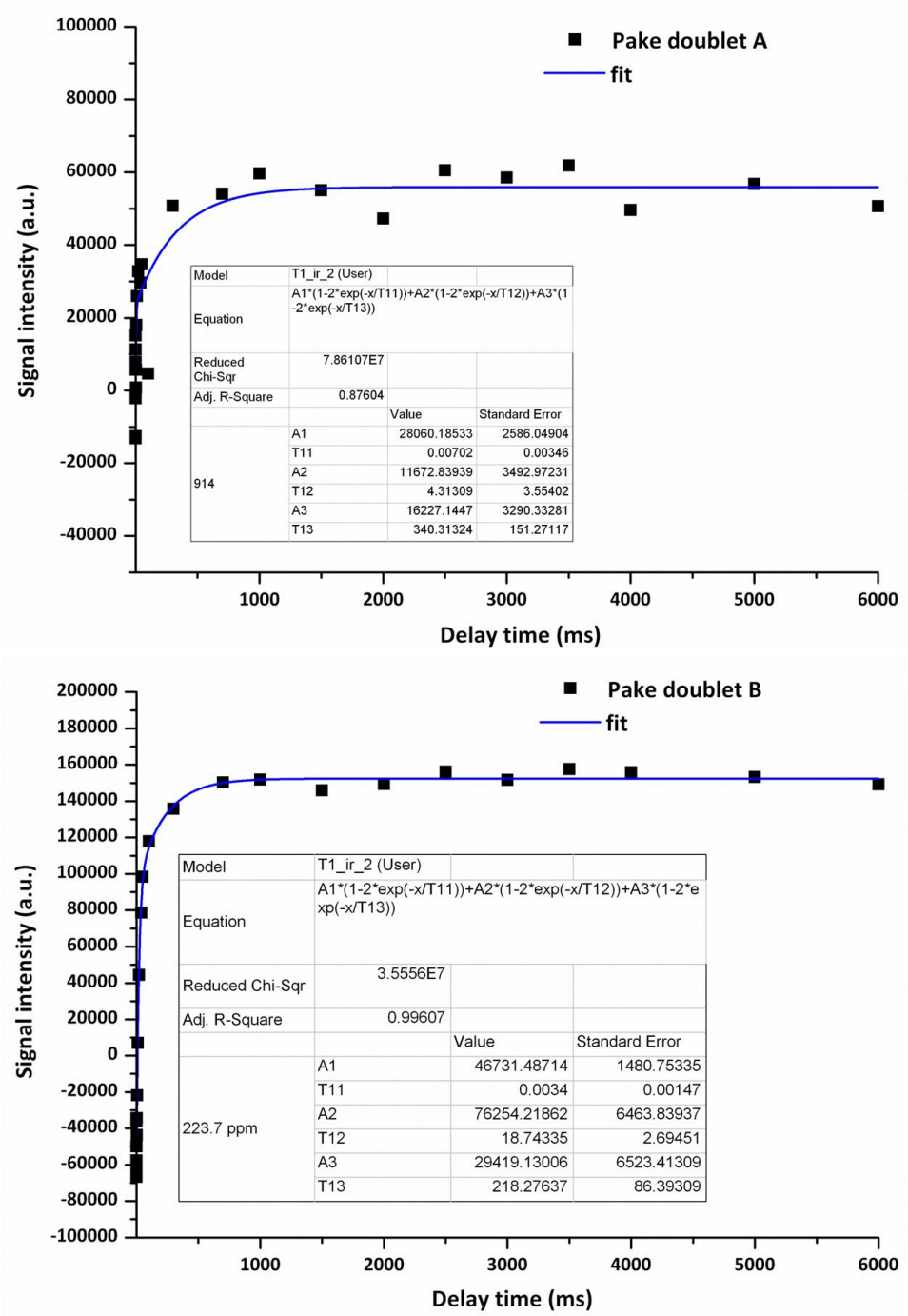

A2: Representative T_1 curves for CMP-2-d_8. Pake doublet A (top), Pake doublet B (bottom). Fitting parameters (inset) are summarised in Error! Reference source not found..

A3: T_1 relaxation parameters derived from ^2H relaxation NMR spectra for CMP-1-d_4 and CMP-2-d_8 networks.

Network	Pake doublet	Temp. (K)	Pre-exponential factors			Relaxation times			R^2
			$T_{1(a)}$ (au)	$T_{1(b)}$ (au)	$T_{1(c)}$ (au)	$T_{1(a)}$ (ms)	$T_{1(b)}$ (ms)	$T_{1(c)}$ (ms)	
CMP-1-d_4	A	373	5100 ± 1100	8400 ± 1600	4400 ± 1900	0.001 ± 0.9	10 ± 6	610 ± 330	0.864
		353	5400 ± 3000	7700 ± 3700	10600 ± 3800	0.01 ± 0.01	15 ± 22	880 ± 710	0.841
		333	7400 ± 600	2600 ± 1700	4600 ± 1600	0.01 ± .005	46 ± 51	1000 ± 650	0.925
		313	14100 ± 5300	4600 ± 5000	17200 ± 4000	0.01 ± 0.009	2 ± 6	1030 ± 440	0.838
		293	6500 ± 1000	4300 ± 900	9600 ± 900	0.008 ±0.005	2 ± 1	1100 ± 500	0.942
CMP-1-d_4	B	373	20300 ± 1700	29500 ± 3700	19200 ± 4200	0.001 ± 0.4	20 ± 7	340 ± 310	0.972
		353	20800 ± 2000	31200 ± 3200	21500 ± 3200	0.003 ± 0.003	17 ± 5	600 ± 580	0.989
		333	11600 ± 600	17000 ± 1000	7800 ± 1000	0.001 ± 0.01	25 ± 4	1100 ± 340	0.992
		313	17600 ± 2300	29200 ± 2600	15200 ± 2800	0.008 ± 0.003	20 ± 5	1200 ± 230	0.987
		293	11700 ± 970	17700 ± 1100	14500 ± 1100	0.005 ± 0.001	26 ± 4	1420 ± 110	0.992
CMP-2-d_8	A	373	28100 ± 2600	11700 ± 3500	16200 ± 3300	0.007 ± 0.003	4 ± 4	340 ± 150	0.876
		353	12000 ± 1400	12400 ± 3000	6100 ± 2900	0.001 ± 0.004	15 ± 9	370 ± 300	0.950
		333	23300 ± 1800	7900 ± 2700	21500 ± 2600	0.003 ± 0.003	8 ± 8	410 ± 150	0.940
		313	17100 ± 900	12700 ± 1600	9600 ± 1600	0.004 ± 0.001	25 ± 8	800 ± 300	0.989
		293	39800 ± 2300	18000 ± 2600	28700 ± 2700	0.007 ± 0.002	20 ± 9	1300 ± 150	0.976
CMP-2-d_8	B	373	46700 ± 1500	76300 ± 6500	29400 ± 6500	0.003 ±0.001	19 ± 3	220 ± 90	0.996
		353	21400 ± 3600	35700 ± 3300	9500 ± 1100	0.006 ±0.002	26 ± 5	220 ± 90	0.994
		333	41400 ± 2300	66700 ± 6700	39600 ± 6700	0.004 ± 0.002	13 ± 3	220 ± 90	0.991
		313	21500 ±1300	38100 ±5900	11700 ± 5800	0.002 ± 0.002	25 ± 6	270 ± 90	0.994
		293	37100 ± 3100	82500 ± 6000	43700 ± 6000	0.01 ± 0.004	12 ± 2	360 ± 90	0.989